

AGARD

ADVISORY GROUP FOR AEROSPACE RESEARCH & DEVELOPMENT
7 RUE ANCELLE, 92200 NEUILLY-SUR-SEINE, FRANCE

AGARD ADVISORY REPORT 319

Hypersonic Experimental and Computational Capability, Improvement and Validation

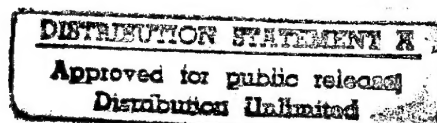
(l'Hypersonique expérimentale et de calcul — capacité,
amélioration et validation)

Volume I

This Advisory Report was prepared at the request of the Fluid Dynamics Panel.



NORTH ATLANTIC TREATY ORGANIZATION



Published May 1996

Distribution and Availability on Back Cover

AGARD

ADVISORY GROUP FOR AEROSPACE RESEARCH & DEVELOPMENT

7 RUE ANCELLE, 92200 NEUILLY-SUR-SEINE, FRANCE

AGARD ADVISORY REPORT 319

Hypersonic Experimental and Computational Capability, Improvement and Validation

(l'Hypersonique expérimentale et de calcul — capacité, amélioration et validation)

Volume I

DTIC QUALITY INSPECTED 4

Editors

William S. Saric
Mechanical and Aerospace
Engineering
Arizona State University
Tempe AZ 85287-6106
USA

Jean Muylaert
ESTEC
Aerothermodynamics Section
Postbus 299
2200 AG Noordwijk
NETHERLANDS

Christian Dujarric
ESA Headquarters
8-10 rue Mario Nikis
75015 Paris
FRANCE

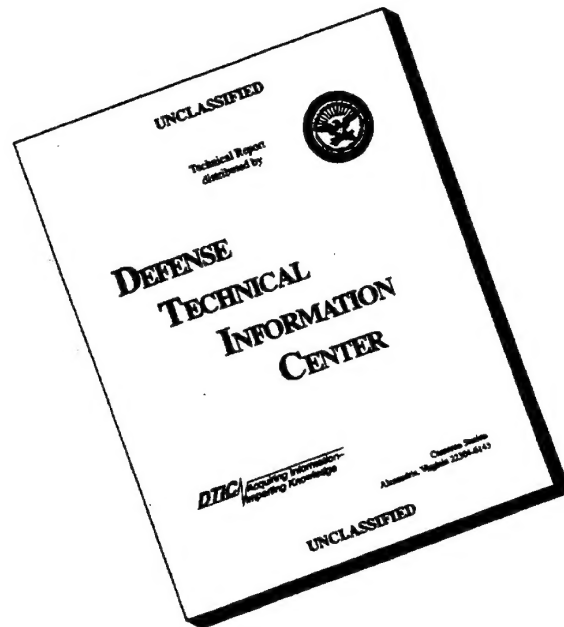
This Advisory Report was prepared at the request of the Fluid Dynamics Panel.



North Atlantic Treaty Organization
Organisation du Traité de l'Atlantique Nord

19960702 019

DISCLAIMER NOTICE



THIS DOCUMENT IS BEST QUALITY AVAILABLE. THE COPY FURNISHED TO DTIC CONTAINED A SIGNIFICANT NUMBER OF PAGES WHICH DO NOT REPRODUCE LEGIBLY.

The Mission of AGARD

According to its Charter, the mission of AGARD is to bring together the leading personalities of the NATO nations in the fields of science and technology relating to aerospace for the following purposes:

- Recommending effective ways for the member nations to use their research and development capabilities for the common benefit of the NATO community;
- Providing scientific and technical advice and assistance to the Military Committee in the field of aerospace research and development (with particular regard to its military application);
- Continuously stimulating advances in the aerospace sciences relevant to strengthening the common defence posture;
- Improving the co-operation among member nations in aerospace research and development;
- Exchange of scientific and technical information;
- Providing assistance to member nations for the purpose of increasing their scientific and technical potential;
- Rendering scientific and technical assistance, as requested, to other NATO bodies and to member nations in connection with research and development problems in the aerospace field.

The highest authority within AGARD is the National Delegates Board consisting of officially appointed senior representatives from each member nation. The mission of AGARD is carried out through the Panels which are composed of experts appointed by the National Delegates, the Consultant and Exchange Programme and the Aerospace Applications Studies Programme. The results of AGARD work are reported to the member nations and the NATO Authorities through the AGARD series of publications of which this is one.

Participation in AGARD activities is by invitation only and is normally limited to citizens of the NATO nations.

The content of this publication has been reproduced
directly from material supplied by AGARD or the authors.

Published May 1996

Copyright © AGARD 1996
All Rights Reserved

ISBN 92-836-1037-7



*Printed by Canada Communication Group
45 Sacré-Cœur Blvd., Hull (Québec), Canada K1A 0S7*

Hypersonic Experimental and Computational Capability, Improvement and Validation

(AGARD AR-319 Volume I)

Executive Summary

In 1987, the Fluid Dynamics Panel held a Symposium on Hypersonics. During this Symposium, it became clear that not a great amount of research had taken place in the preceding 15 years. However, due to a number of space-flight programs that had recently been initiated, there was a renewed interest in Hypersonic Aerothermodynamics.

By 1988, the HERMES and NASP programs were requiring significant advances in Hypersonics, and as a result an ad hoc study group on Hypersonic Research and Technology was formed under the guidance of the Fluid Dynamics Panel. Four technology interchange groups were established in the following topical areas: Rarefied Gases; Viscous Interactions and Transition; High Enthalpy Facilities; and Hypersonic Wind Tunnel Instrumentation. The work of these groups led to the formation of a formal Fluid Dynamics Panel Working Group, WG-18, to continue the work of these ad hoc groups.

A number of experiments have either been performed or are scheduled to be performed within the framework of this Working Group. Due to the complexities involved in assessing experimental data and in the CFD validation program, a two year extension to complete this activity was approved.

The present report is a summary of the initial two years of activity. Each Chapter contains a summary and a set of recommendations for the next period of activity. For this reason, no overall conclusions are presented in this report. A final report (Volume II) will be produced at the end of the Working Group 18 activities.

John K. Molloy
FDP, Executive

L'hypersonique expérimentale et de calcul — capacité amélioration et validation

(AGARD AR-319 Volume I)

Synthèse

En 1987, le Panel AGARD de la dynamique des fluides a organisé un symposium sur l'hypersonique lors duquel il a été constaté que très peu de travaux de recherche avaient été entrepris au cours des 15 années précédentes. Cependant, il y avait eu un regain d'intérêt dans l'aérodynamique hypersonique en raison du lancement récent d'un certain nombre de programmes de vols spatiaux.

Dès 1988, des progrès importants en hypersonique étaient demandés pour permettre la réalisation des programmes HERMES et NASP. Par conséquent, un groupe d'étude ad hoc sur la recherche et le développement de l'hypersonique a été créé sous l'égide du Panel de la dynamique des fluides. Quatre groupes d'échange de technologies ont été créés, couvrant les domaines suivants : les gaz raréfiés; les interactions visqueuses et la transition; les moyens d'essais haute enthalpie; et l'instrumentation des souffleries hypersoniques. Les travaux de ces groupes ont conduit à la création d'un groupe de travail officiel du Panel de la dynamique des fluides, le WG-18, qui a eu pour mandat de poursuivre les travaux de ces groupes ad hoc.

Un certain nombre d'expériences ont déjà été faites et d'autres sont prévues dans le cadre de ce groupe de travail. Vu la complexité de l'évaluation des données expérimentales en question, une prolongation des activités du groupe, d'une durée de deux ans, a été approuvée.

Ce rapport résume les deux premières années d'activité du groupe. Chaque chapitre contient un résumé et des recommandations concernant la prochaine phase des travaux. Par conséquent, le présent rapport ne présente pas de conclusions générales. Un rapport final sera publié à la conclusion des activités du groupe de travail N° 18.

John K. Molloy
Administrateur, FDP

Contents

	Page
Executive Summary	iii
Synthèse	iv
Preface	vi
Recent Publications of the Fluid Dynamics Panel	vii
Classification of Aerodynamic and Aerothermodynamics Issues and Problems by G.S. Deiwert	1
Shock-Wave/Boundary-Layer Interactions in High-Mach-Number Flows by J.M. Détery and A.G. Panaras	2
Laminar-Turbulent Transition by D.I.A. Poll	3
Rarefied Flow by J.N. Moss and J. Allègre	4
Real-Gas Effects by G.S. Deiwert and M. Pandolfi	5
Calibration Procedures for High-Enthalpy Facilities by G. Eitelberg	6
Extrapolation to Flight by J. Muylaert	7
Test Facilities by J. Arnold and J.F. Wendt	8

Preface

During the 1987 AGARD Symposium on Hypersonics, it became apparent that little significant research had taken place in the preceding 15 years. However, due to a number of space-flight programs initiated at or around the time of the symposium, there was a renewed interest in hypersonics.

In 1988, the HERMES and NASP programs were requiring significant advances in hypersonics and as a result, R. Graves and E. Reshotko founded the ad hoc group on hypersonic research and technology under the auspices of the AGARD-FDP in October 1988. During a two-year period, the ad hoc study group, representing Belgium, France, Germany and the USA had the task to prepare for possible formalized activities within AGARD such as a Working Group or Standing Committee. The original contributors to the ad hoc group were Bogdonoff, Delery, Dujarric, Ginoux, Graves, Keinappel, Leynaert, Reshotko, Thery and Wendt.

Four technology interchange groups of specialists were established in the following topical areas:

- Rarefield Gases;
- Viscous Interactions and Transition;
- High Enthalpy Facilities;
- Hypersonic-Wind-Tunnel Instrumentation.

The technology interchange groups organized their separate meetings and in the course of their work, identified research needs in their areas. As a result of this work, at the 66th FDP Business Meeting at Friedrichshafen, Germany in April 1990, K. Keinappel and C. Dujarric proposed the establishment of a FDP Working Group on the topic of "Definition of Calibration Experiments for High Enthalpy Facilities and for Real-Gas Code Validation".

This proposal, with minor modifications, was endorsed by the panel. Working Group 18, "Hypersonic Experimental and Computational Capability, Improvement and Validation" has been active since early 1992. The group is chaired by K. Keinappel and W. Saric. They are supported by the secretary, J. Muylaert. In addition to the usual practice of gathering and collating the existing knowledge base, this working group also coordinates specific trans-Atlantic cooperation. This aspect of its activities has made the membership desirable to all research groups in hypersonics. This has led to an unusually large number of members in this working group. Moreover, the number of panel members participating in the activities of WG-18 is also unusually large.

Within the framework of WG-18, a number of experiments have either been performed or are scheduled to be performed. Since the usual 2-year period for working groups is not of sufficient duration for the assessment of large-scale experiments as well as the applications of CFD validation, a two year extension has been granted for the working group. The present report is a summary of the initial two years of activity. Each Chapter contains a summary and a set of recommendations for the next period of activities. For this reason, no overall conclusions are presented here. A final report (Volume II) will be produced at the end of WG-18 work.

Members of the Working Group were as follows (FDP members are noted):

BELGIUM
J. Muylaert*, ESTEC
J. Wendt, VKI

FRANCE
J. Allègre, Sessia
J. Delery, ONERA
C. Dujarric*, ESA
G. François, ONERA
P. Vancamberg*, AMD

GERMANY
G. Eitelberg, DLR Göttingen
K. Keinappel*, DLR Berlin
P. Krogmann, DLR Göttingen

GREECE
A. Panaras*, HAF

ITALY
M. Borsi*, Alenia CAD
M. Pandolfi, Pol. di Torino

UNITED KINGDOM
D.I.A. Poll*, U. Manchester

UNITED STATES
J. Arnold, NASA Ames
S. Bogdonoff, Princeton
A. Boudreau*, AEDC
W. Calarese, WPAFB
S. Deiwert, Calspan
J. Moss, NASA Langley
W. Piland, NASA Langley
W. Saric*, Arizona State U.
G. Seibert, WPAFB
G. Settles, Penn State U.
L. Williams*, NASA Headquarters

* Fluid Dynamics Panel Member

We should like to acknowledge the support of Arizona State University during the preparation of this report. In particular, the first editor, W.S. Saric, would like to thank Ms. Colleen Leatherman, Mr. Mark Reibert and Mr. Joseph Myers for their contributions and hard work.

K. Keinappel, Chair
W.S. Saric, Co-Chair
January 1996

Recent Publications of the Fluid Dynamics Panel

AGARDOGRAPHS (AG)

Computational Aerodynamics Based on the Euler Equations

AGARD AG-325, September 1994

Scale Effects on Aircraft and Weapon Aerodynamics

AGARD AG-323, July 1994

Design and Testing of High-Performance Parachutes

AGARD AG-319, November 1991

Experimental Techniques in the Field of Low Density Aerodynamics

AGARD AG-318 (E), April 1991

Techniques expérimentales liées à l'aérodynamique à basse densité

AGARD AG-318 (FR), April 1990

A Survey of Measurements and Measuring Techniques in Rapidly Distorted Compressible Turbulent Boundary Layers

AGARD AG-315, May 1989

Reynolds Number Effects in Transonic Flows

AGARD AG-303, December 1988

REPORTS (R)

Parallel Computing in CFD

AGARD R-807, Special Course Notes, October 1995

Optimum Design Methods for Aerodynamics

AGARD R-803, Special Course Notes, November 1994

Missile Aerodynamics

AGARD R-804, Special Course Notes, May 1994

Progress in Transition Modelling

AGARD R-793, Special Course Notes, April 1994

Shock-Wave/Boundary-Layer Interactions in Supersonic and Hypersonic Flows

AGARD R-792, Special Course Notes, August 1993

Unstructured Grid Methods for Advection Dominated Flows

AGARD R-787, Special Course Notes, May 1992

Skin Friction Drag Reduction

AGARD R-786, Special Course Notes, March 1992

Engineering Methods in Aerodynamic Analysis and Design of Aircraft

AGARD R-783, Special Course Notes, January 1992

Aircraft Dynamics at High Angles of Attack: Experiments and Modelling

AGARD R-776, Special Course Notes, March 1991

ADVISORY REPORTS (AR)

Aerodynamics of 3-D Aircraft Afterbodies

AGARD AR-318, Report of WG17, September 1995

A Selection of Experimental Test Cases for the Validation of CFD Codes

AGARD AR-303, Vols. I and II, Report of WG-14, August 1994

Quality Assessment for Wind Tunnel Testing

AGARD AR-304, Report of WG-15, July 1994

Air Intakes of High Speed Vehicles

AGARD AR-270, Report of WG13, September 1991

Appraisal of the Suitability of Turbulence Models in Flow Calculations

AGARD AR-291, Technical Status Review, July 1991

Rotary-Balance Testing for Aircraft Dynamics

AGARD AR-265, Report of WG11, December 1990

Calculation of 3D Separated Turbulent Flows in Boundary Layer Limit

AGARD AR-255, Report of WG10, May 1990

Adaptive Wind Tunnel Walls: Technology and Applications

AGARD AR-269, Report of WG12, April 1990

CONFERENCE PROCEEDINGS (CP)

Aerodynamics of Store Integration and Separation

AGARD CP-570, February 1996

Aerodynamics and Aeroacoustics of Rotorcraft

AGARD CP-552, August 1995

Application of Direct and Large Eddy Simulation to Transition and Turbulence

AGARD CP-551, December 1994

Wall Interference, Support Interference, and Flow Field Measurements

AGARD CP-535, July 1994

Computational and Experimental Assessment of Jets in Cross Flow

AGARD CP-534, November 1993

High-Lift System Aerodynamics

AGARD CP-515, September 1993

Theoretical and Experimental Methods in Hypersonic Flows

AGARD CP-514, April 1993

Aerodynamic Engine/Airframe Integration for High Performance Aircraft and Missiles

AGARD CP-498, September 1992

Effects of Adverse Weather on Aerodynamics

AGARD CP-496, December 1991

Manoeuvring Aerodynamics

AGARD CP-497, November 1991

Vortex Flow Aerodynamics

AGARD CP-494, July 1991

Missile Aerodynamics

AGARD CP-493, October 1990

Aerodynamics of Combat Aircraft Controls and of Ground Effects

AGARD CP-465, April 1990

Computational Methods for Aerodynamic Design (Inverse) and Optimization

AGARD CP-463, March 1990

Applications of Mesh Generation to Complex 3-D Configurations

AGARD CP-464, March 1990

Fluid Dynamics of Three-Dimensional Turbulent Shear Flows and Transition

AGARD CP-438, April 1989

Validation of Computational Fluid Dynamics

AGARD CP-437, December 1988

Aerodynamic Data Accuracy and Quality: Requirements and Capabilities in Wind Tunnel Testing

AGARD CP-429, July 1988

Aerodynamics of Hypersonic Lifting Vehicles

AGARD CP-428, November 1987

Aerodynamic and Related Hydrodynamic Studies Using Water Facilities

AGARD CP-413, June 1987

Applications of Computational Fluid Dynamics in Aeronautics

AGARD CP-412, November 1986

CHAPTER I

CLASSIFICATION OF AERODYNAMIC AND AEROTHERMODYNAMICS ISSUES AND PROBLEMS

George S. Deiwert

MS 230-2/RT
NASA-Ames Research Center
Moffett Field, California, 94035-1000
USA

CONTENTS

1	AERODYNAMIC PARAMETERS	1
2	VISCOUS INTERACTIONS	2
3	LAMINAR-TURBULENT TRANSITION	2
4	FOREBODY HEAT-TRANSFER RATES	2
5	RADIATION AND ABLATION	3
6	LEE AND BASE FLOWS	3
7	LOW DENSITY	3
	REFERENCES	4
	TABLE AND FIGURES	5

For the purpose of discussion, aerothermodynamic phenomena are classified into seven types: aerodynamic parameters, viscous/shock interaction, boundary-layer transition, forebody-heating/heat-transfer, radiation and ablation, lee and base-region flow, and low-density flow. These seven types are listed in the first column of Table 1, are illustrated schematically in Figures 1 - 7, and are discussed in the following. This discussion defines the basis for the first phase of the Working Group 18 activities.

1 AERODYNAMIC PARAMETERS

Aerodynamic parameters including lift, drag, and moment coefficients, in the real flight of blunt vehicles such as Apollo and slender vehicles such as the Shuttle Orbiter, are different from those deduced from calculations or experimental studies made in the perfect-gas facilities (Hillje and Savage 1968; Maus et al. 1984; Park 1990). The difference is particularly prominent in the trim angles of attack of these vehicles at hypersonic Mach numbers: typically the trim angle is larger than predicted by 2° to 4°. The real-gas phenomena are believed to influence the pressure distribution via the changes in the effective specific heat ratio, γ , which occur mostly under equilibrium or near-equilibrium conditions for a blunt body, and via the geometrical imbalance in pressures due to the nonequilibrium phenomena which occur mostly for a body with sharp leading edge.

The effective specific-heat ratio, γ , is well defined for equilibrium or near-equilibrium real-gas flow as well as for perfect-gas flow. When real-gas processes absorb energy, both the specific heat at constant pressure and that at constant volume increase, and γ in a real-gas is smaller than in a perfect gas. The pressure distribution in such a real gas could be calculated approximately by assuming that the gas is perfect but that γ varies appropriately from point to point, always with a value less than that in a perfect gas, if such a γ distribution can be determined a priori. For a perfect gas of constant γ , the pressure at the stagnation point or on a flat plate at an inclined angle with an attached oblique shock can be expressed as a function of the assumed γ . Such a relationship shows that the surface pressure increases when γ decreases. This phenomenon is strong near the blunt nose or blunt leading edge, where the shock angle is large, and weak elsewhere. The greater pressure near the leading edge of a wing causes the center of pressure to move forward, which results in an increase (nose up) in pitching moment. This phenomenon occurs most pronounced under equilibrium or near-equilibrium conditions.

When the flow is in a highly nonequilibrium condition, or when the leading edge is sharp, a different type of phenomenon affects the pressure distribution (Park 1990; Rakich et al. 1983). Consider a thin wing consisting of a flat plate with a sharp leading edge inclined at an angle. The flow approaches equilibrium near the trailing edge and is far from equilibrium near the leading edge because the flow residence time is longer near the trailing edge than near the leading edge. As a result, the effective γ is smaller near the trailing edge than near the leading edge. The smaller γ near the trailing edge implies a greater density and consequently a smaller shock angle. Thus, the oblique shock over the inclined flat plate has the largest shock angle at the leading edge. This decrease in shock angle causes a corresponding decrease in pressure toward the trailing edge, which leads to a forward shift of the center of pressure. This phenomena was, in fact, observed in the early flights of the Space Shuttle Orbiter, although it was not predicted from the ground-test data base.

In both equilibrium and nonequilibrium conditions, the center of pressure in a real-gas flow is located generally ahead of that in a perfect-gas flow. As a result, the trim angle of attack generally increases. Since there are more than one mechanism causing the trim shift, there may be instances where they cancel each other and produce no trim shift. The extent of the shift of center of pressure or trim angle depends delicately on both the state of the gas and body geometry. Numerical calculations of these phenomena are generally difficult because the moment coefficients are sensitive to small errors in calculation.

2 VISCOUS INTERACTIONS

During the first high-speed reentry of the Shuttle Orbiter, the body flaps were deflected to the maximum allowable angle in order to produce upward lift in the tail region and thereby offset the forward shift of the center of pressure mentioned above. A deflected flap produces a flow feature known as a compression corner. In the flight of the Shuttle Orbiter, the compression corner produced by the body flap did perform significantly more effectively than predicted, yet the deflection did not fully compensate for the forward shift of the pressure center produced by the real gas reduced gamma effect (Maus et al. 1984). The phenomenon, which will be discussed in Chapter VII, was incorrectly attributed to the increased size of the viscous interaction region due to the thickening of the boundary layer at the altitudes where the phenomenon was observed (Holden 1986). In actual fact, high temperature real-gas phenomena provide another explanation. In a supersonic flow over a cooled wall, temperature reaches a maximum value inside the boundary layer as a result of recovery of kinetic energy. Vibrational excitation and dissociation will occur in this high-temperature zone. These real-gas phenomena absorb energy and thereby lowers the temperature. This in turn causes the density in the high-temperature region to be higher than in a perfect-gas flow, leading to a thinner boundary layer. The thinner boundary layer results in a weaker shock/boundary-layer interaction and a smaller separation bubble. Therefore, a deflected flap should be more effective in a reacting flow than in a perfect-gas flow, mitigating the reasoning made by Maus et al. (1984). This behavior has recently been fully described by Weilmuenster et al. (1993).

The compression corner is a comparatively simple problem of viscous-inviscid interaction in which the high-temperature real-gas effects may possibly be important. A more complicated viscous-inviscid interaction occurs in a shock/boundary-layer interaction in which a shock intercepts a boundary layer. Such flowfields occur, for example, inside the inlet and the combustion chamber of a scramjet engine (Law 1972). Another complicated flow is one in which two shocks intersect (Edney 1968). Such a flow occurs, for example, when the bow shock from the nose intersects the bow shock from the wing or vertical tail of a vehicle such as the Shuttle Orbiter. In these three types of flows, represented by Figure 2, the peak heat-transfer rates occur immediately downstream of the point of strong pressure gradient where the

boundary layer is the thinnest and are very high, as indicated by the solid curves in the lower figures.

The problem of viscous/shock interaction has been studied for a long time. Until recently (Kortz et al. 1993), the effect of the high-temperature real-gas phenomena on such flows has been neglected. In an arbitrary flow geometry the location of the shock, the thickness of the shock layer, etc., may be affected by the real-gas phenomena. Moreover, the wall heat-transfer rates are affected by the real-gas phenomena via surface catalysis. By making the surface noncatalytic to recombination of atomic species, the wall heat transfer rate can potentially be reduced. The extent of the reduction will depend on the degree of dissociation at the edge of the boundary layer, which is in turn affected by the nonequilibrium rate processes occurring in the region. Theoretical descriptions of such phenomenon are beyond our present capability, and therefore, experimental approaches must be taken. The program of future experiments is presented in Chapter II.

3 LAMINAR-TURBULENT TRANSITION

In a flow over a curved surface with a negative pressure gradient, shown schematically in Figure 3, it is known that the boundary layer may remain laminar to a relatively large Reynolds number. In the case of the Shuttle Orbiter (Goodrich et al. 1983), transition over the portions of the wings where the pressure gradient was negative, occurred at x -Reynolds numbers higher than 10^8 . This occurred despite of the gaps between heat-shield tiles. One may surmise that this delay of transition may be due to the chemistry effects. Turbulent transition is known to be sensitive to inflections in the density profile within the boundary layer. The density profile is related to the temperature profile, which in turn is dictated partly by chemistry. Because of the recovery phenomenon mentioned in the preceding section, the chemical reactions occurring in the high temperature zone of the boundary layer tend to depress the temperature there. According to this reasoning, the density profile in a real-gas should be flatter, and therefore turbulent transition should be less likely. Stability analyses of chemically-reacting hypersonic boundary layers predict these trends (Reed et al. 1992; Stuckert and Reed 1992, 1994). The bulk of these ideas are covered in Chapter III.

4 FOREBODY HEAT-TRANSFER RATES

Data from the Shuttle Orbiter demonstrate that over most of its hypersonic flight range, the heat-transfer rates to the surface of a vehicle can be minimized by making the surface chemically noncatalytic to the reactions involving atomic oxygen, nitrogen, and possibly nitric oxide molecules as shown in the schematic example of Figure 4 and the work of Stewart et al. (1993) and Scott (1983). However, quantitative characterization of this process is found to be difficult, mainly because the surface processes are not easily amenable to theoretical analysis. Thus, the study of this phenomenon is left mostly to experimentation. There are two types of such problems: First, the surface catalytic efficiency of the heat-

shield materials must be measured under realistic thermochemical conditions, in a well characterized flowfield such as at the stagnation point of a sphere. Second, the heat-transfer rates to the surface of specified catalytic efficiency must be measured over a model of given geometry.

5 RADIATION AND ABLATION

Radiative heating of entry vehicles becomes significant at velocities greater than about 9 km/s in the Earth's atmosphere and 7 km/s in the Martian atmosphere (see Figure 5). Radiative heating is a problem for two different types of vehicles: the AeroSpace Transfer Vehicles (ASTVs) and the Apollo-type direct-entry vehicles. The ASTVs fly only at high altitudes and do not descend to the planet surface. Radiative heating for these vehicles is dominated by chemical-nonequilibrium phenomena in shock layers (Park 1985a).

At freestream densities corresponding to altitudes below 70 km, the nonequilibrium-radiation behavior was found through laboratory experiments to conform to the binary-scaling law (Park 1985b; Cauchon 1967). According to this law, the intensity of the nonequilibrium radiation is proportional to density while the shock-layer stand-off distance decreases with density behind the shock. Conceptually, therefore, the radiative heat-transfer rate to the vehicle, which is a product of the mean value of radiation intensity and the thickness of the radiating zone, is approximately a constant. The flight tests made with the Fire vehicle at altitudes above 70 km did not confirm the binary-scaling relationship (Park 1985a; Cauchon 1967). The data were interpreted to mean that the binary-scaling relationship breaks down at altitudes above 70 km because there are insufficient collisions for the radiation to occur, that is, a collision-limiting phenomenon occurs (Cauchon 1967). An alternative description of the same results is that the Fire vehicle was simply not large enough to permit the full nonequilibrium layer to develop before the flow is entrained in the boundary layer or expansion around the body quenched radiation, that is, a truncation phenomenon occurred (Park 1985a). An up-to-date method of calculating nonequilibrium radiation (Park 1985b) indicates that the binary-scaling law is valid up to an altitude of 110 km, and the behavior observed for the Fire vehicle was due to the truncation phenomenon (Park 1989). Experimental verification is needed to determine at what combination of altitude and the vehicle size the binary-scaling law fails and the collision-limiting phenomenon becomes dominant.

For Apollo-type vehicles, peak radiative heating occurs at relatively low altitudes where the shock layer is nearly in chemical equilibrium (Curry and Stephens 1970). The extent of ablation of the heat-shield materials over the Apollo vehicle during the Earth entry flight is different from the predictions made prior to flight (Park 1985a). Calculations indicate that the extent of ablation is only about half of that predicted by the most pessimistic method but twice that predicted by the most optimistic method. Ablation in this case is dictated mostly by radiative heating. Convective heat-transfer rates are nearly zero here because the outward flow of

ablation products prevents the conductive heat flux from the hot region from reaching the wall.

The problem of radiative heating of the Apollo-type vehicle is complicated further by the inevitable ablation of the heat shield. The product gas of ablation forms a layer, which is commonly called ablation-product layer, which shields the hot shock layer gas from reaching the wall. The ablation-product layer absorbs a portion of the radiative flux directed toward the wall. In order to accurately predict the extent of ablation of the heat shield, one must accurately predict the thickness of the ablation-product layer and the thermochemical state therein. There are several difficulties in doing so, aside from the computational problem mentioned above. First, when the ablation rate is substantial, the process could be turbulent (Park 1989). Second, the ablation-product layer may not be in chemical equilibrium (Curry and Stephens 1970). Third, ablation may occur partly through spallation. The spalled particles may penetrate deeply into the inviscid region of the shock layer (Davies and Park 1984; Park 1984), vaporize, and absorb or emit radiation therein. Theoretical calculation of such an environment has not yet been possible.

6 LEE AND BASE FLOWS

The flowfield and heat-transfer rate distribution in the leeward side or base region of the Apollo (Cauchon 1967; Slocumb 1967) and Space Shuttle Orbiter (Kleb and Weilmuenster 1992), depicted symbolically in Figure 6, are difficult to predict. This is because the behavior of such flows is affected by poorly understood crossflow, vortex flows, turbulence, inviscid shear flows, entropy layers, and temporal instability, in these geometries. In a high-enthalpy flow, these effects are combined with the chemical reactions that influence the temperature and density.

At reentry flight speeds in excess of 9 km/s, the radiation emission in the base region may become sufficiently large to warrant attention (Strawa et al. 1992). For a recently envisioned aerobraking vehicle, the payload would be stowed in the base region. As satellites, these vehicles are designed typically to withstand only the rate of radiative heating by the Sun, which is 0.14 W/cm^2 . During atmospheric reentry the radiative heat-transfer rate reaching the payload exceeds this value. The magnitude of the radiative heat transfer rate reaching the base region is presently unknown (Strawa et al. 1992).

7 LOW DENSITY

Low-density, real-gas questions involve such issues as thick shock structure, noncontinuum analysis methods, thermal nonequilibrium, and surface accommodation. Rarefaction effects occur over a wide range of conditions ranging from low-density, high-altitude flight to relatively high-density flows of components with small characteristic lengths. Aerodynamic drag and heating behavior is different from continuum trends and should be considered when significant flight time is expected under these conditions. A particular interest for orbiting satellites which are used to perform aeropass maneuvers to achieve orbit modification, is the

aerodynamic drag and heating and the influence of surface accommodation on these parameters. This is shown schematically in Figure 7.

Two particular areas of present interest involving low-density flows concern 1) the interaction of reactive-control-system jet plumes with control surfaces of vehicles, and 2) the wake closure of bluff-capsule reentry vehicles. These phenomena are described in some detail in Chapter IV.

REFERENCES:

- Cauchon, D.L. 1967 Radiative Heating Results from the Fire 2 Flight Experiment in an Reentry Velocity of 11.3 Kilometers per Second. *NASA TM X-1402*.
- Curry, D.M. and Stephens, E.W. 1970 Apollo Ablator Thermal Performance at Superorbital Entry Velocities. *NASA TN D-5969*.
- Davies, C.B. and Park, C. 1983 Trajectories of Solid Particles Spalled from a Carbonaceous Heat Shield. in: Entry Vehicle Heating and Thermal Protection Systems: Space Shuttle, Solar Starprobe, Jupiter Galileo Probe, *Prog. Astro. and Aero.*, Vol. 85, eds. P.E. Bauer, H.E. AIAA, New York.
- Edney, B. 1984 Anomalous Heat Transfer and Pressure Distributions on Blunt Bodies at Hypersonic Speeds in the Presence of an Impinging Shock. Aeronautical Research Institute of Sweden, *Report 115*, Stockholm.
- Goodrich, W.D., Derry, S.M. and Bertin, J.J. 1983 Shuttle Orbiter Boundary Layer Transition at Flight and Wind Tunnel Conditions. *Shuttle Performance: Lessons Learned*, NASA CP 2283, eds. J.P. Arrington J.J. Jones, 753.
- Hillje, E.R. and Savage, R. 1968 Status of Aerodynamic Characteristics of the Apollo Entry Configuration. *AIAA Paper 68-1143*.
- Holden, M.S. 1986 A Review of Aerothermal Problems Associated with Hypersonic Flight. *AIAA Paper 86-0267*.
- Kleb, W.L. and Weilmuenster, K.J. 1992 Characteristics of the Shuttle Orbiter Leeside Flow During Reentry Condition. *AIAA Paper No. 92-2951*.
- Kortz, R., McIntyre, T. and Eitelberg, G. 1993 *XIX Intn'l Symp. on Shock Waves*, Marseilles, France.
- Law, H. 1972 Two-Dimensional Compression Corner and Planar Shock Wave Interactions with a Supersonic, Turbulent Boundary Layer. *ARL TR 75-0157*, AFSC.
- Maus, J.R., Griffith, B.J., Szema, K.Y. and Best, J.T. 1984 Hypersonic Mach Number and Real Gas Effects on Space Shuttle Orbiter Aerodynamics. *J. Spacecraft Rockets*, Vol. 21, 136.
- Park, C. 1984 Injection-Induced Turbulence in Stagnation-Point Boundary Layers. *AIAA J.*, Vol. 22, 219.
- Park, C. 1985a Radiation Enhancement by Nonequilibrium in Earth's Atmosphere. *J. Spacecraft Rockets*, Vol. 22, 27.
- Park, C. 1985b Calculation of Nonequilibrium Radiation in the Flight Regimes of Aeroassisted Orbital Transfer Vehicles. *Thermal Design of Aeroassisted Orbital Transfer Vehicles*, *Prog. Astro. and Aero.*, Vol. 96, ed. H. F. Nelson, AIAA, New York, NY.
- Park, C. 1989 Assessment of Two-Temperature Kinetic Model for Ionizing Air. *J. Thermophys. Heat Trans.*, Vol. 3, 233.
- Park, C. 1990 *Nonequilibrium Hypersonic Aerothermodynamics*, Wiley, New York.
- Park, C. 1993 Chemical-Kinetic Problems of Future NASA Missions. 1. Earth Entries. *J. Thermophys. Heat Trans.* Vol. 7, 385.
- Rakich, J.V., Bailey, H.E. and Park, C. 1983 Computation of Nonequilibrium, Supersonic Three-Dimensional Inviscid Flow Over Blunt-Nosed Bodies. *AIAA J.*, Vol. 21, 834.
- Reed, H.L., Stuckert, G.K., and Haynes, T.S. 1992 Stability of Hypersonic Boundary-Layer Flows with Chemistry. *Theoretical and Experimental Methods in Hypersonic Flows*, AGARD-CP-514.
- Scott, C.D. 1983 A Review of Nonequilibrium Effects and Surface Catalysis on Shuttle Heating. *Shuttle Performance: Lessons Learned*, NASA CP 2283, eds. J.P. Arrington, J.J. Jones, 865.
- Slocumb, T.H., Jr. 1967 Project Fire Flight 2 Afterbody Temperatures and Pressures at 11.35 Kilometers per Second. *NASA TM X-1319*.
- Stewart, D.A., Rakich, J.V. and Lanfranco, M.J. 1983 Catalytic Surface Effects on Space Shuttle Thermal Protection System. *Shuttle Performance: Lessons Learned*, NASA CP 2283, eds. J.P. Arrington, J.J. Jones, 827.
- Strawa, A.W., Park, C., Davy, W.C., Babikian, D.S. and Prabhu, D.K. 1992 Proposed Radiometric Measurement of the Wake of a Blunt Aerobrake. *J. of Spacecraft Rockets*, Vol. 29, 765.
- Stuckert, G. and Reed, H.L. 1991 Unstable Branches of a Hypersonic, Chemically Reacting Boundary Layer. *Proc. Roy. Aero. Soc.: Boundary-Layer Transition and Control*, Cambridge.
- Stuckert, G. and Reed, H.L. 1992 Linear Disturbances in Hypersonic, Chemically Reacting Shock Layers. *AIAA J.* Vol. 32, 1384.
- Weilmuenster, K.J., Gnoffo, P.A. and Greene, F.A. 1993 Navier-Stokes Simulations of the Shuttle Orbiter Aerodynamic Characteristics with Emphasis on Pitch Trim and Body Flap. *AIAA Paper 93-2814*.

Table 1. Aerothermodynamics Phenomena and Ground Test Capability

Category	Ground test Facility	Facility Uncertainties	Required Calibration
1. Aerodynamic Parameters pressure	shock tunnel	contamination	shock layer emission
	hot-shot tunnel	dissociation	shock stand-off sphere heating
	expansion tube	short test time	shock stand-off sphere heating
Cd, Cl, trim angle	free-flight range	swerving motion	none
2. Viscous/shock interaction	shock tunnel	contamination	shock layer emission
	hot-shot tunnel	dissociation transition	shock stand-off sphere heating cone transition
	expansion tube	short test time transition	shock stand-off sphere heating cone transition
	track range	restricted geometry	sphere heating
3. Boundary layer Transition	pressurized range	restricted geometry tip ablation surface roughness	cone transition
4. Forebody heating/ Heat Transfer	arc-heated tunnel	uncertain enthalpy noneq freestream	shock layer emission stream properties
	simple shapes	track range	instrumentation
	complex shapes	shock tunnel hot-shot tunnel	contamination dissociation shock layer emission stream properties sphere heating
5. Radiation and Ablation	ballistic range with counterflow	contamination	shock layer emission
	equilibrium	arc-heated tunnel	low Reynolds No. uncertain enthalpy shock layer emission sphere heating
	nonequilibrium	large shock tube	contamination none
6. Lee and Base Flow	free-flight range	instrumentation flow visualization	sphere heating
7. Low Density Flow	Low Pressure Tunnel	low enthalpy	stream properties
	Large Shock Tube	contamination	none

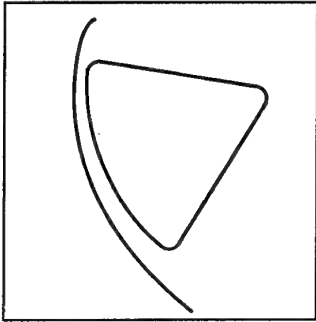


Figure 1. Aerodynamic Parameters:
 p , C_d , C_l , trim angle.

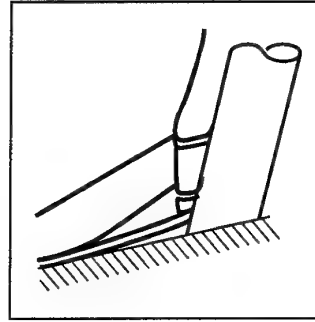


Figure 2. Viscous/shock interaction.

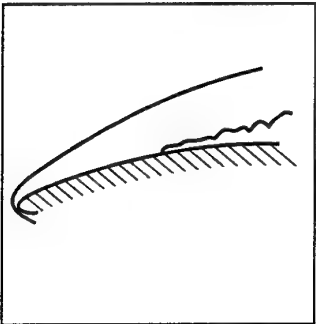


Figure 3. Boundary-layer transition.

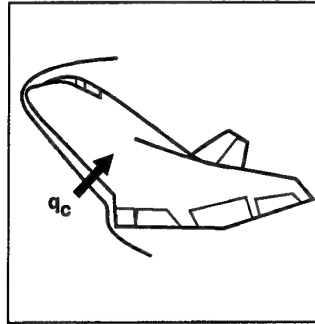


Figure 4. Forebody heating and
heat transfer.

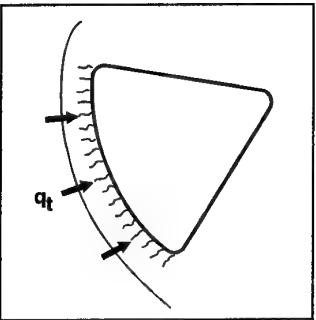


Figure 5. Radiation and ablation.

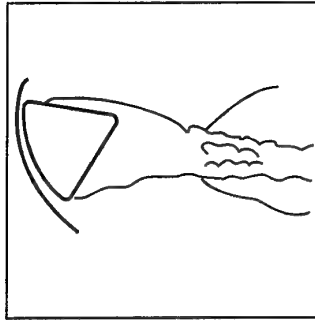


Figure 6. Lee and base flows.

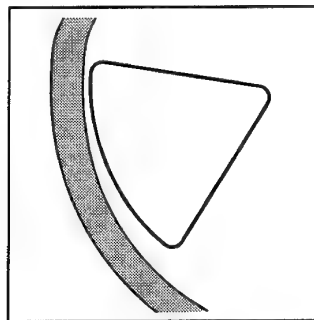


Figure 7. Low-density flow.

CHAPTER II

SHOCK-WAVE/BOUNDARY-LAYER INTERACTIONS IN HIGH-MACH-NUMBER FLOWS

Jean M. Délery

Office National d'Etudes et de Recherches Aérospatiales (ONERA)
92320 Châtillon
FRANCE

Argyris G. Panaras

Hellenic Air Force Academy
Athens
GREECE

CONTENTS

1	INTRODUCTION	8
2	PHYSICAL PROPERTIES	9
2.1	Interactions in Two-Dimensional Flows	9
2.2	Interactions in Three-Dimensional flows	20
2.3	Other Aspects of Interacting Flows	39
3	SURVEY OF PROBLEMS RAISED BY INTERACTION MODELING	40
3.1	General remarks	40
3.2	Modeling of Turbulent Interactions	40
3.3	Status of Modeling Activities and Requirements for Proper Validation	42
4	DEFINITION OF THE SELECTED TEST CASES	46
4.1	General Information	46
4.2	Axisymmetric Configurations	48
4.3	Single Sharp Fin Configurations	50
4.4	Swept Compression Corner	53
4.5	Crossing Shocks	54
5	CONCLUDING REMARKS AND RECOMMENDATIONS	58
5.1	Viscous Interaction Phenomena are Important	58
5.2	The Extent of our Knowledge and Capabilities	58
5.3	The Limits of our Knowledge and Capabilities	59
5.4	The Subgroup Contribution	60
5.5	Recommendation for Future Actions	60

REFERENCES

ABSTRACT

Viscous interactions play a predominant role in hypersonic flows because of the presence of intense shock waves interacting with the boundary layers. These phenomena may strongly affect the aerodynamic performance of a vehicle and lead to the existence of high heat-transfer rates, especially when separation occurs. This chapter first presents a review of the main physical properties of shock-wave/boundary-layer interactions, in two- and three-dimensional flows. Emphasis is placed on the description of the most salient features of the flow with a special attention paid to the thermal effects in two-dimensional flows.

A second part is devoted to a rapid discussion of the problems met in the modeling of interacting flows. The difficulties here come from the necessity to use robust and accurate numerical schemes that are able to capture the rapid variations of the flow properties occurring across shock waves, boundary layers and shear layers, and to adopt realistic turbulence models. This last point is a critical issue in the prediction of hypersonic flows since, in addition to abrupt pressure gradients frequently entailing separation, important compressibility effects are present.

The main task of this chapter is to select a limited number of test cases recommended to validate computer codes. Some of the cases are axisymmetric configurations which are simpler to treat and which do not lead to complex meshing problems. However, most test cases are three-dimensional interactions produced by a fin, a wedge or two fins giving a crossing shock pattern. The information needed to execute calculations is provided in this third part (except for some cases which were not yet tested at the time of the preparation of this report). Most of the experimental results are available on tabular form or on diskettes and can be forwarded upon request. Recommendations for future actions in the field of hypersonic interacting flows are formulated in the last part of the chapter.

1 INTRODUCTION

The flow past a vehicle flying at hypersonic speed is the source of strong shock waves formed ahead of the vehicle nose, the rounded leading edge of wings and tails, at the compression ramp of the air-intake, and at the control surfaces, to name a few examples. These shock waves are the origin of interference phenomena resulting, first from the intersection of two shocks, and second from their interaction with the boundary layers developing on the vehicle surface. Because of their great practical importance, these phenomena have been extensively studied during the past 50 years and are still the subject of active investigations due to their extreme complexity (Liepmann 1946; Bogdonoff et al. 1953; for review articles see: Korgegi 1971; Holden 1986; Détery and Marvin 1986; Settles 1993).

Shock-wave/boundary-layer interactions occur at the impingement of a bow shock, at a deflected flap, along axial corners in wing-body and fin-wing junctions, etc. They are also present in the air intake of an air-breathing propulsion system and in the vicinity of an afterbody where the nozzle jet meets the outer flow. Such interactions can induce separation of the boundary layer which causes loss of control effectiveness or flow degradation in an engine inlet. Also, in high-enthalpy hypersonic flows, the subsequent reattachment on a surface of the separated shear layer gives rise to heat transfer which can be far in excess of those of an attached boundary layer.

A large amount of information is available on shock-wave/boundary-layer interaction in two-dimensional flows, and the experimental results have allowed a rather clear identification of the role played by the parameters involved in the process. Therefore, the physics of two-dimensional interactions can be considered as well known, as far as the *mean flow properties* are concerned. Also, correlation laws have been deduced, giving, for example, the upstream interaction length (limit for shock-induced separation) and the peak heat transfer at reattachment which may be of primary importance for practical applications. However, due to the difficulty to perform "clean" experiments on a nominally two-dimensional geometry, data which can be safely used to validate computer codes are relatively scarce (Settles and Dodson 1991). Indeed, most of the published results are more or less affected by side effects, which makes it difficult to draw clear conclusions from comparisons between experiment and computation. In addition, detailed information on the flow structure (mean velocity and turbulence fields) are most often missing, especially for hypersonic Mach numbers. On the other hand, shock-wave/boundary-layer interactions are affected by more or less strong *unsteady effects* which seem to be a distinctive feature of these phenomena (see Section 2.3). Thus, most of the properties depicted in the coming sections are in fact relative to a *mean flow* resulting from some kind of time averaging of the observed quantities. In some circumstances, such a description can be so far from reality that the question of its physical meaning can be raised. However, since all the calculations made to date have been executed by also considering mean quantities, there is a consistency between the steady physical description and the theoretical models.

In the following section, we shall examine some general properties of flows resulting from shock-wave/boundary-layer interactions without making a well-defined distinction between supersonic and hypersonic flows.

1. First, because the essence of the phenomena is basically the same, independent of the incoming Mach number, the main flow features are similar. This is not true for transonic flows where the hyperbolic-elliptic nature of the outer inviscid flow leads to specific characteristics. Transonic interactions will not be considered here, although transonic situations may exist on a hypersonic vehicle.
2. Second, supersonic interactions actually occur on a vehicle flying at hypersonic Mach number since there is a considerable reduction in the flow Mach number behind the bow shock.

Nevertheless, typical features of hypersonic interactions will be clearly established and emphasis will be placed on the specific problems met for hypersonic flow conditions. For instance, the influence of wall temperature will be discussed when information on the influence of this parameter is available. As a matter of fact, one of the typical features of hypersonic flows is the large difference existing between the wall temperature T_w and the outer flow stagnation temperature T_{st0} . This thermal condition is frequently characterized by the ratio T_r/T_w where T_r is the recovery temperature; i.e., the temperature taken by the wall for adiabatic conditions, which is not necessarily relevant for hypersonic flows in which thermal equilibrium is never reached. This ratio can be well in excess of 10 for re-entry conditions.

The high level of the outer-flow stagnation enthalpy also leads to extremely high heat-transfer rates at the wall, especially in shock-wave/boundary-layer interaction regions. This important problem will receive special attention. Also, because of the high temperature levels, the flow behind the bow shock is dissociated leading to the so called real-gas effects whose influence on viscous interaction phenomena is poorly known, except from calculations which are not yet validated. This question will be briefly considered.

The aim of the following section is to give a brief presentation of the major physical properties of shock-wave/boundary-layer interactions in two-dimensional (planar and/or axisymmetric) and three-dimensional flows. Then (Section 3), a state-of-the-art flow prediction is presented, with emphasis placed on problems raised by the physical modeling of phenomena. In a third part (Section 4), test cases collected to constitute a data bank allowing a validation of computer codes are defined. Finally (Section 5), recommendations are made for a continuation of the research effort in matter of strong viscous interaction in hypersonic flows.

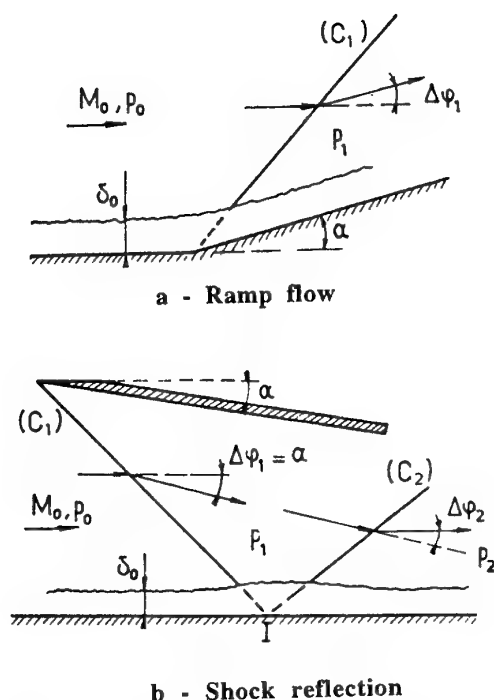


Figure 1: Basic shock-wave/boundary-layer interactions.

2 PHYSICAL PROPERTIES

2.1 Interactions in Two-Dimensional Flows

2.1.1 The Basic Configurations

What can be considered as the two basic configurations involving interaction between a shock wave and a boundary layer in supersonic or hypersonic flows are schematically represented in Figure 1. For the sake of simplicity, in what follows the incoming flow is assumed uniform and streaming along a flat plate.

1. The first, and most conceptually simple situation, is the *ramp* (or *wedge*) flow. Here a discontinuous change in the wall inclination is the origin of a shock wave (C_1) through which the incoming supersonic flow undergoes a deflection $\Delta\varphi$ equal to the corner angle α .
2. The second type of flow is associated with the *impingement* on the wall of an incident shock (C_1). Now, the incoming flow undergoes a deflection $\Delta\varphi_1$ through (C_1) and the necessity for the downstream flow to be again parallel to the wall entails the formation of a reflected shock (C_2) issuing from the impingement point I of (C_1). The deflection $\Delta\varphi_2$ produced by (C_2) must be such that $\Delta\varphi_2 = -\Delta\varphi_1$. The pressure jumps p_1/p_0 and p_2/p_1 through each shock are not equal, though not very different.

In fact, reality is more subtle in the sense that other situations may occur in which the flow is dominated by an interaction process between a shock wave and a boundary layer. This is the case of separation induced by an

obstacle, like a forward facing step. Then, the boundary layer separates well upstream of the step with the accompanying formation of a separation shock. In a situation of this kind, the shock is produced by the rapid coalescence of the compression waves generated in the region where the boundary layer separates. The flow structure results from a strong coupling between the outer inviscid stream and the boundary layer according to a mechanism called by Chapman a *free interaction* (see Section 2.1.3).

In the following sections, physical descriptions of the shock-wave/boundary-layer interactions produced by a ramp flow and an oblique shock reflection are given. We consider in a global manner both *laminar* and *turbulent* flows, since there is no basic difference between the interactions associated with these two regimes. However, the main and essential differences affecting the streamwise scale and intensity of the phenomena is emphasized.

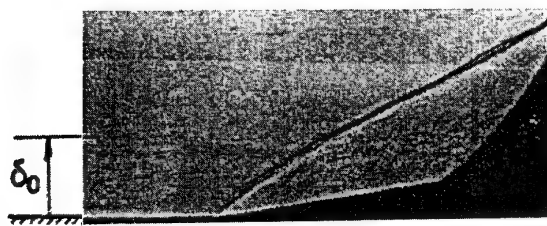
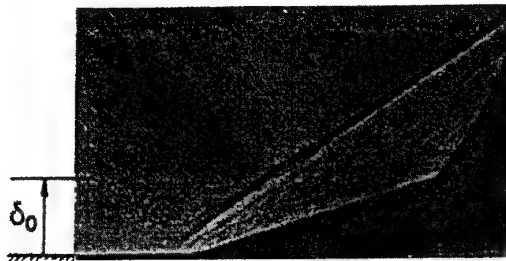
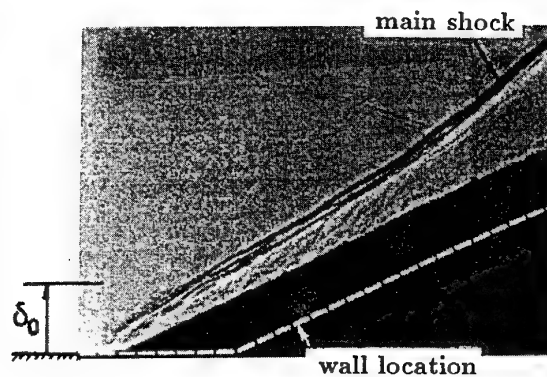
2.1.2 General Flow Organization

The compression ramp flow. The interaction produced by a two-dimensional ramp is illustrated by the sequence of microsecond spark photographs shown in Figure 2 (Settles et al. 1978). The incoming boundary layer is fully turbulent and the four pictures correspond to different values of the ramp angle α .

In the $\alpha = 8^\circ$ case, a distinct shock wave is seen to arise from the corner location. This shock wave forms well within the boundary layer which behaves like an inviscid—but *rotational*—fluid over most of its thickness. Indeed, in such a fast interaction process viscous forces play a negligible role compared to the action of pressure and inertia forces, except in a very thin layer in contact with the wall. Moreover, at high Reynolds number, the velocity profile of the boundary layer is so “filled” that, starting from the outer edge, the Mach number first slowly decreases over the major part of the boundary layer and then tends to zero over an extremely short distance, so that the subsonic layer is extremely thin. These facts explain why the shock originates from a region very close to the wall. The weak influence of viscosity in this kind of flow—when the ramp angle is moderate—was demonstrated by perfect fluid calculations (Roshko and Thomke 1969). This flow structure, which comprises an outer isentropic region, an intermediate rotational part and a thin viscous layer has a rational justification in the Multi-Deck Theory (Lighthill 1953; Stewartson and Willmows 1969). This theory greatly contributed to the understanding of strong interaction phenomena in high Mach number flows.

For $\alpha = 8^\circ$, the upstream influence is very small since the shock emanates practically from the corner angle. On the other hand, for $\alpha = 16^\circ$, the shadowgraph reveals a substantial increase of the upstream influence length due to the intensification of the perturbing agency, namely the shock strength. Also, the “spreading” of the shock near the wall becomes more visible, the shock resulting from the coalescence of compression waves induced by the thickening of the low velocity portion of the boundary layer.

For $\alpha = 24^\circ$, the pressure rise is high enough to provoke

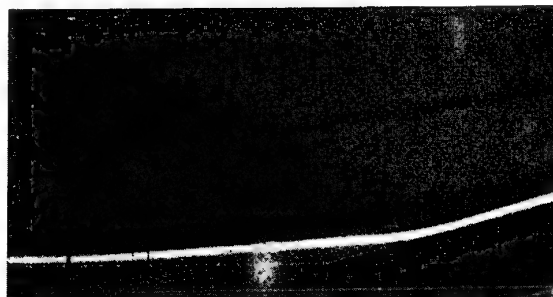
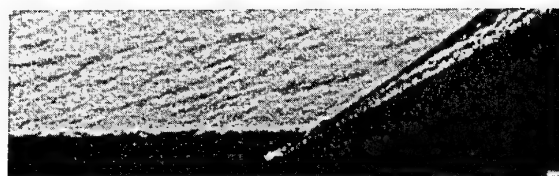
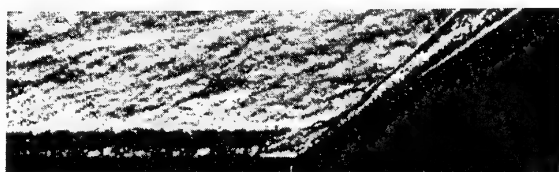
a - $\alpha = 8$ degb - $\alpha = 16$ degc - $\alpha = 24$ degFigure 2: Shadowgraphs of turbulent ramp flows at $M_0 = 2.85$ (Settles et al. 1978).

significant separation of the boundary layer. In this situation

1. the corner upstream influence has considerably increased,
2. a first shock forms well upstream of the ramp, and
3. the compression fan at reattachment meets the separation shock and reinforces it.

At high Mach number, the compression waves at reattachment coalesce before reaching the separation shock to form a reattachment shock which meets the separation shock at a triple point.

The flow organization of a *laminar* hypersonic interaction with separation is shown by the shadowgraph presented in Figure 3. The interacting flow is produced by a ramp of angle $\alpha = 15^\circ$ mounted on a flat plate with a sharp leading edge, at zero incidence, the upstream

Figure 3: Shadowgraph of a laminar hypersonic ramp flow at $M_0 = 10$ (Coët and Chanetz 1993).a - $\alpha = 27$ degb - $\alpha = 33$ degc - $\alpha = 36$ degFigure 4: Shadowgraphs of turbulent hypersonic ramp flows at $M_0 = 8.6$ (Holden 1972).

flow Mach number being equal to 10 (Coët and Chanetz 1993). In this case, separation occurs well upstream of the wedge and reattachment takes place on the ramp. The separation and reattachment shocks are clearly visible on the picture as also the shear layer emanating from the separation point and impinging on the ramp in the reattachment region. The typical features of a hypersonic interaction are the intensity of the shocks and their small inclination relatively to the surface.

The features specific to a *turbulent* interaction in hypersonic flows are illustrated by the shadowgraphs in Figure 4 which are relative to ramp flows for an incoming Mach number of 8.6 (Holden 1972).

1. When there is no separation (see photo a), the main shock (C_1) is very close to the ramp and emanates

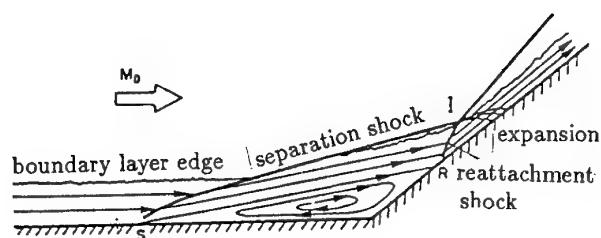


Figure 5: Hypersonic ramp flow. Sketch of the flowfield.

practically from the corner hinge.

2. The boundary-layer thickness on the ramp is much thinner than that of the incoming boundary layer. This important reduction in thickness is due to the large increase in the unit mass flow ρu resulting from the compression through the shock.
3. When separation occurs, the shock pattern depicted above may be embedded within the boundary layer. This situation is more visible in the sketch of Figure 5. One sees that the triple point I can be extremely close to the wall so that the expansion wave emanating from I reaches the wall at a small distance behind reattachment, leading to an important pressure decrease.

The shadowgraphs in Figure 6 give another example of a turbulent hypersonic flow at a wedge compression corner (Elfstrom 1971). In the separated case (see Figure 6b), one clearly sees the separation shock and the shear layer which develops between the outer inviscid flow, below the separation shock, and the "dead-air" region in contact with the wall. Also, one notes the strong reattachment shock which is intersected by the separation shock very close to the ramp.

The Impinging Reflecting Oblique shock. In the present configuration, a shock wave is generated by a shock-generator made up of a flat plate with sharp leading edge, inclined at an angle α_G relative to the uniform incoming flow. The planar oblique shock originating from the plate leading edge impinges on a straight wall facing the shock generator. The sequence of schlieren photographs shown in Figure 7 visualizes the shock reflection for increasing values of the primary deflection $\Delta\varphi_1$ through the incident shock wave. In the present example, the incoming flow Mach number is equal to 1.93 (Délery 1970).

When the incident shock is weak (as for the first photograph in Figure 7), the general flow structure does not differ much from the perfect-fluid model. However, a closer examination of the picture reveals that complex phenomena take place within the boundary layer (see sketch in Figure 8a). Thus, the incident shock (C_1) progressively curves and weakens as it penetrates the boundary layer because of the decrease in Mach number. The pressure rise through (C_1) propagates upstream in the subsonic region making this part thicker, which generates outgoing compression waves (l_1) that

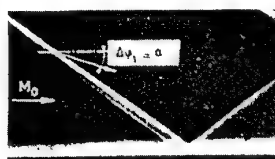


a - Attached flow



b - Separated flow

Figure 6: Shadowgraphs of turbulent hypersonic ramp flows at $M_0 = 9.22$ (Elfstrom 1970).



a - $\alpha = 5$ deg
(no separation)

b - $\alpha = 6$ deg

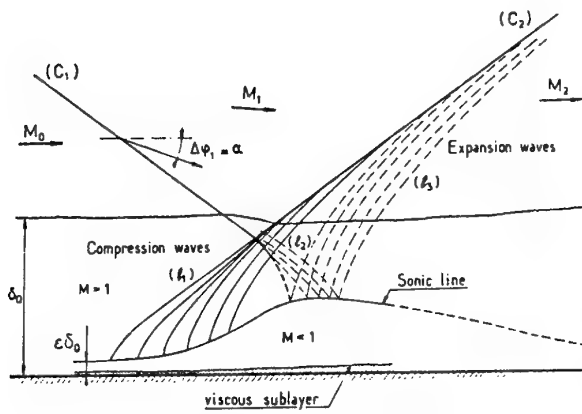


c - $\alpha = 8$ deg
(separation)

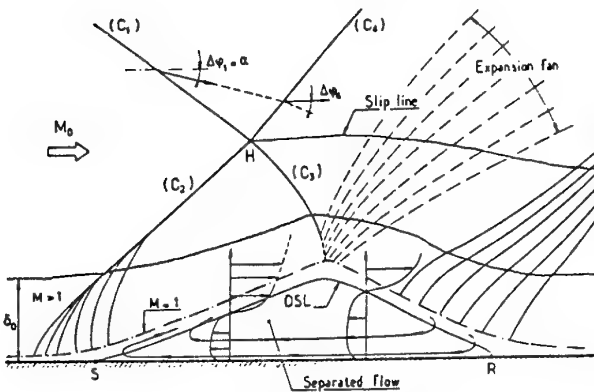
d - $\alpha = 11$ deg
(separation)



Figure 7: Schlieren pictures of turbulent shock reflections at $M_0 = 1.93$ (Délery 1970).



a - Without separation

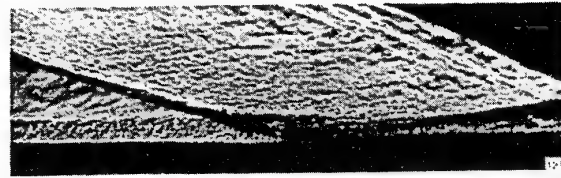
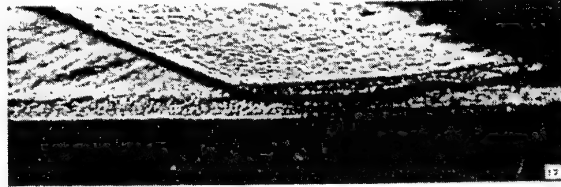


b - With separation

Figure 8: Shock reflection. Schematic representation of the flowfield.

coalesce to form the reflected shock (C_2). The refraction of these waves and of the reflected shock as they propagate through the rotational inviscid layer induces the secondary wave system (l_2). These last waves are reflected by the sonic line as expansion waves (l_3). For weak incident shocks, the upstream interaction distance is extremely short, so that the above flow pattern is embedded within the boundary layer. Thus, at the outflow scale, the only reflected wave is a shock (C_2) causing a deflection $\Delta\varphi_2 = -\Delta\varphi_1$ and the real viscous flow closely resembles the purely inviscid solution.

Let us now consider the case of an incident shock strong enough to separate the boundary layer. The resulting wave pattern is visualized by the last two photographs in Figure 7 and a schematic representation of the flowfield is given in Figure 8b. The boundary layer separates well upstream of the point where the shock would meet the surface if the fluid were inviscid. The pressure rise at separation results in compression waves propagating in the supersonic part of the boundary layer and in the outer inviscid stream. These waves coalesce to constitute the shock (C_2) which intersects the incident shock (C_1) at point H from which emanate the two refracted shocks (C_3) and (C_4). After intersection with (C_1), the shock (C_3) is bent because of the entropy gradient down-

a - $\alpha = 12.5$ degb - $\alpha = 17.5$ degc - $\alpha = 19.8$ degFigure 9: Shadowgraphs of turbulent hypersonic shock reflections at $M_0 = 8.6$ (Holden 1972).

stream of (C_2) and the compression waves generated by the thickening of the boundary layer. Afterwards, (C_3) enters into the separated dissipative layer from which it is refracted into an expansion wave. The viscous flow, which separates at S , reattaches on the surface at a point R , a recirculation bubble forming between S and R . At the same time, the thickness of the dissipative layer decreases and the external stream is progressively turned to become parallel to the wall.

Shadowgraphs of *turbulent* interactions due to shock reflection in a hypersonic flow of Mach number 8.6 are shown in Figure 9 (Holden 1972). Conclusions similar to those pertaining to the wedge flow can be drawn. In particular, one notes the small angle of the reflected shock relative to the surface. Now, the shock pattern associated with flow separation is almost entirely contained within the boundary-layer flow. A *laminar* impinging shock interaction is presented in Figure 10. In this case the incoming flow Mach number is 2.2, but the overall structure of the flow would be similar at higher Mach numbers (Degrez et al. 1987). One sees that the streamwise extent of the interaction domain, scaled to the initial boundary-layer thickness, is far more larger than in the turbulent case. Also, in the laminar regime, coalescence of the compression waves induced by boundary layer separation most often occurs well above the surface, so that the intersecting shock pattern of Figure 9 is generally not observed, except at hypersonic Mach numbers.

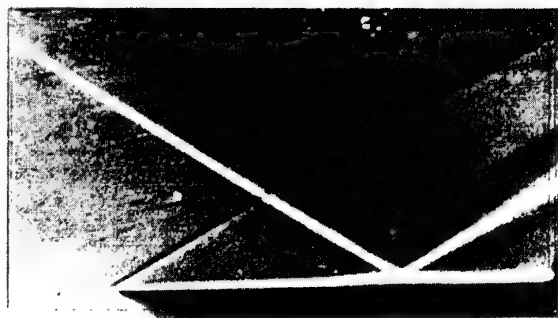


Figure 10: Schlieren pictures of a laminar shock reflection at $M_0 = 2.2$ (Degrez et al. 1987).

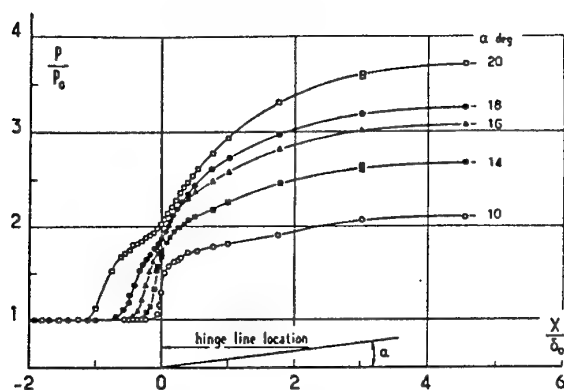
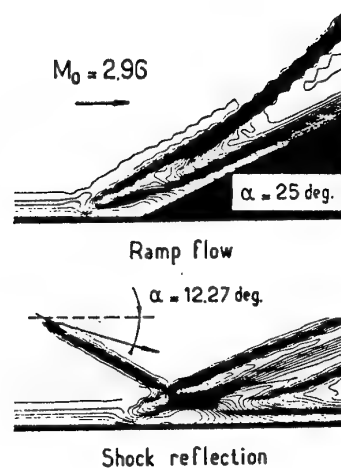


Figure 11: Surface pressure distributions in a ramp flow at $M_0 = 2.95$ (Settles 1975).

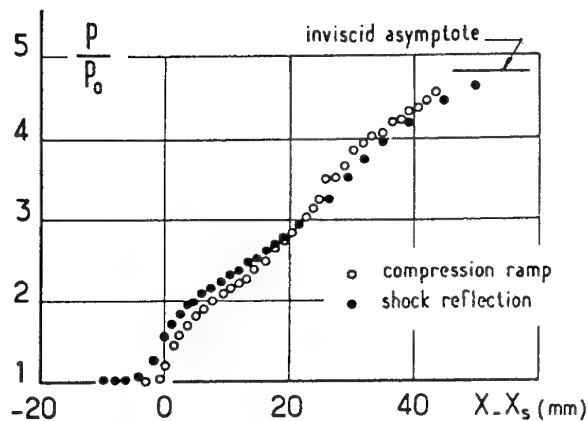
2.1.3 Wall Pressure Distributions and Scaling Laws

The main properties of the wall pressure distribution in a supersonic or hypersonic interaction can be examined by considering typical experimental evidences:

1. The results plotted in Figure 11 are relative to a wedge flow at an upstream Mach number of 2.95 and the incoming boundary layer is turbulent (Settles 1975). It is observed that the pressure starts to rise upstream of the corner by virtue of the upstream propagation mechanism.
2. For the highest values of the wedge angle α , the pressure curves exhibit three inflection points, this shape being typical of an interaction involving a noticeable separation of the boundary layer. For largely separated flows, the pressure at separation rises to reach a constant level, or plateau.
3. The data plotted in Figure 12 are relative to a compression ramp and to an impinging shock giving the same overall pressure rise, with the initial conditions identical in the two cases (Shang et al. 1976). Although the structures of the two flows are very different, as demonstrated by the density contour lines shown in the figure, one sees that the two pressure distributions are nearly coincident. Thus, a ramp



a - Density contour graphs



b - Wall pressure distributions

Figure 12: Comparison of ramp flow and shock reflection flow at $M_0 = 2.96$ (Shang et al. 1976).

flow and a flow induced by an impinging shock have similar properties and scaling laws, the behavior of the interacting boundary layer being primarily dictated by the shock strength and not by the way the shock is generated.

4. As shown by the results plotted in Figure 13 (Elfstrom 1971), the interaction in hypersonic flows is characterized by a large rise in pressure due to the high pressure ratio across an oblique shock at high Mach number. The pressure distributions exhibit the following features:

- For moderate ramp angle ($\alpha < 26^\circ$), the shape of the pressure curve does not differ much from that observed at smaller Mach numbers.
- The pressure rise associated with separation remains similar when the separation point moves in the upstream direction as a consequence of the ramp-angle increase. Thus, the pressure distribution is entirely determined by the flow

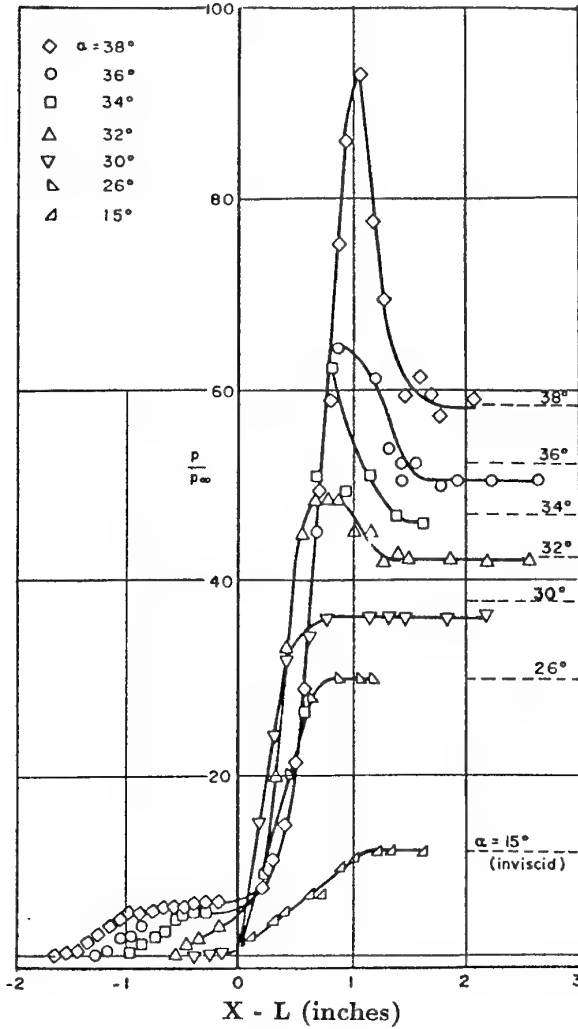


Figure 13: Surface pressure distributions in a hypersonic ramp flow at $M_0 = 9.22$ (Elfstrom 1971).

situation at the interaction onset, the only effect of a rise in the overall pressure jump being to provoke an extension of the pressure plateau.

- Once separation has occurred, there is a large asymmetry between the pressure rises at separation and reattachment, the latter being much more important. As the pressure rise to separation does not depend on downstream conditions, an increase in the overall pressure rise necessarily entails a higher pressure rise at reattachment. This can only be achieved by an increase in the maximum velocity reached on the *discriminating streamline* of the separated zone, hence an increase of the shear-layer length. This fact explains the rapid development of the pressure plateau with the wedge angle.
- When α is greater than 30° , the pressure distribution exhibits a decrease which follows the rise corresponding to reattachment. Then it

tends to the constant level of the inviscid solution with the tendency that the greater the wedge angle, the higher the pressure overshoot. This phenomenon, observed when the flow is separated, could be associated with the shock interference pattern that forms.

Properties of the wall pressure distributions have been discussed by considering turbulent results. In fact, the same trends are noticed in laminar interactions with the major difference that the pressure gradients are far less intense than in turbulent interactions.

The "intensity" of a shock-wave/boundary-layer interaction can be characterized by its *upstream influence*; i.e., the distance at which the shock presence is first felt. This distance is most often measured from the wedge corner or from the point where an incident shock would impinge the wall in a purely inviscid stream. A second point of interest is the *separation length* which is conveniently defined as the distance of the separation point from a suitably chosen origin, for example the start of the interaction. The basic question that arises is as follows: what are the appropriate scaling laws for these characteristic lengths? The answer to this question is important, not only for practical purposes, but also for the physical understanding of the phenomenon. The search for scaling laws has motivated a large number of studies whose classical results will not be reproduced here (see Spaid and Frishett 1972; Settles and Bogdonoff 1973; Roshko and Thomke 1974; Settles 1975). It was found that the main parameters influencing the extent of an interaction are: the upstream Mach number M_0 , the Reynolds number Re_L , the wedge angle (or incident shock intensity), the thickness δ_0 of the incoming boundary layer.

The behavior of the flow during a separation process can be (partly) interpreted by the *Free Interaction Theory* of Chapman whose main conclusions are worth to be recalled (see Chapman et al. 1957). This theory shows that the pressure rise during separation of a supersonic boundary layer is given by

$$\frac{p - p_0}{q_0} = (2C_{f_0})^{\frac{1}{2}} (M_0^2 - 1)^{-\frac{1}{4}} F \left[\frac{X - X_0}{L} \right] \quad (1)$$

where q_0 is the dynamic pressure of the upstream flow of Mach number M_0 , C_{f_0} the skin friction coefficient at the interaction origin X_0 and F is a dimensionless correlation function of the scaled streamwise distance

$$\bar{X} = \frac{X - X_0}{L}$$

The length scale L obeys a law of the form

$$L \propto \delta_0^* C_{f_0} (M_0^2 - 1)^{-\frac{1}{4}}$$

The Free Interaction Theory demonstrates that the pressure rise during the separation process depends only on the flow properties at the onset of the phenomenon, as it was already noticed from experimental evidence. A more rigorous demonstration of this fact was made by Stewartson and Williams (1969) by using asymptotic expansion techniques. Other correlation laws have been proposed for the pressure distribution at separation of

the pressure plateau, frequently derived from the Free Interaction Theory (Popinsky and Ehrlich 1966; Lewis et al. 1967; Stanewsky 1973).

The Free Interaction Theory predicts a decrease of the interaction extent and of the overall pressure rise when the Reynolds number is decreased. This tendency is well verified in laminar flows, but is in contradiction with experiments in turbulent flows as soon as the Reynolds number is greater than 10^5 (Zukoski 1967; Roshko and Thomke 1974; Settles 1975). In fact, it is found that, beyond the above limit, a turbulent boundary offers a greater resistance to separation when the Reynolds number is increased. This conflict, which was the subject of many discussions in the 70's, has been resolved by Settles (1975) who showed that the behavior of the boundary layer results from a competition between viscous and inertia forces, the two having opposite influence. The Free Interaction Theory privileges viscous forces, hence its good results in low-Reynolds-number flows, whereas at high Reynolds numbers, the inertia forces dominate which tends to invalidate this theory.

The definition of a limit for shock induced separation, mainly in turbulent flows, has also been a question of major concern which motivated a great number of investigations and raised some polemics. This limit is most often defined in the plane of two variables: the wedge angle (or equivalent angle for shock reflection) and the Reynolds number, a different curve corresponding to each value of the upstream Mach number M_0 (for details see Détery and Marvin 1986).

2.1.4 Thermal Effects in Hypersonic Interactions

General Remarks. The high-enthalpy level of the outer flow, typical of realistic hypersonic conditions, has three direct and important consequences on strong interaction phenomena:

1. When the temperature of the wall is well below the outer-flow stagnation temperature, a *cold-wall* situation arises which may significantly affect the interaction properties.
2. Heat-transfer processes will take on a fundamental importance, especially in separated flows where, as already seen, the shear layer emanating from a separation point impinges the reattachment surface.
3. Real-gas effects, coming from the dissociation of air, affect the thermodynamic and transport properties in a way that probably influences interaction phenomena.

The first two effects are well characterized from a rather large amount of experimental results. Information on the third effect is very scarce and mostly obtained from calculations.

Wall-Temperature Effect on the Interaction Properties. In carefully made experiments, Spaid and Frishett (1972) found that cooling the wall contracts the interaction domain and reduces the separation distance. This effect is illustrated by Figure 14 which shows variations

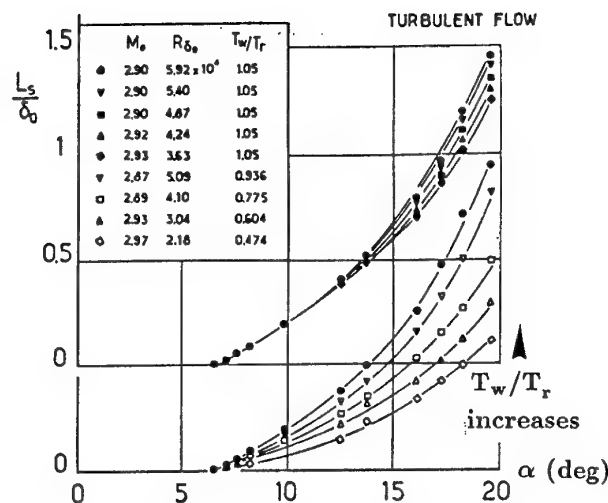


Figure 14: Surface temperature effect on the separation length (Spaid and Frishett 1972).

of the separation length L_s (normalized by the initial boundary-layer thickness δ_0) with the ramp angle α for different values of the Reynolds number and the ratio T_w/T_r . The decrease in L_s/δ_0 with wall temperature occurs either within the framework of the Free Interaction Theory since a decrease of the ratio T_w/T_r provokes an increase of the skin-friction coefficient, hence a contraction of L according to formula (1), or by an overall contraction of the interaction domain resulting from a thinning of the subsonic part of the boundary layer due to the lower temperature levels near the wall. Indeed, experiment shows that wall temperature weakly affects the velocity distribution through a boundary layer; thus, near a cold wall the sound velocity is lower and the Mach number is higher.

The effect of wall temperature on the length of separation in turbulent flows was also investigated by Kilburg and Kotansky (1969), Elfstrom (1971), Don Gray and Rhudy (1973), Holden (1972) and by Back and Cuffel (1976). These investigators also found that wall cooling reduces the streamwise extent of the interaction region. In experiments executed with a *heated* wall ($T_w/T_r > 1$), it was found that a rise in wall temperature induced a substantial increase of the interaction extent, which is consistent with the above findings (Détery 1992). In hypersonic flows, Elfstrom (1971) also noticed that increasing the wall temperature, starting from a cold-wall situation, increased (modestly) the extent of a separated region and magnified the pressure overshoot at reattachment, as is shown by the wall pressure distributions plotted in Figure 15. Further, as observed by Elfstrom, when the wall temperature is increased, the pressure distribution of the attached flow develops an overshoot typical of separated flows. Thus, the incipient separation angle must decrease as the wall temperature is raised. Of course, the reverse is true.

In a more recent study, Détery and Coët (1990) found results apparently in disagreement with previous results. These authors performed experiments on a ramp flow at

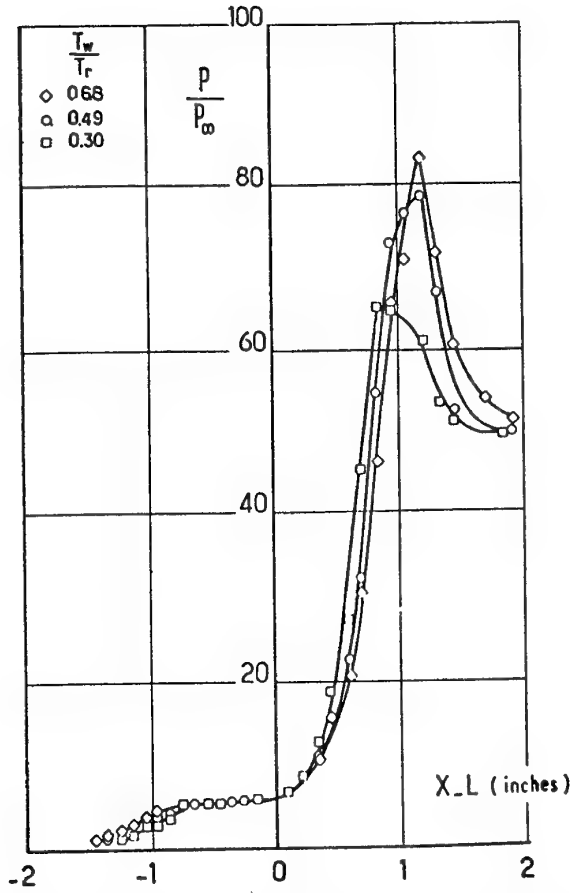


Figure 15: Surface temperature effect on a ramp flow at $M_0 = 9.22$ (Elfstrom 1971).

Mach 10, first with an uncooled model for which the ratio T_w/T_r was equal to 0.3, and second with the same model cooled by circulation of liquid nitrogen, which allowed a value $T_w/T_r = 0.1$. The incoming boundary layer was laminar. It was observed that the flow remained nearly unaffected by this decrease in the wall temperature, in contradiction to well-established results. This unexpected behavior can be explained by the fact that the uncooled model corresponds to an already cold-wall situation, so that the variation of T_w/T_r from 0.3 to 0.1 does not lead to substantial changes in the flow structure.

Heat Transfer in Hypersonic Interactions. The salient feature of hypersonic interactions is the existence of extremely high heat transfer rates in the interaction region, especially when separation occurs. This problem is crucial for the correct sizing of the thermal protection in parts of the vehicle where such interactions are likely to occur. The problem has received considerable attention and has been studied by many investigators in laminar as well as in turbulent flows (see in particular Needham 1965; Holden 1966, 1978, 1986; Nestler 1973; Hung 1973; Hung and Barnett 1973; Stollery 1975).

Heat transfer rates are particularly intense in the vicinity of the point R where the separated flow reattaches. This

rise in heat transfer is associated with the stagnation at R of the shear layer developing from the separation point S . Thus, in some respects, the situation at R is similar to that of a nose stagnation point with the difference that the flow impinging on the wedge (or control surface) has been compressed through a succession of oblique shocks at separation and reattachment, instead of a unique normal shock. Consequently, its (average) stagnation pressure being higher, exchange processes will be much more efficient, leading to high heat transfer rates.

The heat transfer rate is most often represented by the *Stanton number* defined by

$$St = \frac{h}{\rho_{\infty} U_{\infty} C_p (T_{t\infty} - T_w)}$$

where h is the heat-transfer rate (in W/m^2), ρ_{∞} and U_{∞} are the density and velocity of the upstream flow and C_p is the constant-pressure specific heat. It should be noted that the true Stanton number is

$$St = \frac{h}{\rho_e u_e C_p (T_r - T_w)}$$

where ρ_e and u_e are relative to the *local* flow conditions at the edge of the boundary layer. Because these quantities, along with the recovery temperature T_r , are difficult to determine in hypersonic interactions, the first definition of the Stanton number is most often used. Another way to circumvent the difficulty is to plot the ratio h/h_{ref} where h_{ref} is the heat transfer which would be measured at the wall in the absence of the interaction.

A typical heat-transfer distribution in a wedge-induced interaction is shown in Figure 16 (D  lery and Co  t 1990). This result is relative to an upstream Mach number of 10, a Reynolds number $R_L = 2.3 \times 10^6$ and a ratio $T_w/T_r = 0.3$. The model is a 15° ramp placed on a flat plate with sharp leading edge. In these experiments the boundary layer is laminar over the major part of the interaction, but transition probably occurs in the reattachment region. Nevertheless, the overall wall heat-transfer distribution is typical of a *laminar* interaction. The curve plotted shows that the heat transfer decreases slowly in the most upstream part of the flat plate in accordance with laminar boundary-layer theory. A more rapid decrease in heat transfer occurs at a location coincident with separation onset. This decrease is typical of shock-induced separation in laminar flows. Heat transfer goes through a minimum in the separation region and then increases sharply in the reattachment region, the *peak value* being reached slightly downstream of the reattachment point, as determined from the surface flow pattern.

A more detailed view of the heat-transfer evolution near a corner is given by Figure 17 which shows distributions of the ratio h/h_{ref} measured for different ramp angles α . The decrease in heat transfer ahead of the corner, always present even for very small wedge angles, coincides with the initial rise in pressure resulting from the upstream influence of the wedge. Downstream of the corner, the heat transfer rate rapidly rises in the region of high pressure gradient to reach a maximum before decreasing downstream of the interaction. As the wedge angle is increased, a small region of separated flow is

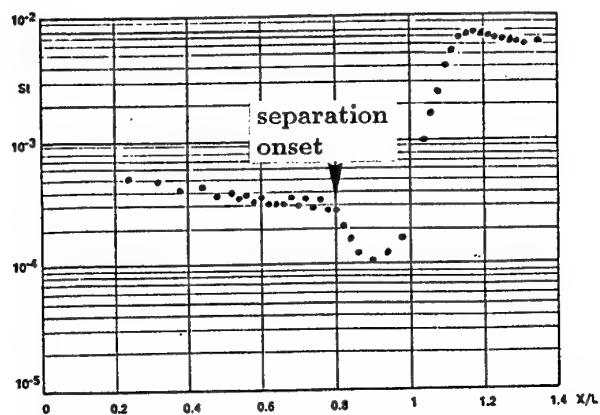


Figure 16: Surface heat transfer distributions in a laminar ramp flow at $M_0 = 10$ (Délery and Coët 1990).

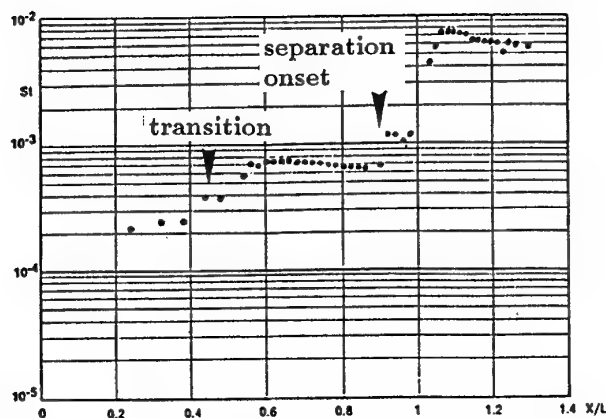


Figure 18: Surface heat transfer distribution in a turbulent ramp flow at $M_0 = 5$ (Délery and Coët 1990).

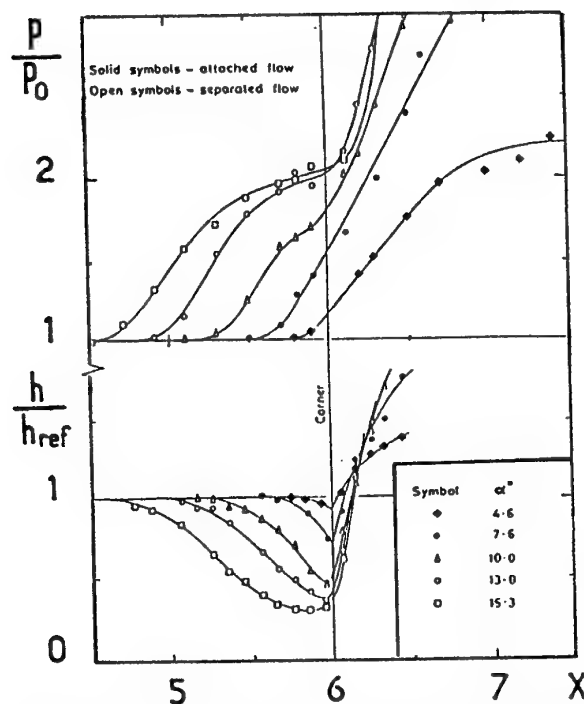


Figure 17: Laminar pressure and heat transfer distributions near the ramp (Needham 1965).

formed at the corner. The pressure distribution then exhibits a knee just upstream of the corner and the heat transfer is seen to develop a smooth minimum with a continuously changing gradient instead of the cusp typical of attached flows.

Results relative to a *turbulent* interaction at Mach 5 produced by a 35° ramp are presented in Figure 18. Although the Mach number is modest, these results are similar to those obtained at higher Mach numbers (see for example, Elfstrom 1971 and Holden 1977). In this case, the heat transfer first decreases slowly in the upstream part of the flat plate and then rises rapidly well upstream of the ramp hinge line. This first rise, fol-

lowed by a slow decrease, can be attributed to laminar-turbulent transition. A second rise takes place at the separation station, this behavior, opposite to that observed in laminar flows, is typical of turbulent shock-induced separation. Further downstream, the heat transfer increases sharply during the reattachment process to reach a well marked peak value downstream of the reattachment point.

Other typical results on heat transfer in a hypersonic flow are shown in Figure 19. They have been obtained on a wedge compression corner for an upstream Mach number equal to 9.22 (Elfstrom 1971). The plotted curves, which correspond to increasing values of the wedge angle α , confirm the fact that, in contrast to laminar results, the heat transfer rate increases in the separated region when the incoming boundary layer is *fully* turbulent. This rise may be explained by the amplification of turbulence intensity taking place in the vicinity of the separation point. The large eddies which then form, promote exchanges between the wall region and the outer high-enthalpy flow, thus leading to a rise in the heat transfer. A close examination of the distributions shows that near the separation point, the heat transfer increases to about three times the flat-plate value before falling again towards the corner. Just upstream of the hinge line, the heat transfer again starts to rise due to the upstream influence of the corner line. Thus, for the present situation the total heat transfer in the separated region ahead of the hinge line can be between two and three times the corresponding flat-plate value.

The heat transfer levels in a separated ramp flow strongly depend on the leading-edge radius of curvature of the plate supporting the ramp (Holden 1978; Don Gray and Rhudy 1973). This fact is illustrated here by the Stanton number distributions plotted in Figure 20 (Coët et al. 1992). These results have been obtained in a Mach 10 flow, for a ramp angle equal to 15° , with a model equipped with an interchangeable leading edge (sharp or rounded with radius equal to 2.5 mm and 5 mm). The stagnation conditions are such that the boundary layer is laminar at the interaction onset. With the rounded leading edges, there is a reduction by a factor of ten of the peak heat transfer at reattachment. There is also a

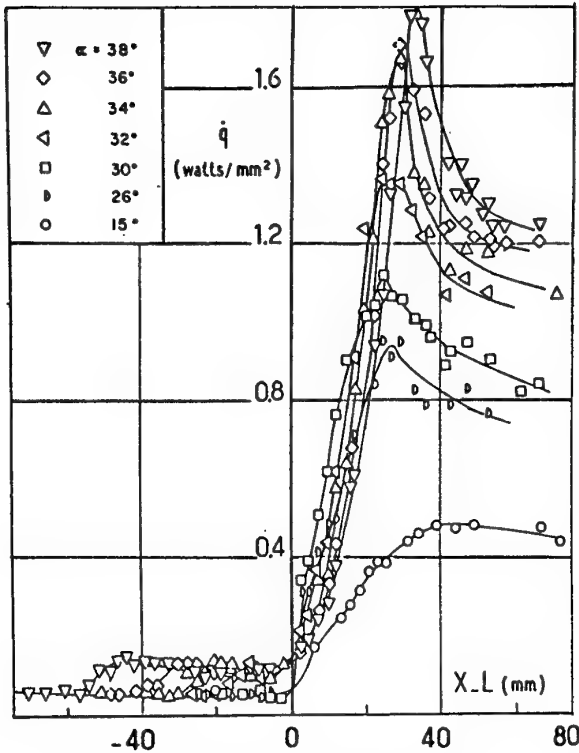


Figure 19: Surface heat transfer distributions in turbulent hypersonic ramp flows at $M_0 = 9.22$ (Elfstrom 1971).

contraction of the separated zone whose origin, denoted by a decrease in heat transfer, moves in the downstream direction when the leading edge is rounded. This *entropy layer* effect is explained by the loss in stagnation pressure provoked by the strong normal shock forming in front of the leading edge. This results in a drop in the local Reynolds number and consequently a greater resistance of the flow to separation, in agreement with the Free Interaction Theory, which compensates the opposite effect of a reduction of the local Mach number.

The effect of *laminar-turbulent transition* on hypersonic interactions is a delicate question which has not yet been elucidated and which would deserve more complete investigations because of its practical importance. Starting from a fully laminar interaction, it is clearly established that a rise in the Reynolds number R_L provokes a move of the transition region in the upstream direction until it reaches the reattachment region. Then, the peak heat transfer becomes much higher than that of the fully laminar case. At the same time, a reversal in the Reynolds number dependence occurs, with the extent of the separation decreasing with an increase of R_L (Heffner 1993). When R_L is raised, transition first tends to stay in the reattachment region until a limit value of R_L is reached beyond which it suddenly moves to the separation zone. With a further increase of the Reynolds number, transition takes place upstream of the interaction region, strongly affecting the flow structure. For

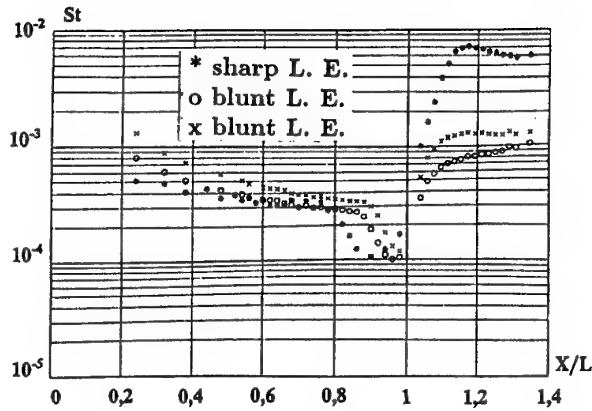


Figure 20: Effect of leading-edge bluntness on surface heat transfer distributions at $M_0 = 10$ (Coët and Chanetz 1993).

example, the separated zone disappears since the ramp angle (or impinging shock strength) is now insufficient to separate the turbulent boundary layer.

Most of the investigated "laminar" hypersonic interactions are in fact transitional since maintaining a laminar flow throughout the interaction region is difficult because of the extreme sensitivity of the separated shear layer to disturbances. This point, which is a major issue in providing really laminar cases for the validation of computer codes, will be discussed in Section 3.3.

Real-Gas Effects. In true hypersonic conditions, the flow over the vehicle will exhibit real-gas effects due to the dissociation of air at the passage through the strong bow shock. Hence, an interaction provoked either by a ramp or a shock reflection will involve a flow whose composition and physical properties may be greatly modified compared to the case of a non-dissociated gas. If the calorically perfect gas (i.e., a gas with constant ratio of specific heats γ) is taken as benchmark, the real-gas or chemical effects will be felt at two stages:

1. Since the thermodynamic properties of the flow are not the same, the structure of the inviscid part of the flow is modified as compared to the constant γ case.
2. The transport properties (viscosity, heat conductivity, diffusion coefficient) are affected by dissociation and chemical phenomena, which affect the behavior of the viscous part of the flow.

To our knowledge, there are no experimental results about the incidence of real-gas effects on shock-wave/boundary-layer interactions. The only available information has been obtained from computations considering fully laminar interactions.

In ramp-type flow, under the assumption of chemical equilibrium, it was found that in dissociated air a smaller separated region tends to form, because of weaker shock waves. Moreover, the heat-transfer rates are lower because of lower temperatures (Grasso and Leone 1992).

In the case of an impinging-reflecting shock and with consideration of nonequilibrium chemistry for air, it is found that the interaction is weakly affected by real-gas effects at low Reynolds numbers (Ballaro and Anderson 1991). Then, the flow can be modeled with a fair degree of accuracy by assuming a constant value for γ (taking into account the flow composition). This simplifying assumption may be invalid in limit situations where the reflection becomes singular (Mach phenomenon). Then, an accurate calculation of the inviscid flow structure is necessary. On the other hand, at high Reynolds numbers, chemistry effects lead to substantial differences in the wall-pressure and heat-transfer distribution, with an increase in the heat-transfer levels.

However, there are major differences between the *non-catalytic* and *catalytic* wall conditions. In the latter case, the interaction is strongly affected by the high energy release which then takes place in the separated region. This provokes a dilatation of the separation bubble and a spectacular increase of the heat transfer levels (Grumet et al. 1991).

2.1.5 Three-Dimensional Structures in Nominally Two-Dimensional Flows

We will not consider in this section the side effects which most often strongly perturb two-dimensional experiments making their use to validate computer codes questionable. These "macroscopic" three-dimensional effects will be addressed in Section 3.3. Here, attention is focused on "microscopic" effects whose existence is inherent to the three-dimensional nature of the world.

Surface visualizations by oil-flow techniques reveal the existence in the reattachment region of a three-dimensional pattern made of a cellular structure. Already observed by Roshko and Thomke (1965) in the reattachment behind an axisymmetric step and in a supersonic ramp flow by Settles et al. (1978), this phenomenon is clearly visible in the photograph of Figure 21 which shows a surface flow pattern observed in a two-dimensional ramp flow at Mach 10 (Coët and Chanetz 1993). A closer examination of such patterns shows that the reattachment line carries in fact, a succession of nodes and saddle points where the skin-friction line pattern adopts the organization sketched in Figure 22a. The reattachment line is thus a separator, according to the terminology of the Critical Point Theory, which is the trace on the wall of the attachment surface represented in Figure 22b. This surface is made up of streamlines ending at separation-type nodes which are coincident with the saddle points of the surface flow. Due to the lack of clear experimental information, the structure of the upstream part of the flow in the separation region is more difficult to establish. The cellular structure is the imprint on the surface of counter-rotating vortices which probably have an origin far upstream of the reattachment region.

Another feature frequently observed in hypersonic reattaching flows is the existence of spanwise variations of the heat-transfer distribution giving rise to characteristic striation patterns. An example of such a pattern is given in Figure 23 which is relative to the Mach 10 ramp

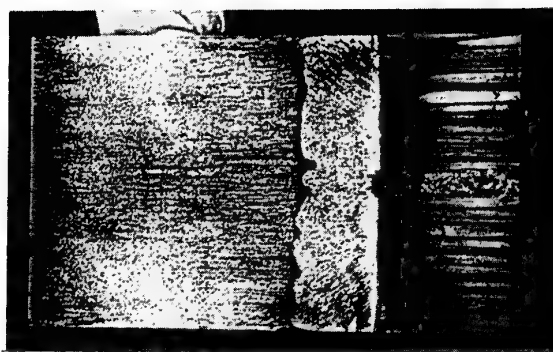


Figure 21: Surface flow visualization in a hypersonic ramp flow at $M_0 = 10$ (Coët and Chanetz 1993).

flow already mentioned. The figure shows the heat transfer distribution on the ramp determined from thermosensitive painting technique. There is a clear repetitive pattern in heat transfer along the ramp spanwise direction, the difference between the greatest and the smallest heat-transfer levels in the striation region being close to 50%. This phenomenon, observed by Miller et al. (1964), has been investigated in some detail by Ginoux (1969) who performed total-pressure surveys in the reattachment region to define spacings and areas affected by these more or less regularly spaced longitudinal perturbations. Ginoux concluded that the features observed in the reattachment region are similar to subsonic Taylor-Görtler vortices on concave walls and it was hypothesized that flow curvature was sufficient to support such a system. The phenomenon was also carefully investigated by Simeonides (1992), Simeonides et al. (1992) and by Vermeulen and Simeonides (1992) who used infra-red thermography to map the heat transfer distribution over an entire ramp type model. In the case of a model equipped with a sharp leading edge, a clear correlation between the striation pattern at reattachment and leading edge irregularities was found. However, striations were also observed with a rounded leading edge producing no disturbance.

An accurate characterization of the Mach 10 ramp flow was made by Coët et al. (1992) by means of detailed heat transfer measurements using thermocouples installed along two rows on the ramp. The spanwise heat-transfer distributions thus obtained at 35 mm and 55 mm downstream of the hinge line are plotted in Figure 24a. One sees that along the first line, located 15 mm downstream of the reattachment, there are large pseudo-periodic variations of the heat transfer with an amplitude reaching $\pm 40\%$ of the average level at this location. This amplitude is grossly divided by 4 along the line located 20 mm further downstream, showing that the spanwise variations of heat transfer tend to level off when going downstream of the reattachment region. In this case, it is not possible to determine a well-defined spatial frequency for the spanwise variations and to establish a correlation between them and the vortical pattern revealed by the surface flow visualizations.

Similar measurements were performed on the model equipped with a rounded leading edge. As shown by the

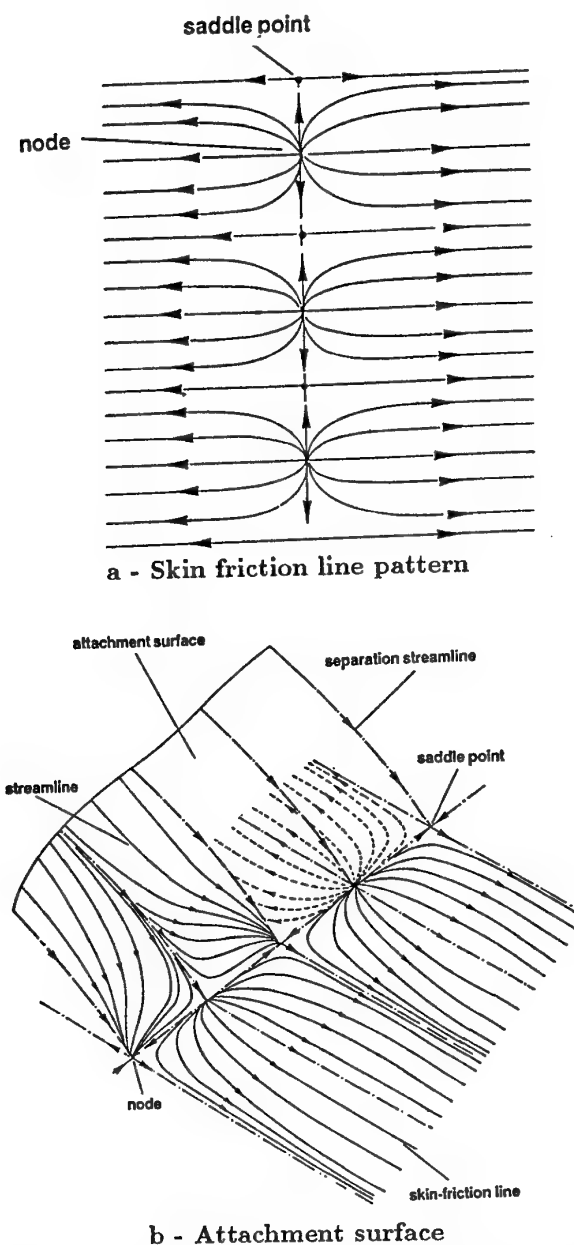


Figure 22: Flow topology in the vicinity of a nominally two-dimensional reattachment.

results plotted in Figure 24b, in this case the spanwise variations of heat transfer are more regular and symmetrical with respect to the model median plane. The amplitude of these variations is respectively equal to $\pm 20\%$ and $\pm 15\%$ of the average level along the lines located at 35 mm and 55 mm of the hinge line. A Fourier analysis of these results allows the definition of a spatial wavelength $\lambda = 13$ mm, identical for the two distributions. Unfortunately, in this case the quality of the surface flow visualization was too poor to reveal the existence of a system of counter-rotating vortices which could be associated with the spanwise variations in heat transfer.

There is no clear explanation of the striation pattern affecting the heat transfer distribution at reattachment.

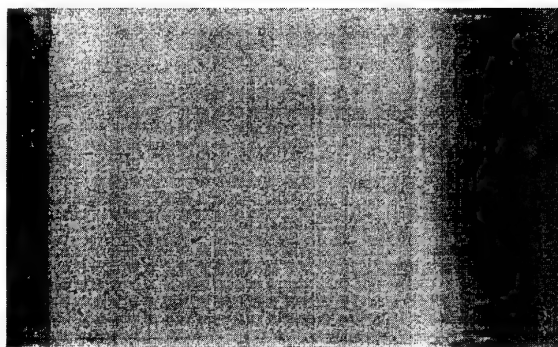


Figure 23: Striation pattern in a hypersonic reattaching flow at $M_0 = 10$ (Coët and Chanetz 1993).

Results obtained with a sharp leading edge show an irregular pattern which cannot be correlated with well-organized longitudinal vortical structures. In this case, the phenomenon seems to be much dependent on the quality of the leading edge. Since most of the published results are relative to transitional interactions, the noticed large spanwise variations could be due to spanwise irregularities in the transition process, high values of the heat transfer being associated to an earlier transition. Then, imperfections affecting the sharpness of the leading edge could have a predominant role.

2.2 Interactions in Three-Dimensional flows

2.2.1 Introductory Remarks

In reality, the vast majority of flows of practical interest are three-dimensional, while planar two-dimensional or axisymmetric configurations are exceptional. It is only for obvious reasons of conceptual simplicity that most studies, both experimental and theoretical, have been devoted to two-dimensional flows. Indeed, in-depth investigation of three-dimensional interactions, especially when separation occurs, is a delicate and lengthy task, due to the complexity of the flowfields and the difficulty to grasp their structure. Moreover, in spite of great progress made in computer technology and numerical methods, accurate computation of three-dimensional flows remains costly for shock-wave/boundary-layer interactions where both strong discontinuities and small scale features must be captured.

However, we have now at our disposal a relatively large amount of recent experimental results on three-dimensional interactions so that it is possible to give a rather complete physical description of the flow organization, even if some features are not yet completely elucidated and still subject to controversy. Most of these data consist of surface flow patterns obtained by oil-film technique, wall-property distributions (pressure, skin friction, heat transfer) and, more rarely, in flowfield visualizations by optical techniques (Settles 1993). Quantitative information on the flow structure (mean velocity and turbulence fields) is relatively scarce because of the difficulty to execute measurements in a three-dimensional

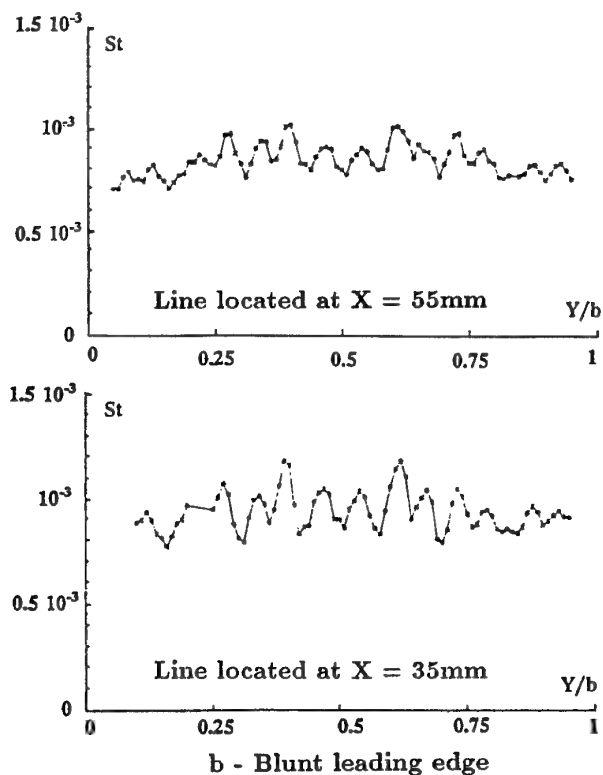
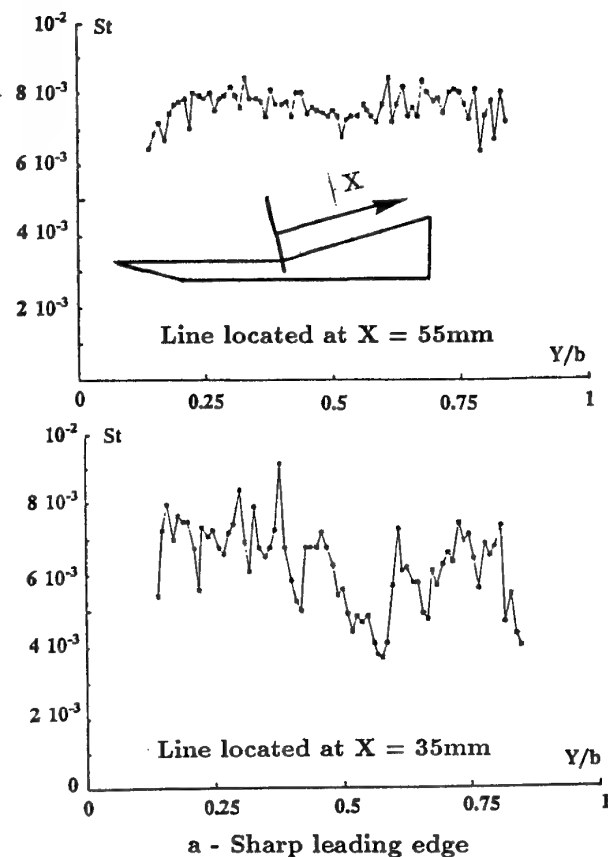


Figure 24: Spanwise heat-transfer distributions in the reattachment region of a ramp flow at $M_0 = 10$ (Coët et al. 1992).

flow. Sophisticated methods have been developed, either intrusive (multi-wire or multi-hole probes) or non-intrusive (Laser Doppler Velocimetry, tomoscopic interferometry), but their use is still delicate and frequently requires assistance of specialized teams, especially in high-speed flows. For these reasons, there is still a general lack of reliable results in the outer flowfield allowing a fine description of three-dimensional interactions and an in depth validation of theoretical models.

In spite of these shortcomings, one should not be negative about our capacity to predict three-dimensional separated flows and, as it will be seen in the coming subsections, impressive results have already been obtained which are in good agreement with available data.

The four basic shock-wave/boundary-layer interactions met in three-dimensional flows are:

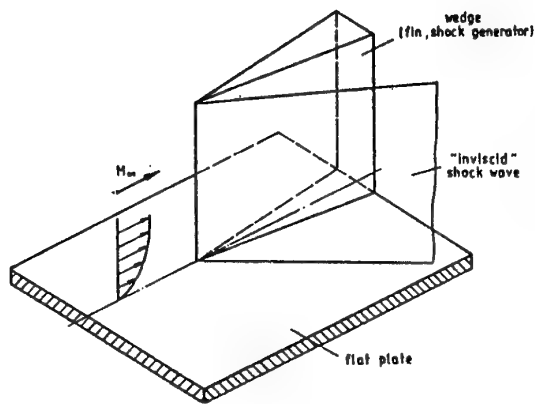
1. The swept wedge.
2. The swept shock, or glancing shock, in which a fin normal to a plate produces an oblique shock interacting with the boundary layer developing on the plate.
3. The corner flow generated by two wedges assembled together with their leading edges perpendicular.
4. The interaction induced by a blunt fin.

Variants of the above configurations may exist, the leading edge of the fin or obstacle may be swept or the blunt obstacle set at an angle of incidence. Thus, a large number of three-dimensional situations may be conceived and this is not the place to examine all of these possible cases. In the present section we shall concentrate on the swept oblique shock, the corner flow and the blunt fin which leads to specific phenomena in the leading-edge region.

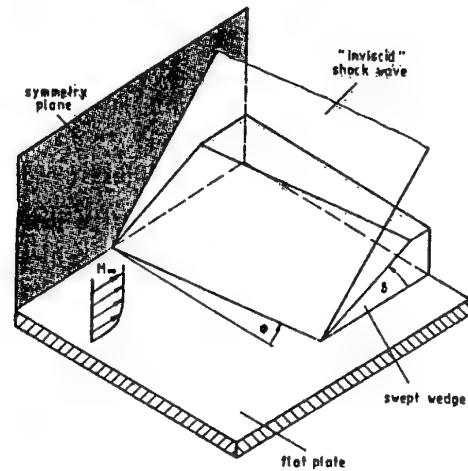
Because of the lack of experimental information on the outer field, the following descriptions will use numerical simulations to establish a consistent description of the flow structure. This approach is typical of three-dimensional flow investigation in which measurements must be completed by computations to arrive at a clear physical understanding of complex phenomena, involving in the present cases, complicated inviscid shock patterns.

2.2.2 The Swept Shock-Wave/Boundary-Layer Interaction

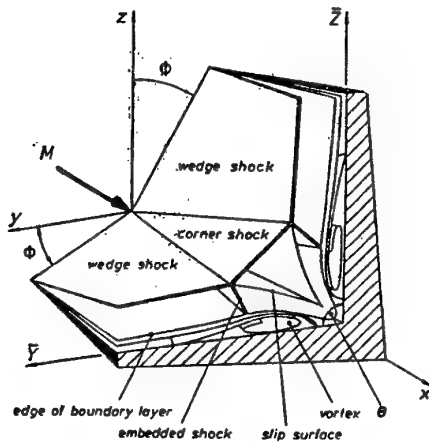
Introduction to the Subject. The phenomenon of swept shock-wave/boundary-layer interaction appears in the axial supersonic or hypersonic flow between two intersecting surfaces. The configurations which have been mostly studied are classified into those with one or two surfaces providing compression. In the former case, basic configurations are the attachment of a sharp fin normal to a flat plate (see Figure 25a) and the attachment of a swept compression corner on a flat plate (see Figure 25b). The flowfields of these two configurations have been found to be similar. The corner formed by the intersection of two wedges (see Figure 25c; Hummel 1989) is the



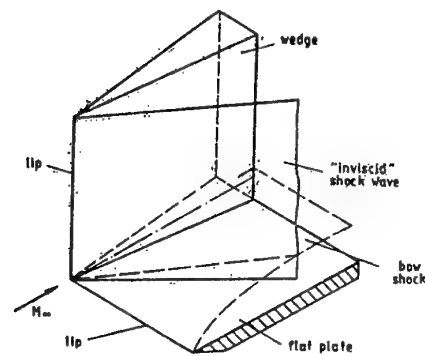
a - Fin/plate configuration



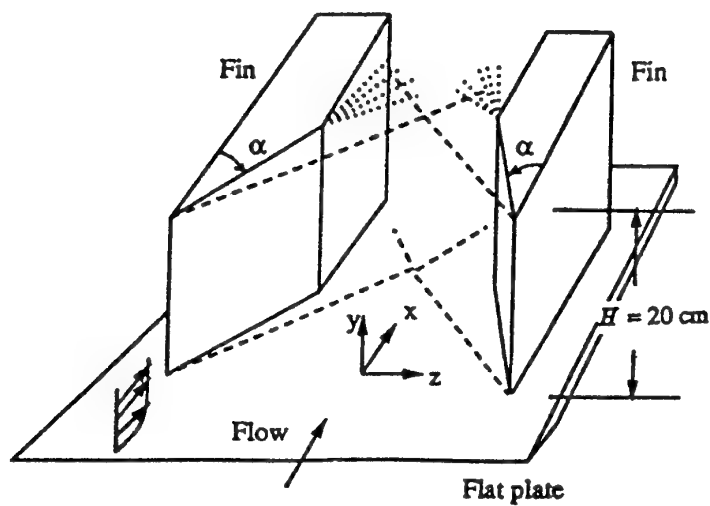
b - Swept corner on a flat plate



c - Wedge/wedge configuration



d - Wedge/plate configuration



e - Double fin

Figure 25: Basic configurations of corner flow.

basic configuration of the flows with two surfaces providing compression. This configuration is usually called an *axial corner*. In the class of the configurations with only one compression surface, the case of the wedge/plate intake (see Figure 25d) has also been considered (Peake and Tobak 1980). Recently, interest has been shown in an extension of the single-fin geometry consisting of two fins or wedges attached normally to a flat plate (Figure 25e). This is the *crossing shock* configuration. The aforementioned configurations are simplified shapes of various elements of high-speed vehicles (junctions between wing/body or fin/body, intake duct of engines, etc.). If the resulting swept shock-wave/boundary-layer interactions are strong, locally high heat-transfer rates and static pressures appear on some surfaces of a vehicle.

Numerous studies of the swept shock-wave/boundary-layer interaction, most of them experimental, have been performed over the past thirty years. The experimental techniques offer reliable results on a surface or on a section of the flow. On the other hand, a numerical solution has the advantage to provide the values of the various parameters in space (more particularly at the grid points of the computational domain). These data can then be transformed into images of the flowfield by applying post-processing techniques. Regarding the flow conditions in the fin/plate configuration, emphasis has been given to supersonic speeds and turbulent boundary layers. In the case of the axial corner, although there are early experimental results on flows with turbulent supersonic conditions, the majority of the studies are related to laminar hypersonic flows.

The structure of the flow in a fin/plate configuration is described in detail in the very recent review of Settles (1993) and Knight (1993) included in the AGARD/FDP-VKI Special Course on *Shock-Wave/Boundary-Layer Interactions in Supersonic and Hypersonic Flows*, while the axial corner flows are examined in the review of Hummel (1989). In the present Section the physics of the swept shock-wave/boundary-layer interactions will be reviewed critically. The axial corner configuration has not been included in the test matrix prepared by the Working Group. However, since there are great similarities between the development of the flow in both types of interactions, with one or two compression surfaces, we will mention some basic common features of the flow in Section 2.2.3.

In general, the interaction domain in these types of flows is quasiconical; i.e., it grows almost linearly in the downstream direction. This feature has been observed experimentally by many researchers, but it is also a conclusion of a theoretical study by Inger (1987). More specifically, through an order-of-magnitude analysis of the governing equations, Inger has found that a swept interaction can approach a quasiconical state at a large distance from the origin of the flow.

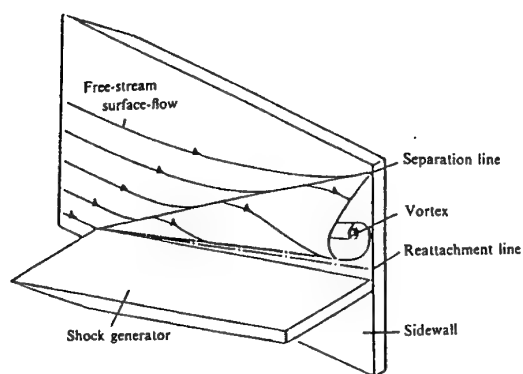
The issues which will be examined in the next section are: the nature of the separation bubble, the conical similarity, the existing flow models and the secondary separation.

Nature of the Separation Bubble. In the case of the fin/plate configuration, the oblique shock generated on the fin crosses the boundary layer which grows along the plate and, owing to the subsonic part of the latter, the shock pressure increase is smeared out on the wall, according to the upstream influence mechanism depicted in Section 2.1.2. Consequently, a disturbed flow pattern appears which covers a significant part of the flow upstream and downstream of the inviscid shock position. If the shock is sufficiently strong, the flow separates and its topology changes significantly. The intensity of the interaction depends on the flow conditions (Mach number, flow direction), the geometry of the fin (blunt or sharp, swept or not) and whether the boundary layer is laminar or turbulent. In the following analysis only strong interactions will be examined which lead to the establishment of separated flow.

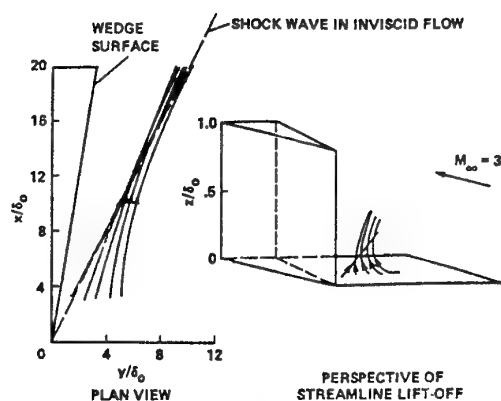
Oil-flow pictures which have been taken during the early years of study of swept shock-wave/boundary-layer interactions, reveal that on the flat plate and ahead of the shock, a separation line is visible, as well as a reattachment line close to the corner. The first flow model of the fin/plate configuration was proposed in 1974 by Token. He suggested that a separation conical vortex appears between the separation and the reattachment lines (see Figure 26a). More recently, Kubota and Stollery (1982) have improved the model of Token. Using the vapor-screen technique, they have detected a smaller vortical structure that appears on the surface of the fin, close to the corner (see Figure 26b(1)). This small structure is always present, according to Kubota and Stollery, even when a weak interaction is established, in which no primary separation vortex is formed (see Figure 26b(2)).

Many numerical simulations of experimentally studied fin/plate flows have been performed (see Section 3.3). Horstman and Hung (1979) have computed a strong-interaction case, in which experimental measurements were done with a wedge angle of 16° at Mach number 4. The calculations show that there is a massive eruption of streamlines away from the surface along the separation line (see Figure 26c). Similar results have been obtained recently by Knight et al. (1987), who examined a flow studied experimentally by Shapey and Bogdonoff (1987). Their results are shown in Figure 26d where it is seen that the streamlines which originate upstream of the separation (or coalescence) line close to the wall rise, cross the separation line, and rotate in the direction in which the separation vortex should rotate. These data strongly support the model of the fin/plate flow that is shown in Figure 26a. However, the following questions have remained unanswered: What is the actual shape of the conical flow? Does the longitudinal vortex of Kubota and Stollery exist? These questions have been answered recently in a paper written by Panaras (1992).

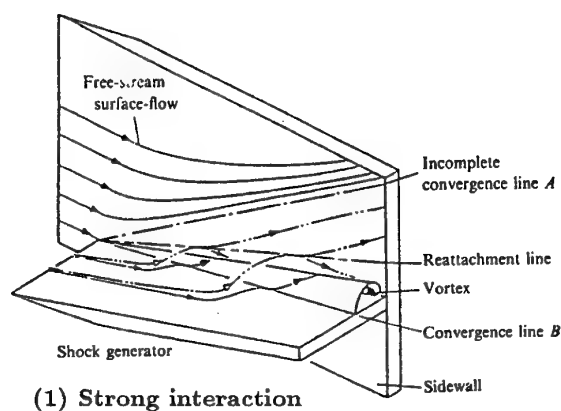
Using a Navier-Stokes solver, Panaras calculated the flow studied experimentally by Shapey and Bogdonoff and computed by Knight et al. (1987). After the validation of the results, Panaras used various post-processing techniques which have been developed at DLR, in order to visualize the elements of the flow structure. As regards the visualization of the vortices, an effective technique has been proposed by Vollmers et al. (1983). These inves-



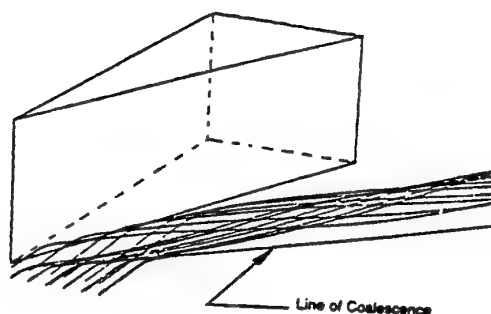
a - Fin/plate configuration. Flow model proposed by Token (1974)



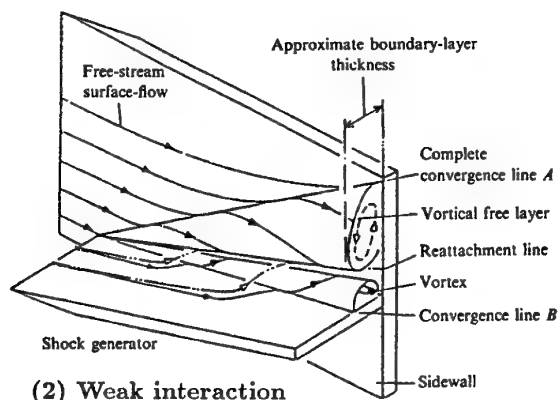
c - Streamline merging and lift-off in a fin/plate flow (Horstman and Hung, 1979)



(1) Strong interaction



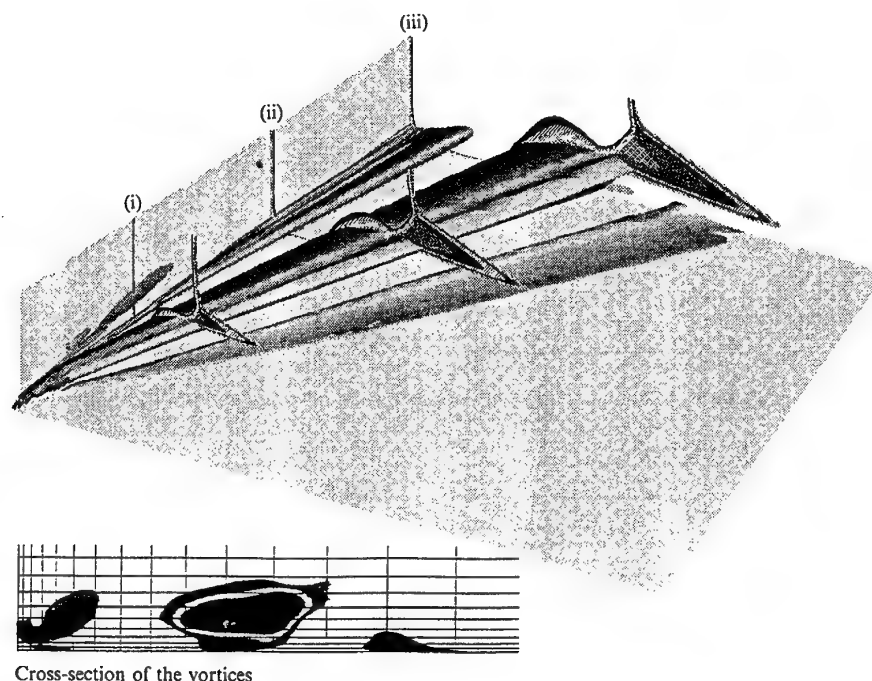
d - Lift-off and rotation of the streamlines in fin/plate flow (Knight et al., 1987)



(2) Weak interaction

b - Fin/plate configuration. Flow model proposed by Kubota and Stollery (1982)

Figure 26: Conical vortex in fin/plate flow.



Cross-section of the vortices

Figure 27: Fin/plate configuration. Perspective view of the conical vortices and of the shock waves. Calculations by Panaras (1992).

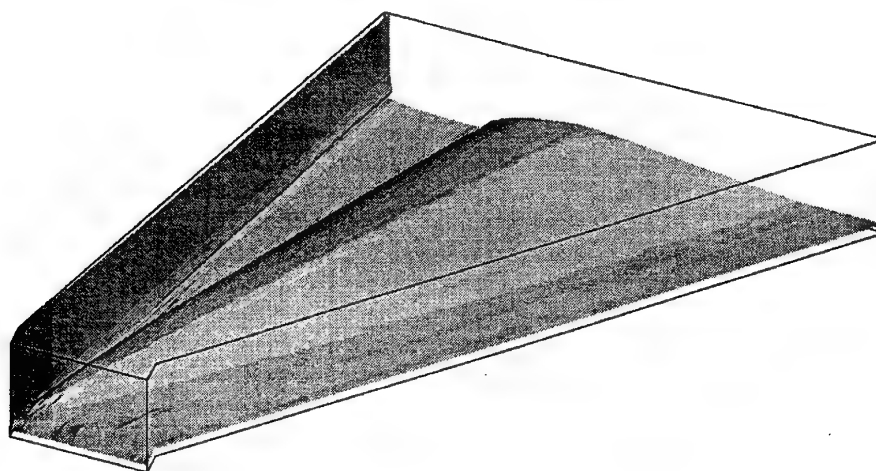


Figure 28: Visualization of the boundary-layer vorticity sheet (Panas 1992).

tigators have shown that vortices exist in those parts of a flow in which the discriminant of the velocity-gradient tensor indicates complex eigenvalues. The discriminant is evaluated numerically at all points of the grid. Contour surfaces of constant values are then created and displayed. These contours indicate where there are vortices. The discriminant technique has been incorporated by Vollmers (1989) in a graphic system called *Comadi*.

All the critical elements of the swept shock-wave/boundary-layer interaction are included in Figure 27 (Panas 1992). The vortices which are expected to appear in this type of flow are visualized in the three-dimensional space by the contours of the

eigenvalues of the velocity-gradient field. In addition, three cross-sections have been drawn on which the density contours are displayed (visualization of shock waves). It is observed that the flow is dominated by a large vortical structure which lies on the flat plate and whose core has a remarkable conical shape with a flattened elliptical cross-section. Also, on the flat-plate side of the main vortex, a thin vortex has developed in the direction of the flow. This is not an independent vortex, but the core of the vorticity sheet which lifts off the surface along the separation line and rolls up to form the conical vortex. Along the vertical fin and close to the corner, the longitudinal vortex (Kubota and

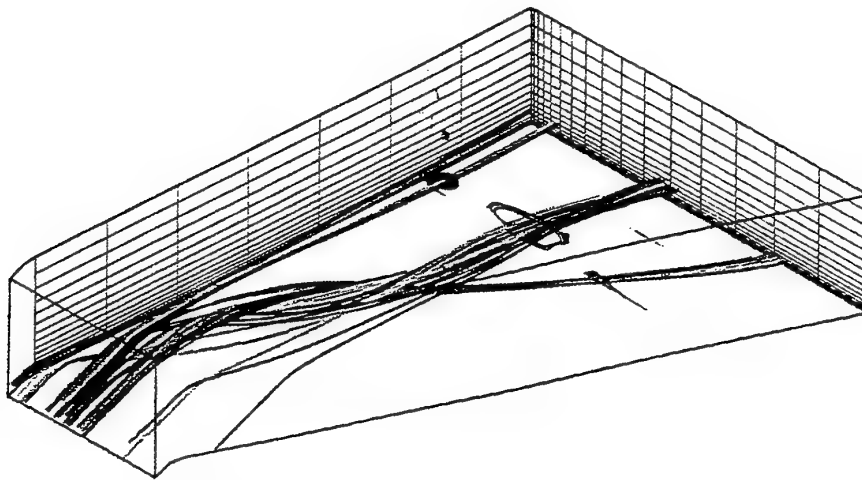


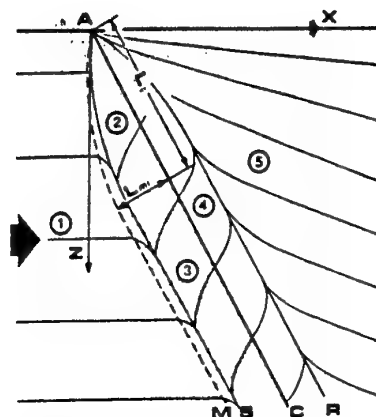
Figure 29: Streamlines passing the core of the vortices (Panaras 1992).

Stollery 1982) is seen. It also develops conically, but with a smaller rate of increase compared to the primary conical structure. In the lower part of the figure, a cross-section of the vortices is shown. There, it is indicated that indeed the flat ground vortex constitutes the initial part of the primary conical vortex.

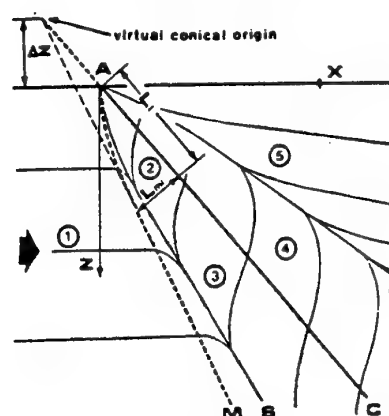
In Figure 28 the vorticity sheet of the boundary layer is shown, as evidence that the boundary layer lifts off the surface of the plate along the separation line to form the conical separation vortex. The formation of the corner vortex along the fin is also clearly seen in Figure 28. The induction characteristics of the vortices of the flowfield are indicated in Figure 29 where some of the streamlines which pass through their cores are shown. It is seen that the conical vortex completes more than one turn in the calculated field, while it is hard to say that the fin vortex turns in the extent of the field.

The density contours in three cross-sections of the flow, which are also displayed in Figure 27, visualize the shock system forming along and on top of the conical vortex. The system is composed of the swept (or sometimes called glancing) shock wave, of the separation shock, produced by the coalescence of the compression wave, and of the rear quasi-normal shock, which extends from the bifurcation point to the surface of the conical vortex. The shear layer which is expected to originate at the triple point is not visible in Figure 27. However, if the absolute value of the vorticity is used as visualization parameter, the shear layer appears. This type of visualization is presented later.

Regarding the features of the flow in a swept corner configuration (see Figure 25b), we have mentioned already in Section 2.2.1 that in general they have been found to be similar to those in a fin/plate configuration. Actually, in a basic experimental study of the swept corner flow, Settles and Teng (1984) have found that in addition to the conical flow regime, a cylindrical one appears under different flow conditions. In Figure 30 an example of the surface flow pattern is shown for these two flow regimes. Interpretation of the surface flow pattern leads to the conclusion that in the case of the conical regime a quasi-conical vortex develops in the corner re-



a - Cylindrical interaction



b - Conical interaction

Figure 30: Schematic of surface streak lines in a swept corner flow (Settles and Teng 1984).

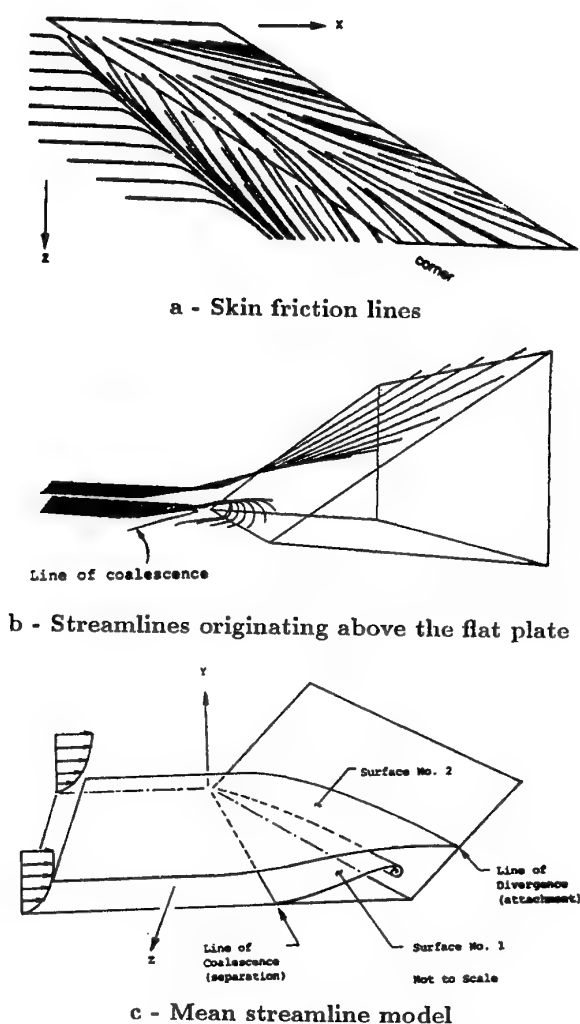


Figure 31: Structure of the flow past a swept compression corner based on calculations of Knight et al. (1992).

gion, while the shape of the separation vortex must be cylindrical in the other regime. According to Settles and Teng, the cylindrical regime is associated with attached shocks and the conical regime with detached ones. To our understanding, no paper has been published related to the numerical simulation of the cylindrical flow regime observed by Settles and Teng.

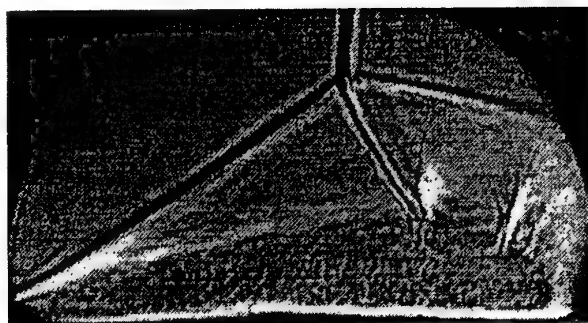
More details regarding the features of the flow in a swept corner are given in papers related to their numerical simulation. The latest publication is that of Knight et al. (1992). The authors initially compared the calculated results with appropriate experimental data with rather good agreement. Then they draw the skin friction lines and some streamlines (see Figures 31a and 31b), which lead them to the development of the mean streamline model shown in Figure 31c. The dominant feature is a large vortex approximately aligned with the corner. A three-dimensional surface of separation originates from the line of separation and spirals into the core of the vortex. The streamlines in this surface are strongly skewed

in the spanwise direction. Another three-dimensional surface, originating within the upstream boundary layer, intersects the compression surface at the line of attachment. This surface marks the extent of the flow entrained into the vortex. Within the upstream boundary, fluid beneath this surface is entrained into the vortex, while fluid above this surface passes over the vortex and up the compression ramp.

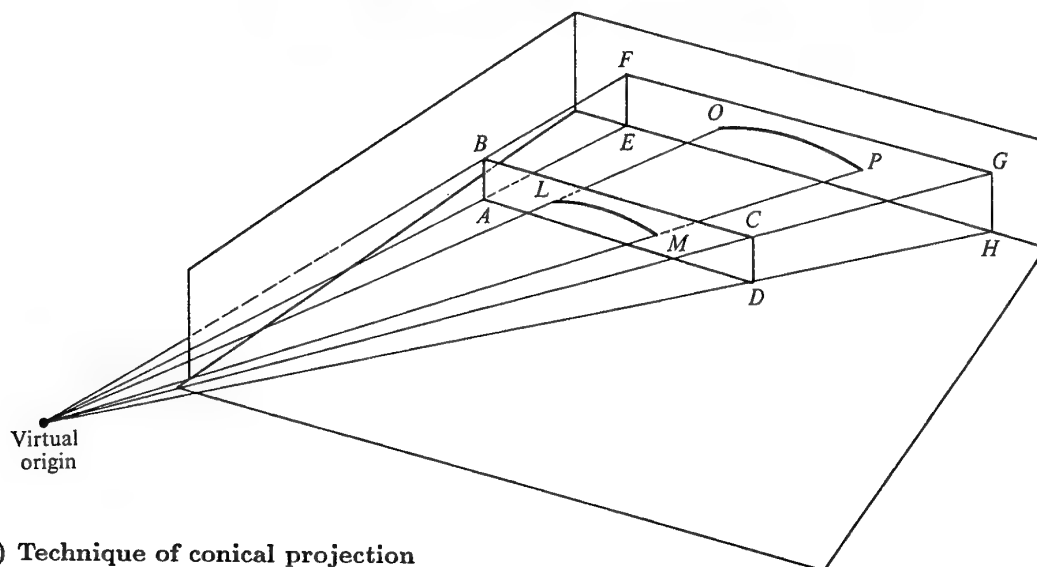
Conical Similarity. In the case of the fin/plate configuration, recent experimental studies have verified the quasi-conical nature of the interaction. In has been found that in addition to the separation and reattachment lines, the extrapolation of the undisturbed oblique shock also converges approximately to the virtual origin of the conical flow (Shapey and Bogdonoff 1987). This origin lies upstream of the fin. At this point we mention that, according to the experimental evidence, the separation line is curved and not straight close to the apex. The initial region of deviation from conical behavior is called by Lu and Settles (1989) the *inception zone*.

According to Alvi and Settles (1990), an important consequence of the quasi-conical nature of the fin/plate flows is the presumption that their features are projected upon the surface of a sphere whose center is the conical origin. They have demonstrated this feature of the conical flow by using conical shadowgraphy. Focusing a light beam at the origin of the approximately conical flowfield and aiming it such that the resulting conical light beam coincided with the rays of the swept interaction, they obtained clear pictures of the flowfield of fin/plate interactions. An example is shown in Figure 32a, for an upstream Mach number equal to 2.91 and a fin incidence $\alpha = 20^\circ$. The cross-section of the flow is normal to the shock. It is seen that on top of the separation bubble lies a well-bifurcated shock. From the shock triple-point, a shear layer emanates and moves towards the corner. The rather good collapse of the flowfield features in the conical optical frame is considered by Alvi and Settles as a proof that the interaction is almost conical in nature.

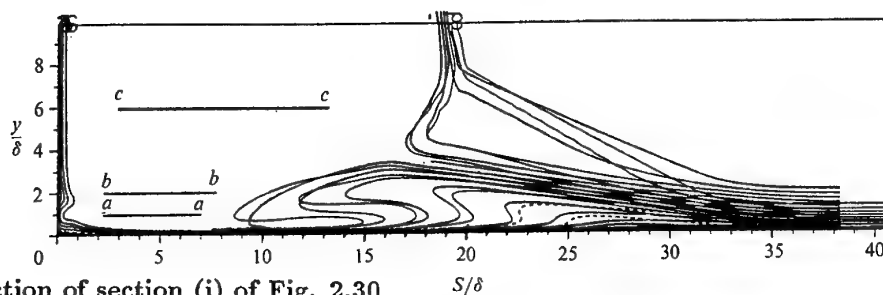
In the conical projection of Alvi and Settles (1990) the flow seems to be quasi-conical and not conical. Then the question arises: What causes this deviation? In this context, Panaras (1992) observes that the different rate of thickening of the conical vortex and of the boundary layer of the plate is expected to affect the conical similarity adversely. For studying this effect, Panaras conically projected the sections (i) and (ii) shown in Figure 27 on the outflow section (iii). The iso-Mach lines have been used as visualization parameters. The results of this correlation are shown in Figure 32b. It is observed in Figure 32b(2), where section (i) is conically projected on the outflow section, that, while good coincidence is observed between the separation bubbles, the swept shock and the shock triple-point, the feet of the lambda-shock system are fairly correlated, especially the separation shocks, while there is no equivalence at all between the boundary layers in the two cross-sections. More particularly, the boundary layer of the first cross-section is about 40% thicker than the boundary layer of the third section. This large difference in the scaling is due to the lower rate of development of the boundary



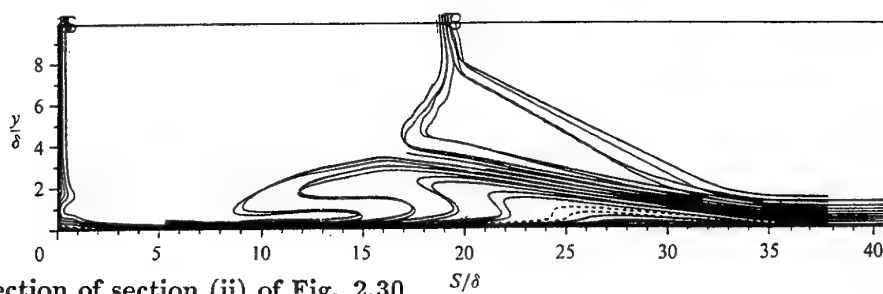
a - Conical shadowgraph in a $M_0 = 3, \alpha = 20^\circ$ fin/plate flow (Alvi and Settles, 1990)



(1) Technique of conical projection



(2) Projection of section (i) of Fig. 2.30



(3) Projection of section (ii) of Fig. 2.30

b - Calculations of Panaras (1992)

Figure 32: Conical similarity of the flow. Conical projection of sections of the flow on the outflow plane.

layer, compared to that of the vortex.

The deviation from the conical behavior is smaller if the two cross-sections which are conically correlated are closer. This is demonstrated in Figure 32b(3) where section (ii) is conically projected on section (iii). At this point we note that in the shadowgraph pictures of Alvi and Settles (see Figure 32a) multiple shock formations exist, one close to the other. However, in this case the effect of the boundary layer is not visible, because in the optical technique used by Alvi and Settles it is not possible to distinguish the various cross-sections of the flow. Panaras, in addition to the aforementioned illustrations has presented quantitative data which verify the observation done in Figure 32b(2) that the deviation from conical similarity is greater at the part of the flow between the separation shock and the plate.

Models of the Cross-Section of a Corner Flow. The first qualitative model of the structure of the viscous part of the flow has been presented by Korgegi (1976). In his paper, Korgegi compares experimental results of laminar and turbulent, supersonic and hypersonic flows about a wedge/plate configuration. More specifically, he compares the surface flow patterns, pressure distributions and heat transfer. From the comparisons he concludes that the characteristics of skewed shock-induced separated regions do not exhibit any basic difference between laminar and turbulent flow for comparable extent of separation, but of course the shock intensities needed for extensive separation are much larger for turbulent than laminar flow. Korgegi presents qualitatively a sequence of flow characteristics (repeated here in Figure 33) from unseparated flow to extensive separation on a planar surface caused by a wedge-induced shock wave of progressively increasing strength. The lines of interaction on the surface are essentially conical. Korgegi assumes that although his model is based on results of a wedge/plate model they are also valid for the wedge/wedge (axial-corner) configuration.

In strong interactions, the model of Korgegi predicts the development of a secondary separation region within the primary one, as shown in Figure 33e. In this figure, S_1 and R_1 are respectively the primary separation and reattachment lines, and S_2 , R_2 the secondary ones. The component of surface shear normal to the lines of interaction τ_n undergoes three reversals in sign. At this point we note that in the actual surface oil-flow photographs presented by Korgegi, the secondary reattachment line exists only in the examined laminar flows. In the turbulent flows, the photographs show that between the primary separation and attachment lines, only the secondary separation line exists. The reattachment line does not clearly appear. We will return to this point in the next section.

In the case of the fin/plate configuration, Kubota and Stollery (1982) in addition to the separation vortices, investigated the structure of the shock system. Of paramount importance for the development of the flow model is whether or not the lambda-foot bifurcation of the fin shock at the region of its interaction with the boundary layer appears, exactly as it happens in a strong two-dimensional shock-wave/boundary-layer in-

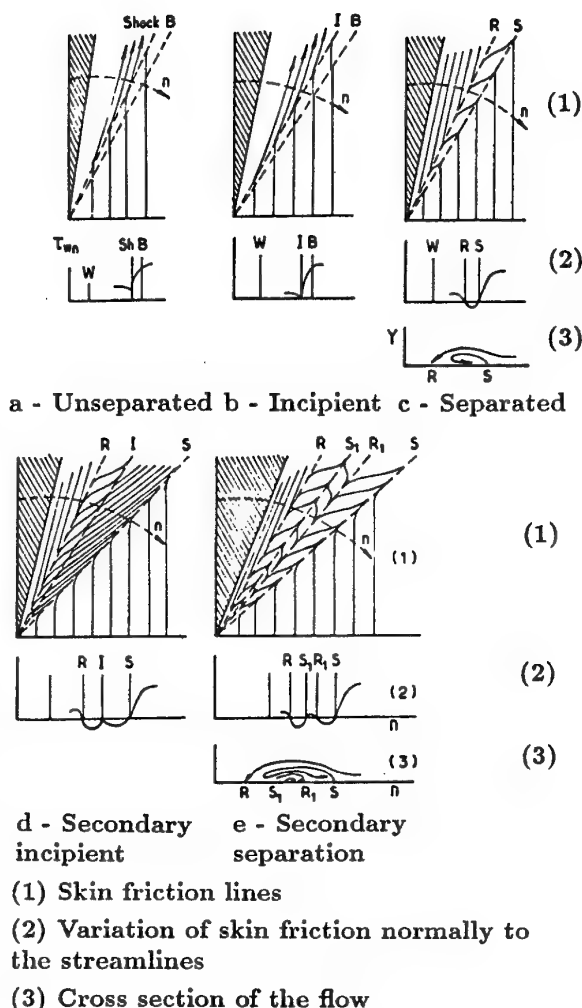


Figure 33: Flow model of Korgegi (1976).

teraction. In order to resolve this question, Kubota and Stollery used the vapor-screen technique in their Mach 3 tests. According to their vapor-screen pictures, when the angle of the fin is smaller than the one required for the appearance of separation, there exists no lambda shock. On the other hand, for larger angles, when the corresponding oil-flow picture suggests a separated flow, there is evidence of the shock splitting into a lambda shape near the edge of the boundary layer (see Figure 34). However, it is seen in Figure 34 that the resolution of the pictures of the vapor-screen technique is not adequate for a firm conclusion. More recently, Bogdonoff (1990) tried to clarify some critical features of the fin/plate interaction, including the question of the lambda shock. To that purpose, he combined experimental (Shapey and Bogdonoff 1987) and calculated results (Knight et al. 1987) to construct the Mach number iso-line picture shown in Figure 35. In this picture it is hard to say that a lambda-shock formation is depicted, though in the examined interaction ($M_0 = 3$, $\alpha = 20^\circ$) the surface oil-flow pictures indicate the existence of separation and reattachment lines. Thus the question of the existence of a lambda-shock formation in a fin/plate configuration remained unresolved.

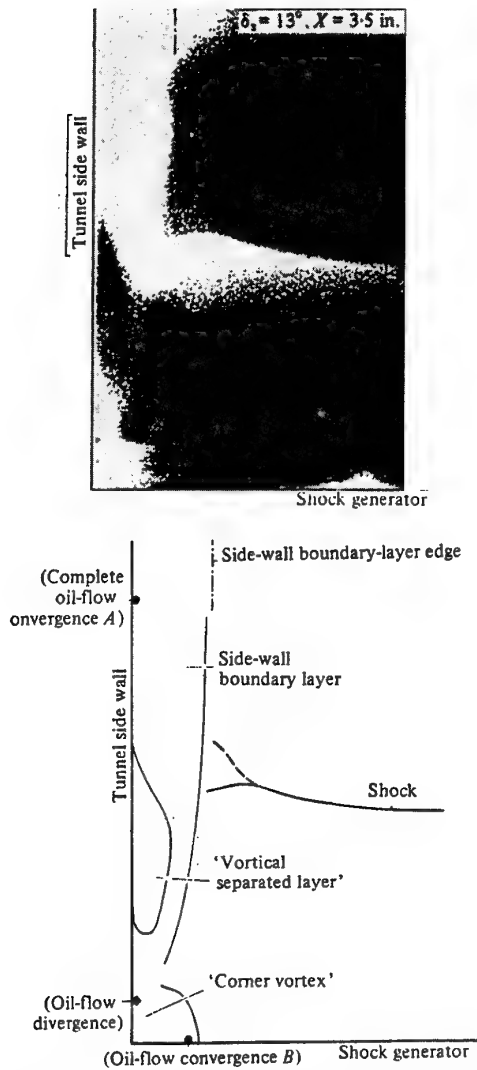


Figure 34: Detection of a lambda shock by Kubota and Stollery (1982).

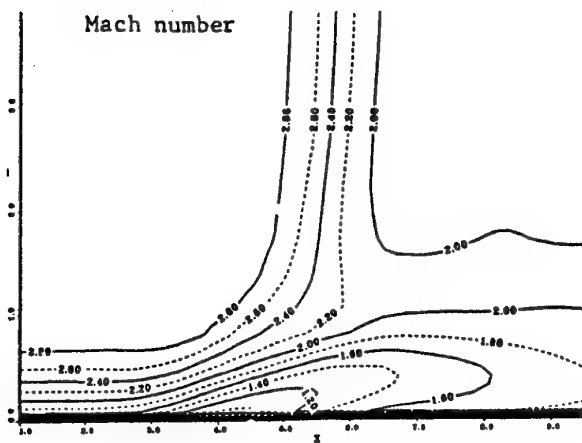


Figure 35: Composition of Bogdonoff (1990).

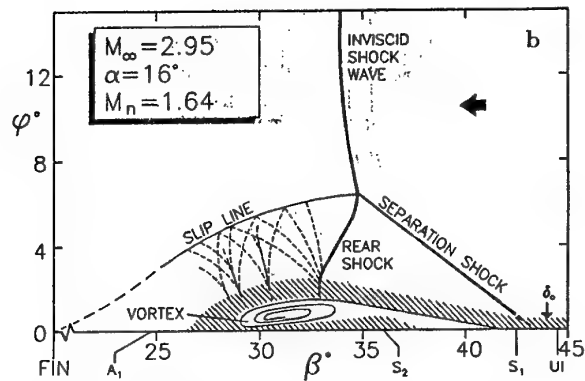
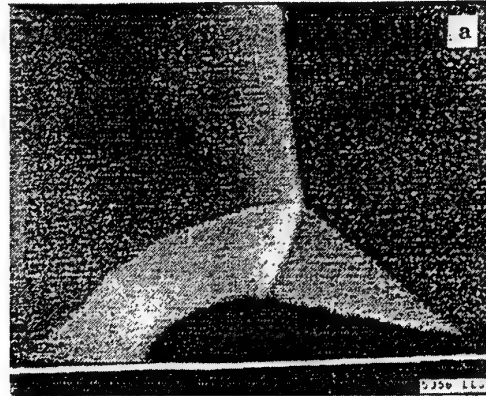


Figure 36: Planar laser picture (a) and flow model (b) of Alvi and Settles (1991).

Recently, Alvi and Settles (1991) obtained clear cuts of the flowfield normal to the shock in a fin/plate configuration using the new planar-laser-scattering technique. Their results led to the construction of a flow model in conical coordinates. An example is shown in Figure 36 for a test case $M_0 = 3$, $\alpha = 16^\circ$. Panaras (1992) has verified numerically the model proposed by Alvi and Settles using the iso-contours of the absolute value of the vorticity as visualization parameter. This is shown in Figure 37 where we see that a remarkable similarity exists between the calculated cross-section of the flow and the model of Alvi and Settles. Later, Knight et al. (1992) presented refined calculations of the test case of Alvi and Settles in which the lambda shock is evident on various colored contour plots, particularly the density plots. According to Knight et al., the computed flowfield exhibits most of the features of the model of Alvi and Settles. The computations do not exhibit the normal shock, transonic shocklets, and secondary separation observed in the experiment.

Regarding the nature of the flow in a crossing shock geometry, Knight (1993) reviews in detail the computed and experimental results and presents a model of the streamline and shock structure. According to this model, the principal feature is a pair of counter-rotating vortices, generated by the individual single-fin interactions, which interact at the plane of symmetry and rise above the surface (see Figure 38a). The shock structure of the

model of Knight (1993) is shown in Figure 38b, at various cross-sections of the flow. Near the leading edge of the fins, the flowfield is comprised of two single-fin interactions which are characterized by a lambda shock (see Figure 38b(1)). Downstream of the leading edge, the separation shocks (2) intersect, forming a reflected shock with two segments (4a) and (4b) (see Figure 38b(2)). The "bridging" segment (4a) rises with increasing downstream distance. The remaining segment (4b) moves towards the fins and interacts with the rear segment (3) of the original lambda shock, forming a localized high pressure region (6). A separate curved shock (5) forms on the center line near the surface and is associated with the turning of the flow near the surface along the plane of symmetry (see Figure 38b(3)). Downstream of the intersection of the inviscid shocks (1), an expansion region (8) forms, while the separate shock (5) remains (see Figure 38b(4)). The reflected shocks (7) move towards the fins.

Secondary Separation in Turbulent Fin/Plate Interactions. In the previous section, we noticed that according to the data of Korkegi (1976) for a wedge/plate configuration, while in a laminar strong swept-shock/boundary-layer interaction, a secondary reattachment line appears (in addition to the separation one), no secondary reattachment line is visible in a turbulent interaction. Also, in the turbulent fin/plate flows studied by Settles and his associates at Penn State University, the existence of a secondary separation line in the surface flow pattern has been detected only in interactions of moderate strength and it disappears in stronger ones. The first data regarding this strange phenomenon were published recently by Kim et al. (1990) and since no other evidence than the separation line has been detected, related to the phenomenon of the secondary vortex, Alvi and Settles state that "this separation is too weak to qualify unequivocally as a secondary separation of the reversed flow within the primary separation zone".

Panaras and Stanewsky (1992) have simulated numerically one of the flows of Alvi and Settles (1990) in which the secondary separation line appears. They found that if the Baldwin-Lomax algebraic-turbulence model is interpreted according to the physics of the flow (Panaras and Steger 1988), the resulting numerical solution agrees well with the experimental evidence (wall pressure, skin friction). Then, post processing of their solution revealed that actually in this type of interaction the secondary-separation phenomenon is similar to that observed in flows about bodies at high incidence.

In Figure 39a a perspective view of the skin-friction lines along with some cross-sections of the vortices are shown (visualized by the discriminant technique). In this figure, it is demonstrated that the secondary vortex is gradually formed along the secondary separation line. In this case there also exists no secondary reattachment line. It seems that a finer grid is necessary in the region of the secondary separation, for resolving the local details of the flow.

In Figure 39b a cross-section of the vortices and the corresponding variation of the wall pressure and of the skin-friction coefficient are shown. It is seen that the sec-

ondary vortex coincides with a peak in the skin-friction distribution in the direction normal to the shock, C_{f_n} , exactly as it has been postulated by Korkegi (see Figure 33e). Furthermore, it lies close to a secondary peak in the total skin friction C_f . In Figure 39c the velocity vectors have been drawn in a cross-section normal to the axis of the secondary vortex. It is seen that a weak circulatory motion exists very close to the surface of the plate at $z/\delta = 12-15.5$. Also, above the secondary vortex a nearly "dead-air" region of triangular shape exists. Panaras and Stanewsky conclude that in the crossflow, the lower part of the conical vortex is channeled between the fin and the secondary vortex, which appears as a "bump" of triangular shape.

In his recent review, Settles (1993) includes some significant experimental data from the Institute for Theoretical and Applied Mechanics in Novosibirsk. These data have originally been published in Russian, and part is related to secondary separation. We transfer here some of the conclusions of the Russian scientists, as they were quoted by Settles. According to Zheltovodov et al. (1987), the secondary separation line first appears once the interaction has achieved a certain strength, showing up in the conical region but not in the inception zone (exactly as it is shown in Figure 39a of Panaras and Stanewsky). Its spanwise extent grows with increasing shock strength but then diminishes again, eventually appearing only in the inception zone and then disappearing altogether. Secondary separation then reappears in the strongest interaction observed today ($M_0 = 4, \alpha = 30.6^\circ$), but in a different position closer to the fin than previously. The experimental results of Zheltovodov et al. demonstrate that the initial behavior of secondary separation is related to laminar, transitional and then turbulent reversed flow in the swept separation bubble. They also ascribe the reappearance of secondary separation to the development of supersonic reversed flow in the separated region with an embedded normal shock wave. Regarding the secondary reattachment line, Zheltovodov and his associates have obtained evidence of its existence in the aforementioned extremely strong interaction (very close to the secondary separation line).

2.2.3 The Axial Corner Flow

Regarding the axial corner established between two intersecting plates or wedges, experimental results at high supersonic and hypersonic Mach numbers have started to appear in the literature in the sixties (Stainback 1960; Stainback and Weinstein 1967). In those early tests, pressure distributions and heat transfer rates were measured on the wall in the corner region. The tests indicated that both parameters have considerably high values in the corner region. The first flowfield measurements were performed by Charwat and Redecopp (1967) and led to the identification of the shock system which is established in these types of flows. Regarding the nature of the viscous part of the flow in a wedge/wedge configuration, Charwat and Redecopp found some indications of separation in the corner. Later it was found that the separation bubble is actually a conical vortex. Strong evidence of corner vortices was provided by Bertram and Henderson (1969) and especially by Kirke and Hummel

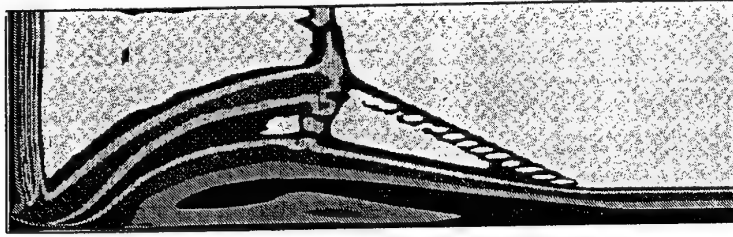


Figure 37: Calculation of Panaras (1992).

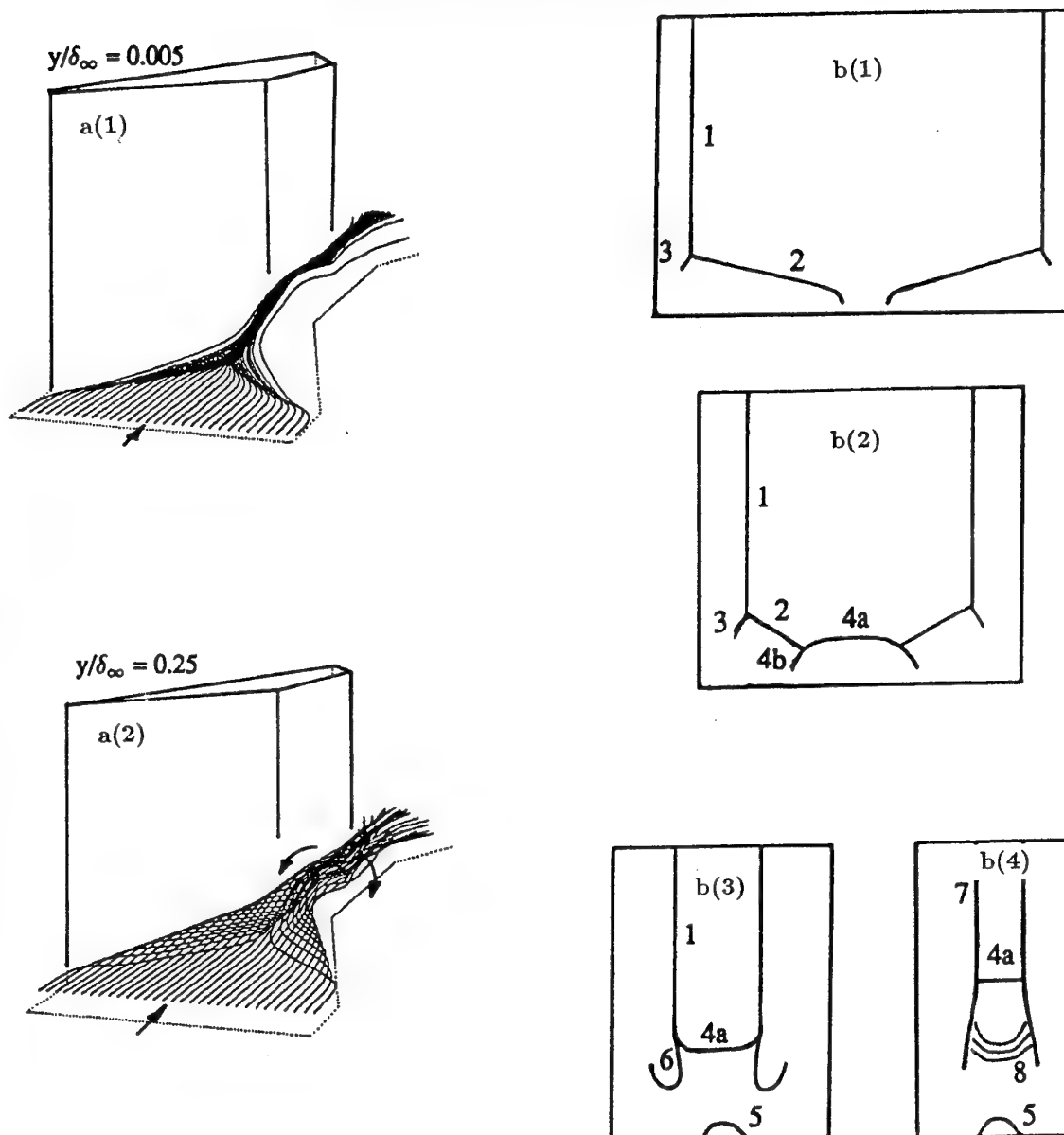
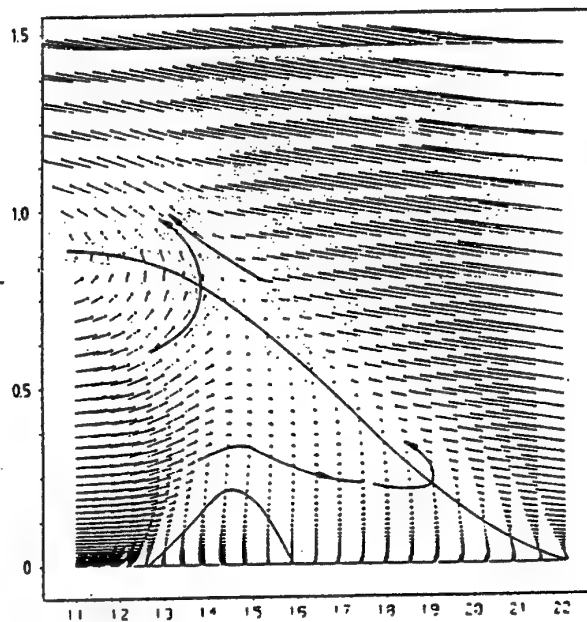
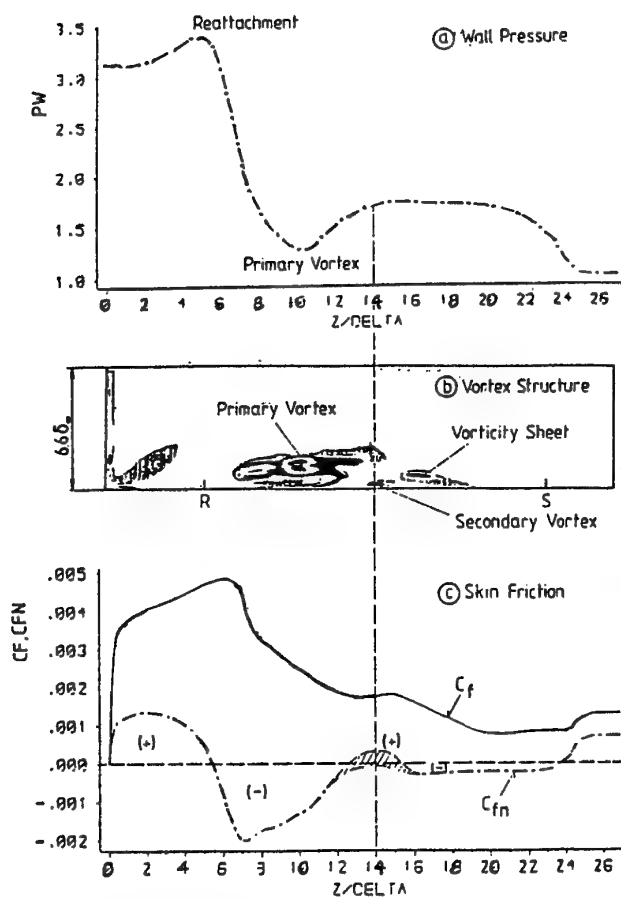
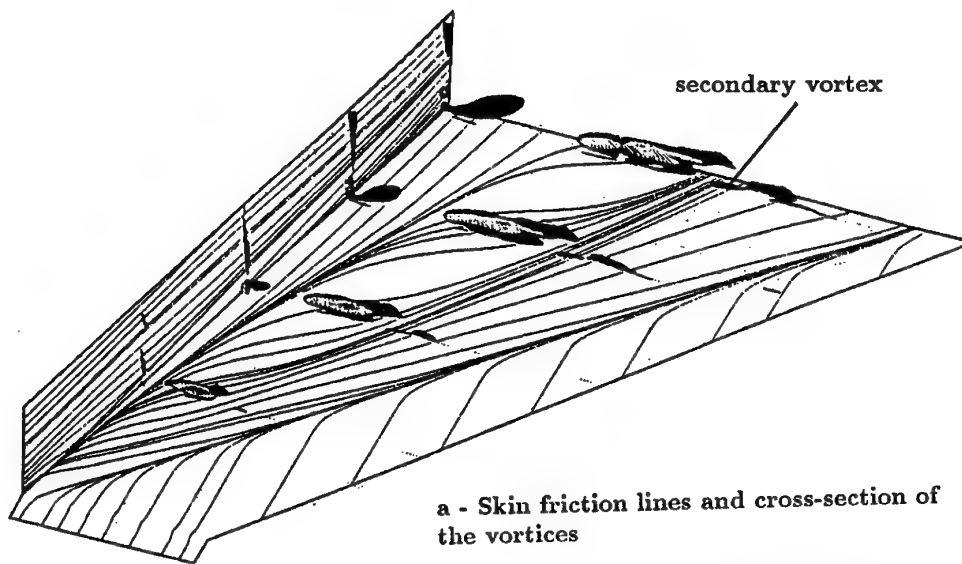


Figure 38: Crossing shock/shock model (Knight 1993).



waves are generated in an axial corner at the region of separation of the boundary layer instead of a shock wave (because the thickening and separation of laminar boundary layers is much smoother than for turbulent boundary layers). Second, in the fin/plate configuration, there exists no secondary reattachment line.

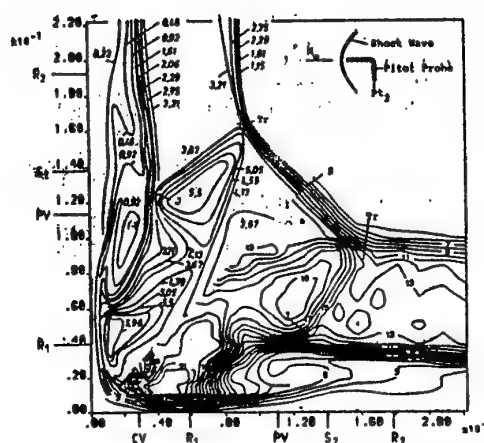
Regarding the numerical simulation of the corner flow the results of Qin and Richards (1987) are significant. Their method is based on the assumption of local conical flow; i.e., the radial derivatives of the flow quantities are taken equal to zero. This is a critical assumption since the conicity of the flow is an issue that should be investigated numerically, and not assumed *a priori*. However, there are other aspects of the cross-section of the flowfield that are clarified by the method of Qin and Richards. An example of calculation of the $M = 12.3$ flow in a wedge/wedge configuration is shown in Figure 41. The agreement with the experiments of Müllestädt (1984) is very good (see Figure 41a). Also the streamlines in the calculated cross-section (see Figure 41b) support the model of Hummel shown in Figure 40a. It is noted that the solution of Qin and Richards predicts a corner vortex which has not been reported earlier. Is it similar to the corner vortex discovered in the fin/plate configuration by Kubota and Stollery? For the clarification of this question a combined experimental/computational program is necessary.

2.2.4 The Blunt Fin

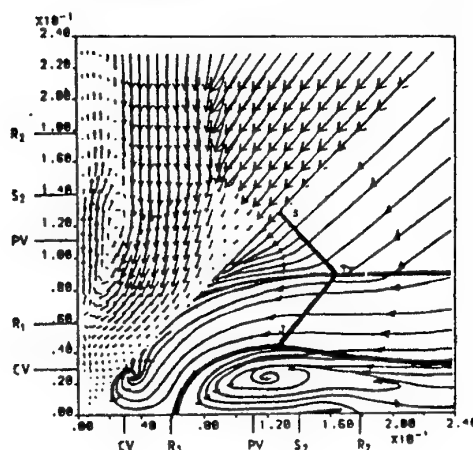
General Remarks. In this configuration, a fin with a rounded leading edge—or *blunt fin*—is mounted perpendicularly to a flat plate on which a boundary layer develops. For the sake of simplicity, the fin will be assumed without incidence and unswept, the incoming supersonic flow being uniform. Although this configuration is not included in the data base, it is worth to recall the main properties of the flow generated by a blunt fin since this geometry is frequently met in practice.

When the obstacle height is sufficient, very high values of the pressure, pressure gradient and heat transfer rate are measured on the obstacle and in its vicinity, on the plate. Hence, this kind of flow has a great practical importance and has been the subject of specific investigations (Price and Stalling 1967; Westkaemper 1968; Korkegi 1971; Winkelman 1972; Kaufman et al. 1972; Dolling et al. 1979; Stollery et al. 1986; Aso et al. 1990). The three-dimensional flow considered here is extremely complex and depends on a large number of parameters: the size, shape and angle of incidence of the obstacle, the upstream Mach number, the Reynolds number, the thickness of the incoming boundary layer, the shape of its velocity distribution. Because of this complexity, information on this type of interaction is more scarce. Hence, the flow organization and its general properties are still far from being entirely elucidated.

The Inviscid Flow Structure. The structure of the inviscid outer flow associated with the interaction is revealed by sketch in Figure 42, established from a schlieren picture of the flow produced by a blunt fin with a circular



a - Comparison with experiment



b - Flow in a cross section

Figure 41: Calculations of Qin and Richards (1987).

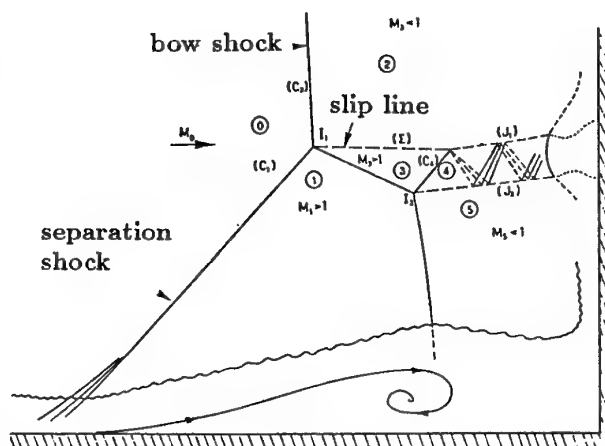


Figure 42: Inviscid flow structure associated with a blunt-fin induced interaction.

leading edge placed in a Mach 3 incoming flow (Dolling et al. 1979).

The sketch shows the trace in the vertical plane of sym-

metry of the wave system forming at the obstacle foot. This system is made of the leading-edge shock (or bow shock) (C_1) and of the separation shock (C_2) originating well upstream of the obstacle, within the boundary layer. Shocks (C_1) and (C_2) generate a transition of the upstream state (0) to states (1) and (2), respectively. Their intersection at point I_1 gives rise, in this case, to a complex wave pattern. From the triple point I_1 emanates the shock (C_3) through which there is a transition from state (2) to state (3). Downstream of (C_2) and (C_3) the flow is still supersonic, whereas it is subsonic after (C_1) which is a strong, nearly normal shock. Consequently, states (3) and (1) are separated by a slip line (Σ) across which velocity and entropy undergo strong discontinuities.

A second triple point I_2 exists, from which—in addition to (C_3)—two oblique shocks (C_4) and (C_5) start. Downstream of (C_4) one observes the formation of a supersonic jet, bounded by the two boundaries (f_1) and (f_2) and surrounded by the subsonic flows (1) and (5) in which the pressure is nearly constant. At the impact point of the jet with the fin, extremely high values of the pressure and heat transfer can be measured if the upstream Mach number M_0 is high. This kind of structure has been designated as a Type IV interference by Edney (1968). Variants, of the Type III for example, can be encountered in obstacle induced separation. However, the permanent features of the wave pattern associated with this kind of interaction are the detached shock (C_1), the separation shock (C_2) and the Mach stem (C_3). In hypersonic flows, the heat transfer in the impact region of the supersonic jet (or shear layer in the case of a Type III interference) can reach 20 times the level existing at the nose of the vehicle, hence the great importance of a careful examination of obstacle induced separation.

The Separated Flow Structure. An example of surface flow visualization is given in Figure 43a. This result has been obtained by Sedney and Kitchens (1977) in a $M = 2.5$ flow for an obstacle constituted of a circular cylinder. This visualization reveals the following features:

1. A critical point S of the saddle type exists well upstream of the cylinder. Through S goes the separation line (S) towards which the skin-friction lines converge.
2. An attachment node R is visible very close to the obstacle. Through R goes the attachment line (A).
3. The two spots of visualization, visible behind the cylinder, denote the existence of two critical points of the focus type. These points are the trace on the surface of two tornado-like vortices escaping into the outer flow where they rapidly bend in the downstream direction. This feature is typical of this kind of obstacle.
4. The picture also reveals the traces of the bow shock and of the Mach stem.

For more clarity, a sketch of the surface flow pattern is shown in Figure 43b. The skin-friction lines converging towards the separation line (S) from downstream all

emanate from the attachment node R . The attachment line (A) separates these lines into a first family tending towards (S) and another family streaming towards a second separation line, very close to the obstacle and for this reason, not visible.

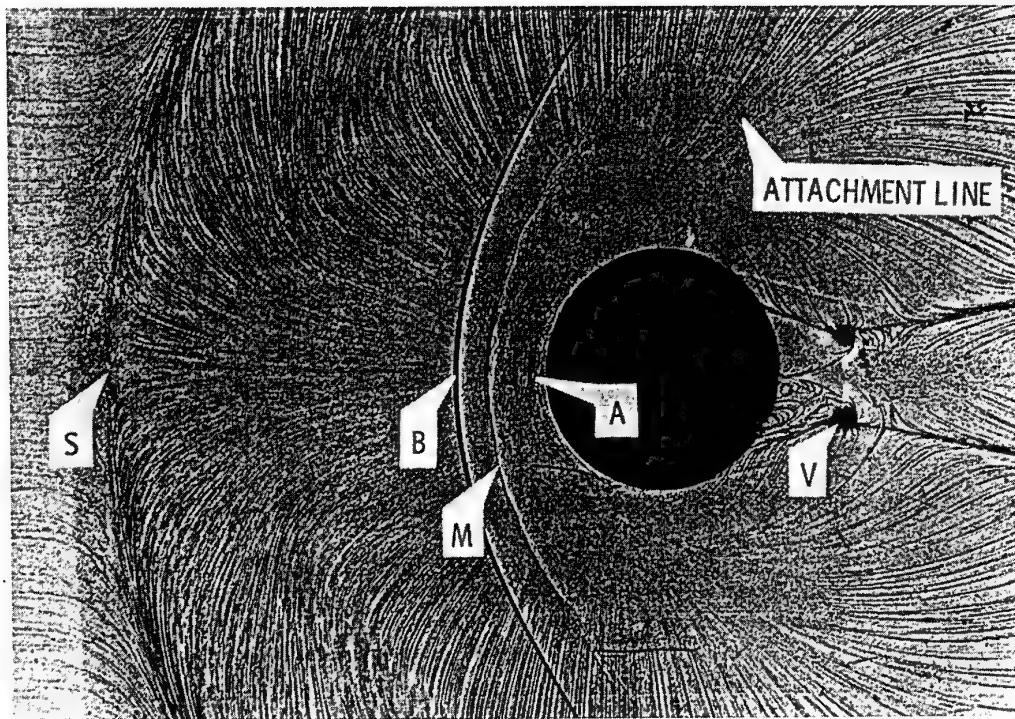
An interpretation of the outer flow structure in the plane of symmetry is shown in Figure 44. The point S is the origin of a streamline, having the character of a separator (S_1), which flows into the focus \mathcal{F}_1 . In a similar way, the attachment point R is the end point of the separator (S_2). It is to be noticed that R , which is a node on the plate, has the character of a half-saddle in the outer flow. The streamlines comprised between (S_1) and (S_2) flow into the focus \mathcal{F}_1 where they “disappear”. Thus, the separated flow is essentially constituted by a horseshoe vortex, surrounding the cylinder, its trace in the vertical plane of symmetry being the focus \mathcal{F}_1 . It is probable that a second vortex, associated to the focus \mathcal{F}_2 exists very close to the cylinder foot, as represented in Figure 44. Then an attachment point R' must be present on the cylinder. Furthermore, a separator emanating from the corner and winding around \mathcal{F}_2 must be introduced to insure the topological consistency of the flow structure.

For a given obstacle and a fixed upstream Mach number M_0 , the separated flow structure can change considerably with the Reynolds number. Figure 45a shows a surface flow visualization where, in addition of the separation line (S), one observes two “secondary” separation lines (S_1) and (S_2). To these lines are associated the attachment lines (A), (A_1) and (A_2). The surface flow pattern is drawn in Figure 45b, while Figure 46 shows the flow organization in the vertical plane of symmetry. Now, four vortices, corresponding to the foci \mathcal{F}_1 , \mathcal{F}_2 , \mathcal{F}_3 and \mathcal{F}_4 , surround the obstacle.

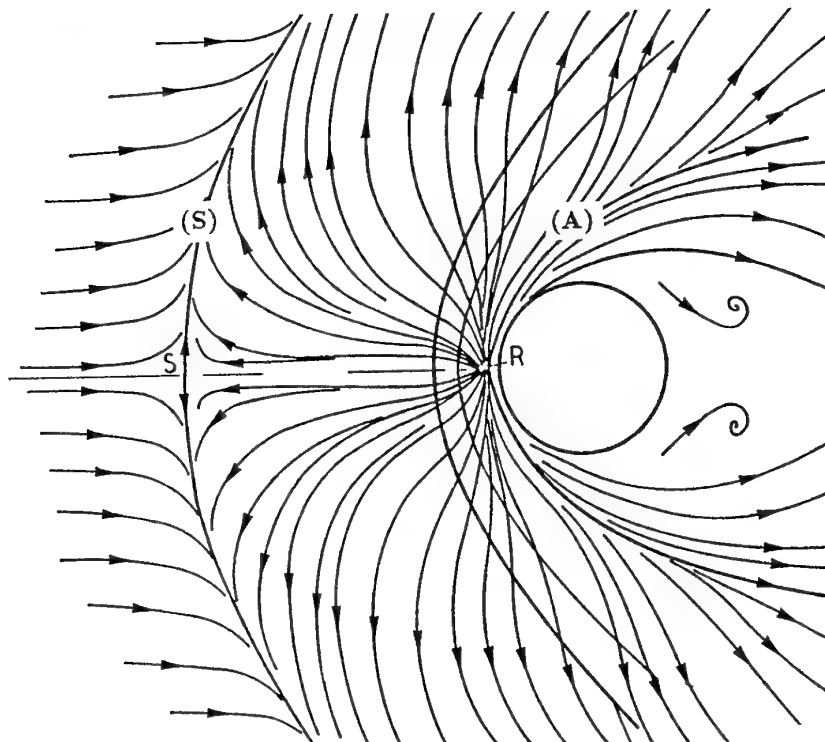
Other vortical structures can be observed such as the transition from one structure to the other occurring for small changes in the Reynolds number and being perfectly reproducible. This behavior suggests a delicate balance of the flow which is easily modified by slight changes in the initial conditions.

Similar observations were reported by Ozcan (1982) who made experiments for laminar conditions. This author noticed that the number of separation lines fall from 3 to 2 and then to 1 when the Reynolds number is raised. However, at still higher values of the Reynolds number, several separation lines were visible again. This behavior presents a strong similarity with the one observed by Zheltovodov et al. in the case of the swept shock wave and which was attributed to an influence of laminar-turbulent transition (see Section 2.2.2 above).

Similarity Properties and Scaling Laws. The question of the similarity properties of the blunt obstacle induced interaction has been considered by several investigators (Uselton 1967; Westkaemper 1968; Lucas 1971; Winkelmann 1972; Sedney and Kitchens 1977; Dolling et al. 1979). Here we will restrict ourselves to the main conclusions of these studies. In particular, Dolling (1982) has shown that in the case of a blunt obstacle, one has to distinguish two regions:



a - Oil flow visualization



b - Sketch of skin friction line pattern

Figure 43: Surface flow pattern of a blunt-fin induced separation at $M_0 = 2.5$. Two vortex configuration (Sedney and Kitchens 1975).

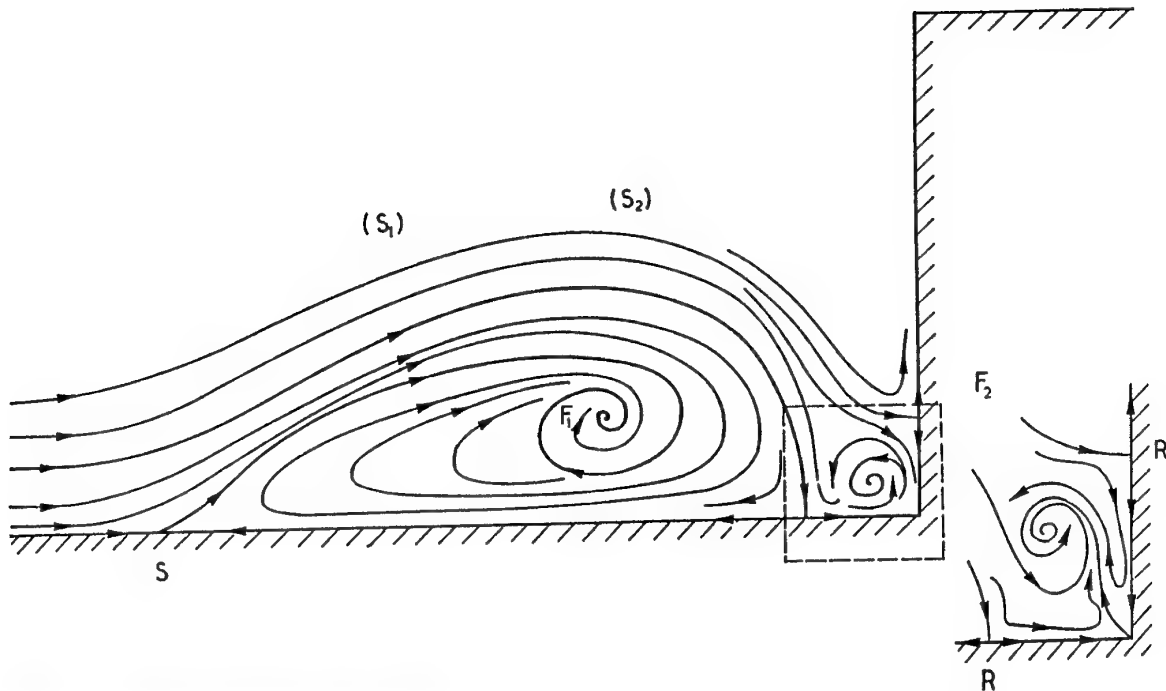
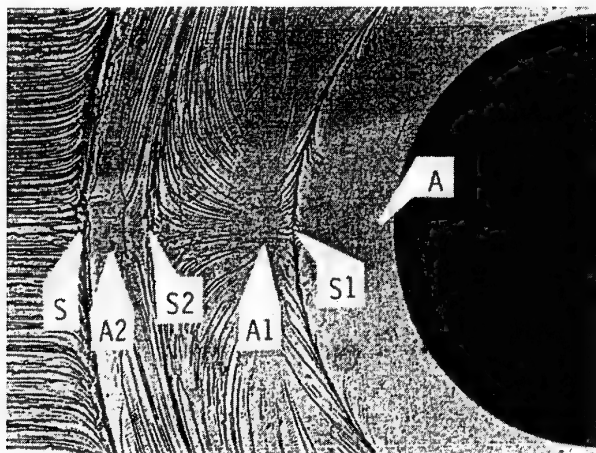
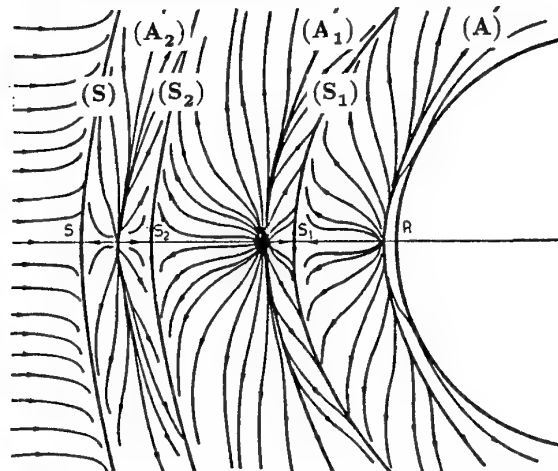


Figure 44: Schematic representation of the flow in the vertical plane of symmetry. Two vortex configuration.



a - Oil flow visualization



b - Sketch of skin friction line pattern

Figure 45: Surface flow pattern of a blunt-fin induced separation at $M_0 = 2.5$. Four vortex configuration (Sedney and Kitchens 1975).

1. Close to the obstacle, in the *inner region*, there is a domain where the flow is dominated by the leading-edge influence. Inside this domain, the flow properties are dictated by the diameter D of the leading edge and are nearly independent of the incoming boundary-layer thickness δ_0 . In particular, the upstream influence length, defined as the distance between the obstacle and the onset of the pressure rise, is practically unaffected by a change of δ_0/D . Thus, the upstream influence is a function of D only, nearly independent of M_0 and δ_0 .

This strong dependence with respect to a geometrical parameter would tend to prove that this kind of interaction has an essentially inviscid character. The phenomenon is thus radically different from the separation process in front of a two-dimensional step, in spite of the similarity of the pressure distributions. Indeed, as we know, for two-dimensional separation the interaction domain is scaled by the incoming boundary-layer thickness (see Section 2.1.3 above). Sedney and Kitchens have demonstrated that for a cylindrical obstacle the pri-

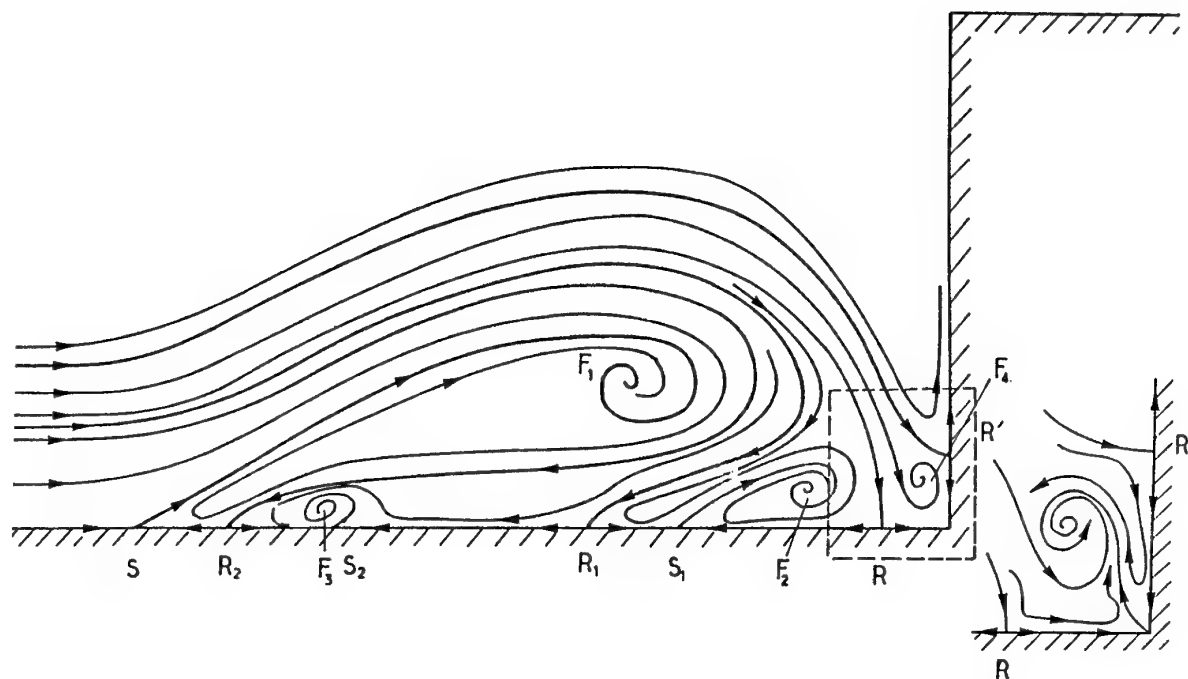


Figure 46: Schematic representation of the flow in the vertical plane of symmetry. Four vortex configuration.

primary separation length L_s , defined as the distance between the cylinder leading edge and the saddle-point S , depends mainly of the diameter D and height h of the cylinder, and to a lesser extent of the Mach number M_0 , but not of δ_0 .

2. At large distances from the obstacle, there exists an *outer region* where the interaction properties are independent of the fin bluntness. Then, as shown by Dolling, the scales of the phenomenon are the same as those of the swept-shock/boundary-layer interaction (see Section 2.2.2 above).

The results relative to the inner region raise the question of the distinction which must be made between a "small" and a "large" obstacle. More precisely, an obstacle will be said to be large if it leads to an asymptotic behavior, which means that any further increase of its height does not change the interaction extent. In particular, once the asymptotic height $h = h_a$ is reached, then the upstream influence length, the primary separation distance and the location of the triple point I_1 are independent of h . The definition of a scaling law for h_a has been carefully examined by Dolling and Bogdonoff (1981) who arrived at the conclusion that the appropriate scale for h_a is the diameter D . A similar behavior was observed by Sedney and Kitchens (1977) who found that h_a depends weakly of the upstream Mach number M_0 and Reynolds number (provided that the regime be fully turbulent). On the other hand, in laminar flows Ozcan (1982) found that L_s depends strongly of the Reynolds number, an increase in this parameter inducing an increase in L_s . The tendency is reversed when the flow becomes transitional.

2.3 Other Aspects of Interacting Flows

The above sections have given a brief description of some of the physical properties of shock-wave/boundary-layer interactions in two- and three-dimensional flows. Due to the lack of space, essential aspects of the phenomenon have not been considered. For example, the behavior of turbulence during an interaction process has not been discussed at all. Thus, detailed experiments executed in transonic and supersonic flows (Seegmiller et al. 1978; Ardonneau et al. 1980; Détery 1981, 1992; Johnson et al. 1981) have clearly shown that during the interaction process, the intensity of turbulence rises sharply, the most intense gradients existing at separation while a strong anisotropy develops. Downstream of the interaction domain, turbulence slowly relaxes towards a new equilibrium state, the entire phenomenon being affected by important relaxation or history effects whose representation is a hard point for turbulence models.

Also, the unsteady aspects of shock-wave/boundary-layer interaction have been ignored, although this important question is the subject of major investigations (see Dolling 1993 for a recent review of the question). A distinction must be made between large-scale fluctuations affecting the whole flowfield like buffeting, and small-scale fluctuations affecting only the interaction region. There is probably a close correlation between these fluctuations and the fluctuating character of a turbulent boundary layer. In this case, the interacting shock "feels" a variable incoming flow and reacts accordingly. Then several questions are raised: What is the interaction between turbulence and induced shock oscillations? Is it possible that such a mechanism operates a transfer of energy from the outer flow to the turbulent field, thus

enhancing considerably the turbulence levels? If this is true, what is the validity of the classical models presently used in interaction calculations and which do not incorporate such a mechanism? Elucidation of these questions is a complex task, requiring sophisticated experimental techniques and advanced modeling approaches.

3 SURVEY OF PROBLEMS RAISED BY INTERACTION MODELING

3.1 General remarks

In spite of the spectacular progress made over the past 20 years, both by numerical methods and computer technology, accurate prediction of shock-wave/boundary-layer interactions remains a challenge for theoreticians. Here, we shall only consider solutions obtained by solving the Navier-Stokes equations, this approach being the most credible to predict interactions in hypersonic flows. Furthermore, the Navier-Stokes approach is certainly the only way to predict three-dimensional flows, which is the true target of theoretical methods, since two-dimensional and/or axisymmetric configurations are very exceptional in practice. There exist several levels of approximations in the Navier-Stokes approach. With the Parabolized Navier-Stokes equations (PNS) the solution can be obtained by a simple forward-marching technique; in the thin-layer approximation only the derivatives of the viscous terms in the wall-normal direction are retained. The PNS form is not suited to treat highly viscous flows in which a recirculation region may form (except if some kind of iterative procedure with successive sweepings of the computational domain is introduced). On the other hand, the thin-layer approximation becomes inaccurate in hypersonic interactions where streamwise variations of the flow properties can be as large as variations normal to the wall.

From the numerical standpoint alone, interacting flows contain regions of high gradients either of the wave type (shocks, expansion waves) or of the boundary-layer type (which includes shear layers) through which the flow properties vary over an extremely short distance. This problem is acute in hypersonic interactions where strong shocks form, which may interfere with themselves to produce complex patterns and where the viscous effects are confined within excessively thin layers. Thus, the numerical schemes must be robust enough to withstand these rapid flow variations while preserving good accuracy. Furthermore, these discontinuities or regions of high gradients have extremely variable locations and directions, difficult to know in advance, which makes their correct capture delicate because of the difficulty to adequately define the computational grid.

The advent of a new class of schemes, based on upwind techniques, has in great part solved the problem of the capture of strong discontinuities. Also, adaptive grids offer the possibility to track the regions of high gradients by properly adjusting the refinement of the grid. Nevertheless, application of most modern codes to strong interactions leading to the formation of an extended separated region may lead to discrepancies with experiments whose origin is not yet entirely elucidated. In addition,

the correct prediction of quantities like skin friction or wall heat transfer necessitates an accurate calculation of derivatives, which imposes a strong demand on computational precision.

Thus, even in the case of a laminar flow of a calorically perfect gas, accurate prediction of an interacting flow still raises questions which have not yet been completely elucidated. In addition, consideration of real-gas effects resulting from air dissociation complicates considerably the solution of the laminar equations, especially if nonequilibrium chemistry is taken into account. Then, one is confronted both with new numerical difficulties, coming from the "stiffness" of the dissociation equations, and with the uncertain character of the available chemical and physical models. These questions will not be discussed here.

3.2 Modeling of Turbulent Interactions

The difficulty of computing shock-wave/boundary-layer interactions in hypersonic flows increases by at least an order of magnitude in turbulent applications, since the problem of turbulence modeling is superposed on purely numerical aspects.

In nearly all the present applications, the time-averaged form of the full Navier-Stokes equations is solved. Very frequently, the Favre averaging method, which defines mass-weighted variables, is adopted since it leads to equations formally simpler than those resulting from the classical Reynolds averaging. This gain in simplicity is obvious for the continuity and momentum equations; it is less clear for the energy equation and has the disadvantage to introduce correlation terms which cannot be directly measured. Nevertheless, Favre averaging tends to be universally employed in the computation of compressible turbulent flows.

This is not the place to present a thorough discussion of turbulence modeling, which would necessitate important developments, going far beyond the scope of this report. We will simply cite the models most commonly used in the computation of shock-wave/boundary-layer interactions in supersonic and hypersonic flows (for a more complete information on turbulence modeling in compressible flows see Cousteix and Aupoix 1989; Vandromme 1993).

Application of the Favre averaging procedure to the momentum equation introduces the Reynolds-tensor components of the form

$$\tau_{ij} \equiv -\overline{\rho u_i' u_j'}$$

and also the turbulent kinetic energy

$$k = \frac{1}{2} \overline{\rho u_i' u_i'}$$

In the above expressions, $\bar{\rho}$ is the mean density and u_i' a fluctuating velocity component in the sense of Favre and u_i' the classical fluctuation, which differs from u_i'' .

In a similar way, the averaging introduces correlations of fluctuating quantities in the energy equation, the most

important being the turbulent heat transfer term (the other terms are frequently neglected):

$$q_{t,j} \equiv \bar{\rho} C_v \widetilde{u_j'' T''}.$$

In most turbulent shock-wave/boundary-layer interaction calculations, the Reynolds-tensor components are expressed via the Boussinesq assumption which leads to the relation

$$\tau_{t,ij} = 2\mu_t \left(S_{ij} - \frac{1}{3} \frac{\partial \tilde{u}_k}{\partial x_k} \delta_{ij} \right) - \frac{2}{3} \bar{\rho} \tilde{k} \delta_{ij}$$

where μ_t is the turbulent eddy viscosity and S_{ij} the mean rate-of-strain tensor:

$$S_{ij} = \frac{1}{2} \left(\frac{\partial \tilde{u}_i}{\partial x_j} + \frac{\partial \tilde{u}_j}{\partial x_i} \right).$$

In addition, the turbulent heat transfer is expressed by means of a Fourier-like law:

$$q_{t,j} = -\lambda_t \frac{\partial \tilde{T}}{\partial x_j} = -\frac{\mu_t}{Pr_t} \frac{\partial \tilde{T}}{\partial x_j}$$

where λ_t is the turbulent thermal conductivity and Pr_t is the turbulent Prandtl number:

$$Pr_t = \frac{\mu_t C_p}{\lambda_t}$$

which is generally assumed constant. Thus, the only problem is to model the eddy viscosity μ_t .

In many applications, because of their simplicity, algebraic turbulence models are still used. In this class of models, μ_t is computed from the mean flow properties by an algebraic relation. The most common among these models are the mixing length model of Michel et al. (1969), the two-layer model of Cebeci and Smith (1974) and the Baldwin-Lomax model (1978), which is very popular among numericists because it does not require a localization of the boundary-layer outer edge. Many variants of these models have been devised to improve their accuracy in the prediction of separated flows. The results obtained with classical algebraic models are generally in poor agreement with experiments, although the overall flow features are faithfully predicted. This is quite evident in two-dimensional interactions, while in three-dimensional cases algebraic models may perform as well as more sophisticated models. The main reason for this bad performance is that these models are of the equilibrium type, which means that the turbulence is supposed to adjust itself instantaneously to changes in the mean flow. Such an assumption is not justified in strongly interacting flows where history effects are known to be important. In order to take these effects into account, ad-hoc modifications have been proposed whose main deficiency was their lack of generality (Shang and Hankey 1975; Deiwert 1975; Horstman 1976; Mateer et al. 1976).

For example, many applications have been made by using the Shang-Hankey relaxation formula in which the local value of μ_t is given by

$$\begin{aligned} \mu_t(x, y) &= \mu_{t_0}(x_0, y) + [\mu_{t_{eq}}(x, y) - \mu_{t_0}(x_0, y)] \\ &\times \left\{ 1 - \exp \left(-\frac{x - x_0}{\lambda} \right) \right\} \end{aligned}$$

in which μ_{t_0} is the value of μ_t at the interaction origin x_0 , $\mu_{t_{eq}}$ the local equilibrium value given by the baseline model (i.e., the Cebeci-Smith or Baldwin-Lomax model) and λ a relaxation length determined in a purely empirical manner.

A more sophisticated algebraic model, including an history effect, was proposed by Johnson and King (1981) with consideration of a transport equation. This model seems more particularly suited to treat transonic interactions.

A more satisfactory way to represent nonequilibrium effects is to determine μ_t by an expression of the form

$$\mu_t = \bar{\rho} C U L$$

in which C represents a dimensionless function, U a characteristic turbulence velocity and L a turbulence length scale. It is usual to adopt for U the value

$$U = \sqrt{k}.$$

In a first approach, L is given by an algebraic relation and the turbulent quantity k is computed by means of a transport equation which is solved in tandem with the Navier-Stokes equations. One-equation models of this type have been proposed by Glushko (1965), Rubesin (1976) and Goldberg-Chakravathy (1990).

In a further step, the quantity L is also transported by an appropriate equation. A very used version of the relation giving μ_t is

$$\mu_t = \bar{\rho} C_\mu f_\mu \frac{k^2}{\epsilon}$$

where ϵ is the dissipation rate of the turbulence kinetic energy ($\epsilon \propto k^{3/2}$), C_μ a constant and f_μ a function introduced to take into account the influence of the wall. The dissipation ϵ is computed by a second transport equation. Among this category of two-equation models, the most known is probably the Jones-Launder model (1972) for which many variants have been proposed in order to improve its accuracy in separated flows (Chien 1982; Chen 1986; Benay et al. 1987).

In the two-equation model of Wilcox and Rubesin (1980), μ_t is given by the relation

$$\mu_t = \bar{\rho} \gamma^* \frac{k}{\omega}$$

where γ^* is a dimensionless function and the transported quantity ω , the rate of dissipation of k per unit of k ($\omega = \epsilon/k$). In the model of Coakley (1983), μ_t is computed by the relation

$$\mu_t = \bar{\rho} C_\mu f_\mu \frac{q^2}{\omega}$$

in which $q = \sqrt{k}$.

The above two-equation transport models (and their variants) perform relatively well in the prediction of interacting flows, provided that the Mach numbers are not too high and the separated zone, if it exists, not too extended. They certainly represent an improvement compared to the algebraic and one-equations models. Major deficiencies appear in hypersonic flows, especially in the prediction of the peak heat transfer at reattachment. An

Key	Meaning
AM	algebraic (turbulence) model
BF	blunt fin
CF	corner flow
CFJ	cylinder-flare junction
NEE	nonequilibrium effects
PNS	parabolized Navier-Stokes
RF	ramp flow
SC	swept compression corner
SF	sharp fin
SR	shock reflection
TEM	transport equation model
TLNS	Navier-Stokes thin-layer approx.
XS	crossing shocks

Table 1: Abbreviations used in Tables 2-5.

examination of this question has been made by Horstman (1987) who took the compressibility terms into consideration (which are negligible at Mach numbers less than 6). These terms need to be modeled by making more or less justified assumptions (Rubesin and Rose 1973). Their consideration led to rather disappointing results in the prediction of the heat transfer levels at reattachment. A thorough discussion of the modeling of compressibility effects in shock-wave/boundary-layer interactions has been recently published by Douay (1994), who arrived at similar conclusions.

The above models are still used to compute three-dimensional interactions, with appropriate modifications to take into account the existence of a third dimension. For example, the derivative $\partial \tilde{u}/\partial y$ of the two-dimensional models is replaced by the modulus of the vorticity vector. As we know, in the vicinity of the wall the turbulence length scale is the distance to the wall y , will leads to a delicate problem in a corner. In this region, authors use appropriate expressions which can be found in the cited publications (see for example the expression given by Hung and MacCormack 1978).

3.3 Status of Modeling Activities and Requirements for Proper Validation

Tables 2-5 list the most representative calculations of supersonic and hypersonic shock-wave/boundary-layer interactions by solution of the Navier-Stokes equations (see Table 1 for abbreviations). Transonic calculations have not been considered as being too far from our subject. The first applications dealt with laminar interactions in two-dimensional supersonic flows (see Table 2) and used explicit schemes, the most popular and widely used being the predictor-corrector scheme of MacCormack. Explicit methods have been used until a relatively recent date, their main advantages being their conceptual simplicity and good accuracy. However, with the need to increase code efficiency, implicit techniques have been progressively introduced. Also, the necessity to achieve a better capture of discontinuities of the wave type led to the development of upwind techniques calling upon the

concept of Riemann solvers. These new codes allowed an efficient computation of hypersonic flows containing strong shock waves.

It seems firmly established that computation of laminar interactions at supersonic Mach numbers can be considered as having reached a high degree of accuracy, at least in two-dimensional and/or axisymmetric flows. The answer is less clear for three-dimensional interactions (see Table 3) because of complex grid problems and the huge number of grid points required to correctly represent all the flow features.

In the case of hypersonic flows, even for two-dimensional configurations, the accuracy and reliability of laminar calculations is not yet unambiguously demonstrated as it results from the thorough comparative study executed at the occasion of the Antibes Workshops on *Hypersonic Flows for Re-entry Problems*. The major discrepancies between codes were observed in the prediction of the extent of separated regions, as also of the heat-transfer peak value at reattachment on the ramp. However, definitive conclusions are difficult to draw for at least two effects plaguing experimental data used to validate the codes:

1. First, results obtained on nominally two-dimensional configurations (ramp flow or impinging-reflecting shock) are affected by unavoidable side effects whose importance is nearly impossible to assess (the use of side plates, or fences, covering the separated region is not a guarantee of two-dimensionality). These unwanted large-scale three-dimensional effects, which make impossible any conclusion about the accuracy or inaccuracy of codes, lead to endless discussion between theoreticians and experimentalists. Thus, it is clear that only *axisymmetric configurations* must be used to validate mathematically two-dimensional solutions. The microscopic three-dimensional structures mentioned in Section 2.1.5 are inherent to the basic physics of flows and cannot be avoided. It is not certain that their consideration is important in the prediction of the macroscopic organization of the flow.
2. Second, in many presumed laminar experiments, where the flow separates, the regime is in fact *transitional*, the separation process having a well-defined laminar character while reattachment is influenced by transition. In this case, the peak pressure and heat transfer on the ramp are well above the truly laminar values and the extent of the separated region is much affected by the transition. Transitional interactions are difficult to avoid, because of the extreme sensitivity of the separated shear-layer to instabilities. Thus, with the additional concave curvature effect at reattachment which tends to promote transition (through a possible mechanism involving the aforementioned Görtler vortices), the keeping of a laminar regime throughout the interaction is difficult. This can only be done in experiments executed at sufficiently low Reynolds numbers.

Because of their obvious practical interest, a great number of *turbulent* applications have been executed with a

Author	Computed Cases	Numerical Method	Remarks
MacCormack (1971)	SR at $M_0 = 2$	MacCormack explicit	
Carter (1972)	RF at $M_0 = 4$	Brailovskaya explicit	
	CFJ at $M_0 = 4$		
	RF at $M_0 = 6$		
Hanin et al. (1974)	SR at $M_0 = 2$	Brailovskaya explicit	
Li (1974)	Flare on blunt cone	MacCormack explicit	
MacCormack-Baldwin (1975)	SR at $M_0 = 2$	MacCormack explicit	
Hung & MacCormack (1976)	RF at $M_0 = 14.1$	MacCormack explicit	
Hussaini et al. (1976)	SR at $M_0 = 2$	Lax-Wendroff explicit	
Li (1977)	SR at $M_0 = 2$	explicit-implicit	
Hodge (1977)	SR at $M_0 = 7.94$ & 7.73	MacCormack explicit	
Issa & Lockwood (1977)	SR at $M_0 = 7.4$	steady iterative	
Lawrence et al. (1986)	RF at $M_0 = 14.1$	forward marching	PNS
Degrez et al. (1987)	SR at $M_0 = 2.15$	central difference	
Ray et al. (1987)	RF at $M_0 = 14.1$ & 18.9	MacCormack explicit	
Liou (1987)	SR at $M_0 = 2$	upwind	
Thomas & Walters (1987)	SR at $M_0 = 2$	upwind	
Hollanders & Marmignon (1989)	RF at $M_0 = 14.1$	upwind	
Rudy et al. (1989)	RF at $M_0 = 14.1$	several	
Thareja et al. (1990)	RF at $M_0 = 14.1$	unstructured grid	
Antibes Workshops (1990,1991,1993)	RF at $M_0 = 10$ and 11.68	several	
Simeonides et al. (1992)	RF at $M_0 = 14.1$	Runge-Kutta with cent. and upwind	
Grumet et al. (1991)	SR at $M_0 = 5$	MacCormack explicit	real gas
Ballaro & Anderson (1991)	SR at $M_0 = 5$ & 12	MacCormack explicit	real gas
Grasso & Leone (1992)	RF at $M_0 = 7.4, 11.7$ and 17.4	Runge-Kutta with cent. differences	real gas
Joulot (1992)	RF at $M_0 = 10$ & 11.7 CJF at $M_0 = 10$		
Daghsstani (1993)	SR at $M_0 = 2$	upwind	true unsteady
Leyland (1993)	RF at $M_0 = 14.1$	upwind	

Table 2: Navier-Stokes calculations of two-dimensional laminar interactions.

large variety of turbulence models (see Tables 4 and 5). The first calculations (except those of Wilcox) used simple algebraic equilibrium models, but it became rapidly clear that some history effect should be included to represent the strongly out-of-equilibrium behavior of turbulence during an interaction. Thus, modifications to the baseline models were introduced either by modifying the wall damping function (Horstman et al. 1975) or by using a relaxation formula, as the one given in the previous subsection (Shang and Hankey 1975). In a further step, transport equation models were implemented in which one and, then, two turbulent quantities were transported. This sophistication certainly improved the quality of the prediction, although really satisfactory agreement with experiment was still far from being achieved. In 1978, Baldwin and Lomax proposed their famous algebraic model in which the outer turbulent length scale is no longer given by the thickness of the boundary layer, but deduced from the distribution of vorticity across the dissipative flow. Apart from its nu-

merical convenience, this model proved to be superior to the other algebraic models in the prediction of separated flows.

It is sometimes difficult to draw clear conclusions about the accuracy of turbulent calculations because of the intimate mixing of numerical and physical problems involved in the codes. However, carefully executed calculations, part of them with the boundary-layer approach which allows great numerical accuracy (Benay 1991), show that none of the above turbulence model gives satisfactory results in strong interactions. In particular, the level of peak heat transfer at reattachment in hypersonic interactions is poorly predicted, even by two-equation models (Horstman 1987). Compressibility, as also unsteady effects are suspected to be at the origin of these deficiencies, but the answer is not obvious, the poor results can be in great part due to the inadequacy of the above models in the prediction of separated flows. Introduction of higher-order models, in which the full Reynolds tensor

Author	Computed Cases	Turbulence Model	Remarks
Wilcox (1973)	SR at $M_0 = 2.96$	Saffman TEM	
Wilcox (1974)	RF & SR at $M_0 = 2.96$	Saffman TEM	
Balwin-MacCormack (1974)	SR	Cebeci-Smith Saffman-Wilcox	
Horstmann et al. (1975)	SR at $M_0 = 6.9$	Cebeci-Smith + NEE	axisym.
Shang & Hankey (1975)	RF at $M_0 = 2.96$	Cebeci-Smith Cebeci-Smith + NEE	
Shang et al. (1976)	SR at $M_0 = 2.96$	Cebeci-Smith Cebeci-Smith + NEE	
Balwin-MacCormack (1976)	SR at $M_0 = 3$ & 8.47	mod. Mellor-Gibson	
Hung & MacCormack (1977)	RF at $M_0 = 2.96$ & 8.66	two-layer AM two-layer AM + NEE	
Viegas & Coakley (1977)	several	Cebeci-Smith Shang-Hankey + NEE Glushko-Rubesin	
Horstmann et al. (1977)	RF at $M_0 = 2.85$	two-layer AM two-layer AM + NEE (3 variants)	
Viegas & Coakley (1978)	SR at $M_0 = 6.84$	two-layer AM two-layer AM + NEE Glushko-Rubesin	
Viegas & Horstmann (1978)	RF at $M_0 = 2.8$	Cebeci-Smith Glushko-Rubesin Jones-Launder Wilcox-Rubesin	
Baldwin & Lomax (1978)	RF and SR	Baldwin-Lomax	TLNS
Degani & Stegar (1983)	SR at $M_0 = 2.85$	Baldwin-Lomax	
Visbal & Knight (1984)	RF at $M_0 = 2.9$	Baldwin-Lomax mod. Baldwin-Lomax Baldwin-Lomax + NEE	
Deese & Agarwall (1985)	RF at $M_0 = 2.85$	Baldwin-Lomax mod. Baldwin-Lomax	
Ong & Knight (1986)	RF at $M_0 = 1.96$ & 2.83	Baldwin-Lomax + NEE	
Peters et al. (1986)	RF at $M_0 = 2.9$ SR at $M_0 = 2.9$	Baldwin-Lomax Jones-Launder	TLNS
Horstmann (1987)	RF at $M_0 = 9.22$ SR at $M_0 = 11.33$ CFJ at $M_0 = 9.22$	Cebeci-Smith Baldwin-Lomax Jones-Launder	compr. corrections
Wilcox (1990)	RF at $M_0 = 2.79$ & 2.84 CFJ at $M_0 = 2.85$	Wilcox $[k, \omega]$ multiscale	
Joulot (1992)	CFJ at $M_0 = 5$	Baldwin-Lomax Chien $[k, \epsilon]$	
Simeonides et al. (1992)	RF at $M_0 = 14$	Cebeci-Smith transition model	
Goldberg et al. (1993)	RF at $M_0 = 3$ CFJ at $M_0 = 7$	Baldwin-Barth	
Haidinger-Friedrich (1993)	RF at $M_0 = 2.85$ SR at $M_0 = 2.9$	Baldwin-Lomax Wilcox $[k, \omega]$	compr. corrections

Table 3: Navier-Stokes calculations of two-dimensional turbulent interactions.

Author	Computed Cases	Numerical Method
Shang & Hankey (1977)	SF at $M_0 = 12.5$	MacCormack explicit
Hung & MacCormack (1976)	RF with side effects	explicit-implicit
Degrez (1985)	SF at $M_0 = 2.25$	Beam-Warming implicit
Hung (1989)	SF at $M_0 = 2.25$	MacCormack explicit
Chen & Hung (1992)	BF at $M_0 = 2$	upwind

Table 4: Navier-Stokes calculations of three-dimensional laminar interactions.

Author	Computed Cases	Turbulence Model	Remarks
Hung & MacCormack (1978)	SF at $M_0 = 5.9$	Escudier AM	
Shang et al. (1978)	CF at $M_0 = 3$	Cebeci-Smith	
Horstmann & Hung (1979)	SF at $M_0 = 2, 3, \& 4$	Escudier AM	
Hung & Kordulla (1983)	BF at $M_0 = 2.95$	Baldwin-Lomax	
Knight (1984)	SF at $M_0 = 2.94$	Baldwin-Lomax	
Hung (1985)	oblique SC on cyl. BF at $M_0 = 2.95$		
Hung & Buning (1985)	BF at $M_0 = 2.95$	Baldwin-Lomax	
Knight et al. (1987)	SF at $M_0 = 2.9$	Baldwin-Lomax Jones-Launder	
McMaster & Shang (1988)	BF at $M_0 = 2.95$	Baldwin-Lomax	
Gaitonde & Knight (1988)	SF at $M_0 = 3$	Baldwin-Lomax	bleed effect
Cambier et al. (1988)	SF at $M_0 = 3$	Michel AM	
Knight et al. (1988)	SC at $M_0 = 3$	Cebeci-Smith Baldwin-Lomax Jones-Launder	
Horstmann (1989)	SF at $M_0 = 4$	Jones-Launder Speziale TEM	
Zang & Knight (1989)	SC at $M_0 = 2.95$	Baldwin-Lomax	
Hung (1989)	BF at $M_0 = 5$	Baldwin-Lomax	
Gaitonde & Knight (1989)	SF & XS at $M_0 = 2.95$	Baldwin-Lomax	bleed effect
Lu et al. (1990)	SC at $M_0 = 2.95$	Jones-Launder	
Narayanswami et al. (1991)	XS at $M_0 = 2.95$	Baldwin-Lomax Jones-Launder	
Reddy (1991)	XS at $M_0 = 3.5 \& 4$	Baldwin-Lomax	
Knight & Badekas (1991)	SF at $M_0 = 4$	Baldwin-Lomax	
Panaras (1992)	SF at $M_0 = 2.95$	Baldwin-Lomax	
Chen & Hung (1992)	BF at $M_0 = 2.5$	mod. Baldwin-Lomax	
Leung & Squire (1993)	SF at $M_0 = 2.45$	Cebeci-Smith Johnson-King	
Narayanswami et al. (1993)	XS at $M_0 = 8.3$	Baldwin-Lomax Rodi $[k, \epsilon]$	
Garrison et al. (1993)	XS at $M_0 = 4$	Baldwin-Lomax	

Table 5: Navier-Stokes calculations of three-dimensional turbulent interactions.

is transported, could perhaps improve the situation. Up to now, there is no demonstration of this fact in strongly interacting flows, to our knowledge.

As shown in Table 5, a large number of turbulent three-dimensional calculations have already been executed because of the great practical importance of this case (a more comprehensive list can be found in a recent review by Knight 1993). Very complex configurations, such as the crossing of two shocks interacting with a side plate, can now be treated with results in fair agreement with experiment. Of course, as for two-dimensional flows, the details of the flow, the turbulence levels, the heat transfer rates at the wall are still poorly predicted. However, one should not be unduly negative or pessimistic, when considering the spectacular progress made in interacting flow prediction over the past 20 years. It should be realized that the perception and understanding of three-dimensional flows is an extremely difficult operation. In this perspective, even if the results have still a limited accuracy, the theoretical models constitute a very powerful substitute to experimental investigations which would be complex, lengthy, when not impossible.

4 DEFINITION OF THE SELECTED TEST CASES

4.1 General Information

4.1.1 Test Geometries and Boundary Conditions

Common feature of the various test geometries is the existence of a shock-wave/boundary-layer interaction in the vicinity of intersection of a flat plate (or a cylinder) with a surface that provides compression (a fin, or a swept ramp, or a flare). Usually the compression surface is attached to the flat plate (or cylinder) far from its leading edge, to avoid interaction of its shock wave with the leading-edge shock. Also, care is taken so that the vertical extent of the fins or the lateral extent of the compression corners is much greater than the size of the interaction domain. These rules simplify the computations, because

1. It is not necessary to start the calculation from the leading edge of the flat plate or the flare. Instead, the calculation may start a few boundary-layer thicknesses upstream of the interaction. Then the required grid points are considerably reduced. However, in this case for starting the calculation it is necessary to know the boundary-layer profile upstream of the interaction region. This profile is used as a boundary condition in the inflow plane, as well as initial condition of the flowfield. Furthermore, the thickness of the undisturbed boundary layer is the length scale of the interaction.
2. The gradients of the flow parameters are set equal to zero in the farfield (upper and lateral boundaries). These boundary conditions implicitly mean that the fins or the compression corners have unlimited dimensions. It is evident that by this selection the number of required grid points is reduced and the

calculations are considerably simplified. If alternatively, the compression surface is assumed to have finite dimensions, the calculations will be complicated. For example in the case of the fin/plate configuration, the whole fin has to be included within the computational domain (like a wing attached on a plate). Then apart from the considerable increase of the grid points, more complicated grid generators must be used, while the square edges on the fin would probably create numerical problems.

In conclusion, it seems that if the confinement of the computation domain in the immediate interaction region is possible, less computer resources and simpler computational tools will be required for the computation of the flow about the selected configurations. However for the application of this option some data are required and some conditions have to be satisfied. The knowledge of the profile of the boundary layer upstream of the interaction, or at least of its thickness, is a prerequisite for such an option. Still some test cases, especially in the hypersonic regime, do not include this critical information. Thus, someone who is interested to validate his code at higher speeds, will have to calculate initially the development of the boundary layer along the flat plate (or the cylinder), from its leading edge to the vicinity of the compression corner. Fortunately a two-dimensional boundary layer solver is sufficient for such a task (independent calculation, not a part of the computation of the interaction domain).

In order to provide reliable test cases to validate computational methods, the subgroup on viscous interactions has selected a set of experiments by considering axisymmetric and fully three-dimensional interactions, two-dimensional ramp flows having been excluded for the reasons given in the previous section. These experiments cover a Mach number range from 2 to 8 and include laminar and turbulent cases, transitional interactions having been rejected. The selected experiments have been executed with great care and can be considered as safe for validation purposes.

The matrix in Figure 47 gives the selected configurations. Only simple geometrical shapes have been considered in order to focus the validation task on basic problems (capture of strong shocks and thin shear layers, modeling of turbulence in strong interaction regions and in the vicinity of a corner).

4.1.2 Measured Flow Parameters

It is well known that in any flow it is easier to calculate pressure distributions than the skin friction or heat-transfer rates. Factors that affect the output of the calculations in this sense are the numerical dissipation of the numerical scheme, the turbulence model and the fineness of the grid close to the wall.

This general rule was confirmed by Knight (1993) for the particular case of the shock-wave/boundary-layer interaction. In his review Knight examines all the configurations which are object of the present report. It is remarkable to note that according to his data, in a flow about the fin/plate configuration, use of two turbulence

AGARD FDP WG 18 Subgroup 1: Viscous Interactions
Shock Wave / Boundary Layer Interaction Test Matrix




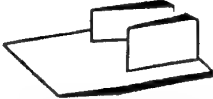
Test Geometry Country	 Cylinder Flare	 Single Fin	 Swept Corner	 Crossing Shocks
USA	NASA M = 3 & 7 Turbulent	NASA M = 8 Turbulent	Princeton M = 4 Turbulent	NASA M = 8 Turbulent
		PennState M = 3 & 4 Turbulent		PennState M = 3 & 4 Turbulent
		Princeton M = 3 Turbulent		Princeton M = 3 Turbulent
		U. of Texas M = 5 Turbulent		
Germany		DLR M = 5 & 7 Turbulent		DLR M = 5 & 7 Turbulent
France	ONERA M = 5 Turbulent	CEAT M = 2 Turbulent	ONERA M = 10 Laminar	
	ONERA M = 10 Laminar			

Figure 47: Test case matrix.

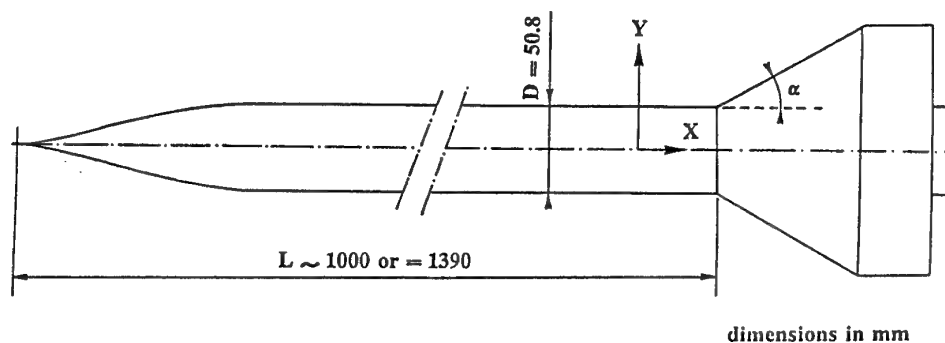


Figure 48: NASA ogive-cylinder flare model. $M = 3$ and $M = 7$ turbulent experiments.

models (Baldwin-Lomax and Jones-Launder) that provide eddy viscosities which differ by as much as a factor of 14 resulted in similar flowfield predictions. Knight has concluded that in the shock-wave/boundary-layer interaction there is a triple-deck structure. The viscous effects are restricted on a thin layer adjacent to solid boundaries, while the remainder of the boundary layer is effectively rotational and inviscid (see Section 2.1.2 above).

In view of the aforementioned comments it seems that those test cases will be more appropriate for the validation of a code which in the measured quantities include

skin-friction distributions and, more important, surface heat-transfer rates. Furthermore, more reliable will be those test cases which in the test conditions include the surface temperature. That because the wall temperature is a necessary boundary condition for the calculation of the heat transfer rates, while for an adiabatic flow it is sufficient to assume zero value for the gradient of the temperature normal to the wall.

Regarding the physics of the flow, it has been mentioned in the first part of this section that the most critical issue for the fin or double-fin configuration, as well as for the swept corner is the conical nature of the flow. Particu-

larly for the fin/plate configuration the secondary separation is another important issue, still not clearly understood. For the investigation of the conical nature of the flow, the surface parameters (pressure, oil-flow lines) are not adequate but flowfield data are necessary. Furthermore, non-intrusive measurements of flowfield quantities are more accurate, than those obtained with Pitot tubes, while more than two cuts of the flow are necessary for the confirmation of the quasi-conical nature of the flow. At this point we mention that according to the calculations of Panaras (1992) the deviations from the conical behavior are not detected if the two cuts which are compared are closer than 15δ . Remarkable differences appear for a distance greater than 25δ (see Figure 32b of Section 2.2.2).

The data relative to the selected test cases include mean surface flow quantities (pressure, heat transfer, in some cases skin friction) and flowfield properties (mainly Pitot pressure, mean velocity and turbulence by LDV in a limited number of cases). In some experiments, wall pressure fluctuations were measured. Surface flow visualizations, giving precious indications on the skin-friction line pattern are available for nearly all the selected experiments.

The following subsections give the information required to calculate each test case (for experiments not executed at the date of the preparation of this report, some indications can be missing). In most turbulent cases, the parameters of the incoming boundary layer, at a station just upstream of the interaction, are given. From these parameters, an analytical definition of the velocity profile can be determined (in some cases, this profile is available in the data). If this is not the case, the location of transition is indicated to allow a calculation of the boundary layer on the upstream part of the plate.

To insure consistency of the data, the unit Reynolds number has been computed from the freestream Mach number and stagnation conditions given in the test cases definition, by assuming a constant ratio of specific heats ($\gamma = 1.4$), the molecular viscosity being computed by Sutherland's formula.

The system of coordinates used to represent the data is indicated in the figures defining the configuration. As a general rule, X is the streamwise distance, Y the distance normal to the wall and Z the transverse distance. In three-dimensional experiments, X and Z are contained in the flat plate bearing the fin(s) or ramp.

After the description of each case, references are given in which complementary information and results can be found.

A majority of the test cases given here come from a data bank on hypersonic interactions constituted by G. Settles and L. Dodson, from Penn State University. Complementary information on these cases can be found in the following documents:

Settles, G.S. and Dodson, L.J. 1991 Hypersonic shock/boundary-layer interaction data base. *NASA CR-177577*.

Settles, G.S. and Dodson, L.J. Interaction data base:

new and corrected data. NASA Contractor Report (to be published).

Because of space limitation, the data are not given in the present report. Contributors to the modeling activity can obtain them upon request to:

J. Détery
ONERA - Aerodynamics Department
29 Avenue de la Division Leclerc
92320 CHATILLON - France

The requested data will be transmitted on diskettes or in tabulated form.

4.2 Axisymmetric Configurations

4.2.1 NASA Ogive-Cylinder Flare $M = 3$ and $M = 7$ Turbulent Experiments

General Testing Conditions. The model used for these experiments is shown in Figure 48. It is made of a long sting-supported cylinder having a diameter of 50.8 mm and aligned with the tunnel axis. The cusped nose at the upstream end of the cylinder was especially designed to minimize the strength of shock waves produced here. Flare of different angle α can be mounted on the cylinder.

The cylinder-flare junction lies at ~ 1000 mm downstream from the tip of the ogival nose for the Mach 3 experiment and 1390 mm for the Mach 7 experiment. Other experiments at Mach 3 were also executed with the flare axis inclined to the cylinder axis to obtain three-dimensional interactions. Here, only the axisymmetric case is considered (flare axis aligned with the cylinder axis). For the Mach 7 case, the range of tested flare angles spans conditions from fully unseparated to well-separated flow.

- Freestream flow Mach number: $M_0 = 2.85$
- Flare angle: $\alpha = 30^\circ$
- Freestream stagnation pressure: $p_{st0} = 1.7 \times 10^5$ Pa
- Freestream stagnation temperature: $T_{st0} = 265$ K
- Wall temperature: $T_w \approx 300$ K
- Unit Reynolds number: $R_u = 1.6 \times 10^7$ m $^{-1}$
- Incoming boundary-layer parameters:
 - Physical thickness: $\delta_0 = 11$ mm
 - Skin-friction coefficient: $C_{f0} = 0.00175$

Due to the length of the cylinder, the regime is fully turbulent upstream of the interaction region. The incoming boundary layer velocity profile is provided with the data:

- Freestream flow Mach number: $M_0 = 7.05$
- Flare angles: $\alpha = 20^\circ, 30^\circ, 32.5^\circ$ and 35°
- Freestream static pressure: $p_0 = 576$ Pa
- Freestream static temperature: $T_0 = 81.2$ K

- Wall temperature: $T_w = 311 \text{ K}$
- Unit Reynolds number: $R_u = 5.66 \times 10^6 \text{ m}^{-1}$
- Incoming boundary-layer parameters:
 - Physical thickness: $\delta_0 = 25 \text{ mm}$
 - Displacement thickness: $\delta_0^* = 7.4 \text{ mm}$
 - Momentum thickness: $\theta_0 = 0.65 \text{ mm}$
 - Skin-friction coefficient: $C_{f_0} = 0.00122$
 - Heat transfer coefficient: $S_{t_0} = 0.00059$

Available Data

- Surface pressure distributions: $p_w(X)$
- Surface heat transfer distributions: $h_w(X)$
- Flowfield surveys by pressure probes: $p_t(X, Y)$ (Mach 3 & 7 experiments)
- Mean velocity and turbulence profiles from LDV surveys (Mach 3 experiment)

References

- Brown, J.D., Brown, J.L. and Kussoy, M.I. 1988 A documentation of two- and three-dimensional separated turbulent boundary layers. *NASA TM-101008*.
- Kussoy, M.I. and Horstman, C.C. 1989 Documentation of two- and three-dimensional hypersonic shock-wave/turbulent boundary-layer interaction flows. *NASA TM-101075*.

4.2.2 ONERA Hollow-Cylinder Flare $M = 5$ Turbulent Experiment

General Testing Conditions. This experiment was performed in the R2Ch wind tunnel of the Chalais-Meudon Establishment. As shown in Figure 49, the model consists of a hollow cylinder with an external diameter of 131 mm and an internal diameter of 106 mm. The leading edge is sharp with an angle of 10° . A 35° flare is mounted 250 mm aft of the cylinder leading edge. The total length of the model is 300 mm.

- Freestream Mach number: $M_0 = 5.01$
- Flare angle: $\alpha = 35^\circ$
- Freestream stagnation pressure: $p_{st_0} = 3.5 \times 10^6 \text{ Pa}$
- Freestream stagnation temperature: $T_{st_0} = 500 \text{ K}$
- Wall Temperature: $T_w \approx 300 \text{ K}$
- Freestream unit Reynolds number: $R_u = 4.41 \times 10^7 \text{ m}^{-1}$
- Incoming boundary layer parameters. The Reynolds number was sufficiently high to insure a fully turbulent boundary layer well upstream of the cylinder-flare junction. The end of transition took place $\sim 125 \text{ mm}$ downstream of the cylinder leading edge.

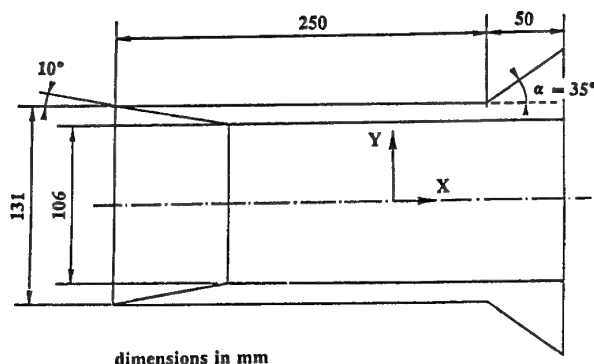


Figure 49: ONERA hollow-cylinder flare model. $M = 5$ turbulent experiment.

The incoming boundary layer has been probed with a two component LDV system at a station located 200 mm downstream of the cylinder leading edge. The measurements were not fine enough to allow the calculation of the displacement and momentum thicknesses. The boundary layer physical thickness at this location was 2.5 mm.

Available Data

- Surface pressure distribution: $p_w(X)$
- Surface heat transfer distribution: $h_w(X)$
- Surface flow visualization (skin-friction line pattern)

References

- Joulot, A. 1992 Contribution à l'étude de l'interaction onde de choc-couche limite sur rampe bidimensionnelle en régime hypersonique. *Ph.D. Thesis*, Université Pierre et Marie Curie, Paris.

4.2.3 ONERA Hollow-Cylinder-Flare $M = 10$ Laminar Experiment

General Testing Conditions. This experiment was executed in the R5Ch Hypersonic wind tunnel. As shown in Figure 50, the model consists of a hollow cylinder with an external diameter of 65 mm and an internal diameter of 45 mm. The leading edge is sharp with an angle of 15° . A 30° flare is located 101.7 mm downstream of the cylinder leading edge. The flare is followed by a cylindrical part having a diameter of 115 mm and a length of 25 mm.

- Freestream Mach number: $M_0 = 9.90$
- Flare angle: $\alpha = 30^\circ$
- Freestream stagnation pressure: $p_{st_0} = 2.5 \times 10^5 \text{ Pa}$
- Freestream stagnation temperature: $T_{st_0} \approx 1050 \text{ K}$
- Wall temperature: $T_w = 290 \text{ K}$
- Unit Reynolds number: $R_u = 1.86 \times 10^5 \text{ m}^{-1}$

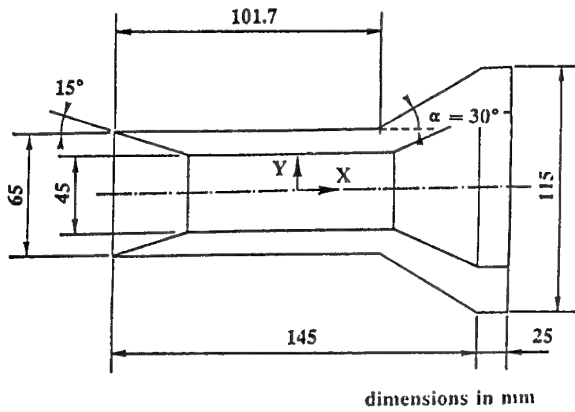


Figure 50: ONERA hollow-cylinder flare model. $M = 10$ laminar experiment.

Available Data

- Surface pressure distribution: $p_w(X)$
- Surface heat-transfer distribution: $h_w(X)$
- Surface flow visualization (skin-friction line pattern)
- Flowfield visualization by the electron beam technique

4.3 Single Sharp Fin Configurations

4.3.1 NASA $M = 8$ Turbulent Experiment

General Testing Conditions. This experiment was executed in the NASA-Ames 3.5-foot hypersonic wind tunnel. The sharp fin, with unswept leading edge, was mounted perpendicular to a flat plate having a length of 2200 mm and a span of 760 mm, the fin leading edge being 1760 mm aft of the plate leading edge (see Figure 51). Natural transition occurred on this plate for all test conditions. While no turbulence data are available to establish the condition of the incoming boundary layer ahead of the interaction, a mean profile included in the data set shows typical law-of-the-wall and wake behavior, albeit with a lower wake strength parameter than usual. Tests were performed for several values of the fin yaw angle.

This fin interaction involves a relatively thick incoming boundary layer. The reason for this is the long flat-plate run required to naturally establish a turbulent boundary layer at Mach 8. Thus, the present fin is only $8\delta_0$ long, the net effect being that the present interaction lies entirely within its turbulent boundary layer.

- Freestream Mach number: $M_0 = 8.18$
- Fin angles of incidence: $\alpha = 5^\circ, 7.5^\circ, 10^\circ, 12.5^\circ$ and 15°
- Freestream static pressure: $p_0 = 430$ Pa
- Freestream static temperature: $T_0 = 81$ K

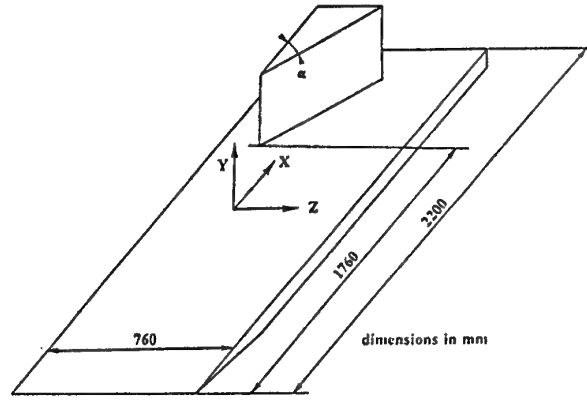


Figure 51: NASA single sharp fin model. $M = 8$ turbulent experiment.

- Wall temperature: $T_w = 300$ K
- Unit Reynolds number: $R_u = 4.92 \times 10^6 \text{ m}^{-1}$
- Incoming boundary-layer parameters:
 - Physical thickness: $\delta_0 = 37$ mm
 - Displacement thickness: $\delta_0^* = 15.9$ mm
 - Momentum thickness: $\theta_0 = 0.94$ mm
 - Skin-friction coefficient: $C_{f_0} = 0.000988$
 - Heat-transfer coefficient: $S_{t_0} = 0.000538$

Available Data

- Surface pressure distribution: $p_w(X, Z)$
- Surface heat-transfer distribution: $h_w(X, Z)$
- Skin friction coefficient: $C_f(X, Z)$
- Flowfield Pitot surveys: $p_t(X, Y)$

References

Settles, G.S. and Dodson, L.J. Interaction data base: new and corrected data. NASA Contractor Report (to be published).

4.3.2 Penn State University $M = 3$ and $M = 4$ Turbulent Experiments

General Testing Conditions. The tested geometry consists of a sharp, unswept leading edge, fin mounted at angle of incidence α to the freestream, with its leading edge 216 mm downstream from the leading edge of a flat plate upon which a turbulent boundary layer was generated.

- Freestream Mach number: $M_0 = 3.03$
- Fin angles of attack: $\alpha = 10^\circ$ and 16°

- Freestream stagnation pressure: $p_{st0} = 8.27 \times 10^5$ Pa
- Freestream stagnation temperature: $T_{st0} = 294$ K
- Wall temperature: roughly adiabatic ($T_w/T_r = 1.06$)
- Unit Reynolds number: $R_u = 6.19 \times 10^7 \text{ m}^{-1}$
- Incoming boundary-layer parameters:
 - Physical thickness: $\delta_0 = 3.02$ mm
 - Displacement thickness: $\delta_0^* = 0.895$ mm
 - Momentum thickness: $\theta_0 = 0.184$ mm
 - Skin-friction coefficient: $C_{f0} = 0.00152$

-
- Freestream Mach number: $M_0 = 3.98$
 - Fin angles of attack: $\alpha = 16^\circ$ and 20°
 - Freestream stagnation pressure: $p_{st0} = 15.24 \times 10^5$ Pa
 - Freestream stagnation temperature: $T_{st0} = 293$ K
 - Wall temperature: roughly adiabatic ($T_w/T_r = 1.06$)
 - Unit Reynolds number: $R_u = 7.20 \times 10^7 \text{ m}^{-1}$
 - Incoming boundary-layer parameters:
 - Physical thickness: $\delta_0 = 2.87$ mm
 - Displacement thickness: $\delta_0^* = 0.950$ mm
 - Momentum thickness: $\theta_0 = 0.128$ mm
 - Skin-friction coefficient: $C_{f0} = 0.001325$

Available Data

- Surface pressure distributions: $p_w(\beta)$
- Skin friction distributions: $C_f(\beta)$
- Surface streamline angle distributions: $\varphi(\beta)$

The above quantities are given as functions of the conical ray angle β (measured from the fin leading edge, with respect to the freestream direction). The surface streamline angle φ represents the local angle of surface flow pattern streamlines, measured with respect to the freestream direction.

References

- Kim, K.S. and Settles, G.S. 1988 Skin friction measurements by laser interferometry in swept-shock/turbulent boundary-layer interactions. *AIAA Paper 88-0498*. Also: *AIAA J.*, Vol. 28, No. 1, pp. 133–139.
- Kim, K.S. 1989 Skin friction measurements by laser interferometry in supersonic flows. *Ph.D. Thesis*, M.E. Dept., Penn State University.

4.3.3 Princeton University $M = 3$ Turbulent Experiment

General Testing Conditions. The model is constituted by a sharp fin, with unswept leading edge, mounted perpendicular to the tunnel wall in a region where the incoming supersonic flow is uniform and the boundary layer turbulent.

- Freestream Mach number: $M_0 = 2.93$
- Fin angle of incidence: $\alpha = 20^\circ$
- Freestream stagnation pressure: $p_{st0} = 6.90 \times 10^5$ Pa
- Freestream stagnation temperature: $T_{st0} = 270$ K
- Wall temperature: $T_w \approx 270$ K
- Unit Reynolds number: $R_u = 6.2 \times 10^8 \text{ m}^{-1}$
- Incoming boundary-layer parameters:
 - Physical thickness: $\delta_0 \approx 13$ mm
 - Displacement thickness: $\delta_0^* = 3.9$ mm
 - Momentum thickness: $\theta_0 = 0.72$ mm

Available Data

- Surface pressure distributions: $p_w(X, Z)$
- Pitot pressure profiles: $p_t(Y, Z)$
- Yaw angle profiles: $\beta(Y, Z)$. (β is the velocity direction with respect to the local velocity at the boundary layer outer edge.)
- Wall pressure fluctuations

The surface pressures were measured along row of orifices aligned with the freestream (X) direction.

The flow has been probed with a computer-controlled nulling yaw probe ("cobra probe"). This probe measured Pitot pressure and yaw angle along survey lines in the Y -direction; i.e., normal to the tunnel wall which supported the model. The yaw angles thus measured lie in the horizontal (X, Z) plane. The survey locations were chosen to provide detailed information within the separated region produced by this relatively strong swept shock-wave/boundary-layer interaction.

References

- Knight, D.D., Horstman, C.C., Bogdonoff, S.M. and Shapey, B.L. 1986 The flowfield structure of the 3-D shock-wave/boundary-layer interaction generated by a 20° sharp fin at Mach 3. *AIAA Paper 86-0343*.
- Knight, D.D., Horstman, C.C., Shapey, B.L. and Bogdonoff, S.M. 1987 Structure of supersonic turbulent flow past a sharp fin. *AIAA J.*, Vol. 25, No. 10, pp. 1331–1337.

Bogdonoff, S.M. and Shapey, B.L. 1987 Three-dimensional shock-wave/turbulent boundary-layer interaction for a 20° sharp fin at Mach 5. *AIAA Paper 86-0554*.

4.3.4 University of Texas $M = 5$ Turbulent Experiment

General Testing Conditions. In this experiment the fin, with unswept leading edge, was mounted perpendicular to a flat plate, the incoming boundary layer being turbulent.

- Freestream Mach number: $M_0 = 4.9$
- Fin angles of incidence: $\alpha = 6^\circ, 8^\circ, 10^\circ, 12^\circ, 14^\circ$ and 16°
- Freestream stagnation pressure: $p_{st0} = 27 \times 10^5$ Pa
- Freestream stagnation temperature: $T_{st0} = 422$ K
- Wall temperature: $T_w \approx 300$ K ($T_w/T_r = 0.8$)
- Unit Reynolds number: $R_u = 4.67 \times 10^7 \text{ m}^{-1}$
- Incoming boundary-layer parameters. The incoming boundary layer, probed with a Pitot tube just ahead of the fin leading edge, had a physical thickness $\delta_0 = 7.9$ mm. Its profile is provided with the data.

Available Data

- Surface pressure distributions: $p_w(XZ)$
- Surface heat-transfer distributions: $h_w(X, Z)$
- Surface flow visualizations (skin-friction line pattern)
- Wall pressure fluctuations

The surface heat transfer and surface pressure data were measured on the test plate along spanwise rows. Additional heat transfer data were taken along conical rays from the virtual origin for fin angles of incidence 8° and 15° . Three different rotatable instrumentation "plugs" were used to make the present measurements. By rotating this plug, the pressure tap rows could be reoriented to better approximate conical cross planes.

References

Dolling, D.S., Boitnott, T. and Erengil, M.E. 1991 Effects of moderate sweepback on the separation shock wave dynamics in a Mach 5 compression ramp interaction. *AIAA Paper 91-0254*.

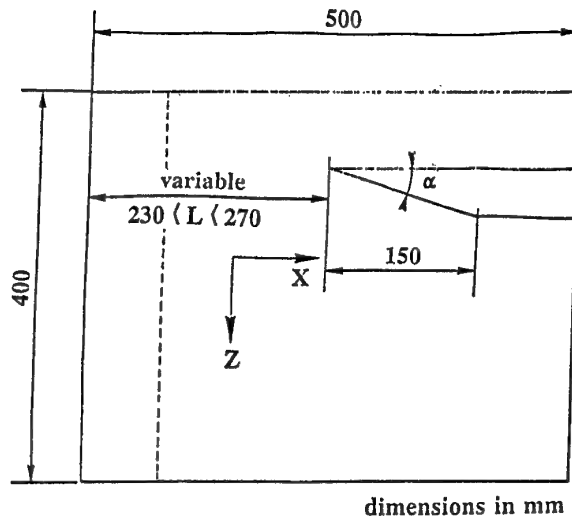


Figure 52: DLR single sharp fin model. $M = 5$ and $M = 6.83$ turbulent experiments.

4.3.5 DLR $M = 5$ and $M = 7$ Turbulent Experiments

General Testing Conditions. The model is made of a fin mounted on a flat plate having a sharp leading edge (see Figure 52). The total length of the plate is 500 mm, its width being equal to 400 mm. Three fin angles will be tested.

- Freestream flow Mach number: $M_0 = 5$
- Fin angles: $\alpha = 6^\circ, 10^\circ$ and 16°
- Freestream stagnation pressure: $p_{st0} = 3.2 \times 10^6$ Pa
- Freestream stagnation temperature: $T_{st0} = 420$ K
- Wall temperature: $T_w \approx 290$ K
- Unit Reynolds number: $R_u = 5.34 \times 10^7 \text{ m}^{-1}$

- Freestream flow Mach number: $M_0 = 6.83$
- Fin angles: $\alpha = 6^\circ, 10^\circ$ and 16°
- Freestream stagnation pressure: $p_{st0} = 32 \times 10^5$ Pa
- Freestream stagnation temperature: $T_{st0} = 600$ K
- Unit Reynolds number: $R_u = 1.48 \times 10^7 \text{ m}^{-1}$
- Wall temperature: $T_w \approx 290$ K

- Incoming boundary-layer parameters. These parameters are not yet known. It is believed that at least at Mach 5 the Reynolds number is sufficiently high to provide a natural turbulent boundary layer at the interaction region. This fact has to be checked for Mach 6.83, otherwise the boundary layer will be tripped artificially.

Available Data

- Surface pressure distributions: $p_w(X, Z)$
- Surface flow visualization (skin-friction line pattern)

4.3.6 CEAT/Poitiers $M = 2$ Turbulent Experiment

General Testing Conditions. In these experiments the fin, with unswept leading edge, was mounted perpendicular to the tunnel wall in a region where the incoming flow is uniform and the boundary layer turbulent. The fin spanned the full height of the tunnel (150 mm) and its edge was located 670 mm downstream of the nozzle exit. A better spatial resolution was obtained by moving the fin while keeping the measurement locations fixed with respect to the tunnel.

- Freestream Mach number: $M_0 = 2$
- Fin angles of incidence:
 - $\alpha = 6^\circ, 7^\circ, 8^\circ, 9^\circ, 10^\circ, 11^\circ, 12^\circ$ and 13° for surface flow visualizations
 - $\alpha = 12^\circ$ and 13° for mean wall-pressure measurements
 - $\alpha = 12^\circ$ for wall pressure-fluctuation measurements
- Freestream stagnation pressure: $p_{st0} = 6 \times 10^5$ Pa
- Freestream stagnation temperature: $T_{st0} = 265$ K
- Wall temperature: $T_w \approx 260$ K
- Unit Reynolds number: $R_u = 8.76 \times 10^7 \text{ m}^{-1}$
- Incoming boundary-layer parameters:
 - Physical thickness: $\delta_0 = 14.6$ mm
 - Displacement thickness: $\delta_0^* = 3.29$
 - Momentum thickness: $\theta_0 = 1.08$
 - Skin-friction coefficient: $C_{f0} \approx 0.0012$

Available Data

- Surface pressure distribution: $p_w(X, Z)$
- Surface flow visualizations (skin-friction line pattern)
- Wall pressure fluctuations

References

- Daghsstani, K. and Alziary de Roquefort, T. 1992 Measurements of wall pressure fluctuations in 3-D turbulent boundary-layer/shock-wave interaction. Final Report, BRITE-EURAM Contract No. AERO-0027-C(A).
- Daghsstani, K. 1993 Rôle des fluctuations de pression dans les interactions onde de choc-couche limite. *Ph.D. Thesis*, University of Poitiers, France.

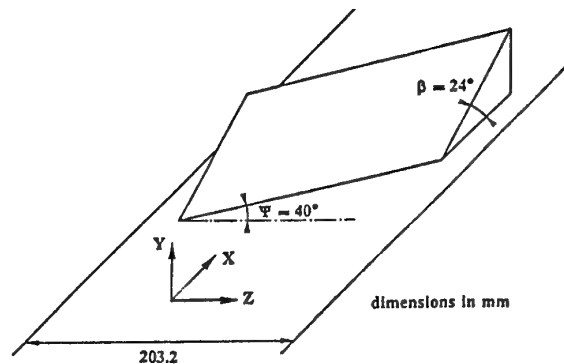


Figure 53: Princeton University swept-ramp model. $M = 3$ turbulent experiment.

Alziary de Roquefort, T. and Daghsstani, K. 1993 Experimental study of unsteadiness in sharp fin-induced turbulent boundary-layer/shock-wave interaction. *2nd French-Russian Workshop on Experimentation, Modelization and Computation*, INRIA, Sophia Antipolis. To appear John Wiley & Sons.

4.4 Swept Compression Corner

4.4.1 Princeton University $M = 3$ Turbulent Experiment

General Testing Conditions. As shown in Figure 53, the tested configuration consisted of a swept compression corner mounted on the floor of the wind tunnel. The corner was swept back 40° from the normal to the freestream direction and had a streamwise compression angle of 24° .

- Freestream Mach number: $M_0 = 2.95$
- Freestream stagnation pressure: $p_{st0} = 6.90 \times 10^5$ Pa
- Freestream stagnation temperature: $T_{st0} = 270$ K
- Wall temperature: $T_w \approx 270$ K
- Unit Reynolds number: $R_u = 6.17 \times 10^7 \text{ m}^{-1}$
- Incoming boundary-layer parameters:
 - Physical thickness: $\delta_0 = 15.4$ mm
 - Displacement thickness: $\delta_0^* = 4.08$ mm
 - Momentum thickness: $\theta_0 = 0.807$ mm
 - Skin-friction coefficient: $C_{f0} = 0.00116$

Available Data

- Surface pressure distributions: $p_w(X, Z)$
- Pitot pressure profiles: $p_t(Y, Z)$
- Yaw angle profiles: $\beta(Y, Z)$ (β is the velocity direction with respect to the local velocity at the boundary layer outer edge.)

- Wall pressure fluctuations

The surface pressure data were taken along 4 streamwise cuts located at different distances from the apex of the swept corner. Cobra probe data were taken at 14 stations in a vertical (X, Y) plane located 88.9 mm spanwise from the apex of the swept corner.

References

- Settles, G.S., Horstman, C.C. and McKenzie, T.M. 1984 Flowfield scaling of a swept compression corner interaction. A comparison of experiment and computation. *AIAA Paper 84-0096*. Also *AIAA J.*, Vol. 24, No. 5, pp. 744-752.
- Knight, D.D., Horstman, C.C., Bogdonoff, S.M., Raufer, D. and Ketchum, A. 1988 Supersonic turbulent flow past a swept compression corner at Mach 3. Part I. *AIAA Paper 88-0310*.

4.4.2 ONERA $M = 10$ Laminar Experiment

General Testing Conditions. This experiment was executed in the R3Ch hypersonic wind tunnel. As shown in Figure 54, the model was made of a three-dimensional obstacle mounted on a flat plate with sharp leading edge placed at zero incidence in a uniform flow. The plate had a total length of 300 mm and a span of 200 mm, the leading edge angle being equal to 15° . The obstacle is a double wedge body whose apex is displaced towards one side of the flat plate to allow a larger spanwise extent of the interaction under study. It was verified that there is no mutual influence of the flows on each side of the apex for the tested configuration. Thus, the vertical streamwise plane containing the obstacle apex can be considered as a symmetry plane. The apex of the obstacle is located 100 mm downstream of the plate leading edge.

The obstacle corner line is swept back 60° from the normal to the freestream direction and has a compression angle, in a plane normal to the corner line, equal to 30° .

- Freestream Mach number: $M_0 = 9.95$
- Freestream stagnation pressure: $p_{st0} = 125 \times 10^5$ Pa
- Freestream stagnation temperature: $T_{st0} = 1050$ K
- Wall temperature: $T_w \approx 300$ K
- Unit Reynolds number: $R_u = 9.18 \times 10^6 \text{ m}^{-1}$

Available Data

- Surface pressure distributions: $p_w(X, Z)$
- Surface heat-transfer distributions: $h_w(X, Z)$
- Surface flow visualizations (skin-friction line pattern)

The surface pressure was measured along 3 lines (designated 2, 4 and 6 in Figure 54) normal to the plate leading edge and extending over the obstacle. The surface heat transfer was measured along the 6 lines 2 to 7 (measurements were also made along line 1 to check flow symmetry).

References

- Coët, M.-C. 1991 Etude expérimentale de l'effet d'une couche d'entropie sur les transferts de chaleur associés aux phénomènes d'interaction onde de choc-couche limite en écoulement hypersonique. *ONERA RT No. 23/4362AY*.
- Coët, M.-C., Détery, J. and Chanetz, B. 1991 Experimental study of shock-wave/boundary-layer interaction at high Mach number with entropy layer effect. *IUTAM Symposium on Aerothermochemistry of Spacecraft and Associated Hypersonic Flows*, Marseille, France.

4.5 Crossing Shocks

4.5.1 NASA $M = 8$ Turbulent Experiment

General Testing Conditions. This experiment was executed in the NASA-Ames 3.5-foot hypersonic wind tunnel using a flat-plate model with a length of 2200 mm. Natural transition occurred for all test conditions. While no turbulence data are available to establish the condition of the incoming boundary layer ahead of the interaction, a mean profile included in the data set shows typical law-of-the-wall and wake behavior, albeit with a lower wake-strength parameter than usual.

As shown in Figure 55, opposing pairs of fins, each having either 10° or 15° angles of incidence were mounted on the flat plate.

- Freestream Mach number: $M_0 = 8.28$
- Fin angles of incidence: $\alpha = 10^\circ$ and 15°
- Freestream static pressure: $p_0 = 430$ Pa
- Freestream static temperature: $T_0 = 80$ K
- Wall temperature: $T_w = 300$ K
- Unit Reynolds number: $R_u = 4.99 \times 10^6 \text{ m}^{-1}$
- Incoming boundary-layer parameters:
 - Physical thickness: $\delta_0 = 32.5$ mm
 - Displacement thickness: $\delta_0^* = 12.6$ mm
 - Momentum thickness: $\theta_0 = 0.83$ mm
 - Skin-friction coefficient: $C_{f0} = 0.000998$
 - Heat-transfer coefficient: $S_{t0} = 0.000568$

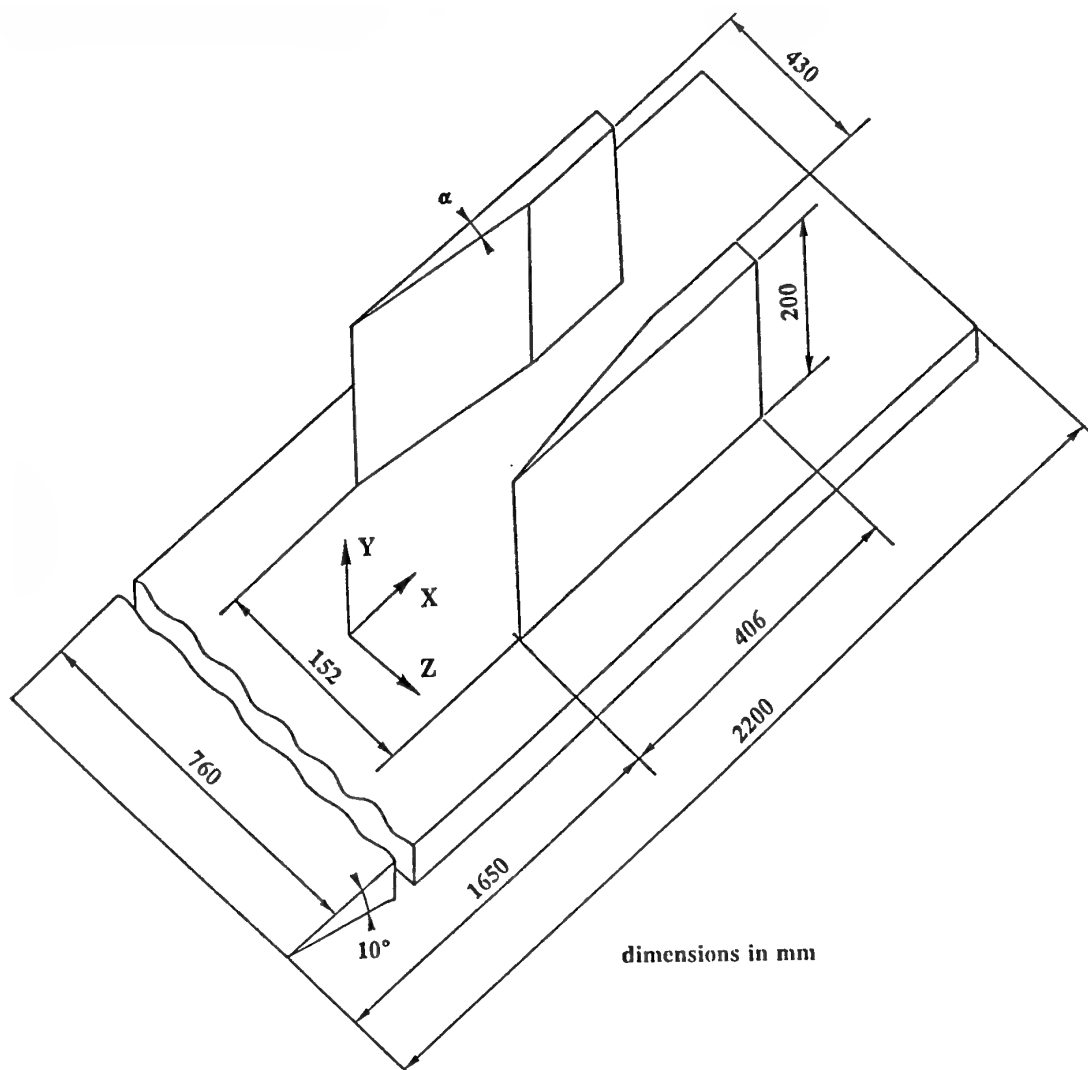


Figure 55: NASA crossing shock model. $M = 8$ turbulent experiment.

Available Data

- Surface pressure distributions: $p_w(X, Z)$
- Skin-friction distributions: $C_f(X, Z)$
- Surface flow visualization (skin-friction line pattern)
- Flowfield Pitot profiles: $p_t(X, Z, Y)$

The surface pressures were measured only on the center line of the symmetric interactions studied. Skin-friction data were measured both on the center line and on certain spanwise "cuts" located at specific streamwise locations. Only one Pitot profile was obtained.

References

Garrison, T.J. and Settles, G.S. 1993 Interaction strength and model geometry effects on the structure of crossing shock-wave/turbulent boundary-layer interactions. *AIAA Paper 93-0780*.

Settles, G.S. and Dodson, L.J. Interaction data base: new and corrected data. NASA Contractor Report (to be published).

4.5.3 Princeton University $M = 3$ Turbulent Experiment

General Testing Conditions. The model was made of two sharp fins mounted symmetrically between two sharp flat plates, 610 mm long, installed approximately 51 mm off the floor and ceiling of the test section (see Figure 56). The sharp leading edges of the fins were located 25.4 mm off each side wall and 194 mm downstream from the plate leading edges (the geometry is symmetrical both in a vertical and horizontal plane).

- Freestream Mach number: $M_0 = 2.95$
- Fin angles: $\alpha = 7^\circ, 9^\circ$ and 11°
- Freestream stagnation pressure: $p_{st0} = 6.90 \times 10^5$ Pa

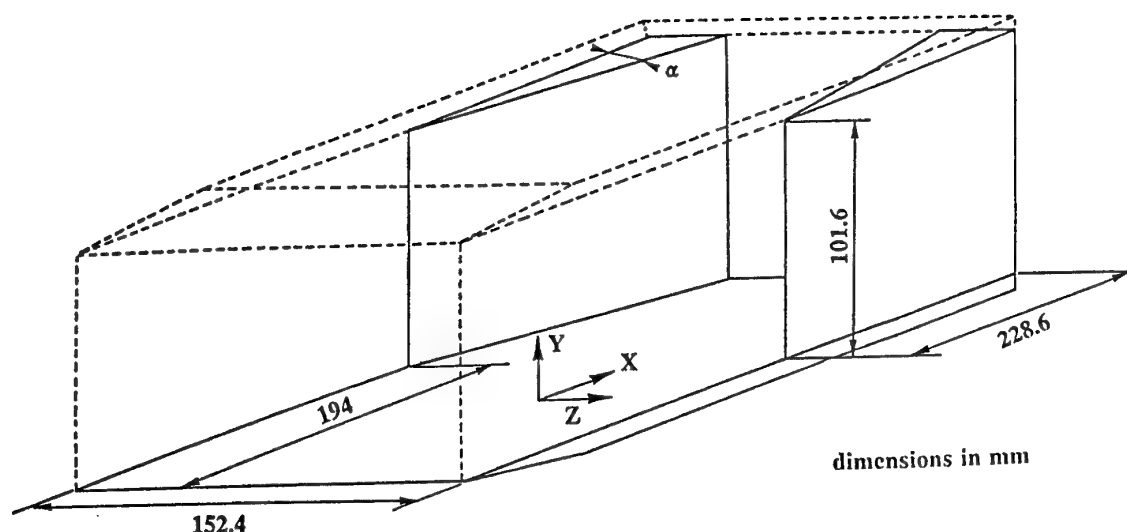


Figure 56: Princeton University $M = 3$ turbulent experiment.

- Freestream stagnation temperature: $T_{st0} = 265$ K
- Wall temperature: $T_w \approx 270$ K
- Unit Reynolds number: $R_u = 6.35 \times 10^7 \text{ m}^{-1}$
- Incoming boundary-layer parameters. The boundary layer is turbulent with transition occurring close to the leading edge of all surfaces. Its profile satisfies the law-of-the-wall and wake and has a thickness δ_0 of about 4 mm at the leading edge of the fins.

Available Data

- Surface pressure distributions: $p_w(X, Z)$
- Surface flow visualization (surface flow pattern).
- Wall pressure fluctuations

The high-resolution surface pressure field extended 65 incoming boundary-layer thicknesses downstream from the fins apex and spanned most of the interaction region. By using moving plates of closely spaced orifices, a total field of about 3000 static pressure points could be obtained for any flow configuration.

References

Batcho, P.F., Ketchum, A.C., Bogdonoff, S.M. and Fernando, E.M. 1989 Preliminary study of the interactions caused by crossing shock waves and a turbulent boundary layer. *AIAA Paper 89-0358*.

Narayanswami, N., Knight, D., Bogdonoff, S.M. and Horstman, C.C. 1991 Crossing shock-wave/turbulent boundary-layer interactions. *AIAA Paper 91-0649*.

4.5.4 DLR/Göttingen $M = 5$ and $M = 7$ Turbulent Experiments

General Testing Conditions. The model is made of two fins mounted symmetrically on a flat plate having a sharp leading edge (see Figure 57). The total length of the plate is 500 mm; its width is 400 mm. Three fin angles will be tested.

- Freestream flow Mach number: $M_0 = 5$
- Fin angles: $\alpha = 6^\circ, 10^\circ$ and 16°
- Freestream stagnation pressure: $p_{st0} = 3.2 \times 10^6$ Pa
- Freestream stagnation temperature: $T_{st0} = 420$ K
- Wall temperature: $T_w \approx 290$ K
- Unit Reynolds number: $R_u = 5.34 \times 10^7 \text{ m}^{-1}$

- Freestream flow Mach number: $M_0 = 6.83$
- Fin angles: $\alpha = 6^\circ, 10^\circ$ and 16°
- Freestream stagnation pressure: $p_{st0} = 32 \times 10^5$ Pa
- Freestream stagnation temperature: $T_{st0} = 600$ K
- Unit Reynolds number: $R_u = 1.48 \times 10^7 \text{ m}^{-1}$
- Wall temperature: $T_w \approx 290$ K
- Incoming boundary-layer parameters: These parameters are not yet known. It is believed that at least at $M_0 = 5$ the Reynolds number is sufficiently high to provide a natural turbulent boundary layer at the interaction region. This fact has to be checked for $M_0 = 6.83$, otherwise the boundary layer will be tripped artificially.

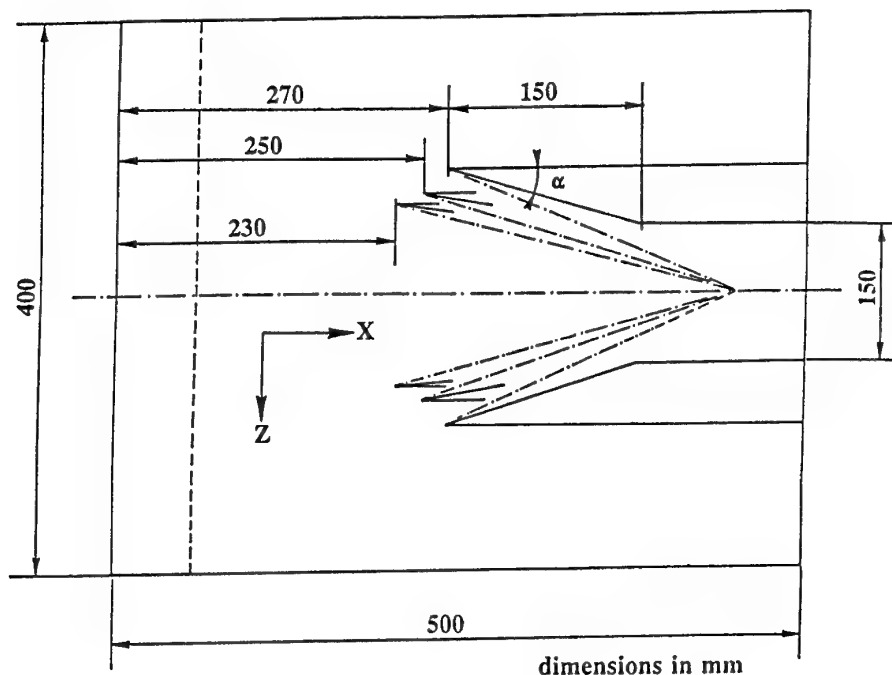


Figure 57: DLR crossing shock model. $M = 5$ and $M = 7$ turbulent experiments.

Available Data

- Surface pressure distributions: $p_w(X, Z)$
- Surface flow visualization (skin-friction line pattern)

5 CONCLUDING REMARKS AND RECOMMENDATIONS

5.1 Viscous Interaction Phenomena are Important

Because of the presence of intense shock waves, hypersonic flows are the seat of strong shock-wave/boundary-layer interactions which nearly always have detrimental effects. For instance, when the shock induced by a control surface is strong enough to separate the boundary layer, there is a loss of aerodynamic efficiency with, in addition, high heat transfer rates in the region where the separated shear layer impinges the control surface at reattachment. Similarly, in air intakes, interactions of the compression shocks with the wall boundary layers can induce massive separation provoking a dramatic fall of pressure recovery. Furthermore, turbulent interactions are affected by fluctuations which are most often amplified if separation occurs. Then, the whole flowfield may oscillate, inducing intense variable loads on the vehicle surface or air-intake buzz. In some circumstances, the interaction process leads to the formation of complex shock patterns, giving rise to interferences which may generate destructive local heating on a nearby surface.

Thus, there is a pressing need of methods allowing a reliable and accurate prediction of shock-wave/boundary-layer interaction in high-Mach-number flows, the devel-

opment of such methods requiring that a certain number of conditions be fulfilled.

5.2 The Extent of our Knowledge and Capabilities

5.2.1 The physics of the flow

A sound physical understanding of interacting flows is a prerequisite to the development of theoretical models. The influence of the main parameters affecting the phenomenon, the scaling factors, and also the detailed flow structure, must be clearly elucidated. Because of their simpler nature and of the vast amount of published experimental results, two-dimensional (planar and/or axisymmetric) interactions can be considered as well understood. Thus, the factors acting on the upstream propagation mechanism, the conditions for incipient shock-induced separation, have been safely identified, and the overall flow structure associated with two-dimensional interactions has been well established. Many results on surface heat transfer in hypersonic interactions as also on the influence of the wall temperature are at our disposal.

The physical understanding of three-dimensional interactions is a far more difficult task because of the conceptual difficulty to grasp three-dimensional fields and of the large variety of situations which can be met in this case. In this task, numerical simulations, even if they are not always accurate, are of great help to understand the structure of the flow, especially when a complex shock pattern forms in the outer inviscid stream. Until recently, the most studied configurations were the single sharp fin, the swept wedge and the blunt fin at zero incidence. These cases constitute the basic three-dimensional interactions, to which many variants are

possible. More recently, the double-fin configuration inducing two crossing shocks has raised much interest because of its obvious relation with hypersonic air intakes. Also, the corner flow produced by two intersecting wedges is of great interest, although relatively few results have been published for this case.

Substantial information on the basic configurations is now available, so that the physics of these flows can be considered as fairly well understood, although some behavior is still unclear and subject to controversy (conical properties, multiple separation, etc.).

5.2.2 *The predictive capabilities*

Due to the progress made by computer technology and numerical methods, it is now possible to compute complex flows containing intense shock waves and large separated regions. Spectacular results have been obtained in the calculation of three-dimensional configurations (corner flows, crossing shocks, blunt obstacles), the essential flow features being faithfully predicted, even for the turbulent regime. The first equilibrium algebraic models, in which turbulence is assumed to adjust itself instantly to changes in the mean flow, are now replaced by nonequilibrium models using transport equations to represent the specific behavior of turbulence. Many variants of these models have been proposed to improve their accuracy in the near wall region or in separated zones.

Thus, if one observes the evolution of our knowledge of interacting flows over the past forty years, the present situation can be considered as satisfactory and our predictive capabilities spectacular. However, a more critical evaluation of the situation shows that many points remain obscure and insufficiently investigated. Furthermore, theoretical models still give a too coarse and uncertain prediction to allow their routine use in design applications.

5.3 *The Limits of our Knowledge and Capabilities*

5.3.1 *The physics of the flow*

As far as the physics of shock-wave/boundary-layer interactions are concerned, the following points would merit a special attention in the coming years:

1. The unsteady character of interacting flows seems to be a key factor in the process. In spite of a rather broad information on the subject, there is not yet a clear philosophy about this fact: what is the triggering mechanism of the fluctuations? Is it the turbulence of the incoming boundary layer? Does a well-defined demarcation exist between high-frequency fluctuations, which could be induced by the incoming boundary-layer turbulence, and low-frequency fluctuations resulting from a coupling between the outer flow and a separated region, like in buffeting? What is the interaction between real turbulence and large-scale fluctuations, involving oscillations of the shock system attached to the interaction? This last

point could be a critical issue for turbulence modeling in interacting flows. The above questions remain unanswered.

2. Except in transonic or moderately supersonic flows, results on turbulence in shock-wave/boundary-layer interactions are nearly nonexistent. The probing of high-Mach-number flows, even with advanced optical techniques like Laser Doppler Velocimetry or Laser Induced Fluorescence, is a difficult task, which explains the scarcity of results. Significant advances in turbulence modeling will necessitate reliable and detailed results on the evolution of turbulence properties, at least the Reynolds-tensor components, through an interaction. It is unwise to try to devise sophisticated models by basing their justification and validation on surface pressure and heat transfer distributions only.
3. Experimental information on the incidence of real-gas effects on shock-wave/boundary-layer interaction is completely lacking. It can be anticipated (according to computations) that these effects are important, but we have no measurements to substantiate this opinion. Such experiments are difficult to execute since they require expensive high-enthalpy facilities in which the incoming flow properties are frequently not well understood. However, if this point has to be clarified, these experiments are indispensable.
4. At high altitude, rarefaction effects certainly play a large role in interacting flows. This point has also to be elucidated and, for this purpose, experiments in low density wind tunnels are desirable.

5.3.2 *The predictive capabilities*

On the theoretical side, progress has still to be made to arrive at a satisfactory situation. The numerical accuracy of the existing codes is not always firmly assessed in hypersonic interactions. Indeed, these flows contain intense shock waves, in some cases centered expansion waves, as also boundary layers and shear layers across which the flow properties undergo rapid variations. An accurate capture of these discontinuities and zones of large gradients raises difficulties which are considerably amplified in three-dimensional flows. However, the most critical issue is the modeling of turbulence, most of the presently used models giving poor prediction of surface heat transfer distributions, especially when the flow is separated. In three-dimensional interactions, even if the overall flowfield structure is well reproduced, many of the details of the flow are missed by the computation and its surface properties are often badly predicted.

The cause of these deficiencies is not clear. Part of the discrepancies is due to a lack of numerical accuracy, as it is the case in three-dimensional applications where a huge number of mesh points is required to capture the finest flow features. Disagreement with experiment is frequently attributed to compressibility effects whose influence becomes noticeable above Mach 6. However, the various attempts to introduce these effects in turbulence models have led to disappointing results. Here also the

situation is not clear, the compressibility terms being added to a baseline model which is probably not suited for the computation of interacting flows, even at low Mach numbers. Some investigators attribute the failure of the models to the aforementioned unsteady effects which are not accounted for and which may be of prime importance as a source of intense turbulence production. This conclusion is not free of critics, the failure of the models being observed in the calculation of subsonic separated flows. Thus, the real cause of discrepancies can be in the chosen baseline models which may be inadequate to compute such complex flows.

5.4 The Subgroup Contribution

With the aim of establishing the state of the art in matter of shock-wave/boundary-layer prediction and to bring elements to improve the present situation, the Subgroup 1 on "Viscous Interactions" has collected a limited number of well-documented experiments which can be safely used to validate computational methods. The proposed test cases have been selected according to the following criteria:

1. Reject planar two-dimensional geometries which are nearly always affected by side effects.
2. Avoid too complex cases leading to still insurmountable modeling problems, like transitional interactions, or to great experimental difficulties rendering the results (if they exist) inaccurate, like real-gas effects.
3. Cover a Mach number range extending from 2 to hypersonic values.
4. Consider fully laminar cases in order to assess the numerical accuracy of the codes.
5. Consider a limited number of axisymmetric configurations for which high grid refinement can be achieved without requiring large computer memory and costly computing time.
6. Put emphasis on three-dimensional configurations which are of greater practical interest than axisymmetric cases.
7. Select three-dimensional configurations of increasing difficulty.

Thus, 15 basic test cases (giving in fact 20 cases, some configurations having been tested for several values of the Mach number) have been collected, for which the initial and boundary conditions are well identified and reliable results available.

5.5 Recommendation for Future Actions

The above validation action constitute a first step in the elucidation of viscous interactions at hypersonic Mach numbers. At the issue of this step, some clear conclusions should be drawn about the accuracy of the present numerical methods and turbulence models in relatively

simple situations. Thus, to make real progress in the prediction of interacting flows, a continuation of the action is necessary along the following lines:

1. The numerical accuracy of the codes should be more completely assessed in three-dimensional flows. For this purpose, other experiments involving fully laminar interactions should be executed on geometries more complex than those tested to this date.
2. The data bank should be extended by incorporating other three-dimensional configurations which are of great practical interest, like the corner flow and the blunt fin. This would necessitate execution of new experiments to complete the existing results on these flows.
3. A special effort must be made to improve turbulence modeling in shock-separated flows and to elucidate the aforementioned problems. This will require execution of detailed experiments, including turbulence measurements with the simultaneous characterization of the unsteady effects. In a first step, it is not necessary to consider high-Mach-number flows in which these measurements are difficult to perform. An upper limit of 4 would be adequate. Furthermore, for modest Mach numbers, compressibility effects are negligible thus, by working below Mach 4, one will avoid the mixing of complex phenomena. The question of compressibility has first to be examined on simpler situations, free of a wall influence (shear layers, jets, wakes).
4. Although they have been excluded from the present data bank, as being too difficult to compute, transitional interactions are of great practical interest. For this reason, they justify more complete and in depth investigations than those already made. In particular, the mechanism of transition in high Mach number interactions should be elucidated in conjunction with theoretical studies.
5. Real-gas effects have multiple incidences on a shock-wave/boundary-layer interaction since they affect both the outer inviscid-flow structure and the transport properties (viscosity, thermal conductivity) of the viscous regions. In addition, it is clear that wall catalicity dramatically affects the surface heat transfer. These effects are predicted by computations, but experiments to validate the results are still lacking. To obtain good test cases, it is not necessary to achieve very high Mach numbers. Thus, experiments in a shock tube could provide results on simple configurations at low cost, with well identified flow conditions.
6. Rarefaction effects should also be investigated in adequate facilities to provide good test cases.

The main task of a future Working Group will be to clearly identify the above problems, to recommend the execution of specific experiments to fill gaps in existing data, and to collect the results in order to promote an extended modeling action.

REFERENCES

- Alvi, F.S. and Settles, G.S. 1990 Structure of swept shock-wave/boundary-layer interactions using conical shadowgraphy. *AIAA Paper 90-1644*.
- Alvi, F.S. and Settles, G.S. 1991 A physical model of the swept shock-wave/boundary-layer interaction flow-field. *AIAA Paper 91-1768*.
- Ardonceanu, P., Lee, D.H., Alziary de Roquefort, T. and Goethals, R. 1980 Turbulence behavior in a shock-wave/boundary-layer interaction. *AGARD CP-271*, Paper No. 8.
- Aso, S., Tan, A. and Hayashi, M. 1990 The structure of aerodynamics heating in three-dimensional shock-wave/turbulent boundary-layer interactions induced by sweptback blunt fins. *AIAA Paper 90-0381*.
- Back, L.H. and Cuffel, R.F. 1976 Shock-wave/turbulent boundary-layer interactions with and without surface cooling. *AIAA J.*, Vol. 14, No. 4, pp. 526-532.
- Baldwin, B.S. and MacCormack, R.W. 1974 Numerical solution of the interaction of a strong shock wave with a hypersonic turbulent boundary layer. *AIAA Paper 74-0558*.
- Baldwin, B.S. and Lomax, H. 1978 Thin layer approximation and algebraic model for separated turbulent flows. *AIAA Paper 78-0257*.
- Baldwin, B.S. and MacCormack, R.W. 1976 Modification of the law of the wall and algebraic turbulence modeling for separated boundary layers. *AIAA Paper 76-0350*.
- Ballaro, C.A. and Anderson, J.D., Jr. 1991 Shock strength effects on separated flows in nonequilibrium chemically reacting air shock-wave/boundary-layer interaction. *AIAA Paper 91-0250*.
- Benay, R. 1991 Modélisation de la turbulence dans une interaction onde de choc-couche limite sur une paroi chauffée. *La Recherche Aéronautique*, No. 1991-5, pp. 45-68, French and English editions.
- Benay, R., Coët, M.-C. and Délery, J. 1987 Validation of turbulence models applied to transonic shock-wave/boundary-layer interaction. *La Recherche Aéronautique*, No. 1987-3, pp. 1-16.
- Bertram, M.H. and Henderson, A. 1969 Some recent research with viscous interacting flow in hypersonic streams. *ARL 75-0212*.
- Bogdonoff, S.M. 1990 The modeling of three-dimensional shock-wave/turbulent boundary-layer interaction. The Dryden Lectureship. *AIAA Paper 90-0766*.
- Bogdonoff, S.M., Keppler, E.C. and Sanlorenzo, E. 1953 A study of shock-wave/turbulent boundary-layer interaction at $M = 3$. Princeton University, Dept. of Aero Eng., Report No. 222.
- Cambier, L., Escande, B. and Veillot, J.-P. 1988 Calculs d'écoulements turbulents tridimensionnels par résolution numérique des équations de Navier-Stokes moyennées. *ONERA RTS*, No. 33/7077AY.
- Carter, J.E. 1973 Numerical solution of the supersonic, laminar flow over a two-dimensional compression corner. *Lectures Notes in Physics*, Vol. 19, pp. 69-78.
- Cebeci, T. and Smith, A.M.O. 1974 *Analysis of Turbulent Boundary Layers*, Academic Press, New York.
- Chapman, D.R., Kuehn, D.M. and Larson, H.K. 1957. Investigation of separated flows in supersonic and subsonic streams with emphasis on the effect of transition. *NACA TN-3869*.
- Charwat, A.F. and Redecopp, L.G. 1967 Supersonic interference flow along the corner of intersecting wedges. *AIAA J.*, Vol. 5, pp. 480-488.
- Chen, Y. S. 1986 Application of new wall function to turbulent flow computations. *AIAA Paper 86-0438*.
- Chen, C.L. and Hung, C.M. 1992 Numerical study of juncture flows. *AIAA J.*, Vol. 30, No. 7, pp. 1800-1807.
- Chien, K.Y. 1982 Prediction of channel and boundary-layer flows with a low-Reynolds-number turbulence model. *AIAA J.*, Vol. 20, No. 1, pp. 33-38.
- Coakley, T.J. 1983 Turbulence modeling methods for the compressible Navier-Stokes equations. *AIAA Paper 83-1693*.
- Coët, M.-C. and Chanetz, B. 1993 Etude expérimentale de l'interaction onde de choc-couche limite en écoulement hypersonique. *La Recherche Aéronautique*, No. 1993-1, pp. 61-74, French and English editions.
- Coët, M.-C., Délery, J. and Chanetz, B. 1992 Experimental study of shock-wave/boundary-layer interaction at high Mach number with entropy layer effect. *IUTAM Symposium on Aerothermochemistry of Spacecraft and Associated Hypersonic Flows*, Marseille, France.
- Cousteix, J. and Aupoix, B. 1989 Turbulence models for compressible flows, *AGARD/FDP-VKI Special Course on Three-Dimensional Supersonic and Hypersonic Flows Including Separation*, Rhode-Saint-Genèse, Belgium.
- Deese, J.E. and Agarwal, R.K. 1985 Shock/turbulent boundary-layer interaction in a compression corner. *AIAA Paper 85-1567*.
- Degani, D. and Steger, J.L. 1983 Comparison between Navier-Stokes and thin-layer computations for separated supersonic flow. *AIAA J.*, Vol. 21, No. 11, pp. 1604-1606.

- Degrez, G. 1985 Computation of a three-dimensional skewed shock wave laminar boundary layer interaction. *AIAA Paper 85-1565*.
- Degrez, G, Boccadoro, C.H. and Wendt, J.F. 1987 The interaction of an oblique shock wave with a laminar boundary layer revisited. An experimental and numerical study. *J. Fluid Mech.*, Vol. 177, pp. 247-263.
- Deiwert, G.S. 1975 Computation of separated transonic turbulent flows. *AIAA Paper 75-0829*.
- Délery, J. 1970 Examen des phénomènes d'interaction choc-couche limite dans un canal interaubes. *ON-ERA NT*, No. 2/7078AY.
- Délery, J. 1981 Investigation of strong-shock/turbulent boundary-layer interactions in 2D transonic flows with emphasis on turbulence phenomena. *AIAA Paper 81-1245*. Also *AIAA J.*, Vol. 21, No. 2, pp. 180-185.
- Délery, J. 1992 Etude expérimentale de la réflexion d'une onde de choc sur une paroi chauffée en présence d'une couche limite turbulente. *La Recherche Aéronautique*, No. 1992-1, pp. 1-23, French and English editions.
- Délery, J. and Coët, M.-C. 1990 Experiments on shock-wave/boundary-layer interactions produced by two-dimensional ramps and three-dimensional obstacles. *Workshop on Hypersonic Flows for Re-entry Problems*, Antibes, France.
- Délery, J. and Marvin, J.G. 1986 *Shock-Wave/Boundary-Layer Interactions*, AGARDograph No. 280.
- Dolling, D.S. 1982 Comparison of sharp and blunt-fin induced shock-wave/turbulent boundary-layer interactions. *AIAA J.*, Vol. 20, No. 10, pp. 1385-1391.
- Dolling, D.S. 1993 Unsteady phenomena in shock-wave/boundary-layer interaction. *AGARD/FDP-VKI Special Course on Shock-Wave/Boundary-Layer Interactions in Supersonic and Hypersonic Flows*, AGARD Report 792.
- Dolling, D.S. and Bogdonoff, S.M. 1981 Scaling of interactions of cylinders with supersonic turbulent boundary layers. *AIAA J.*, Vol. 19, No. 5, pp. 655-657.
- Dolling, D.S., Cosad, C.D. and Bogdonoff, S.M. 1979 A examination of blunt-fin-induced shock-wave/turbulent boundary-layer interaction. *AIAA Paper 79-0068*.
- Don Gray, J. and Rhudy, R.W. 1973 Effects of blunting and cooling on separation of laminar supersonic flow. *AIAA J.*, Vol. 11, No. 9, pp. 1296-1301.
- Douay, G. 1994 Modélisation et étude numérique de la turbulence compressible en écoulements supersoniques. *Ph.D. Thesis*, University of Rouen, France.
- Edney, B. 1968 Anomalous heat transfer and pressure distributions on blunt bodies at hypersonic speeds in the presence of an impinging shock. *FFA Report No. 115*.
- Elfstrom, G.M. 1971 Turbulent separation in hypersonic flow. Imperial College Aero Report 71-16.
- Elfstrom, G.M. 1972 Turbulent hypersonic flow at a wedge compression corner. *J. Fluid Mech.*, Vol. 53, Part 1, pp. 113-129.
- Gaitonde, D. and Knight, D. 1988 Numerical experiments on the 3-D shock-wave/boundary-layer interaction generated by a sharp fin. *AIAA Paper 88-0309*.
- Gaitonde, D. and Knight, D. 1989 Numerical investigation of some control methods for 3-D turbulent interactions due to sharp fins. *AIAA Paper 89-0360*.
- Garrison, T.J., Settles, G.S., Narayanswami, N. and Knight, D.D. 1993 Structure of crossing shock-wave/turbulent boundary-layer interactions. *AIAA J.*, Vol. 31, No. 12, pp. 2204-2211.
- Ginoux, J. 1969 On some properties of reattaching laminar and transitional high speed flows. VKI TN No. 53.
- Glushko, G.S. 1965 Turbulent boundary layer on a flat plate in an incompressible fluid. *Bull. Acad. Sci., USSR*, No. 4, pp. 13-23.
- Goldberg, U.C. and Chakravarthy, S.R. 1990 Separated flow predictions using a hybrid $k-L$ /backflow model. *AIAA J.*, Vol. 28, No. 6, pp. 1005-1009.
- Goldberg, U.C. and Ramakrishnan, S.V. 1993 A point-wise version of the Baldwin-Barth turbulence model. *AIAA Paper 93-3523*.
- Grasso, F. and Leone, G. 1992 Chemistry effects in shock-wave/boundary-layer interaction problems. *IUTAM Symposium on Aerothermochemistry of Spacecraft and Associated Hypersonic Flows*, Marseille, France.
- Grumet, A.A., Anderson, J.D. and Lewis, M.J. 1991 A numerical study of shock-wave/boundary-layer interaction in nonequilibrium chemically reacting air: The effects of catalytic walls. *AIAA Paper 91-0245*.
- Haidinger, F.A. and Friedrich, R. 1993 Computation of shock-wave/turbulent boundary-layer interactions using a two-equation model with compressibility corrections. *Applied Scientific Research*, Vol. 51, pp. 501-505, *Advances in Turbulence IV*, Kluwer Academic Publishers.

- Hanin, M., Wolfshtein, M. and Landau, U.E. 1974 Numerical solution of Navier-Stokes equations for interaction of shock wave with laminar boundary layer. *ICAS Paper No. 74-17*.
- Heffner, K. 1993 Contribution à l'étude d'une rampe de compression en écoulement hypersonique. Partie I: Régime de transition laminaire-turbulent de la couche limite. Partie II: Régime de transition écoulement continu-écoulement moléculaire libre. *Ph.D. Thesis*, Université Pierre et Marie Curie, Paris.
- Hodge, B.K. 1977 Prediction of hypersonic laminar boundary layer/shock wave interactions. *AIAA J.*, Vol. 15, No. 7, pp. 903-904.
- Holden, M.S. 1966 Experimental studies of separated flows at hypersonic speed II: Two-dimensional wedge separated flow studies. *AIAA J.*, Vol. 4, No. 5, pp. 790-799.
- Holden, M.S. 1972 Shock-wave/turbulent boundary-layer interactions in hypersonic flows. *AIAA Paper 72-0074*.
- Holden, M.S. 1977 Shock-wave/turbulent boundary-layer interaction in hypersonic flow. *AIAA Paper 77-0045*.
- Holden, M.S. 1978 A study of flow separation in regions of shock-wave/boundary-layer interaction in hypersonic flow. *AIAA Paper 78-1169*.
- Holden, M.S. 1986 A review of aerothermal problems associated with hypersonic flights. *AIAA Paper 86-0267*.
- Hollanders, H. and Marmignon, C. 1989 Navier-Stokes high-speed flow calculations by an implicit non-centered method. *AIAA Paper 89-0282*.
- Horstman, C.C. 1976 A turbulence model for nonequilibrium adverse pressure gradient flows. *AIAA Paper 76-412*, July 1976. Also: *AIAA J.*, Vol. 15, No. 2, pp. 131-132.
- Horstman, C.C. 1987 Prediction of hypersonic shock-wave/turbulent boundary-layer interaction flow. *AIAA Paper 87-1367*.
- Horstman, C.C. 1989 Prediction of secondary separation in shock-wave/boundary-layer interactions. *Computers & Fluids*, Vol. 17, No. 4, pp. 611-614.
- Horstman, C.C. and Hung, C.M. 1979 Computation of three-dimensional turbulent separated flows at supersonic speeds. *AIAA Paper 79-0002*. Also: *AIAA J.*, Vol. 17, No. 11, pp. 1155-1156.
- Horstman, C.C., Kussoy, M.I., Coakley, T.J., Rubesin, M.W. and Marvin, J.G. 1975 Shock-wave-induced turbulent boundary layer separation at hypersonic speeds. *AIAA Paper 75-0004*.
- Horstman, C.C., Hung, C.M., Settles, G.S., Vas, I.E. and Bogdonoff, S.M. 1977 Reynolds number effects on shock-wave/turbulent boundary-layer interactions. A comparison of numerical and experimental results. *AIAA Paper 77-0042*.
- Hummel, D. 1987 Experimental investigations on blunt bodies and corner configurations in hypersonic flow. *AGARD CP-428*, Paper No. 6.
- Hummel, D. 1989 Axial flow in corners at supersonic speeds. *AGARD Report No. 764*, Paper No. 5.
- Hung, F.T. 1973 Interference heating due to shock wave impingement on laminar boundary layers. *AIAA Paper 73-0678*.
- Hung, F.T. and Barnett, D.O. 1973 Shock-wave/boundary-layer interference heating analysis. *AIAA Paper 72-0237*.
- Hung, C.M. and MacCormack, R.W. 1977 Numerical solution of supersonic laminar flow over a three-dimensional compression corner. *AIAA Paper 77-0694*.
- Hung, C.M. and Kordulla, W. 1983 A time split finite volume algorithm for three-dimensional flow simulation. *AIAA Paper 83-1958*.
- Hung, C.M. and Buning, P.G. 1985 Simulation of blunt-fin-induced shock wave and turbulent boundary-layer interaction. *J. Fluid Mech.*, Vol. 154, pp. 163-185.
- Hung, C.M. and MacCormack, R.W. 1976 Numerical solutions of supersonic and hypersonic laminar compression corner flows. *AIAA J.*, Vol. 14, No. 4, pp. 475-481.
- Hung, C.M. and MacCormack, R.W. 1977 Numerical simulation of supersonic and hypersonic turbulent compression corner flows. *AIAA J.*, Vol. 15, No. 3, pp. 410-416.
- Hussaini, M.Y., Sankara Rao, K. and Purohit, S.C. 1976 Numerical study of two-dimensional laminar boundary-layer/shock-wave interaction. *J. Aero. Soc. of India*, Vol. 28, No. 3, pp. 297-307.
- Hypersonic Flows for Re-entry Problems, Vol. III, *Proc. of the INRIA-GAMNI/SMAI Workshop*, Antibes, France, Springer-Verlag, 1992.
- Inger, G.R. 1987 Spanwise propagation of upstream influence in conical swept-shock/boundary-layer interactions. *AIAA J.*, Vol. 25, No. 2, pp. 287-293.
- Issa, R.I. and Lockwood, F.C. 1977 On the prediction of two-dimensional supersonic viscous interactions near walls. *AIAA J.*, Vol. 15, No. 2, pp. 182-188.
- Johnson, D.A. and King, L.S. 1984 A new turbulence closure model for boundary layer flows with strong

- adverse pressure gradients and separation. *AIAA Paper 84-0175*.
- Johnson, D.A., Bachalo, W.D. and Owen, F.K. 1981 Transonic flow past a symmetrical airfoil at high angle of attack. *J. Aircraft*, Vol. 18, No. 1, pp. 7-14.
- Jones, W.P. and Launder, B.E. 1972 The prediction of laminarization with a two-equation model of turbulence. *Int. J. Heat and Mass Transfer*, Vol. 15, pp. 301-314.
- Joulot, A. 1992 Contribution à l'étude de l'interaction onde de choc-couche limite sur rampe bidimensionnelle en régime hypersonique. *Ph.D. Thesis*, Université Pierre et Marie Curie, Paris.
- Kaufman, L.G. II, Korkegi, R.H. and Morton, L.G. 1972 Shock impingement caused by boundary-layer separation ahead of blunt fins. *ARL 72-0118*. Also: *AIAA J.*, Vol. 11, No. 10, pp. 1163-1164.
- Kilburg, R.F. and Kotansky, D.R. 1969 Experimental investigation of the interaction of a plane oblique incident-reflecting shock with a turbulent boundary layer on a cooled surface. *NASA CR-66-841*.
- Kim, K.S., Lee, Y., Alvi, F.S., Settles, G.S. and Horstman, C.C. 1990 Laser skin-friction measurements and CFD comparison of weak to strong swept-shock/boundary-layer interaction. *AIAA Paper 90-0378*.
- Kirke, K. and Hummel, D. 1975 Untersuchungen an längsangeströmten Eckenkonfigurationen in hyperschallbereich. Teil II: Ecken zwischen gepfeilten Keiten. *Z. Flugwiss.*, 23, pp. 417-429.
- Knight, D.D. 1984 A hybrid explicit-implicit numerical algorithm for the three-dimensional compressible Navier-Stokes equations. *AIAA J.*, Vol. 22, No. 8, pp. 1056-1063.
- Knight, D.D. 1993 Numerical simulation of 3-D shock-wave/turbulent boundary-layer interaction. *AGARD/FDP-VKI Special Course on Shock-Wave/Boundary-Layer Interactions in Supersonic and Hypersonic Flows*, Rhode-Saint-Genève, Belgium, AGARD Report 792.
- Knight, D. and Badekas, D. 1991 On the quasiconical flowfield structure of the swept shock-wave/turbulent boundary-layer interaction. *AIAA Paper 91-1759*.
- Knight, D.D., Horstman, C.C. and Bogdonoff, S.M. 1992 Structure of supersonic turbulent flow past a swept compression corner. *AIAA J.*, Vol. 30, pp. 890-896.
- Knight, D.D., Horstman, C.C., Shapey, B. and Bogdonoff, S.M. 1987 Structure of supersonic turbulent flow past a sharp fin. *AIAA J.*, Vol. 25, pp. 1331-1337.
- Knight, D., Raufer, D., Horstman, C.C., Ketchum, A. and Bogdonoff, S. 1988 Supersonic turbulent flow past a 3-D swept compression corner at Mach 3. Part II. *AIAA Paper 88-0310*.
- Knight, D.D., Badekas, D., Horstman, C.C., Shapey, B. and Settles, G.S. 1992 Quasiconical flowfield structure of the three-dimensional sharp fin interaction. *AIAA J.*, Vol. 30, No. 12, pp. 2809-2816.
- Korkegi, R.H. 1971 Survey of viscous interactions associated with high-Mach-number flight. *AIAA J.*, Vol. 9, No. 5, pp. 771-784.
- Korkegi, R.H. 1976 On the structure of three-dimensional shock-induced separated flow regions. *AIAA J.*, Vol. 14, No. 5, pp. 597-600.
- Kubota, H. and Stollery, J.L. 1982 An experimental study of the interaction between a glancing shock wave and a turbulent boundary layer. *J. Fluid Mech.*, Vol. 116, pp. 431-458.
- Lawrence, S.L., Tannehill, J.C. and Chaussee, D.S. 1986 An upwind algorithm for the parabolized Navier-Stokes equations. *AIAA Paper 86-1117*.
- Leung, A.W.C. and Squire, L.C. 1993 Numerical simulation of three-dimensional shock-wave/turbulent boundary-layer interaction. *AIAA Paper 93-2937*.
- Lewis, J.E., Kubota, T. and Lees, L. 1967 Experimental investigation of supersonic laminar two-dimensional boundary-layer separation in a compression corner with and without cooling. *AIAA Paper 67-0191*. Also *AIAA J.*, Vol. 6, No. 1, pp. 7-14.
- Leyland, P. 1993 Shock-wave/boundary-layer interactions at hypersonic speeds by an implicit Navier-Stokes solver. *AIAA Paper 93-2938*.
- Li, C.P. 1977 A numerical study of separated flows induced by shock-wave/boundary-layer interaction. *AIAA Paper 77-0168*.
- Lighthill, M.J. 1953 On boundary layers upstream influence. Part II: Supersonic flows without separation. *Proc. Roy. Soc., A*(217), pp. 478-507.
- Liepmann, H.W. 1946 The interaction between boundary layer and shock waves in transonic flows. *Jas.*, Vol. 13, No. 12, pp. 623-638.
- Lu, F.K. and Settles, G.S. 1989 Inception length to a fully-developed fin-generated shock-wave/boundary-layer interaction. *AIAA Paper 89-1850*. Also: *AIAA J.*, Vol. 29, No. 5, pp. 758-762.
- Lu, F.K., Settles, G.S. and Horstman, C.C. 1990 Mach-number effects on conical surface features of swept shock-wave/boundary-layer interactions. *AIAA J.*, Vol. 28, No. 1, pp. 91-97.

- Lucas, E.J. 1971 Investigation of blunt-fin-induced flow separation on a flat plate at Mach number 2.5 to 4.0. *AEDC-TR-70-265*.
- MacCormack, R.W. 1971 Numerical solution of the interaction of a shock wave with a laminar boundary layer. *Lectures Notes in Physics*, Vol. 8, pp. 151-163.
- MacCormack, R.W. and Baldwin, B.S. 1975 A numerical method for solving the Navier-Stokes equations with application to shock/boundary-layer interactions. *AIAA Paper 75-0001*.
- McMaster, D.L. and Shang, J.S. 1988 A numerical study of three-dimensional separated flows around a sweptback blunt fin. *AIAA Paper 88-0125*.
- Mateer, P.G., Brosh, A. and Viegas, J.R. 1976 A normal shock-wave/turbulent boundary-layer interaction at transonic speeds. *AIAA Paper 76-0161*.
- Michel, R., Quémard, C. and Durant, R. 1969 Application d'un schéma de longueur de mélange à l'étude des couches limites d'équilibre. *ONERA Note Technique No. 154*.
- Miller, D.S., Hijman, R. and Childs, M.E. 1964 Mach 8 to 22 studies of flow separations due to deflected control surfaces. *AIAA J.*, Vol. 2, No. 2, pp. 312-321.
- Müllenstädt, W. 1984 Untersuchungen an längsangeströmten, gepfeilten Eckenkonfigurationen in hyperschallbereich. *Dissertation*, TU Braunschweig.
- Narayanswami, N., Knight, D., Bogdonoff, S.M. and Horstman, C.C. 1991 Crossing shock-wave/turbulent boundary-layer interactions. *AIAA Paper 91-0649*.
- Narayanswami, N., Horstman, C.C. and Knight, D.D. 1993 Numerical simulation of crossing shock: turbulent boundary-layer interaction at Mach 8.3. Comparison of zero- and two-equation turbulence models. *AIAA Paper 93-0779*.
- Needham, D.A. 1965 Laminar separation in hypersonic flow. *Ph.D. Thesis*, University of London.
- Nestler, D.E. 1973 Engineering analysis of re-attaching shear-layer heat transfer. *AIAA J.*, Vol. 11, No. 3, pp. 390-393.
- Ong, C. and Knight, D. 1986 A comparative study of the hybrid MacCormack and implicit Beam-Warming algorithms for a two-dimensional supersonic compression corner. *AIAA Paper 86-0204*.
- Ozcan, O. 1982 An experimental investigation of three-dimensional boundary-layer separation in supersonic flow past a circular cylinder on a flat plate. *Ph.D. Thesis*, University of California, Berkeley.
- Panaras, A.G. 1992 Numerical investigation of the high-speed conical flow past a sharp fin. *J. Fluid Mech.*, Vol. 236, pp. 607-633.
- Panaras, A.G. and Steger, J.L. 1988 A thin-layer Navier-Stokes solution of the flow about a prolate ellipsoid. *Z. Flugwiss.*, 12, Heft 3, pp. 173-180.
- Panaras, A.G. and Stanewsky, E. 1992 Numerical study of secondary separation in glancing-shock/turbulent boundary-layer interactions. *AIAA Paper 92-3666*.
- Panaras, A.G., Vollmers, H. and Müller, B. 1991 Simulation of laminar hypersonic flow about a longitudinal corner. *Proc. of the 2nd Workshop on Hypersonic Flows for Re-entry Problems*, Antibes, France, Tome 3, pp. 413-424.
- Peake, D.J. and Tobak, M. 1980 *Three-dimensional interactions and vortical flows with emphasis on high speeds*. AGARDograph No. 252.
- Peters, G.R., Agarwal, R.K. and Deese, J.E. 1986 Numerical simulation of several shock-separated boundary-layer interaction flows using zero- and two-equation turbulence models. *AIAA Paper 86-0248*.
- Popinski, Z. and Ehrlich, C.F. 1966 Development design methods for predicting hypersonic control characteristics. *AFFDL-TR-66-85*.
- Price, E.A. and Stalling, R.L. 1967 Investigation of turbulent separated flows in the vicinity of fin-induced protuberances at supersonic Mach numbers. *NASA TN-D-3804*.
- Qin, N. and Richards, B.E. 1987 Numerical experiments with hypersonic flows beneath a cone/delta-wing combination. *AGARD CP-428*, Paper No. 20.
- Ray, R., Erdos, J. and Pulsonetti, M.V. 1987 Hypersonic laminar strong interaction theory and experiment revisited using a Navier-Stokes code. *AIAA Paper 87-1191*.
- Reddy, D.R. 1991 3-D Navier-Stokes analysis of crossing, glancing shocks/turbulent boundary-layer interactions. *AIAA Paper 91-1758*.
- Roshko, A. and Thomke, G.J. 1965 Observations of turbulent reattachment behind an axisymmetric downstream facing step in supersonic flow. *Douglas Report SM-4 3069*.
- Roshko, A. and Thomke, G.J. 1969 Supersonic turbulent boundary-layer interaction with a compression corner at very high Reynolds number. *McDonnell Douglas Paper 10163*.
- Roshko, A. and Thomke, G.J. 1974 Flare-induced interaction lengths in supersonic, turbulent boundary layers. *McDonnell Douglas MDAC Paper WD 2416*. Also: *AIAA J.*, Vol. 14, No. 7, pp. 873-879.

- Rubeson, M.W. 1976 A one-equation model of turbulence for use with the compressible Navier-Stokes equations. *NASA TM X-73-128*.
- Rubeson, M.W. and Rose, W.C. 1973 The turbulent mean-flow, Reynolds-stress and heat-flux equations in mass-averaged dependent variables. *NASA TM X-62-248*.
- Rudy, D.H., Kumar, A., Gnoffo, P.A. and Chakravarthy, S.R. 1989 A validation study of four Navier-Stokes codes for high-speed flows. *AIAA Paper 89-1838*.
- Sedney, R. and Kitchens, C.W., Jr. 1977 Separation ahead of protuberances in supersonic turbulent boundary layers. *BRL Report No. 1958*. Also *AIAA J.*, Vol. 15, No. 4, pp. 546-552.
- Seegmiller, H.L., Marvin, J.G., and Levy, L.L., Jr. 1978 Steady and unsteady transonic flow. *AIAA Paper 78-0160*. Also: *AIAA J.*, Vol. 16, No. 12, pp. 1262-1270.
- Settles, G.S. 1975 An experimental study of compressible boundary-layer separation at high Reynolds number. *Ph.D. Thesis*, Princeton University.
- Settles, G.S. 1993 Swept-shock/boundary-layer interactions scaling laws, flowfield structure and experimental methods. *AGARD/FDP-VKI Special Course on Shock-Wave/Boundary-Layer Interactions in Supersonic and Hypersonic Flows*, AGARD Report 792.
- Settles, G.S. and Bogdonoff, S.M. 1973 Separation of a supersonic turbulent boundary layer at moderate to high Reynolds numbers. *AIAA Paper 73-0666*.
- Settles, G.S. and Teng, H.Y. 1984 Cylindrical and conical flow regimes of three-dimensional shock/boundary-layer interactions. *AIAA J.*, Vol. 22, No. 2, pp. 194-200.
- Settles, G.S. and Dodson, L.J. 1991 Hypersonic shock/boundary-layer interaction database. *NASA CR-177577*. Available on diskette.
- Settles, G.S., Fitzpatrick, T.J. and Bogdonoff, S.M. 1978 A detailed study of attached and separated compression corner flowfields in high Reynolds number supersonic flow. *AIAA Paper 78-1167*. Also: *AIAA J.*, Vol. 17, No. 6, pp. 579-585.
- Shang, J.S. and Hankey, W.L., Jr. 1975 Numerical solution for supersonic turbulent flow over a compression ramp. *AIAA J.*, Vol. 13, No. 10, pp. 1369-1374.
- Shang, J.S. and Hankey, W.L. 1977 Numerical solution of the Navier-Stokes equations for a three-dimensional corner. *AIAA J.*, Vol. 15, No. 11, pp. 1575-1582.
- Shang, J.S., Hankey, W.L., Jr. and Law, C.H. 1976 Numerical simulation of shock-wave/turbulent boundary-layer interaction. *AIAA J.*, Vol. 14, No. 10, pp. 1451-1457.
- Shang, J.S., Hankey, W.L. and Petty, J.S. 1979 Three-dimensional supersonic interacting turbulent flow along a corner. *AIAA J.*, Vol. 17, No. 7, pp. 706-713.
- Shapey, B.L. and Bogdonoff, S.M. 1987 Three-dimensional shock-wave/turbulent boundary-layer interactions for a 20° sharp fin at Mach 3. *AIAA Paper 87-0554*.
- Simeonides, G. 1992 Hypersonic shock-wave/boundary-layer interactions over compression corners. *Ph.D. Thesis*, von Kàrmàn Institute/University of Bristol.
- Simeonides, G., Haase, W. and Manna, M. 1992 Experimental, analytical and computational methods applied to hypersonic compression ramp flows. *AGARD/FDP Symposium on Theoretical and Experimental Methods in Hypersonic Flows*, Torino, Italy, AGARD-CP-514.
- Spaid, F.W. and Frisheet, J.C. 1972 Incipient separation of a supersonic, turbulent boundary layer, including effects of heat transfer. *AIAA J.*, Vol. 10, No. 7, pp. 915-922.
- Stainback, P.C. 1960 An experimental investigation at a Mach number of 4.95 of the flow in the vicinity of a 90° interior corner aligned with the free stream velocity. *NASA TN D-184*.
- Stainback, P.C. and Weinstein, L.M. 1967 Aerodynamic heating in the vicinity of corners at hypersonic speeds. *NASA TN D-4130*.
- Stanewsky, E. 1973 Shock/boundary-layer interaction in transonic and supersonic flows. *VKI Lecture Series 59 on Transonic Flow in Turbomachinery*.
- Stewartson, K. and Williams, P.G. 1969 Self-induced separation. *Proc. Roy. Soc.*, **A(312)**, pp. 181-206.
- Stollery, J.L. 1975 Laminar and turbulent boundary-layer separation at supersonic and hypersonic speeds. *AGARD CP-169*.
- Stollery, J.L., Fomison, N.R. and Hussain, S. 1986 The effects of sweep and bluntness on glancing interactions at supersonic speeds. *Proc. 5th ICAS Symposium*, London, pp. 172-182.
- Thareja, R.R., Prabhu, R.K., Morgan, K., Peraire, J., Peiro, J. and Soltani, S. 1990 Applications of an adaptive unstructured solution algorithm to the analysis of high-speed flows. *AIAA Paper 90-0395*.
- Thomas, J.L. and Walters, R.W. 1987 Upwind relaxation algorithms for the Navier-Stokes equations. *AIAA J.*, Vol. 25, No. 4, pp. 527-534.
- Token, K.H. 1974 Heat transfer due to shock-wave/turbulent boundary-layer interactions on high speed weapon systems. *AFFDL TR-74-77*.

- Usselton, J.C. 1967 Fin-shock/boundary-layer interaction tests on a flat plate with blunted fins at $M = 3$ and 5. *AEDC TR-67-113*.
- Vandromme, D. 1993 Turbulence modeling for shock-wave/boundary-layer interactions (specific issues and examples of applications). *AGARD/FDP-VKI Special Course on Shock-Wave/Boundary-Layer Interactions in Supersonic and Hypersonic Flows*, AGARD Report 792.
- Vermeulen, J.P. and Simeonides, G. 1992 Parametric studies of shock-wave/boundary-layer interactions over 2D compression corners at Mach 6. *VKI TN 181*.
- Viegas, J.R. and Horstman, C.C. 1978 Comparison of multiequation turbulence models for several shock/boundary-layer interaction flows. *AIAA Paper 78-1165*. Also: *AIAA J.*, Vol. 17, No. 8, pp. 811-820.
- Viegas, J.R. and Coakley, T.J. 1978 Numerical investigation of turbulence models for shock-separated boundary-layer flows. *AIAA J.*, Vol. 16, No. 4, pp. 293-294.
- Vollmers, H. 1989 A concise introduction to COMADI. *DLR IB 221-89 1 22*.
- Vollmers, H., Kreplin, H.P. and Meier, H.U. 1983 Aerodynamics of vortical type flows in three dimensions. *AGARD CP-342*, Paper 14.
- Westkaemper, J.C. 1968 Turbulent boundary-layer separation ahead of cylinders. *AIAA J.*, Vol. 6, No. 7, pp. 1352-1355.
- Wilcox, D.C. 1973 Calculation of turbulent boundary-layer/shock-wave interaction. *AIAA J.*, Vol. 11, No. 11, pp. 1592-1594.
- Wilcox, D.C. 1974 Numerical study of separated turbulent flows. *AIAA Paper 74-0584*. Also: *AIAA J.*, Vol. 13, No. 5, pp. 555-556.
- Winkelmann, A.E. 1972 Experimental investigation of fin protuberances partially immersed in a turbulent boundary layer at Mach 5. *NOLTR-72-33*.
- Zhel'tovodov, A.A., Maksimov, A.I. and Shilein, E.K. 1987 Development of turbulent separated flows in the vicinity of swept shock waves. *The Interactions of Complex 3-D Flows*, edited by M. Kharitonov, USSR Academy of Sciences, Institute for Theoretical and Applied Mechanics, Novosibirsk, pp. 67-91.
- Zukoski, E.E. 1967 Turbulent boundary-layer separation in front of a forward-facing step. *AIAA J.*, Vol. 5, No. 10, pp. 1746-1753.

CHAPTER III

LAMINAR-TURBULENT TRANSITION

D.I.A. Poll

College of Aeronautics
Cranfield University
Cranfield
Bedford MK43 OAL
UNITED KINGDOM

CONTENTS

1 INTRODUCTION	69	turbulent transition to the forefront of poorly understood physical problems.
2 GENERAL CONSIDERATIONS	70	
3 STATE-OF-THE-ART ANALYSIS	71	
3.1 Attachment-Line Contamination	71	
3.2 Crossflow Instability	72	
3.3 Streamwise Instability	72	
3.4 Görtler Instability	72	
4 INFLUENCE OF FREESTREAM DISTURBANCES AND SURFACE ROUGHNESS ON TRANSITION ONSET	72	
5 GROUND-BASED TEST FACILITIES	73	
6 IMPORTANT QUESTIONS	74	
6.1 Attachment-Line Transition	74	
6.2 Crossflow Instability	74	
6.3 Tripping Away From The Leading Edge	74	
6.4 General Issues	74	
7 THE PRESENT POSITION	75	
7.1 Attachment-Line Transition	75	
7.2 Crossflow Transition	76	
8 FUTURE WORK	79	
REFERENCES	80	
FIGURES	83	

1 INTRODUCTION

It is now taken for granted that long-term future requirements for transporting cargo and people into low-earth orbit will be satisfied by the development of single-stage to orbit, or multiple-stage to orbit space planes i.e. the so-called trans-atmospheric class of vehicle. The combination of heat-transfer and propulsion requirements at low Reynolds numbers brings laminar-

turbulent transition to the forefront of poorly understood physical problems.

The Orbiter is an example of a first generation "space plane". However, although it has the external appearance of a conventional aircraft it is, in fact, more closely related to the vehicles developed for the Mercury, Gemini and Apollo space programs than those proposed in recent space-plane studies e.g. Sänger, NASP or Hotol. The Orbiter, the Russian *Buran* and the European *Hermes* are classic examples of the "boost-glide" concept conceived in the late 1950's-(Anderson 1989). In such a case, the ascent, or boost phase is accomplished by use of a conventional multi-staged rocket. This provides the vehicle with a relatively benign aerodynamic environment since, at low altitudes, the speeds achieved are low, with the rapid acceleration to those speeds necessary for orbit occurring at very high-altitude. It follows that the aerodynamic loads and the aerodynamic heating are modest. This, in turn, means that the total heat soak during ascent is low. This is a feature which is particularly important since, once in orbit, it is difficult to get rid of heat stored in the vehicle structure. For the initial stages of the descent, or glide phase, the vehicle adopts a very-high-drag configuration, i.e. an angle of attack about 40°. During descent there are two critically important points which are associated with the heating loads. The first is the maximum laminar heating condition which occurs at high altitude (≈ 70 km) and high speed (\approx Mach 20). The second is the maximum turbulent heating condition which occurs at a much lower speed (\approx Mach 10) and altitude (≈ 45 km), but at a much greater Reynolds number, and follows transition in the vehicle boundary layer. This turbulent peak can be very large and may exceed the levels experienced at the laminar peak. In this context, it is interesting to note that, in the case of the Orbiter, the two peaks are approximately equal in magnitude. In order to minimize the heating peaks the vehicle is kept in the high-drag configuration until the turbulent peak has been passed. When the heating rates have reduced to an acceptably low level, the vehicle is placed in a high lift-to-drag (low α) configuration in order to enable maneuverability, high

cross-range capability, and landings on conventional runways. For the Orbiter the "efficient" glide phase takes place at Mach numbers below 10, i.e. the high lift-to-drag configuration is limited to low altitudes and relatively low Mach numbers. One of the most important consequences of this was that the very sketchy understanding of boundary-layer transition available to the designers in the early 1970's was sufficient to limit the uncertainties associated with key parameters to be reduced to a level where a safe vehicle could be built. Nevertheless, it is important to note that much potential payload capacity was sacrificed to provide acceptable safety margins (Kipp and Masek 1986). Consequently, the Orbiter is, in all probability far from optimum, even for the boost-glide class of vehicles.

The trans-atmospheric vehicles differ from the boost-glide variety in that during the early stages of the ascent the vertical rocket boost phase is replaced by an aerodynamic lifting phase using airbreathing propulsion with rocket power being used only in the later high-altitude, high-Mach-number stages. In the case of a rocket ascent, most of the fuel is consumed at low altitude whilst the vehicle is flying through an oxygen-rich atmosphere. By using airbreathing engines at these lower altitudes and generating large amounts of aerodynamic lift, a very large improvement in efficiency can be achieved. However, there are difficulties associated with this strategy. In order to achieve the high levels of lift-to-drag, the vehicle must have a large wing operating at low angles of attack ($< 5^\circ$). Moreover, for low drag, the leading edge must be highly swept (to reduce the normal-to-leading-edge Mach number) and the leading-edge radius must be small (typically 3% of the chord or less). This combination has very important implications. In the first instance, the small leading-edge radius produces a very-large heating rate irrespective of the state of the flow. This leads to a heating problem at high supersonic and low hypersonic Mach numbers which are being achieved at relatively low altitude. The problem is compounded by the fact that an aerodynamic lifting ascent is relatively slow - typically taking 90 minutes as opposed to the 10 minutes required for the pure rocket. As a consequence of this, the total amount of heat soaking into the structure is very high compared to the rocket powered ascent -remembering that in orbit the only mechanism available for cooling is radiation. For the descent phase the problems are very similar to those encountered with the boost-glide vehicles.

Analyses performed on projected trans-atmospheric vehicles, have revealed that the heating problem on the ascent phase may be more severe than on the descent phase. Moreover, because there is prolonged flight at high-Reynolds-number, medium-range-Mach-number conditions, there is a strong possibility that turbulent flow may be established for extended periods. Indeed, at the lowest altitudes and Mach numbers (subsonic and supersonic), our expectation is that the majority of the

boundary layer flow will be fully turbulent. The question to be answered then becomes one of estimating under what conditions turbulent flow gives way to laminar flow, i.e. re-laminarization. If this happens early in the ascent there will be considerable alleviation of the heating problems. However, if the turbulent flow persists to very high altitudes, the practicality of the concept may be threatened.

As has already been noted, the existing (large) engineering database is biased heavily towards conditions and configurations appropriate to ballistic descent. The ascent configuration of a trans-atmospheric vehicle is one for which there is very little direct experimental data. Moreover, the highly three-dimensional nature of the flows over the wings and control surfaces means that there are important questions concerning the mechanisms which are available for transition. Some of these have received very little attention and, in many cases, there is insufficient information to assess their importance relative to one another (Hefner 1975). A determination of the mechanisms which are dominant at any given stage in the flight is an important prerequisite for the predictions of the aerodynamic characteristics of the vehicle.

2 GENERAL CONSIDERATIONS

The problem of transition to turbulence has now been studied formally for over 100 years. Despite this, one of the very few things upon which all research workers agree is that the issue is a complex and difficult one. At the present time, there is no general theory of transition - nor are we even close to developing one. Consequently, an important philosophical gap exists between those who perform theoretical work and those who have to produce estimates for transition to be used in engineering design. This has resulted in a dual and largely unrelated approach to the problem. As a rather general statement, the theoreticians (and the experimental scientists) have concentrated on trying to understand transition in certain types of very simple flows where the number of variables is reduced to the absolute minimum. Examples of those which have been studied are flat-plate flow, pipe and channel flow and flow over simple shapes such as cones.

Extensive work has revealed that, even though the shapes may be simple, the physics of the transition process is always complex. The consequence of this has been that all attempts to predict the details of transition - usually through stability theory (not transition theory) or, occasionally, turbulence modeling (not strictly a theoretical approach) have required a detailed and accurate description of the basic flow upon which a very large number of computations need to be performed. This approach is of little use in an industrial design process where candidate configurations may be changed repeatedly in an attempt to find a solution which satisfies a very large number of absolute constraints.

The implications of shape change must be assessed

rapidly and, particularly in the early stages, an extensive knowledge of detail and a high level of accuracy are not always needed. Consequently, the "industrial" approach has been to produce simple estimation techniques based upon correlations of data from wind-tunnel tests and, whenever possible, from flight using overall characteristics such as length Reynolds number, freestream Mach number, incidence, etc., i.e. configuration-specific correlations. A good example of this approach is contained in Kipp and Masek (1986). However, as the design tends towards its final form, the uncertainties relating to the various predictions have to be reduced to a level which guarantees the vehicle integrity with suitable margins of safety. It is at this stage that the inadequacies of correlation methods become serious and considerable effort may be spent upon the application of more advanced, semi-empirical methods.

In the context of the present work it is important to recognize that boundary-layer transition is a very complex physical phenomenon about which we know very little and that this is particularly true in the context of transition in high-speed flows. For a good summary of the position see Stetson (1990) and Reshotko (1990). Therefore, the broad approach to be followed will be

1. The generic characteristics of trans-atmospheric vehicles must be identified. This must include forebody, wing control surface and intake geometry together with the ascent and descent trajectories, i.e. speed, altitude and vehicle incidence.
2. Those mechanisms which can cause transition should be identified and a priority order assessed.
3. The current level of knowledge available for each mechanism should be determined.
4. Important gaps in the knowledge should be highlighted - particular attention being paid to situations where the absence of information prevents a proper assessment of priority.
5. To propose a two-year plan for a combined experimental and theoretical program to generate new knowledge in the areas assigned the highest priority with the specific objective of reducing uncertainty.
6. Make recommendations for future work.

3 STATE-OF-THE-ART ANALYSIS

A slender, delta wing which is intended to operate at a high, lift-to-drag ratio will have highly swept, slightly blunt leading edges and will operate at relatively small angles of attack. Consequently, there are a number of mechanisms which may cause transition to turbulence depending upon a wide variety of surface and freestream conditions. Starting at the leading edge and working towards the trailing edge the mechanisms are given in the following sections.

3.1 Attachment-Line Contamination

The attachment line divides the air which flows over the upper surface of the wing from that which flows over the lower surface as shown in Figure 1. If the wing is unswept, the attachment line is the locus of the two-dimensional stagnation points. However, when the wing is swept, there is a spanwise velocity component along the attachment line and this supports a viscous boundary layer which may be either laminar, transitional or turbulent depending upon conditions.

This flow has been studied extensively for low Mach number, incompressible conditions (Poll 1979). It is well known that, above a set of certain critical conditions, the flow becomes very sensitive to surface roughness and transition can begin at Reynolds numbers much smaller than those indicated by stability theory. The process by which the transition in the attachment line "by-passes" linear instability is generally referred to as "contamination".

In the past there have been attempts to extend the criterion for attachment-line contamination in incompressible flow to more general situations involving compressibility and surface heat transfer (Poll 1983). This extension has been achieved with some degree of success, although the range of freestream Mach numbers for which data have been available has, until recently, been limited to Mach 8. The extended criterion has been used to provide an accurate assessment of the transition "flashing" process which occurs on the windward face of the Orbiter during re-entry (Poll 1986). The success of the contamination model in describing the movement of transition on the Orbiter and providing good quantitative estimates of the condition under which transition occurs, has demonstrated its relevance to the flight situation for vehicles with rough surfaces.

Contamination on wing leading edges can come from a variety of sources.

Surface Roughness. Roughness could be an isolated element e.g. a tile edge, or it could be distributed e.g. rough surface texture for the Thermal Protection System (TPS). It is also known that holes in the surface can trip the flow.

Junction Flows. When the wing meets a fuselage there is a complex wing/body junction flow. Under the appropriate conditions turbulence in the junction can contaminate the wing attachment line. In effect the fuselage acts like a very large trip (Alizary de Roquefort 1987). Recognition of this is of major importance since contamination will occur even though both the fuselage and the wing are individually perfectly aerodynamically smooth.

Shock Interactions. Under hypersonic (and high supersonic) conditions there exists the possibility that there may be interactions between the various shock

waves established in the flow. For example, the bow shock may impinge upon the shock wave established at the wing leading edge. Depending upon conditions a transmitted shock wave may strike the boundary layer and could cause transition. Alternatively, a free shear layer may be established which crosses the shock layer and becomes entrained into the leading edge, boundary layer as was the case in Bushnell (1965). If the Reynolds number associated with the shear layer is high enough it may be transitional, or even turbulent, before it enters the wing boundary layer. This being the case, contamination of the attachment line could occur.

Even if no gross contamination source is available, the attachment-line flow can still undergo transition through the process of instability and the amplification of low-level background disturbances such as freestream turbulence, noise and surface vibration. However, if gross contamination does not occur, there is a window of Reynolds-number, Mach-number, and surface-temperature conditions which will allow laminar flow to be established at the leading edge. This being the case then, other mechanisms must be considered as possible harbingers of transition.

3.2 Crossflow Instability

When a wing is swept the streamlines at the edge of the viscous layer in the immediate vicinity of the attachment line are highly curved in planes drawn parallel to the surface as shown in Figure 1. Consequently, as the flow moves away from the attachment line in the streamwise direction, the normal-to-external streamline pressure gradients produce a crossflow within the viscous layer as shown in Figure 2. The crossflow velocity profiles contain at least one point of inflection and, consequently, by Rayleigh's theorem, they are unstable to a range of disturbances at infinite Reynolds number. However, in practice, the existence of Rayleigh instability usually means that the flow will become unstable at very low Reynolds numbers. It is this mechanism which can lead to transition on an aerodynamically smooth surface at very low Reynolds numbers and very close to the leading edge of the wing (Poll 1989). As in the case of attachment line, our understanding of transition via crossflow instability comes primarily from experiments performed in incompressible flow e.g. Poll (1985). However, there is a limited amount of good quality, semi-quantitative evidence which shows that crossflow instability is a route to turbulence in supersonic and hypersonic flow (Jillie and Hopkins 1961; Pate and Groth 1966).

For a configuration typical of an efficient hypersonic wing there are several ways in which large crossflow can be developed.

Combined Sweep and Bluntness. When the leading edge is blunt the pressure distribution varies from a maximum at the attachment line to a minimum where the curved leading edge meets the flat wing surface. Thereafter, the

pressure rises to a second local maximum beyond which it falls asymptotically to some near constant value as shown in Figure 3. The combination of this pressure field and the leading edge sweep produces a situation in which the characteristic boundary-layer, crossflow Reynolds number, χ , exhibits a double peak- see Figure 4. One maximum corresponds to the pressure minimum at the leading edge whilst the second is approached asymptotically and corresponds to the pressure drop over the flat surface. It is immediately apparent that, depending upon conditions, the crossflow Reynolds number may have the same value at up to three streamwise locations. Consequently, any transition criterion based upon a single value of the crossflow Reynolds number is likely to be of limited value.

Viscous-Inviscid Interaction. On the assumption that the wing incidences are small and the leading edge radius is small, it has been recognized that crossflow can be generated by the combination of sweep and the induced pressure distribution. This mechanism exists (and is at its largest) when the angle of attack is zero and the wing leading edge is sharp. Experimental evidence of the effect is provided in East and Baxter (1990).

Although the above description may appear to be rather complex, there is the possibility that the problem may be simplified by proper use of the appropriate hypersonic similarity parameters. If the essential parameters can be identified then data obtained from a series of carefully selected configurations could be used to gain an overall quantitative picture of the process. These experiments would have to include smooth and rough surfaces.

3.3 Streamwise Instability

If the flow coming out of the leading edge region has not been forced to the turbulent state by either attachment-line contamination or crossflow instability, then as the boundary layer develops the Reynolds numbers in the streamwise direction will continue to grow until typical "two-dimensional" flow instabilities appear. At present these, essentially two-dimensional, flows with some streamwise convergence or divergence are not well understood and very little hard experimental information is available. However, provided the mean flow can be computed accurately, it is likely that linear stability theory can be used to assess trends and produce approximate transition locations.

3.4 Görtler Instability

Görtler instability is associated with flow situations which involve concave curvature in the streamwise direction (Saric 1994). The basis for the instability is centrifugal imbalance within the viscous layer. Once again the majority of knowledge and understanding is confined to low-speed flow. However, it is known that the mechanism plays a role in transition under hypersonic conditions particularly over deflected control

surfaces-see de Luca, et al. (1993). Under high-speed conditions very small amounts of streamline curvature can induce large wall-normal pressure gradients.

4 INFLUENCE OF FREESTREAM DISTURBANCES AND SURFACE ROUGHNESS ON TRANSITION ONSET

All the transition mechanisms outlined above are directly influenced by the nature of the disturbances in the freestream - the so-called freestream environment and the detailed condition of the surface. In general, it is now accepted that these effects couple strongly with surface roughness providing one (important) receptivity mechanism by which freestream disturbances become initialized into the boundary layer. The location of the transition position is determined by the amplitude of the input disturbances and these depend directly upon a combination of the amplitude and spectral distribution of disturbances found in the freestream and the size distribution and character of the surface roughness.

Inevitably, there are extreme conditions which may be particularly relevant when one considers, for example, the role of wind-tunnel testing in transition research or when the worst case scenario is being considered for vehicle thermal protection system design. The latter condition is clearly of great importance since the specification of the TPS is one of the most difficult decisions which has to be taken.

In this context, it is important to recognize that on two very-well-documented occasions, state-of-the-art transition predictions have failed the designer. The first occurred in the late 1950's when the US was designing nose cones for ballistic missiles. One particular design involved the use of a blunt copper-heat-sink system which was required to have laminar flow throughout the trajectory. All the indications of stability theory suggested that the combination of the cold wall and favorable pressure gradient would produce highly-stable laminar flow - a result which was not contradicted by the rather limited flight data available at the time. However, the design failed spectacularly in flight (vehicle completely destroyed!) and subsequent shock-tube tests confirmed that, despite the logical expectation of laminar flow, the boundary layer was turbulent and the resulting heat transfer rates were approximately ten times the level assumed in the design calculations. It is perhaps even more worrying that this "blunt-body paradox" is still unexplained despite the large improvement of our understanding of the transition process which has taken place over the last 20 years.

The second case involves the Orbiter. Thermal protection for most of the windward surface of the Shuttle is provided by the small silica tiles. As originally envisaged, the requirement was for a "smooth" TPS surface, with the maximum permissible step size being maintained below the level corresponding to a critical trip - as given by the Van Driest and Blumer (1968)

criterion. However, during construction of the first Orbiter (Enterprise) it was found that the technique being used to attach the tiles to the structure was such that this particular requirement could not be achieved. Therefore, in the final stages of assembly, it was discovered that a critical assumption in the design process was invalid (Goodrich and Derry 1973). The result was that an additional series of wind-tunnel tests had to be performed to assess the performance of the TPS in the presence of gross isolated roughness (Bertin and Idar 1978). Overall, the problem resulted in both delay and cost increases to the project. There was also considerable concern amongst the aerodynamic community that the vehicle integrity might be marginal with roughness-dominated transition. In the end, the Orbiter flew successfully, although it was clearly demonstrated that transition was indeed fixed by a series of identifiable, large-scale, surface excrescences and that attachment-line contamination was the most likely cause of early (high-altitude) transition (Poll 1986).

These two experiences have demonstrated that, despite the very large amount of theoretical and experimental work which has been conducted on smooth-surface transition, designers will always need to be aware of the worst-case scenario. This is undoubtedly associated with roughness and it is somewhat ironic that this aspect of transition research has received very little attention in the past. The inescapable conclusion is that, when the objective is data for vehicle design, transition research should always include the effects of roughness.

5 USE OF GROUND-BASED TEST FACILITIES

It is well known that conventional supersonic and hypersonic wind tunnels generate a freestream, disturbance environment which is very different from that experienced in flight. There are two reasons for this. The first is that the disturbance levels within the test jet may be poor because of processing in the wind-tunnel valves, corners diffusers etc. Secondly there are boundary layers formed on the nozzle and test section walls and these are invariably turbulent.

A turbulent boundary layer is characterized by the existence of large-scale, unsteady, "eddy" motion in the outer region. When the edge velocity is supersonic, the eddies generate Mach waves (sound waves) which propagate through the freestream and reflect from other solid surfaces. The result is that the test section is filled with an intense acoustic field. When a model is being tested, any laminar boundary layers formed on surfaces with small intrinsic roughness are subjected to this acoustic field and transition may then be determined by the acoustic forcing. However, in the flight case, there are no walls surrounding the vehicle and therefore, the disturbance field must come from other sources. The different character of the two forcing fields must produce different transition behavior and, consequently, the validity of assessing the flight transition location from

data obtained in a conventional wind tunnel is, in general, highly questionable (Pate and Schueler 1969).

In order to shed some light on the problem, NASA developed the concept of the "Quiet Tunnel" and built a pilot version which operates at a Mach number of 3.5. The design objective was simply to maintain the nozzle-wall boundary layer in the laminar state long enough for there to be a portion of the test rhombus within which there would be very little acoustic disturbance. Experience with this tunnel has revealed the following.

1. For cones at zero incidence and two-dimensional flat plates, transition Reynolds numbers on an adiabatic surface at a Mach number of 3.5 increase by almost a factor of 10 when the turbulent nozzle acoustic field is removed - Beckwith et al. (1990).
2. The conditions necessary for a large isolated excrescence to produce immediate transition to turbulence (fully effective trip) are independent of the level of freestream acoustic disturbance (Morrisette and Creel 1987).
3. When the configuration is smooth and essentially three-dimensional e.g. a cone at incidence, the influence of the acoustic disturbance field upon transition Reynolds numbers is very much smaller than in the two-dimensional case and the influence appears to decrease as the degree of three-dimensionality increases (King 1992).

These results, in turn, suggest that when testing in a conventional wind tunnel the following caveats should be noted.

1. Transition Reynolds number may be conservative relative to flight and, as such, may be useful for design (but no use for investigating the physics of transition in the flight case).
2. Testing to determine the effect of large roughness should be accurate for the case where transition occurs at the roughness location. Hence, roughness dominated transition is correctly represented since freestream, acoustic disturbances play little, or no, role in the transition process.
3. When transition results from mechanisms which are essentially three-dimensional the conventional tunnel gives reasonable results. This may be because the coupling between the boundary layer and the acoustic field is reduced when the flow is three-dimensional, i.e. disturbances are locked out. Alternatively, the primary instability mechanisms may be inviscid in nature. In this case the amplification rates are so large that the location of transition onset is hardly affected by the level of forcing.

This being the case, it may well be that accurate transition data for use in the design of space plane configurations can be obtained in conventional wind tunnels.

6 IMPORTANT QUESTIONS

In view of the foregoing, the following questions need to be asked.

6.1 Attachment-Line Transition

1. Where is the gross-contamination transition boundary i.e. the combination of \bar{R} , M_e , and T_w/T_0 for which turbulent flow occurs in the presence of a large source of disturbance?
2. Where is the smooth-surface transition boundary in terms of the same parameters?
3. What are the criteria for critical and effective roughness heights?
4. To what extent are the above consistent with stability theory?
5. What are the likely differences between wind-tunnel conditions and flight?
6. What are the consequences for vehicle heat transfer, drag etc. when transition occurs through attachment-line contamination?

6.2 Crossflow Instability

1. How do leading-edge bluntness, viscous-inviscid interaction and incidence affect the generation of crossflow?
2. How do the crossflow Reynolds numbers vary with sweep angle and surface temperature?
3. What conditions (crossflow Reynolds number, edge Mach number etc.) are necessary for crossflow to produce transition?
4. To what extent are the above consistent with stability theory?
5. What are the effects of surface roughness and freestream turbulence on crossflow induced transition?
6. What are the differences between results obtained in ground-based facilities and flight?
7. What are the consequences for vehicle heat transfer drag, etc. when transition occurs through crossflow instability?

6.3 Tripping Away From The Leading Edge

1. What are the conditions necessary for an isolated roughness element to produce immediate transition (fully effective trip) on a delta wing?
2. How do the wedges of turbulence spread relative to the surface streamlines?
3. What are the consequences for vehicle heat transfer, drag, etc. when transition occurs through fully-effective roughness?

6.4 General Issues

In addition to the above questions, the following general issues are also relevant.

1. For typical ascent and descent trajectories, what are the largest Mach numbers at which transition by each mechanism is likely to occur? On the basis of this, the role of real-gas effects on both the transition process and the subsequent turbulent flow can be assessed.
2. In the case of cones at zero incidence and two-dimensional flat-plate flows, it is well known that the transition Reynolds numbers depend upon the freestream unit Reynolds number. This unusual phenomenon has perplexed research workers for 40 years. However, it is not at all clear that the "unit Reynolds number effect" occurs in situations where three-dimensional mechanisms and surface roughness are responsible for transition. The issue needs to be addressed.
3. In three-dimensional flow fields, situations sometimes arise in which shock waves impinge upon a surface, impinge upon each other and create a shear layer which subsequently impinges upon a surface or, in regions of over expansion, a jet can be formed which may also impinge upon a surface. All these mechanisms are associated with the shock layer and under high-Reynolds-number conditions the shock layer is effectively independent of viscosity. However, the occurrence of inviscid instability modes within the shock layer is potentially very important since the flow features exhibiting the instability may impinge upon surface viscous layers and initiate transition. In this way, the configuration may be able to trip itself to turbulence through the action of spontaneously developed, large-amplitude disturbances. These may be as effective as gross surface roughness even through all the surfaces of the vehicle are aerodynamically smooth.

7 THE PRESENT POSITION

7.1 Attachment-Line Transition

Experimental data on attachment line flows has been accumulating over the years through work on delta wings with blunt leading edges (Stainback 1961; Gunn 1961; Nagel et al. 1966; Bertram and Everhart 1963; Bertram et al. 1960; Everhart and Dunavant 1964; Stallings et al. 1964), swept cylinders (Creel et al. 1987; Bushnell 1965; Beckwith and Gallagher 1961; Beckwith 1964; Yeoh 1980; Beckwith and Gallagher 1961; Feller 1961; Creel and Beckwith 1962; Creel et al. 1988; Ellison 1962; Beckwith and Gallagher 1959; Goodwin et al. 1956; Skuratov and Fedorov 1990; Da Costa 1990) and swept fins with blunt leading edges (O'Neal 1962; Hunt,

et al. 1971; Bushnell and Jones 1965; Bushnell and Huffman 1967; Fleming and Krauss 1966; Jones 1964; O'Neal and Bond 1962; Price et al. 1964; Howard 1964; and Amirkabirian and Bertin 1987). Despite the fact that very few of these investigations involved the direct study of transition, there is enough information available to make some preliminary assessment of the situation.

When the attachment-line flow develops from the intersection between a blunt leading edge and a streamwise end plate - as shown in Figure 3, Bushnell and Huffman (Bushnell and Huffman 1967) observed that the boundary layer flow on the leading edge was turbulent if

$$\begin{aligned} 2 < M_\infty < 8 \\ \Lambda > 40^\circ \\ R_{\delta\infty} \geq 2 \times 10^5 \end{aligned} \quad (1)$$

This was the first attempt to quantify the attachment-line contamination boundary. However, whilst it is surprisingly effective as a "rule of thumb", it is not suitable for general applications since it is based upon freestream parameters. A more useful criterion has been proposed by Poll (Poll 1983) which is based upon the local attachment-line parameters.

$$\bar{R} = \left(\frac{V_e^2}{v_e dU_e/dx} \right)_{x=0}^{1/2}, M_e, \text{ and } \frac{T_w}{T_0}$$

By examining those experiments in which attachment-line transition was observed it was found that, with a streamwise end plate in place, the transition to turbulence took place when

$$\bar{R}_* = \left(\frac{V_e^2}{v_* dU_e/dx} \right)_{x=0}^{1/2} = 245 \quad (2)$$

where

$$\frac{T_*}{T_e} = 1 + 0.10 \left(\frac{T_w}{T_e} - 1 \right) + 0.60 \left(\frac{T_r}{T_e} - 1 \right) \quad (3)$$

From the data available at the time, it appeared that this "attachment-line contamination" criterion was valid for flows with heat transfer ($T_w/T_0 = 0.2 - 1.0$) and edge Mach numbers, M_e , in the range 0 to 6. All the more recent experiments (Skuratov and Fedorov 1991; Da Costa 1990) support the \bar{R}_* criterion. However, it is clear that there is some room for improvement via a more accurate representation of the reference temperature, T_* . In order to establish a more reliable criterion there is a need for additional tests with edge Mach numbers in excess of 3 and covering a range of wall to total temperature ratios.

The use of an end plate (fuselage side) represents an extreme form of attachment-line disturbance. As demonstrated in Poll (1979), as large trips are replaced

by progressively smaller ones a stage is eventually reached when the value of \bar{R} at transition onset will be greater than 245. This is called the "fully effective" trip size. For incompressible flows the fully effective roughness size for two-dimensional trip wires is

$$\frac{d}{\eta} = 2.0$$

where

$$\eta = \left(\frac{v_e}{dU_e/dx} \right)_{x=0}^{1/2} \quad (4)$$

Although there appears to be no logical agreement to support the proposition, data presented in Creel et al. (1987), Skuratov and Fedorov (1991), and Da Costa (1990) suggest that for compressible flows with heat transfer the critical roughness height is given (approximately) by

$$\frac{d}{\eta_*} \approx 1.5 \rightarrow 3.0 \quad (5)$$

where η_* uses (4) evaluated at T_* given in (3).

For trip sizes below the fully-effective height, the Reynolds number for transition rises rapidly until the trip is reduced to the "critical" size below which the Reynolds number for transition is constant. The available data indicate that the critical size is given by

$$\frac{d}{\eta_*} \approx 0.8 \rightarrow 1.2$$

The value of \bar{R} at which transition occurs for trip sizes below the critical level is not known. Moreover there is currently a degree of contradiction in the evidence. Bushnell and Huffman (1967), observed that, in the absence of any deliberate tripping by surface roughness, laminar flow was observed up to at least

$$\begin{aligned} 2 < M_\infty < 8 \\ \Lambda_\infty > 40^\circ \\ R_{des} \approx 8 \times 10^5 \end{aligned} \quad (6)$$

It should be emphasized that this is not a criterion for transition but merely an achievable limit. Using Poll's approach to the problem, the corresponding local criterion is

$$\bar{R}_* \approx 650$$

Given this situation it is very interesting to note that, in the NASA Langley Quiet Tunnel, the "natural transition" on a swept cylinder occurred at an \bar{R}_* of 700 and the result was virtually dependent of freestream acoustic disturbances. It is not yet clear whether this is a typical result or just coincidence. Moreover, when attempts have

been made to predict the "natural" transition condition using linear compressible stability theory and the e^N method (Malik and Beckwith 1988) - the predicted transition Reynolds numbers have been much higher than those observed in experiments. This discrepancy is still unresolved and represents a major challenge to both theoreticians and experimentalists. The current level of empirical understanding of attachment-line transition is given in Figure 5 which is taken from Arnal et al. (1989).

All the experimental data published to date have been obtained in cold wind tunnels where the test flows obey the perfect-gas law. However in a recent paper Poll (1993) has considered the implications of real-gas effects for leading edges on vehicles experiencing a very wide range of speeds and altitudes. It was noted that, by assuming transition via attachment-line contamination to be given by Equation 2, real-gas effects would cause transition to occur at a higher altitude (lower Reynolds number) than would be expected if the gas was perfect. The clear implication is that real-gas effects will need to be quantified experimentally by using one or more of the high-enthalpy facilities which are now available. As a rough guide, under hypervelocity conditions, Equation 2 can be expressed approximately as

$$\begin{aligned} \Lambda &> 50^\circ \\ \rho_\infty D &\approx 0.0005 \text{ kg/m}^2 \end{aligned}$$

where D is the leading-edge diameter.

7.2 Crossflow Transition

As has already been noted, a general three-dimensional boundary-layer flow is characterized by curvature of the streamlines in planes drawn parallel to the surface. Referring to Figure 1, it is clear that, for x greater than zero, the streamlines at the edge of the boundary layer are highly curved. If the velocity variation within the viscous layer is resolved in the direction parallel to the external streamline, the resulting profile is similar to the conventional two-dimensional form as seen in Figure 2.

However, unlike the two-dimensional situation, there is also a profile obtained when the solution is carried out in a direction normal to the external streamline. This "crossflow" profile exists since, in accordance with the boundary-layer approximations, the static pressure is invariant with the wall-normal coordinate, z . Consequently, whereas at the edge of the layer the pressure gradient and the centrifugal acceleration are in balance, as the wall is approached the pressure gradient remains the same but the velocity is reduced. In order to maintain the local force balance, the curvature of the streamlines must change and this leads to the appearance of the crossflow component of velocity.

All crossflow velocity profiles have zero velocity at the wall and zero velocity at the viscous layer edge. Within the layer, the profiles may take a variety of shapes

depending upon the variation of the surface pressure as seen in Figure 6. However, in the vicinity of a swept leading-edge the crossflow profile has the "C" form with a single maximum as indicated in Figure 2.

In general, it is rather difficult to formulate a characteristic Reynolds number and over the years authors have suggested a variety of forms, none of which is entirely satisfactory. If the maximum value of the crossflow velocity is denoted by C_{max} , then the crossflow Reynolds number χ may be defined as (Poll 1984).

$$\chi_1 = \frac{C_{max} \delta_{0.1C_{max}}}{\nu_e} \quad (7)$$

or

$$\chi_2 = \frac{C_{max} \delta_{0.01C_{max}}}{\nu_e} \quad (8)$$

where $\delta_{0.1C_{max}}$ and $\delta_{0.01C_{max}}$ are the largest values of the wall-normal coordinate where the crossflow velocity equals 10% C_{max} and 1% C_{max} , respectively.

Alternatively, an integral form may be used e.g.

$$\chi = \frac{\rho_e C_{max}}{\mu_e} \int_0^{\infty} \frac{\rho c}{\rho_e C_{max}} dz$$

or

$$\chi = \frac{1}{\mu_e} \int_0^{\infty} \rho c dz \quad (9)$$

This latter form can be described as a Reynolds number based upon the crossflow "displacement" thickness. However, it should be noted that, in this context the "displacement" is not related to the actual displacement of the inviscid flow, nor does the definition uniquely characterize the velocity profile. Nevertheless, this integral definition will be used in the present work.

It is clear from the above that for a swept-back wing, crossflow profiles will develop wherever there is a pressure gradient. Therefore, referring to Figure 3, a strong crossflow will be generated initially in region (a). This will be moderated in region (b) and, finally, reinforced in region (c). It follows that crossflow instability is likely to be important in regions (a) and (c).

For incompressible flow on the windward face of a swept cylinder, transition due to crossflow instability takes place when χ is of order 100. However, as shown in Poll (1985), a single value of χ is insufficient to adequately describe the conditions necessary for transition. In fact, for transition very close to the leading edge of an infinite swept wing in incompressible flow two independent parameters are needed. Figure 7

shows that, in this case, χ_2 and the streamwise flow shape factor H_{11} are a suitable combination.

In the general area of compressible flow with heat transfer, an extensive literature search has revealed that only a small number of experimental investigations have been carried out into the problem of transition via crossflow instability when the freestream Mach number is supersonic. Most significantly, no example has been found in which crossflow induced transition has occurred on the windward face of a swept circular cylinder. Although in several cases, (Creel et al 1987), there is clear evidence of the presence of streamwise vortices in the laminar layer. These vortices are characteristic of crossflow instability.

However, Stainback (1961) presents heat transfer data taken on a slab delta wing with cylindrically blunted leading edges. The leading edge is swept at 60°, the freestream Mach number is 4.95, and the wall-to-total temperature ratio is 0.60. Figure 8 shows results for Stainback's plain delta model at zero angle of attack. It is apparent that the attachment line is laminar as is the entire cylindrical portion of the leading edge. However, at the highest freestream unit Reynolds number ($3.73 \times 10^6 \text{ m}^{-1}$), transition occurred on the flat part of the wing very close to the shoulder.

Under these conditions, the value of \bar{R}_e on the attachment-line is 530 and, since the delta wing has a smooth surface with no obvious source of attachment-line contamination, the observation of laminar flow is consistent with our current expectations (see the previous section).

Figure 9 shows the development of the crossflow Reynolds number χ given in Equation 9 as a function of the surface distance measured from the attachment line. The variation exhibits all the characteristic features for flow close to a swept leading edge. At the attachment line ($x = 0$), χ is zero. Over the cylindrical leading edge, χ increases very rapidly reaching a maximum at the "shoulder" ($x = 1.571R$). Beyond the shoulder there is a modest reduction of χ leading to a local minimum when x/R is approximately 4.5. Thereafter, as the local surface pressure reduces with increasing distance from the leading edge, χ increases slowly, but monotonically. The point of transition onset is marked on the Figure showing that, in this case, transition is occurring when χ is 400. However, it is immediately apparent that there are problems. First, the variation of χ with x is multivalued. There are three values of x at which χ is equal to 400! Moreover, the value of 400 for transition onset is three times the value for transition onset in incompressible flow. Further increases in freestream Reynolds number could well produce transition on the attachment line since \bar{R}_e is close to 600 i.e. it may be impossible to bring transition onto the cylindrical leading edge through the mechanism of crossflow instability.

A second important experimental study of transition on swept wings is that conducted by Jillie and Hopkins (1961). In this case, a flat plate with varying degrees of small, leading-edge blunting was tested at different sweep angles for freestream Mach numbers ranging from 2.5 to 4.0. A typical configuration is shown in Figure 10 which illustrates the type of results obtained with their surface sublimation technique (naphthalene and petroleum ether). The transition front is clearly indicated as is the streak pattern in the laminar region, which is characteristic of the presence of crossflow instability. When the plate leading edge was swept, the streamwise Reynolds number for transition was reduced relative to the unswept value and a typical example of the behavior is given in Figure 11. As sweep angle was increased the transition Reynolds number ratio decreased monotonically. Moreover, as is also clear from the Figure, increasing the leading-edge bluntness also reduced the transition-Reynolds-number ratio.

There is an important difference between the Jillie and Hopkins (1961) experiment and that of Stainback (1961). In the latter case, transition occurred very close to the leading edge whilst in the former, transition is occurring some distance back along the chord e.g. in Figure 10, transition is at $x/d = 16$. The consequence of transition being a large distance from the leading edge is that the pressure field is of the "blast wave" type and entropy swallowing may become an issue. If it is assumed that the flow at the edge of the boundary layer has been processed by the plane part of the leading-edge bow shock, then, as the sweep is increased at fixed freestream conditions, the local value of the Reynolds number is increased. Provided the local value of the Reynolds number at transition remained constant, the effect of sweep would be to move the transition front forward. The dashed line drawn on Figure 11 indicates how the freestream streamwise transition Reynolds number would vary in response to sweep changes if the local streamwise transition Reynolds number was constant. It is clear that, whilst the general shape of the curves is rather similar to the dashed line, the results do not support the concept of a fixed transition Reynolds number. This means that the sweep must be modifying the value of the local transition Reynolds number i.e. this is evidence of the existence of crossflow instability. It is also clear that increasing the leading-edge bluntness reduces the transition Reynolds number and it is conjectured that this is due to the consequential change in the pressure distribution.

A sample computation of the crossflow Reynolds number, χ , has been carried out for the case in which the leading edge radius was 0.5 mm ($R_d = 0.5 \times 10^{-5}$). The distribution of χ is given in Figure 12 for a range of sweep angles. The calculations show that the crossflow Reynolds number reaches a maximum at sweep angles between 60° and 70°. This corresponds to the conditions that give the minimum values of the transition Reynolds

number. Moreover, the experimentally observed transition locations for 60° and 68° of sweep correspond to a constant value of χ . The critical value of χ is approximately 140. This value is very different from that found in Stainback experiment but it is typical of the values found in incompressible flow.

The work of Jillie and Hopkins (1961) has been complemented by a similar study performed by Pate and Groth (1966). In this case a swept, slightly blunt plate was tested over a range of freestream unit Reynolds numbers. The results for a single value of leading edge bluntness ($t \approx 0.15$ mm) are given in Figure 13. These show that increasing the sweep reduces the freestream transition Reynolds number substantially. Moreover there is a variation with the freestream unit Reynolds number. However the data clearly show that, as sweep angle is increased, the influence of unit Reynolds number is substantially reduced. This is demonstrated in Figure 14 where a coefficient N has been determined from the relation

$$R_{tr} = A(\text{Unit } R_e)^N$$

N is found to decrease in proportion to $\cos^2 \Lambda$. The reduced dependence of transition Reynolds number upon freestream Reynolds number has also been observed by King (1992) who studied transition on a circular cone at incidence in the Mach 3.5 Quiet Tunnel at NASA Langley. It is tempting to conclude from this that useful work on transition for three-dimensional shapes may be performed in conventional wind tunnels. In order to reinforce this point, it is possible to compare the data of Jillie and Hopkins (1961) and Pate and Groth (1966) for a freestream Mach number of 3, with similar leading-edge bluntness, but with a factor of three difference in the freestream unit Reynolds numbers. These results are presented in Figure 15, where it can be seen that the agreement is quite good.

Of particular interest is the way in which the role of leading-edge bluntness changes with sweep angle. At the lower sweep angles, increasing the leading-edge bluntness increases the freestream transition Reynolds number i.e. at a fixed freestream unit Reynolds number the transition location moves back along the chord. However, at a sweep angle of about 25°, this effect is reversed i.e. increasing the bluntness causes transition to move forward. The clear implication is that sweep angle variations are producing a fundamental change in the underlying instability mechanism which is causing the transition. Finally Figure 16 shows good agreement between the two data sets when the ratio of the swept to unswept transition Reynolds numbers is plotted against sweep angle. Once again there is no indication of a strong unit Reynolds number effect.

When the performance of space-plane configurations is being considered, it is important to recognize that the flight Mach numbers may become very large. Under

high-Mach-number conditions there is an interaction between the viscous, near-surface flow and the inviscid outer flow. The consequence of this is that even for a sharp-edged flat plate at zero angle of attack, a shock wave will be formed at the leading edge and a surface pressure field will be established (see Figure 17). If the plate is yawed, the strength of the leading-edge shock wave will be reduced and a crossflow will be established in the viscous layer. This may affect the location of transition. Strong evidence that the swept interaction can cause major changes to the location of transition is provided by East and Baxter (1990). Using the thermochromic liquid-crystal technique, they were able to show that the effect of sweeping the wing was to bring boundary-layer transition forward to a position close to, and parallel to, the leading edge as shown in Figure 18. By quantitative analysis of the color changes in the crystals, East and Baxter were also able to demonstrate that, when transition takes place, the local heating rate rises very rapidly as indicated in Figure 19. This demonstrates the importance of understanding transition when designing a vehicle which will travel at hypersonic speed.

The parameter which characterizes the flow modifications due to the interaction is Ω_N where

$$\Omega_N = \cos^{1/2} \Lambda M_\infty^3 \left[\frac{\mu_\infty}{a_\infty \rho_\infty x} \right]^{1/2}$$

In the interacting flow, a pressure distribution is established and, when the leading edge is swept, a crossflow develops in the viscous layer. For an infinite-swept, leading edge, the crossflow Reynolds number χ is such that

$$\chi = \chi(\Lambda, M_\infty, \Omega_N, T_w/T_0)$$

By way of an illustrative example, the development of χ has been computed for flow with a Mach number of 9 over a plate with a range of leading edge sweep back angles. The resulting variation of χ with chordwise position, x , is shown in Figure 20. There are a number of features which should be noted. Initially, χ rises rapidly with x . However, as x increases the rate of rise reduces. At large values of x , χ has an asymptotic value i.e. once the crossflow Reynolds number has been established it remains in the flow. The crossflow Reynolds number has a maximum value when the sweep angle is approximately 50° .

An initial analysis of this problem has been carried out by Poll (1993). This has revealed that the maximum value of χ occurs close to the leading edge (as in Figure 20) and that

$$\chi_{max} \propto (\sin \Lambda \cos \Lambda) M_\infty^3$$

where the constant of proportionality is a weak function

of sweep, Mach number, and wall-to-total temperature ratio. This result indicates that the maximum crossflow Reynolds number occurs at 45° which is in agreement with the more complete calculations. However, more remarkable is the fact that the magnitude of χ depends upon M_∞^3 and not upon the value of the freestream unit Reynolds number! To test these features, additional calculations have been carried out and the results are given in Figure 21. It is clear that the peak χ occurs at between 45° and 50° , the peak value is independent of freestream unit Reynolds number and the peak value is approximately proportional to M_∞^3 as predicted by the simple theory. However, the magnitudes of χ are smaller than those which are normally associated with transition due to crossflow instability. Nevertheless, as the flight Mach number increases towards the levels necessary for orbital insertion, very large crossflow Reynolds numbers may be generated. This could constitute a transition mechanism which can operate at very high altitudes.

Over the years, there have been a number of attempts to correlate the experimentally observed transition fronts in terms of particular values of the crossflow Reynolds number χ . The earliest attempt was by Owen and Randall (1952) who concluded, on the basis of a single low-speed experiment, that transition occurred at the chordwise location at which χ reached its maximum value when the maximum value of χ was approximately 150.

An attempt to extend the criterion to include the effects of compressibility and heat transfer was made by Chapman (1961). However, before 1960, most workers (and certainly Owen and Randall and Chapman) did not appreciate the overriding importance of attachment-line transition. Consequently, much of the data used to calibrate the " $\chi = \text{constant}$ " methods were, in fact, the results of attachment-line contamination. Unfortunately, in the case of the Chapman paper all the transition data were the result of attachment-line contamination and, therefore, the Chapman crossflow induced transition criterion is completely erroneous. The inadequacy of the simple criterion has been clearly demonstrated by King (1992) who found that no single value of χ could correlate the transition data taken on a cone at incidence. However, he was able to concoct a criterion which involved the geometric properties of the cone. This approach has the disadvantage that, by virtue of its formulation, the criterion can only be used for cones similar to the one tested by King. This latter point has been addressed recently by Reed and Haynes (1994) who have attempted to produce criterion which is applicable to a variety of body geometries and a wide range of flow conditions that include body spin. By considering predictions (linear stability theory and e^N correlations) for a spinning cone at zero angle of attack and experimental transition data for two cones at incidence in supersonic flow, they have produced a correlation based upon a "transformed" crossflow-velocity Reynolds number and the ratio of maximum crossflow to boundary-

layer edge velocity. Their results show substantial improvement over previous attempts but comparisons have yet to be made with all the available transition data. Therefore the general validity of the method is still to be demonstrated.

8 FUTURE WORK

In 1991, the transition sub-group of WG-18 outlined a series of experiments that would answer some of the important questions that have been raised earlier in this report. By limiting the experiments to yawed cones and cylinders, it is possible to test these configurations in a variety of facilities and freestream disturbances with some overlap of Mach number and Reynolds number. The proposed test matrix follows.

Transition Test Matrix

	Swept Cylinder Mach	Sharp Cone Mach	Comments
USA:			
NASA-LaRC	3.5	3.5, 6	Quiet
Calspan	11, 13		moderate noise
Caltech	8		Hypulse (real gas)
GERMANY:			
DLR	3.6	3.6	Conventional
DLR	6, 7, 11	6, 7, 11	Ludwig Tube
FRANCE:			
ONERA	3, 7, 10	3, 7, 10	Noisy
UK:			
Imperial	9	9	Gun Tunnel
Cranfield	9	9	Gun Tunnel
AUSTRALIA:			
Brisbane	8		Real Gas

In each case, the models are to be tested yawed and un-yawed, smooth and rough. The objectives are:

1. Provide documentation of freestream environment
2. Provide documentation of basic state
3. Provide quantitative information on surface roughness
4. Quantify the role of (1) - (3) on transition location in different facilities

The experimental work will be buttressed by computational work to take place at NASA-LaRC, Arizona State University, Cranfield University, DLR-Göttingen, and CERT-ONERA.

A true hypersonic experiment is planned by NASA-LaRC (Bertlerud and Graves 1995) on a wing of the Pegasus launch vehicle during the ascent phase. The details of this work and that of the test matrix will be available at the conclusion of the WG-18 activities.

REFERENCES

- Alziary de Roquefort, T. 1987 Leading Edge Transition in Hypersonic Flows. *First Joint Europe - US Short Course on Hypersonics*, ESA Paris.
- Amirkabirian, I. and Bertin, J.J. 1987 Aerothermodynamic Environment About a Highly Swept Wing Leading Edge. *J. Spacecraft*, Vol. 24, No. 3.
- Anderson, J.D. 1989 *Hypersonic and High Temperature Gas Dynamics*, McGraw-Hill.
- Arnal, D., Juillen, J.C., Jallade, S. 1989 Recherches Sur la Transition aux Vitesses Élevées. *Rapport 27/5005. 15 DY. DERAT, CERT-ONERA*.
- Beckwith, I.E. 1964 Experimental Investigation of Heat Transfer and Pressures on a Swept Cylinder in the Vicinity of its Intersection With a Wedge and Flat Plate at Mach Number 4.15 and High Reynolds numbers. *NASA-TN-D-2020*.
- Beckwith, I.E. and Gallagher, J.J. 1959 Local Heat Transfer and Recovery Temperatures on a Yawed Cylinder at a Mach Number of 4.15 and High Reynolds Numbers. *NASA TM 2-27-59L*.
- Beckwith, I.E. and Gallagher, J.J. 1961 Local Heat Transfer and Recovery Temperatures on a Yawed Cylinder at a Mach Number of 4.15 and High Reynolds Numbers. *NASA-TR-R-104*.
- Beckwith, I.E. and Gallagher, J.J. 1961 Local Heat Transfer and Recovery Temperatures on a Yawed Cylinder at a Mach Number of 4.15 and High Reynolds numbers. *NASA-TR-R-104*.
- Beckwith, I.E., Chen, F.-J. and Malik, M.R. 1990 Transition in Low Disturbance High Speed Wind Tunnels. *Laminar-Turbulent Transition III*, Ed. D. Arnal; R. Michel. Springer.
- Bertlerud, A. and Graves, S. 1995 Transition in Flight at Supersonic and Hypersonic Mach Numbers. *Proc. Royal Netherlands Academy of Arts and Sciences*, Amsterdam.
- Bertin, J.J. and Idar, E.S. 1978 Effect of Surface Cooling and Roughness on Transition for the Shuttle Orbiter. *J. Space. Rockets*. Vol. 15, No. 2.
- Bertram, M.H., Feller, W.V. and Dunavant, J.C. 1960 Flow Fields, Pressure Distributions, and Heat Transfer for Delta Wings at Hypersonic Speeds. *NASA-TM-X-316*.
- Bertram, M.H. and Everhart, P.E. 1963 An Experimental Study of the Pressure and Heat-Transfer Distribution on a 70° Sweep Slab Delta Wing in Hypersonic Flow. *NASA-TR-R-153*.
- Burbank, P.B., Newlander, R.A. and Collins, I.K. 1962 Heat-Transfer and Pressure Measurements on a Flat-Plate Surface and Heat-Transfer Measurements on Attached Protuberances in a Supersonic Turbulent Boundary Layer at Mach Numbers of 2.65, 3.51 and 4.44. *NASA-TN-D-1372*.
- Bushnell, D.M. 1965 Interference Heating on a Swept Cylinder in Region of Intersection With a Wedge at Mach Number 8. *NASA-TN-D-3094*.
- Bushnell, D.M. and Jones, R.A. 1965 Heat Transfer to a 70° Swept Fin Partly Submerged in a Turbulent

- Boundary Layer at Mach 6. *NASA-TM-X-1191*.
- Bushnell, D.M. and Huffman, J.K. 1967 Investigation of Heat Transfer to Leading Edge of a 76° Swept Fin With and Without Chordwise Slots and Correlations of Swept-Leading-Edge Transition Data for Mach 2 to 8. *NASA-TM-X-1475*.
- Chapman, G.T. 1961 Some Effects of Leading Edge Swept on Boundary-Layer Transition at Supersonic Speeds. *NASA-TN-D-1075*.
- Creel, T.R. and Beckwith, I.E. 1986 Effects of Wind-Tunnel Noise on Swept Cylinder Transition at Mach 3.5. *AIAA Paper No. 86-1085*.
- Creel, T.R., Beckwith I.E. and Chen, F.J. 1987 Transition on Swept Leading Edges at Mach 3.5. *J. Aircraft, Vol. 25, No. 10*.
- Creel, T.R., Malik, M.R. and Beckwith, I.E. 1988 Boundary-Layer Instability Mechanisms on a Swept-Leading Edge at Mach 3.5. *SAE Paper No. 871858*.
- Da Costa, J.L. 1990 Contribution a l'etude de la Transition de Bord D'attaque Par Contamination en Ecoulement Hypersonique. *Docteur de l'Universite de Poitiers*.
- de Luca, L., Cardone, G., Aymer de la Chevalene, D. and Fonteneau, A. 1993 Görtler Instability of a Hypersonic Boundary Layer. *Exper. Fluids, Vol. 16*.
- East, R.A. and Baxter, D.R.J. 1990 Comparative Heat Transfer Measurements on Caret and Flat Compression Surfaces for Hypersonic Intakes. *First International Hypersonic Waverider Symposium, University of Maryland*.
- Ellison, R.K. 1962 Turbulent Reference, Roughness, Leakage and Deflected-Surface Heat Transfer and Pressure Tests for the Boeing Company Conducted in the Cal 48-Inch Hypersonic Shock Tunnel. *Cornell Aero Lab, Inc. Report No. AA-1661-Y-1*.
- Everhart, P.E. and Dunavant, J.C. 1964 Heat-Transfer Distribution on 70° Swept Slab Delta Wings at a Mach Number of 9.86 and Angles of Attack up to 90°. *NASA-TN-D-2302*.
- Feller, W.V. 1961 Investigation of Equilibrium Temperatures and Average Laminar Heat-Transfer Coefficients for the Front Half of Swept Circular Cylinders at a Mach Number of 6.9. *NACA RM L55F08a*.
- Fleming, W.J. and Krauss, W.E. 1966 Aerodynamic Heating From Turbulent Boundary Layers to Swept surfaces. *Proc. 3rd Int. Heat Transfer Conf.*
- Goodrich, W.M. and Derry, S.M. 1973 Shuttle Orbiter Boundary-Layer Transition: a Comparison of Flight and Wind Tunnel Data. *AIAA Paper No. 83-0485*.
- Goodwin, G., Creager, M.O. and Winkler, E.L. 1956 Investigation of Local Heat-Transfer and Pressure Drag Characteristics of a Yawed Circular Cylinder at Supersonic Speeds. *NACA Memorandum A55H31*.
- Gunn, C.R. 1961 Heat-Transfer Measurements on the Apexes of Two 60° Sweptback Delta Wings (Panel Semiapex Angle of 30°) Having 0° and 45° Dihedral at a Mach Number of 4.95. *NASA-TN-D-550*.
- Hefner, J.N. 1975 Boundary-layer Transition for Space-Shuttle Type Configurations at Angles of Attack. *NASA-TM-X-2254*.
- Howard, F.G. 1964 Heat Transfer on Onswep and 38° Swept Cylindrically Blunted Wedge Fins in Free Flight to Mach Number 4.11. *NASA-TN-D-2386*.
- Hunt, J.L., Bushnell, D.M. and Beckwith, I.E. 1971 The Compressible Turbulent Boundary Layer on a Blunt Swept Slab With and Without Leading-Edge Blowing. *NASA-TN-D-6203*.
- Jillie, D.W. and Hopkins, E.J. 1961 Effects of Mach Number, Leading Edge Bluntness and Sweep on Boundary-Layer Transition on a Flat Plate. *NASA-TN-1071*.
- Jones, R.A. 1964 Heat-Transfer and Pressure Investigation of a Fin-Plate Interference Model at a Mach Number of 6. *NASA-TN-D-2028*.
- King, R.A. 1992 Three-Dimensional Boundary-Layer Transition on a Cone at Mach 3.5. *Exp. Fluids, Vol. 13*.
- Kipp, H.W. and Masek, R.V. 1986 Aerodynamic Heating Constraints on Space Shuttle Vehicle Design. *AIAA Paper No. 86-1257*.
- Malik, M.R. and Beckwith, I.E. 1988 Stability of a Supersonic Boundary Layer Along a Swept Leading Edge. *Paper No. 3*.
- Morrisette, E.L. and Creel, T.R. 1987 The Effects of Wall Surface Defects on Boundary-Layer Transition in Quiet and Noisy Supersonic Flow. *NASA Symposium Natural Laminar Flow and Laminar Flow Control Research*.
- Nagel, A.L., Fitzsimmons H.D. and Doyle, L.B. 1966 Analysis of Hypersonic Pressure and Heat Transfer Tests on Delta Wings with Laminar and Turbulent Boundary Layers. *NASA-CR-535*.
- O'Neal, R.L. and Bond, A.C. 1962 Heat Transfer to 0° and 75° Swept Blunt Leading Edges in Free Flight at Mach Numbers From 1.90 to 3.07. *NASA-TN-D-1256*.
- O'Neal, R.L. 1952 Heat Transfer to 36.75° and 45° Swept Blunt Leading Edges in Free Flight at Mach Numbers From 1.70 to 2.99 and From 2.50 to 4.05. *NASA-TM-X-208*.
- Owen, P.R. and Randall, D.G. 1952 Boundary Layer Transition on the Swept Wing. *RAE-TM-Aero 277*.
- Pate, S.R. and Groth, E.E. 1966 Boundary-Layer Transition Measurements on Swept Wings with Supersonic Leading Edges. *AIAA J., Vol. 4, No. 4*.
- Pate, S.R. and Schueler, C.J. 1969 Radiated aerodynamic Noise Effects on Boundary-Layer Transition in Supersonic and Hypersonic Wind Tunnels. *AIAA J., Vol. 7, No. 3*.
- Poll, D.I.A. 1979 Transition in the Infinite Swept Attachment Line Boundary Layer. *Aero. Q., Vol. XXX*.
- Poll, D.I.A. 1983 The Development of Intermittent Turbulence on a Swept Attachment Line Including the Effects of Compressibility. *Aero. Q., Vol. XXXIV*.
- Poll, D.I.A. 1984 Transition Description and Prediction in Three-Dimensional Flows. *AGARD Report 709*.
- Poll, D.I.A. 1985 Some Observations of the Transition Process on the Windward Face of a Long Yawed

- Cylinder. *J. Fluid Mech.*, Vol. 150.
- Poll, D.I.A. 1986 A New Hypothesis for Transition on the Windward Face of Space Shuttle. *J. Space. Rockets*, Vol. 23, No. 6.
- Poll, D.I.A. 1992 Heat Transfer to a Swept Leading Edge in Hypersonic Flow Including Effects of Transition. *IUTAM Symp. on Aerothermochemistry of Spacecraft and Associated Hypersonic Flows*, Marseille, France.
- Poll, D.I.A., 1993 Role of Viscous-Inviscid Interaction on Transition Near a Swept Leading Edge in Hypersonic Flow. *1993 Hypersonics Symposium*, Wright-Patterson Airforce Base, Ohio, USA.
- Price, E.A., Howard, P.W. and Stallings Jr, R.L. 1964 Heat-Transfer Measurements on a Flat Plate and Attached Fins at Mach Numbers of 3.51 and 4.44. *NASA-TN-D-3340*.
- Reed, H.L. and Haynes, T.S. 1994 Transition Correlations in 3-D Boundary Layers. *AIAA J.*, Vol. 32, No. 5.
- Reshotko, E. 1990 Hypersonic Stability and Transition. *Workshop on Hypersonic flows for Reentry Problems*, Antibes, France.
- Saric, W.S. 1994 Görtler Vortices. *Ann. Rev. Fluid Mech.*, Vol 26.
- Skuratov, A.S. and Fedorov, A.V. 1991 Supersonic Boundary Layer Transition Induced by Roughness on the Attachment Line of a Yawed Cylinder. Moscow. *Translated from Izvestiya Akademii Nauk SSSR, Mekhanika Zhidkosti i Gaza*, No. 6, pp 28-35.
- Stainback, P.C. 1961 Heat-Transfer Measurements at a Mach Number of 4.95 on Two 60° Swept Delta Wings With Blunt Leading Edges and Dihedral Angles of 0° and 45°. *NASA-TN-D-549*.
- Stallings Jr. R.L., Burbank, P.B. and Howell, D.T. 1964 Heat-Transfer and Pressure Measurements on Delta Wings at Mach Numbers of 3.51 and 4.65 and Angles of Attack from -45° to 45°. *NASA-TN-D-2387*.
- Stetson, K.F. 1990 Hypersonic Boundary-Layer Transition. *Third Joint Europe/US Short Course on Hypersonics*, University of Aachen.
- Van Driest, E.R. and Blumer, C.B. 1968 Boundary-Layer Transition at Supersonic Speeds: Roughness Effects with Heat Transfer. *AIAA J.*, Vol. 6, No. 4.
- Yeoh, K.B. 1980 Transition Along the Attachment Line of a Swept Circular Cylinder in Supersonic flow. *M.Sc. Thesis. Cranfield Inst. of Tech.*

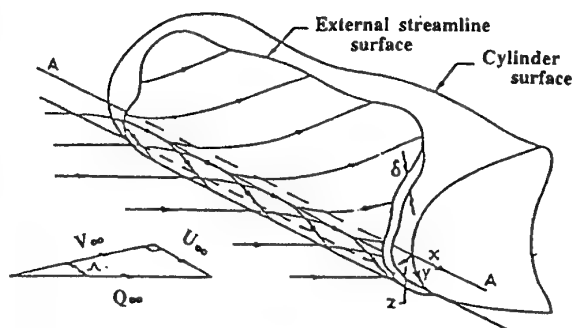


Figure 1. Flow in the vicinity of a swept attachment line.

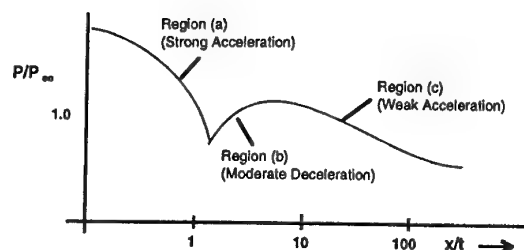


Figure 3. Typical pressure distribution near the leading edge of a blunt swept wing.

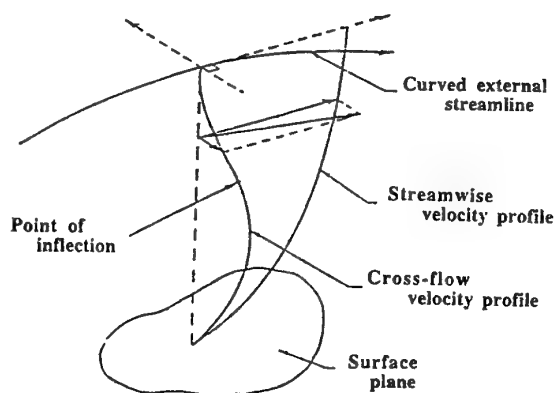


Figure 2. Typical boundary-layer velocity distribution near the leading edge of a yawed cylinder.

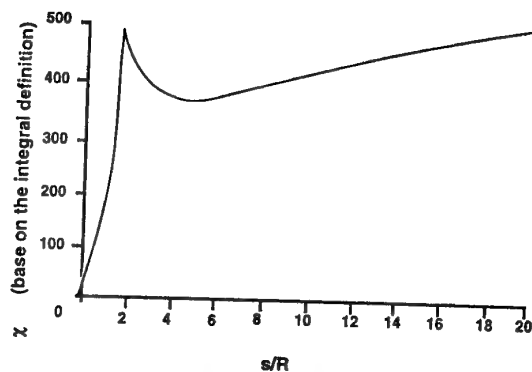


Figure 4. Typical Chordwise variation of crossflow Reynolds number for a delta wing.

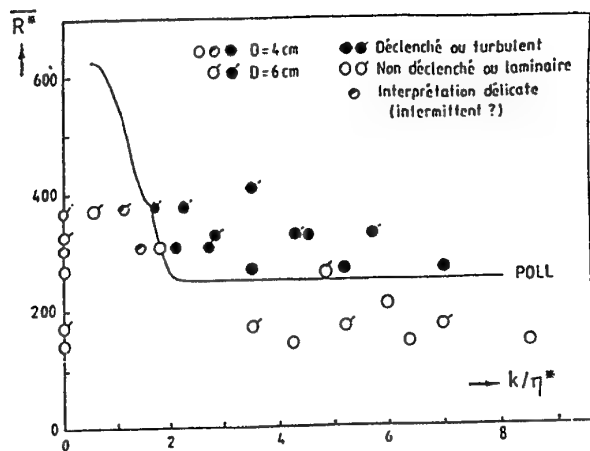


Figure 5. The variation of critical Reynolds number with roughness height for the onset of attachment-line transition in compressible flow (Arnal et al. 1989).

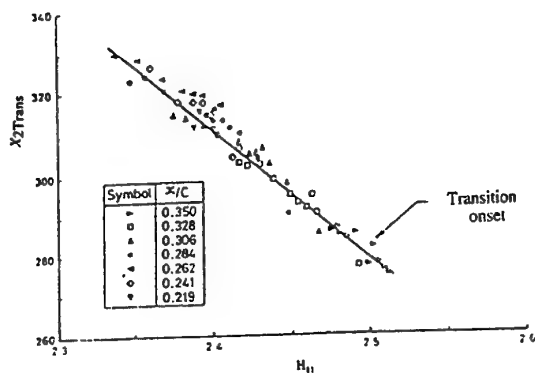


Figure 7. The variation of crossflow Reynolds number with streamwise shape factor for transition on a yawed cylinder in low-speed flow.

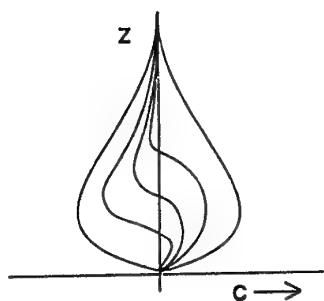


Figure 6. Various possible forms of the crossflow velocity profile.

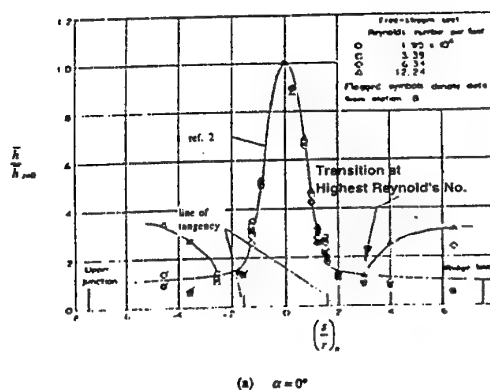


Figure 8. Chordwise distribution of heat transfer for a 60° swept cylindrically blunted slab wing at Mach number 4.95 and 0° angle of attack.

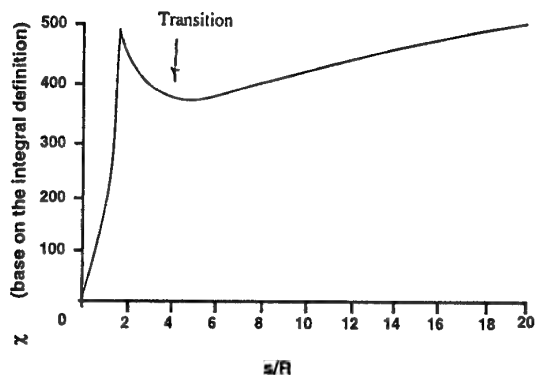


Figure 9. Chordwise variation of crossflow Reynolds number for Stainback's delta wing.



Figure 10. An example of crossflow induced transition on a wing swept at 45° with a leading edge radius of 0.5mm in a Mach 4 flow (after Jillie and Hopkins, 1961).

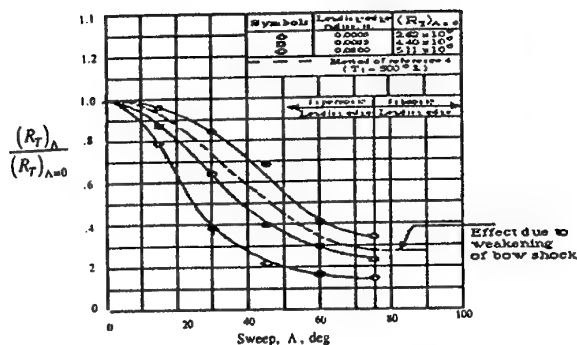


Figure 11. Variation of streamwise transition Reynolds number with sweep and bluntness at Mach 4 (after Jillie and Hopkins, 1961).

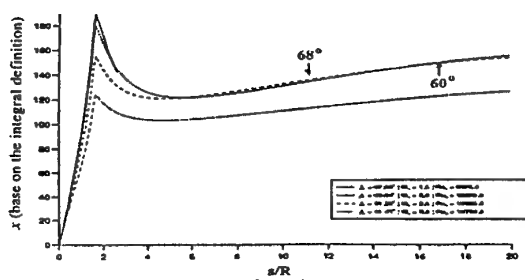


Figure 12. Variation of crossflow Reynolds number with surface position and sweep angle for the Jillie and Hopkins experiment.

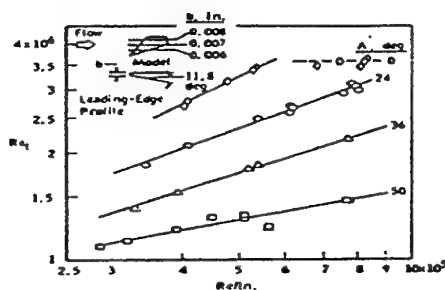


Figure 13. Variation of streamwise transition Reynolds number with freestream unit Reynolds number and sweep angle for a flat plate at Mach 3 (after Pate and Groth, 1966).

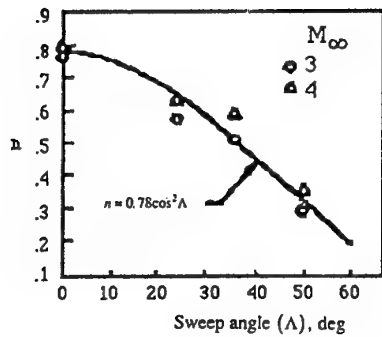


Figure 14. Dependence of the unit Reynolds number exponent upon sweep angle for the Pate and Groth data.

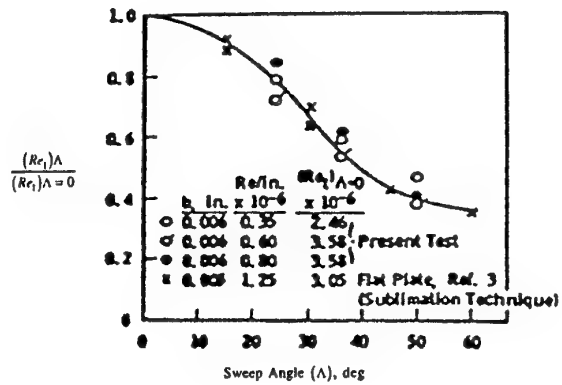


Figure 16. Normalized transition Reynolds number as a function of sweep angle for fixed nose bluntness and varying freestream unit Reynolds number.

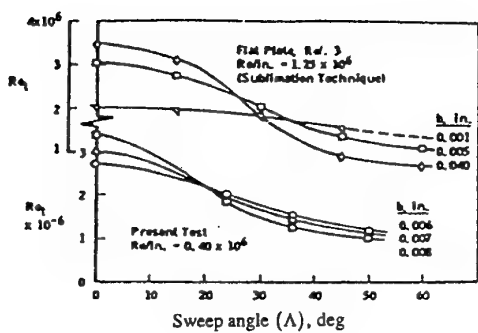


Figure 15. Effect of leading-edge bluntness and sweep angle upon the streamwise transition Reynolds number for a flat plate (after Pate and Groth, 1966).

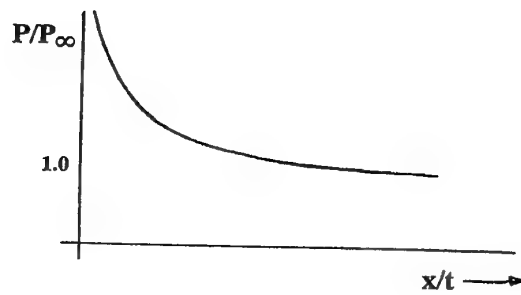


Figure 17. Form of the pressure distribution induced by viscous-inviscid interaction.

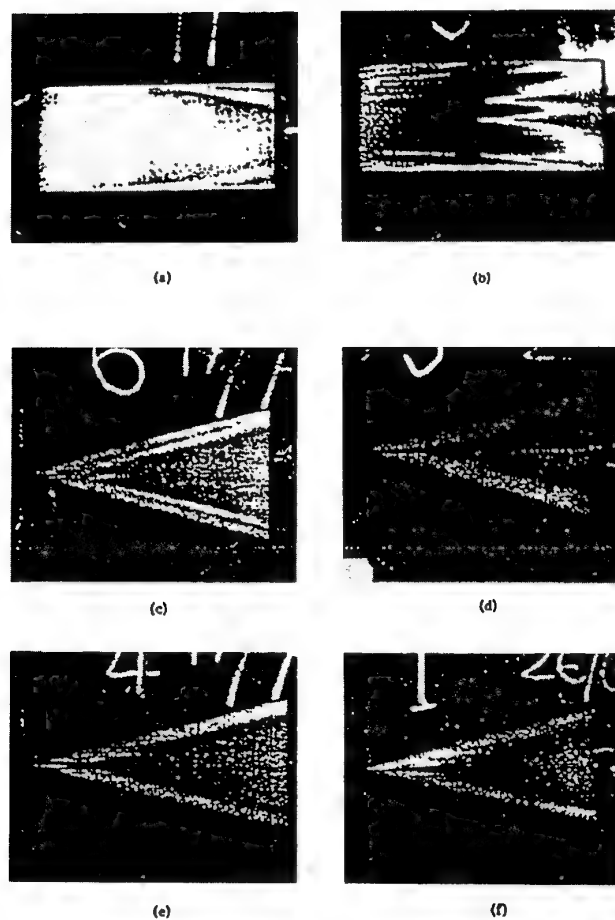


Figure 18. Experimental evidence of the forward movement of transition as a result of the application of leading-edge sweepback after East and Baxter (Saric 1994).

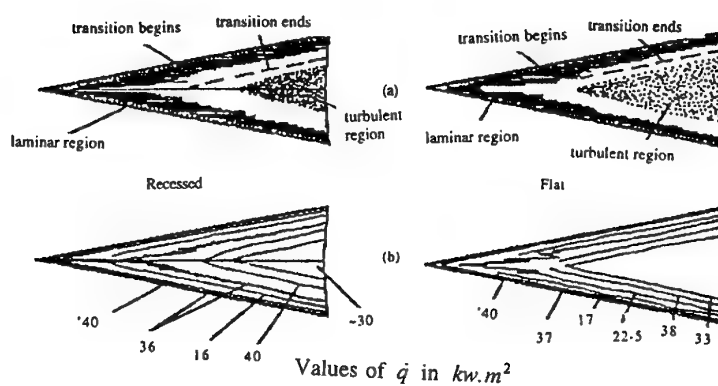


Figure 19. General features and heat transfer contours for delta wings in hypersonic flow (East and Baxter).

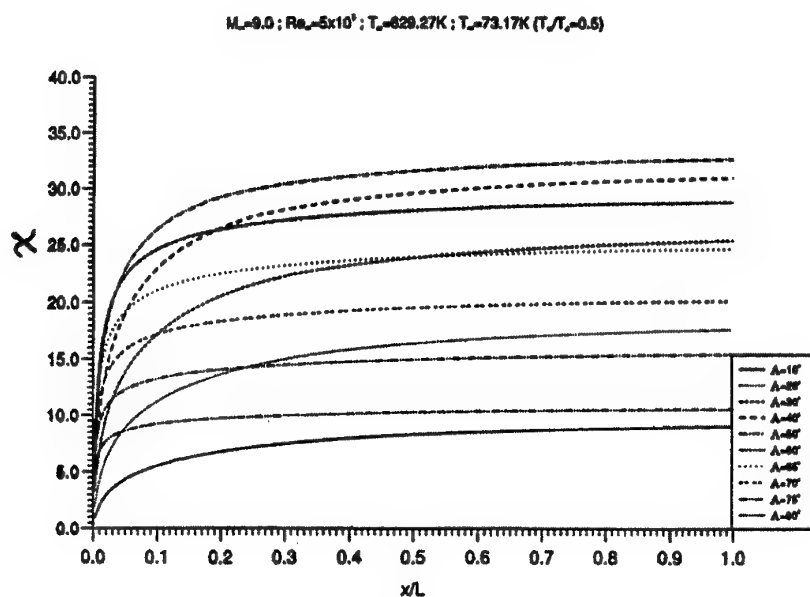


Figure 20. Variation of crossflow Reynolds number with chordwise position for a swept flat plate with a sharp leading edge.

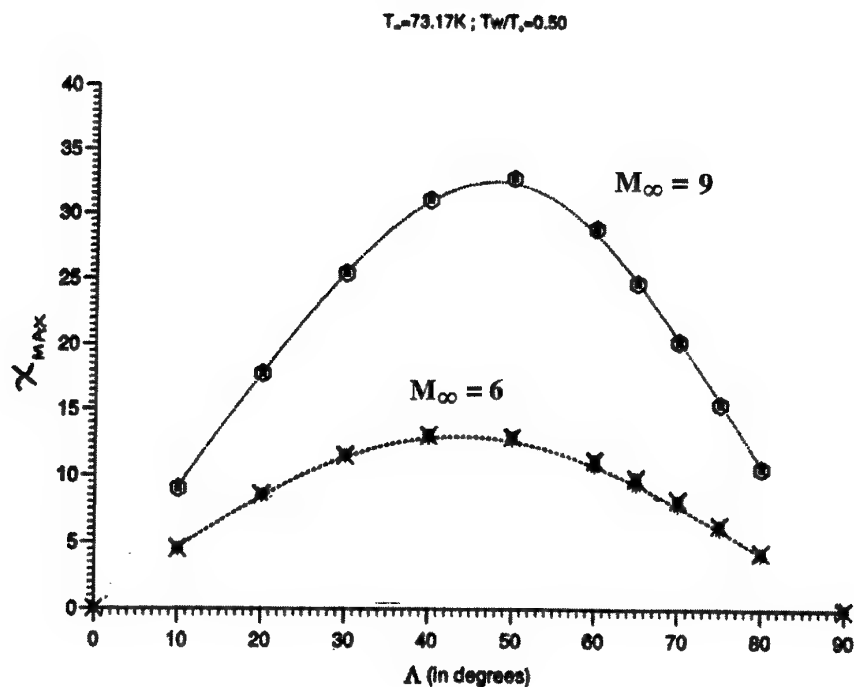


Figure 21. Effect of sweep angle and freestream Reynolds number on the maximum crossflow Reynolds number generated on a swept, sharp-edged, flat plate.

CHAPTER IV

RAREFIED FLOW

James N. Moss

Aerothermodynamics Branch
Space Systems Division
NASA Langley Research Center
Hampton, VA 23681-0001
USA

and

Jean Allègre

Laboratoire Aérothermique
CNRS
4 Ter, Route des Gardes
92190 Meudon
FRANCE

CONTENTS		7.5 Flow-Density Measurements	96
1	INTRODUCTION	8 AVAILABLE TEST RESULTS	96
2	TEST CASE DEFINITION	8.1 Corner-Flow/Jet Interaction	96
2.1	Corner-Flow/Jet Interaction Test Model	8.2 Blunt-Body/Wake-Closure	96
2.2	Blunt-Body/Wake-Closure Test Model	9 AVAILABLE COMPUTATIONAL RESULTS AND COMPARISONS WITH EXPERIMENTS	97
3	COMPUTATIONS AND EXPERIMENTS	9.1 Corner-Flow/Jet Interaction Test Model	97
3.1	Computational Participation	9.2 Blunt-Body/Wake-Closure	97
3.2	Experimental Participation	9.3 Issues Associated with Experimental and Computational Comparisons	98
4	MODEL FEATURES	10 WORK PROGRESS AND EXPECTED SCHEDULE	98
4.1	Corner-Flow/Jet Interaction Test Model	10.1 Experimental Research	98
4.2	Blunt-Body/Wake-Closure Test Model	10.2 Computations	99
5	TEST CONDITIONS	11 OTHER EXISTING DATA BASES	99
5.1	Experimental Test Conditions	12 RECOMMENDATIONS	99
5.2	Flight Test Conditions	REFERENCES	99
6	SURFACE AND FLOWFIELD MEASUREMENTS	TABLE AND FIGURES	101
6.1	Corner-Flow/Jet Interaction Test Model		
6.2	Blunt-Body/Wake-Closure Test Model		
7	TEST TECHNIQUES	1 INTRODUCTION	
7.1	Wall-Pressure Measurement	Hypersonic flows where rarefaction effects are important occur over a wide spectrum of conditions ranging from low-density (high-altitude) situations to relatively high- density flows where the characteristic dimension is small. Examples are the overall aerothermodynamics of space vehicles at high altitude (reentry flows, satellite	
7.2	Surface-Flow Visualizations		
7.3	Heat-Transfer Measurements		
7.4	Aerodynamic Forces and Moments		

contamination, and plume interactions), the heating along the leading edges at lower altitudes, and very localized aerothermal loads occurring at even lower altitudes such as that resulting from a shock on cowl lip interaction.

The objective of the present investigation is to enhance our understanding of the importance of rarefaction for two problems common to entry and aeroassist vehicles; (1) the forces generated on surfaces as a result of the interaction between exhaust plumes and the flowfield surrounding a vehicle and (2) the near-wake structure and how its closure is influenced by rarefaction. The objective is to be accomplished through a series of experimental and computational studies with emphasis on obtaining data with existing capabilities while identifying future needs. Multiple data sources from both experimental and computational contributions are realized. High priority is assigned to fundamental data that can be used to calibrate computational tools and facilities.

Most space vehicles are controlled with reaction thrusters during atmospheric entry. These reaction control system (RCS) jets can be used independently or in conjunction with moveable aerodynamic surfaces depending on the specific vehicle configuration and flight conditions. The exhaust plumes of these control jets act as barriers to the external flow creating an effect that can change the pressure distribution along the vehicle surface containing the jet, as well as on surfaces surrounding the exhaust plume. These surface pressure perturbations lead to interaction forces which must be accurately predicted in order to obtain the desired vehicle performance.

The use of RCS jets becomes vital at higher altitudes where the density is low enough to render the control surfaces ineffective. As the altitude increases and the freestream flow becomes more rarefied, the level of interaction between the control jet and the freestream diminishes and is practically nonexistent when the freestream mean free path is very large. Therefore, it is crucial to accurately model RCS firings at intermediate altitudes where reaction controls are needed and significant control jet interactions are expected.

In an effort to gain further insight into the control jet interaction problem, an experimental study was conducted by the European Space Agency (ESA) at the SR3 low-density wind tunnel of CNRS in Meudon, France (Allègre and Raffin 1991, 1992). A second experimental study has been recently performed at the DLR in Göttingen utilizing the V2G low-density wind tunnel.

The data base resulting from these two experiments will serve as a basis for testing elements of the numerical simulation tools. The problem addressed is fundamental and complex in that the problem has both rarefied and continuum components i.e. the rarefied external flow interacting with a jet whose central core is at continuum conditions. The ultimate objective of the numerical studies is to provide a methodology for accurately

simulating control jet interactions for hypersonic low density flows. Numerical studies are currently in progress at Aerospatiale, CNRS, and NASA Langley.

The second problem concerns the wake closure which is important for entry probes and aerobrakes. It is a critical issue for aerobrakes because the low lift-to-drag ratio aeroshell designs impose constraints on payload configuration/spacecraft design. The issue is that the payload must fit into the wake cone to minimize heating since a heating spike is generally associated with reattachment of the separated near-wake flows.

A number of fundamental questions exists concerning such flows: How does the wake structure change as a function of rarefaction? What role does thermochemical nonequilibrium play in the near-wake structure? To what limits are continuum models realistic as rarefaction in the wake is progressively increased? The potential for rarefaction effects on wake structure exists for much of an aerobraking maneuver since the expansion of even continuum forebody flow into the near wake can result in relatively large local Knudsen numbers.

The experimental test plan for this problem consists of two parts: one is the high-enthalpy tests obtained with impulse facilities (discussed in Chapter VI) and the second is tests at intermediate- to high-Knudsen-number conditions. The rarefied tests will be performed primarily in low-enthalpy facilities at chemically-inert conditions. Also, the plan is to conduct tests using small models in the DLR Göttingen high-enthalpy facility (the HEG as described in Chapter VI) where the effects of both chemistry and rarefaction are present. For both sets of experiments, the same model configuration is used. The forebody is a 70° spherically-blunted cone that has been proposed as a possible candidate for the Mars Environmental SURvey (MESUR) Network probes and the MESUR Pathfinder probe (Tauber et al. 1992).

The low-density experiments will be performed in seven facilities: six in Europe and one in the U.S. The Knudsen number range for these facilities is 0.001 to 1.17 based on freestream mean free path and base diameter. The data base extracted from these studies will include aerodynamics (C_L , C_D , C_m , and the center of pressure); local surface heating rate along the forebody, base plane, and sting; and wake structure as inferred from density and potentially velocity measurements in the near wake. Model support for these tests will include stings, wires, and magnetic suspension.

Numerical computations will complement the experimental results. The numerical studies will include, at a minimum, direct simulation Monte Carlo (DSMC) and Navier-Stokes algorithms. The computational results will be tested against selected experimental results. In addition, results of different numerical methods will be compared with each other to clarify the boundaries for realistic application of Navier-Stokes algorithms with respect to rarefaction effects.

Finally, by expanding the computational problems to include high altitude flight conditions, an assessment of the combined effects of rarefaction and thermochemical nonequilibrium on wake structure will be made. Two flight conditions will be examined: one in the Earth's atmosphere and one in the Mars atmosphere, both at the same freestream velocity (7 km/s) and number density ($1.654 \times 10^{20} \text{ m}^{-3}$).

Numerical computations have been performed for selected SR3 facility conditions (Mach 20 nitrogen flow around 50 mm diameter models) by the following organizations: CNRS Meudon; Middle East Technical University, Ankara (Çelenligil 1993); and NASA Langley (Dogra et al. 1993; Wilmouth et al. 1993; Moss et al. 1993a,b). All three organizations employed DSMC algorithms. The NASA Langley studies (Moss et al. 1993a) included the application of Navier-Stokes solvers to the same wind tunnel cases. Also a zonally-decoupled DSMC methodology (Wilmouth et al. 1993) has been validated for the wind tunnel cases by comparing with fully coupled solutions. For the flight tests cases, DSMC (Çelenligil 1993; Dogra et al. 1994) and Navier-Stokes (Dogra et al. 1994) solutions have been obtained for Earth entry.

2 TEST CASE DEFINITION

Two test cases have been proposed. The corner-flow/jet interaction test model is used to analyze transverse flows interacting with external rarefied hypersonic flows. The blunt-body/wake-closure test model is investigated to characterize the wake structure at different rarefaction levels of the external hypersonic flow.

2.1 Corner-Flow/Jet Interaction Test Model

As shown in Figure 1, the corner-flow model is made of two perpendicular flat plates with sharp leading edges. A transverse jet is issued from a hypersonic nozzle located in the horizontal plate. This under-expanded jet interacts with the external flow and with the surrounding surfaces.

2.2 Blunt-Body/Wake-Closure Test Model

The blunt body is an axisymmetric ASTV (Aeroassist Space Transfer Vehicle) type model. Depending upon the test facility, models will be supported by stings, wires, and magnetic suspension. For the sting-mounted models, the sting radius should be $R_b/4$ and the length $6R_b$ to be consistent with the high-enthalpy tests (Chapter VI). Some of the test facilities will not be able to accommodate stings of this length as is the case for the CNRS tests where the sting length is $3R_b$. Blunt body and rear sting dimensions are indicated in Figure 2 where the base radius will range from 2.5 to about 25 mm. The forebody geometry is compared in Figure 3 with other planetary vehicle configurations.

3 COMPUTATIONS AND EXPERIMENTS

3.1 Computational Participation

Several organizations have expressed an intent to contribute to the computational studies subject to the realization of the experiments. As the experimental tests are completed, it is hoped that additional participants will join this activity. Each participant is encouraged to compute as many of the experimental and flight test cases as practicable. The following list is a summary of those organizations that have agreed to participate.

3.1.1 Corner-Flow/Jet Interaction Test Model

Committed organizations:

Aerospatiale les Mureaux, France

CNRS Meudon, France

NASA Langley, U.S.A.

NASA Marshall, U.S.A.

Sandia Albuquerque, U.S.A.

3.1.2 Blunt-Body/Wake-Closure Test Model

Committed organizations:

CNRS Meudon, France

Fluid Gravity, Hampshire, U.K.

Imperial College, U.K.

Middle East Technical University, Turkey

NASA Langley, U.S.A.

NASA Marshall, U.S.A.

North Carolina State University, U.S.A.

Sandia Albuquerque, U.S.A.

3.2 Experimental Participation

3.2.1 Corner-Flow/Jet Interaction Test Model

Committed organizations:

CNRS Meudon, France

DLR Göttingen, Germany

3.2.2 Blunt-Body/Wake-Closure Test Model

Committed organizations:

CNRS Meudon, France

DLR Göttingen, Germany

DRA Farnborough, U.K.

UCB, Berkeley, U.S.A.

UOO, Oxford, U.K.

4 MODEL FEATURES

4.1 Corner-Flow/Jet Interaction Test Model

4.1.1 CNRS Meudon

The model, 120 mm long, is made of two perpendicular flat plates. The horizontal plate, 80 mm wide, is parallel to the external flow direction. A hypersonic conical nozzle is embedded in the plate. The nozzle axis is vertical and the exit section is made flush with the plate surface. The nozzle is located 60 mm downstream from the leading edge. The other plate is vertical, 60 mm high, and parallel to the external flow direction. The two configurations investigated [(Figures 4(a) and (b))] correspond to the two distances of 15 mm and 30 mm between the nozzle and the vertical plate. Both the horizontal and vertical plates have sharp leading edges with bevel angles of 20°. The plates are equipped with 38 wall pressure orifices in order to obtain wall pressure distributions along some arbitrary lines. Coordinates of wall pressure orifices are indicated in Figures 4 through 5 for model configurations 1 and 2.

4.1.2 DLR Göttingen

The model is 230 mm long and 160 mm wide and is composed of two perpendicular flat plates. The horizontal plate includes a turntable with 14 wall pressure orifices. The jet nozzle (described in Section 5.1.2) is located at the center of the turntable. Excluding the turntable, 5 pressure orifices are integrated in the horizontal wall and 29 in the vertical wall. The vertical wall may be displaced to vary its distance from the jet nozzle. A sketch of the water-cooled model is presented in Figure 6.

4.2 Blunt-Body/Wake-Closure Test Model

4.2.1 CNRS Meudon

Three different models are used according to the type of measurement. For aerodynamic force measurements, the model is made of aluminum and uncooled (Figure 7). It is directly mounted on the external balance mounted around the open-jet test section of the SR3 wind tunnel. The model utilized for the flow-density measurements is made of brass and is water cooled. It is fixed to a sting support as indicated in Figure 8. For heat-flux measurements, the thin-wall model is made of Armco Steel elements (Figure 9). Chromel alumel thermocouples are embedded through the wall thickness on the forebody, on the base surface, and around the cylindrical sting.

4.2.2 DLR Göttingen

Blunted cone models with base diameters of 5, 25, and 50 mm are utilized in the DLR Göttingen test programs. The test models are suspended by one of three means: wires, sting, thermocouple leads. Three different test

facilities are used: V3G, V2G, and HEG. Figure 10 shows schematically the model (base diameter = 5 mm) and thermocouple suspension system for the tests that have been completed using V3G. Models that are tested in V2G consist of three base diameters using wires and sting for suspension. The tests in the HEG use 5 mm diameter sting-mounted models.

4.2.3 DRA Farnborough

Two aluminum models with base diameters of 25.4 and 50.8 mm are to be used for the force and moment tests. The machined ceramic heat transfer model will be the same size as the larger force model and instrumented with thin film sensors.

4.2.4 University of California Berkeley

The models will have a 20 mm base diameter. Models to be utilized are thin-wall models for heat transfer measurements, water cooled models for wake flowfield density mappings, and an uncooled model for force measurements. The length of the sting for the heat flux and density measurement models will be $6R_b$.

4.2.5 University of Oxford

The University of Oxford Hypersonic Low Density Wind Tunnel is equipped with a magnetic suspension and balance system. The suspension and force measuring system has recently been upgraded so that a wider range of geometries can be suspended. Preliminary aerobrake tests have been performed on 70° half-angle blunted cones with an 18 mm base diameter and afterbodies. The afterbodies were either 25 or 30 mm in length and diverged at a half angle to facilitate suspension. The new measurement system will allow aerobrake models with other afterbody geometries to be tested.

5 TEST CONDITIONS

5.1 Experimental Test Conditions

Table 1 presents a summary of flow conditions that can be realized with the low-density wind tunnels utilized in this study. Figure 11 displays $M_\infty/\sqrt{Re_\infty}$ while Figure 12 shows the freestream parameters density vs. speed.

5.1.1 Corner-Flow/Jet Interaction Test Conditions

Two sets of experiments are planned for this test case: the CNRS Meudon and the DLR Göttingen experiments. The CNRS experiments have been completed and are documented by Allègre and Raffin (1992, 1993). The test model for the DLR experiments has been fabricated, but the details of the test conditions and test schedule have not been defined. The next two sections outline the test conditions for this test case.

CNRS Meudon The external flow conditions are the three test conditions listed as part (a) of Table 1. The jet emerges from a hypersonic conical nozzle with the nozzle exit in the plane of the horizontal plate (Figure

4). Nozzle geometry and flow parameters are: nitrogen test gas; throat and exit diameters of 0.213 and 1.53 mm, respectively; divergent nozzle half angle of 9° ; nominal exit Mach number of 5.96; stagnation temperature of 300 K; and stagnation pressures of 4, 12, 20 bars. In addition to the three external flow and three jet conditions, the matrix of flow conditions include the external flow without the jet and the jet with no external flow at a background pressure of about 2 Pa.

DLR Göttingen The specifics of this test program have not been defined; however, the test hardware has been fabricated. When the tests are performed, the external flow will be generated in the V2G wind tunnel. The conditions listed in part (b) of Table 1 are representative of potential conditions. The jet flow will emerge from a conical nozzle with the following specifications: throat and exit diameters of 0.6 and 2.89 mm, respectively; nozzle divergent half angle of 20° ; and stagnation pressures of 1, 2, 3, 5, 10, 15, and 20 bars. The test gas will be both nitrogen and argon.

5.1.2 Blunt-Body/Wake-Closure Test Conditions

Information concerning the facility characteristics and freestream conditions for the 6 low-density facilities that will potentially contribute to the blunt-body/wake closure test case is given in Table 1 and Figures 11 and 12. The test conditions for the small models ($d_b = 5$ mm) that will be tested in the HEG have not been defined.

The conditions listed in part (a) of Table 1 are the conditions that are being used for the CNRS tests and the conditions listed in part (b) of Table 1 are conditions for which exploration and calibration tests have been performed in the V2G facility.

Details of the test that have been completed in V3G are given in Legge (1993). Briefly, these tests were made at 5 levels of rarefaction and 2 values of stagnation temperature ($T_0 \approx 300$ and 500 K). For $T_0 \approx 300$ K, the wall temperature was varied between 290 and 450 K. For $T_0 \approx 500$ K, the wall temperature was varied between 400 and 750 K.

The UCB research will conduct studies not only in nitrogen but also in air and CO_2 . In fact, the primary test gas will be CO_2 because of its relevance to the Martian atmosphere. Since UCB uses a ceramic heater tube as the flow reservoir, these tests will be able to operate at somewhat higher stagnation temperatures than the other low-density facilities. Recent calibration tests with CO_2 indicate that it is possible to produce a mass flow potential of about 2 grams/s at a pressure of 1 torr.

5.2 Flight Test Conditions

5.2.1 Earth Atmosphere

The freestream conditions correspond to an altitude of 85 km in the Earth's atmosphere at a velocity of 7 km/s.

The freestream conditions are

$$\text{Number density} = 1.654 \times 10^{20} \text{ m}^{-3}$$

$$\text{Density} = 7.955 \times 10^{-6} \text{ kg/m}^3$$

$$\text{Temperature} = 180.65 \text{ K}$$

$$\text{Velocity} = 7.0 \text{ km/s}$$

$$\text{Mole Fraction of } \text{O}_2 = 0.2372$$

$$\text{Mole Fraction of } \text{N}_2 = 0.7628$$

and the wall conditions are assumed to be diffuse with full thermal accommodation and noncatalytic. The wall temperature is assumed to be constant at 1000 K. These flow conditions produce Mach 26 flow at a freestream Reynolds number of 9×10^3 and a freestream Knudsen number of 0.0036 where the characteristics length is the base diameter (2.0 m).

The probe configuration (Figure 13) used in this study is a forebody proposed (Tauber et al. 1992) for the Mars Environmental SURvey (MESUR) Network probes where the objective is to place a globally distributed network of landers (16 total) on the Martian surface in order to make both short- and long-term observations of the atmosphere and surface.

The forebody description is as follows:

$$\text{Base radius, } R_b = 1.0 \text{ m}$$

$$\text{Nose radius, } R_n = 0.5 \text{ m}$$

$$\text{Corner radius, } R_c = 0.05 \text{ m}$$

$$\text{Body half angle, } \theta = 70^\circ$$

This configuration is the same as that used for the wind tunnel conditions.

Solutions for the 85 km condition at 7 km/s will be obtained for both a reacting air gas mixture (no ionization) and a 2-species non-reacting gas consisting of freestream oxygen and nitrogen.

5.2.2 Mars Atmosphere

Body configuration and surface boundary conditions are the same as that for Earth entry.

The freestream conditions are:

$$\text{Number density} = 1.654 \times 10^{20} \text{ m}^{-3}$$

$$\text{Temperature} = 141 \text{ K}$$

$$\text{Velocity} = 7.0 \text{ km/s}$$

$$\text{Mole Fraction of } \text{CO}_2 = 0.95$$

$$\text{Mole Fraction of } \text{N}_2 = 0.05$$

This number density corresponds to an altitude of 68 km in the Martian atmosphere. Solutions will be obtained for a non ionizing but reacting gas and a 2-species non-reacting gas consisting of the freestream species.

6 SURFACE AND FLOWFIELD MEASUREMENTS

6.1 Corner-Flow/Jet Interaction Model

Measurements concern mainly wall pressure distributions on the two plate surfaces as described in Section 4. In addition and when possible, visualizations by oil film deposit are used to identify the limits of the interaction zones ahead of the transverse jet injection.

6.2 Blunt-Body/Wake-Closure Model

The types of measurements depend on the instrumentation existing at each facility. Proposed measurements are the following:

6.2.1 CNRS Meudon

Aerodynamic measurements for C_l , C_d , C_m , and center of pressure will be measured by means of a three-component external balance with an accuracy varying from $\pm 2\%$ to $\pm 5\%$ according to the force range. Forces will be measured for the 3 flow conditions at unit Reynolds numbers of $28.5 \times 10^3 \text{ m}^{-1}$, $83.8 \times 10^3 \text{ m}^{-1}$, and $727.7 \times 10^3 \text{ m}^{-1}$ [part (a) of Table 1] and for model angles of attack of 0° , 5° , 10° , 15° , 20° , and 30° .

Heat fluxes will be measured by using the thin-wall technique with possible comparisons with infrared thermography mappings. Heat fluxes will be measured on the forebody, on the base surface, and along the rear sting. They will be recorded for the 3 flow conditions and for model angles of attack of 0° , 10° , 20° , and 30° . The near-wake density flowfield mapping will be achieved by means of electron-beam fluorescence. These measurements will be limited to 2 angles of incidence (0° and 10°) for only test conditions 1 and 2 as listed in part (a) of Table 1.

6.2.2 DLR Göttingen

The DLR research will examine the effects of rarefaction using the wind tunnels V3G, V2G, and HEG. The tests that have been conducted by Legge (1993) with V3G concentrated on the aerodynamics and heating of a 5 mm base diameter copper model suspended by means of 0.06 mm diameter thermocouple leads. Lift and drag were determined by means of an electromagnetic two-component balance. The global aerodynamic heat transfer rate to the blunted cone model was determined by using the model itself as a calorimeter. The desired wall temperature is established and maintained at a constant value before the flow is started by means of two radiators (Figure 14). Specific details of measurements and data reduction are included in Legge (1993).

The studies that will be conducted in the V2G wind tunnel will concentrate on the wake flow along with flow visualization, force, and heat transfer measurements. Measurement techniques to be utilized are gas glow

discharge, liquid crystals, oil flow, and pitot and Patterson probes.

The studies to be conducted in HEG with 5 mm diameter models will focus on the combined effects of rarefaction and chemistry. The measurements will be confined to local surface heating rates on an array of four models, each with different thermocouple sensors.

6.2.3 DRA Farnborough

The DRA proposed tests would provide aerodynamic force and heat transfer measurements on NASA Langley supplied models. The force and moment measurements are to be made on two different size models in order to extend the Knudsen number range of the tests. Thin-film heat transfer gages will be used to infer wake features by measuring the heating-rate distributions along an instrumented sting. Heat transfer measurements are also to be made along the forebody and base plane of the heat transfer model.

6.2.4 University of California Berkeley

Aerodynamic measurements for C_l , C_d , C_m , will be obtained by means of a torsion balance for all test conditions and for angles of incidence of 0° , 5° , 10° , 15° , and 20° .

Surface heating rates will be measured by using the thin-wall technique along the forebody. Comparisons are possible with infrared surface temperature mappings. Heating rates will be measured at angles of incidence of 0° , 10° , and 20° for a model instrumented at 5 locations.

Near wake density mapping should be realized at 0° and 20° for flow conditions to be specified. Density measurements will be made using the electron-beam fluorescence method. Rotational and vibrational temperature measurements will also be made for N_2 , Air, and CO_2 . The use of the Patterson probe will also be explored to determine velocity and Mach number.

6.2.5 University of Oxford

Exploratory studies have been conducted in the Oxford hypersonic low-density wind tunnel for 70° blunted-cone configurations. Future tests on aerobrake models with afterbodies are planned as part of the continuing studies at Oxford on a wide range of geometries. Incidence up to 10° is planned and drag, lift, and moments are to be measured. Measurement options, as a minimum, would include aerodynamic forces, flow pitot probe measurements in the wake region and flow visualization.

7 TEST TECHNIQUES

Techniques of measurement may be specific for each facility. Devices and procedures described in the present Section concern the measurements performed in the SR3 wind tunnel of CNRS Meudon.

7.1 Wall-Pressure Measurement

Considering the open-jet configuration of the test section, the chosen procedure to measure wall pressures is to start the wind-tunnel without the model and, as soon as the flow conditions are correctly stabilized, to inject the model through the test section.

This procedure has two main advantages: firstly, it reduces the risk of flow blockage during wind-tunnel startup, and secondly, due to the short period of pressure measurement, it avoids a significant heating of the model. Without a water cooling system, the wall-temperature rise is limited to about 10 to 15 C during the pressure measurement. This makes it unnecessary to water cool the model, and, consequently, this allows an easier integration of the pressure tubes through the model walls.

A sting, rigidly fixed to the rear part of the model, provides the connection to a streamlined transverse support. This transverse support is mounted on a pneumatic jack which allows one to either inject or to remove the model from the test section.

A pressure bench, including 5 pressure transducers, is mounted inside the test chamber at a distance of about 400 mm from the test model. Validyne DP 103 transducers have a high sensitivity and allow wall pressure measurements as low as a fraction of a Pascal. The measurement principle is based on an inductance variation resulting from the displacement of a diaphragm inserted between two symmetrical pressure cavities. One cavity (measurement side) communicates to one of the pressure tubes leading to the pressure orifice on the model. The other cavity (reference side) communicates to a vacuum reference generated by a turbomolecular Turbovac 50 integrated to the pressure bench. The turbomolecular pump achieves a vacuum level of about 10^{-4} Pa. Output signals delivered by the transducers are applied to a five-channel recording unit. Due to the low level of wall pressures which have to be measured, out-gassing of the pressure tubes is made prior to each pressure measurement. Also, repeated pressure calibrations are necessary to get rid of possible zero shifts on the output signal.

7.2 Surface-Flow Visualizations

To define the flow mechanism over the corner-flow/jet interaction test model, flow visualizations have been obtained in addition to the wall pressure measurements. Surface-flow visualizations by oil-film deposit on a model are currently performed in conventional wind-tunnels. Nevertheless, they are more questionable at low flow densities characterized by a lower skin friction at the model surface. For the SR3 test conditions indicated in Section 5.1.1, oil-film visualizations have been possible only for the two highest flow densities (conditions 2 and 3).

7.3 Heat-Transfer Measurements

To measure heat fluxes, the thin wall technique is one of the most accurate methods. It gives heat-flux values with an uncertainty generally less than 10%.

The measurement procedure consists of starting the wind-tunnel without the model, and, as soon as the flow conditions are correct, the thin-wall model is rapidly injected through the test section. The surface temperature is locally measured using thermocouples embedded in the thin wall.

Knowing locally the thickness of the model wall and the thermal capacity of the material, the measured derivative of the wall temperature is directly related to the heat flux value. For the present experiment, Ch/Al thermocouple wires, 0.2 mm in diameter, are embedded in a thin wall, 0.4 mm thick, made of ARMCO steel of well known characteristics.

To avoid conduction effects through the wall, the temperature derivative is measured within the fractions of a second following the model injection, limiting to a few degrees the wall-temperature rise during the measurement.

7.4 Aerodynamic Forces and Moments

Under rarefied flow conditions, aerodynamic forces and moments are very small. Consequently, specific balances appropriate to low-density test conditions are necessary.

The sting balance configuration is commonly used for conventional wind-tunnel testing. In low-density wind tunnels, this configuration may also be replaced by external specific balances. The SR3 open-jet configuration makes easier the mechanical integration of such an external balance in the volume surrounding the test section. The three-component balance used for the present experiments is shown in Figure 15.

The balance makes possible the direct measurement of drag, lift, and pitching moment, and, indirectly, the determination of the center of pressure.

This type of balance requires prior calibrations to account for the drag of the wires connecting the external circular frame to the model. Due to the interchangeability of sensitive elements, the balance may cover a large range of forces extending from a few milligrams to a few tens of grams. The balance configuration is also designed to establish the center of pressure on models with fairly good accuracy.

Three independent dynamometers are utilized to measure the drag and the two lift components. A circular frame surrounding the test section is connected by a horizontal wire to the model. This frame transmits both the upstream lift component and the drag on the two corresponding dynamometers. The downstream lift component is transmitted through the vertical link wire.

During the test, the drag of the horizontal wire alone is measured and subtracted from the total drag measured with the model. The drag of the rear vertical wire is eliminated by enclosing the wire in a fairing. To avoid any interaction between the flow in the test section and the circular frame, a removable cylindrical screen is located, during the measurements, between the test section and the balance.

7.5 Flow-Density Measurements

Flow-density measurements are made by electron-beam fluorescence technique. In the SR3 test chamber, the electrons, accelerated by a 20 kV field, emerge from the gun through an orifice 1 mm in diameter, pass through the flow and are collected by a beam receiver located at some 500 mm from the gun exit. A photo multiplier collects the light emission of the fluorescent gas. The electron gun is mounted on a three-axis support, which is convenient to get density profiles through the whole volume of the test section. At rarefied conditions, corresponding to densities less than 10^{21} mol/m³, the fluorescence emitted by the gas is roughly proportional to the local density. For higher densities, quenching effects have to be taken into account in the data reduction. Also, due to possible parasite light reflection between the electron beam and the model wall, the density signal is not interpreted when the beam is located at distances less than 1 mm from the model wall.

8 AVAILABLE TEST RESULTS

8.1 Corner-Flow/Jet Interaction Experiment

The CNRS tests have been completed and the results are documented in Allègre and Raffin (1991, 1992). The 1991 experiments were performed with a model 100 mm in length. The 1992 experiments were made with a model 120 mm in length. The primary data from these experiments are wall pressure measurements (measurement coordinates for horizontal and vertical plates denoted in Figures 4 and 5). Data presented have not been corrected for orifice effects due to rarefaction (1 mm diameter orifices). Tabulated data along with selected graphical results for surface pressures are included in Allègre and Raffin (1991, 1992). The matrix of test conditions included three external flow conditions [part (a) of Table 1] at Mach 20, the jet at four stagnation chamber conditions (one is no injection), the vertical plate at two different locations relative to the jet, and the condition of no external flow with the jet operated at three flow conditions. Representative data are shown in Figure 16 for the most rarefied external flow case where the vertical plate is 15 mm from the jet. Wall pressure data are shown along Section A1 of the horizontal plate [(Figure 16(a))] and along the vertical plate in Figure 16(b).

For no external flow and a background pressure of about 2 Pa, the measurements show negligible interaction between the control jet and the external surface. With an

external flow, however, the interactions are very pronounced producing a separated region just ahead of the jet with a substantial increase in wall pressure on the horizontal plate. In the wake behind the jet, the horizontal plate experiences lower pressure than that for the no-jet test. The extent of the interaction is strongly dependent on the rarefaction level of the external flow as demonstrated in Figure 17 for two model configurations where the vertical plate is located 15 mm and 30 mm from the jet.

The maximum surface pressure occurs along the vertical plate [Figure 16(b)] as the control jet induced shock interacts with the vertical surface. The strength of the shock is a function of both the control jet and external flow conditions.

8.2 Blunt-Body/Wake-Closure

The first of several experimental test programs for the 70° blunted cone have been conducted with the V3G free-jet facility of the DLR, Göttingen. Drag, lift, global heat transfer, and recovery temperature were measured in a Mach 9 nitrogen free-jet flow. These measurements were made for various degrees of rarefaction by including most of the transitional regime ($0.03 < Kn_0 < 6$) for stagnation temperatures of 300 K and 500 K. The wall-to-stagnation temperature ratio was varied between 0.8 and 1.5. The copper model with a base diameter of 5 mm was suspended with a thermocouple (Figure 10) at angles of attack of $\alpha = 0^\circ$, 20° , and 40° . Details concerning the experiments, data reduction, data accuracy, and results are included in Legge (1993).

The drag coefficient (Figure 18) along with the other force coefficients have the usual behavior between continuum and free-molecular flow. That is, there is a smooth transition between the continuum and free-molecular values for complete accommodation. The aerodynamic curves for $T_0 = 300$ K and 500 K agree well, which means that the Knudsen number, $Kn_0 = 3.2\mu_0 d_b / \sqrt{\rho^2 2\pi RT_0}$ is a reasonable correlation parameter when T_0 is changed. This behavior is demonstrated in Figure 18 where the drag coefficient is plotted for $T_0 = 300$ K and $T_0 = 500$ K at $T_w/T_0 = 1$. For $\alpha = 0$, $T_0 = 1100$ K and $T_w = 300$ K, two numerical results (Dogra et al. 1993) are also included: (1) $M_\infty = 20.2$, $\rho_\infty = 1.73 \times 10^{-5}$ kg/m³, $C_D = 1.61$, $Kn_0 = 0.11$ and (2) $M_\infty = 19.7$, $\rho_\infty = 5.19 \times 10^{-5}$ kg/m³, $C_D = 1.54$ and $Kn_0 = 0.038$. The smooth transition from continuum to free-molecular values was not observed for the heat transfer and recovery temperature data at the higher wall-to-total temperature ratios. The heat transfer coefficient, $C'_h = 2\dot{Q}/(\rho_\infty U_\infty^3 A \cos \alpha)$ where \dot{Q} is the global heat transfer rate and the cone reference area is, $A = \pi R_b^2$, follows the same curves for both $T_0 = 300$ K and $T_0 = 500$ K at $T_w/T_0 = 1.0$ as shown in Figure 19(a). At larger T_w/T_0 values, however, the absolute value of C'_h becomes smaller for $T_0 = 500$ K than $T_0 = 300$ K, indicating that the accommodation coefficients becomes

less with increasing T_w . This behavior is demonstrated in Figure 19(b) where C'_h is plotted as a function of Kn_0 for $T_w/T_0 = 1.4$, for the two total temperature conditions and three angles of attack.

9 AVAILABLE COMPUTATIONAL RESULTS AND COMPARISONS WITH EXPERIMENT

9.1 Corner-Flow/Jet Interaction

A sparse amount of computational data has been reported for this problem. Tartabini et al. (1993) included results of a DSMC simulation for the corner-flow problem without the jet for the most rarefied test case ($M_\infty = 20.2$ and $P_0 = 3.5$ bars). Comparisons of the computational and experimental surface pressures are shown in Figures 20(a) and 20(b) for the horizontal and vertical plates, respectively. The experimental data are shown in two forms: the data as published (Allègre and Raffin 1992) which were not corrected for orifice effects and the experimental data modified by an orifice correction factor (Potter and Blanchard 1990). For the orifice-corrected pressures, an energy accommodation coefficient of 1.0 and an orifice temperature of 300 K are assumed. In general, the corrected experimental data provides a better match to the calculated results. Overall, the agreement between the measured and calculated results is good.

For the case without a jet, good agreement between computed (DSMC) and experimental pressures have also been reported for the most rarefied case by Dupuis and Chauvot (1993). They also carried out the simulation for the jet interaction for the same external flow conditions where the jet was operated at a chamber pressure of 20 bars. For this case, it has been more difficult to realize good agreement between experiment and calculation. Figure 21 shows the extent of agreement on the vertical plate at the F1 Section (directly opposite the jet).

Results for the jet interaction are reported in Tartabini et al. (1994) for the same external flow conditions as the two previous examples with the jet operating at a chamber pressure of 4 bars (most rarefied conditions of the CNRS test matrix). The jet nozzle exit flow conditions were calculated by Cline (1981) with the Viscous Nozzle Analysis Program (VNAP2). This code is a time-dependent, finite-difference, full Navier-Stokes solver. The output of the VNAP2 solution at the nozzle exit plane was then interfaced with the external 3-D DSMC solution. For the calculated results included in Figure 22, the interfacing was accomplished by maintaining the VNAP2 exit mass flow rate, imposing a constant density at the interface, and maintaining the VNAP2 axial velocity with a superimposed random thermal velocity. Comparison of the experimental (without orifice correction) and computational data are presented in Figure 22 along the vertical plate for Section F1. The agreement is seen to be poor.

The computational results that have been obtained with jet interaction involved interfacing continuum and DSMC

procedures. Currently, the computational studies have not demonstrated the sensitivity of the results to how the interfacing is implemented, nor have they demonstrated the sensitivity to grid resolution. As additional studies are made to resolve these issues, the credibility of the computational results will become more secure. Furthermore, Navier-Stokes solutions coupling the nozzle and external corner-flow/jet interaction would be a valuable contribution.

9.2 Blunt-Body/Wake-Closure

9.2.1 Wind-Tunnel Conditions

Results of calculations are presented in Moss et al. (1993a,b) for the three freestream test conditions for which experiments will be performed in the SR3 tunnel at CNRS. The specific test conditions are included in part (a) of Table 1, and all of the calculated results are for zero angle of incidence. Moss et al. (1993b) is a data report that presents in considerable detail the flowfield and surface results as obtained with an axisymmetric DSMC code (Bird 1976). The results presented in Moss et al. (1993a,b) include a sting afterbody with the same diameter as that for the proposed CNRS tests. Wilmoth et al. (1993) present results for the blunted cone without an afterbody. Comparisons of DSMC and Navier-Stokes results for these test cases are included in these references. Examples of the computed results are presented in Figures 23 and 24 for the near-wake density contours and surface heating, respectively, for test condition 2 [(Table 1, part (a))]. These calculations show (Figure 25) that the wake stagnation point (the point in the wake where the separated flow reattaches) and the location of the maximum convective heating rate along a sting/afterbody is not coincident. Furthermore, the separation between the two locations is a function of rarefaction. The heating along the base plane is two to three orders of magnitude lower than the forebody stagnation point value; the ratio decreasing as rarefaction increases. Comparisons of Navier-Stokes results [obtained with the Langley Aerothermodynamic Upwind Relaxation Algorithm (LAURA) by Gnoffo (1990)] with DSMC results are discussed in Wilmoth et al. (1993) and Moss et al. (1993a). The surface heating rate comparisons show good agreement along the cone forebody but significant difference along the base plane and sting. As for the flowfield structure in the wake, the comparisons show poor agreement for the most rarefied case and good agreement for the least rarefied case. Use of the slip boundary condition option in the LAURA code provided, in general, improved agreement with the DSMC results. Direct comparison with experiment can be made when the experiments are completed. As shown in Figure 18, the DSMC calculated drag coefficient is in good agreement with the data obtained in the V3G facility of DLR when plotted as a function of total Knudsen number, Kn_0 (Dogra et al. 1993).

9.2.2 Flight-Test Cases

The flight test cases consists of four individual cases to provide code-to-code comparisons. No experimental results are available for these test cases. The test cases are for both Earth and Mars entry using both reacting and non-reacting gas models. The freestream and surface boundary conditions are specified in Section 5. Only results for Earth-entry conditions have been reported (Çelenligil 1993; Dogra et al. 1994). Dogra et al. (1994) present results for both reacting and non-reacting air using the DSMC model and results for reacting air using an axisymmetric 3-temperature, 5-species implicit Navier-Stokes code (Olynick and Hassan 1993). In addition, DSMC solutions for a reacting 5-species air model have been obtained by Çelenligil.

The DSMC and Navier-Stokes results of Dogra et al. (1994) were in close agreement for the wake flowfield quantities. Also, the size of the vortex as measured from the base of the blunted cone to the wake stagnation point is identical for the two solutions. However, there are some noticeable differences in the chemical composition within the wake. The most significant difference between the two solution methodologies is in the surface heating calculations along the base plane (Figure 26). The Navier-Stokes results are 25 to 200 percent greater than the DSMC results, while good agreement exists along the forebody. Also, the two DSMC calculations using 5-species reacting air gas models are in good agreement for the surface heating rates. When the calculation is made with a non-reacting gas model as was done in Dogra et al. (1994), the results when compared with the reacting air solution shows: much higher surface heating rates, particularly along the base plane (240% higher); a smaller vortex; similar values for the wake density contours (Figure 27); and essentially the same value for drag.

9.3 Issues Associated with Experimental and Computational Comparisons

Experimental data comes from investigations conducted in low-density hypersonic facilities. For such flows, it is difficult to design contoured nozzles of good quality. Consequently, many facilities utilize conical nozzles (CNRS, DLR) or free jets (DLR, UCB, LDWT Oxford). This implies the existence of density and Mach gradients through the test section.

As an example, for a SR3 conical nozzle which corresponds to a Mach number of 20 and to an unit Reynolds number of $83.8 \times 10^3 \text{ m}^{-1}$, the Mach-number gradient $\Delta M/M$ along the test section centerline is about 3% over a distance of 100 mm distance which corresponds to typical model lengths for slender bodies. The transverse Mach-number gradient is approximately 5% over a diameter of 80 mm.

The Mach-number gradient along the test section may be lowered by reducing the angle of divergence of the nozzle, but, on the other hand, the correlative lengthening of the divergent section leads to increased boundary-layer thickness, which may contribute to reducing the test core of the nozzle. For the conical hypersonic nozzles used in the SR3 wind tunnel, and according to the level of flow rarefaction, the divergent half angles are 15° ($\text{Re} = 28.5 \times 10^3 \text{ m}^{-1}$), 12.5° ($\text{Re} = 83.8 \times 10^3 \text{ m}^{-1}$) and 10° ($\text{Re} = 727.7 \times 10^3 \text{ m}^{-1}$).

Flow gradients through the test section may lead to some uncertainty in the experimental data. However, despite this limited uncertainty, computational and experimental comparison still remain a basic element for establishing the credibility of the computational approach.

10 PROGRESS AND EXPECTED SCHEDULE

10.1 Experimental Research

10.1.1 Corner-Flow/Jet Interaction Tests

The CNRS Meudon test (Allègre and Raffin 1991, 1992) are completed. Discussions, however, are taking place concerning additional calibration tests for the jet mass flow rate. A final determination has not been made concerning additional calibration tests.

As indicated in Section 5.1.1, the DLR Göttingen test model exists; however, details concerning the test conditions and schedule have not been established.

10.1.2 Blunt-Body/Wake-Closure Tests

The CNRS Meudon experiments are to be completed during the first quarter of 1994. The DLR Göttingen tests in V3G are completed (Legge 1993). Wake measurements using the Patterson probe for 25 and 50 mm diameter models suspended by wires in V2G are to be completed in the first quarter of 1994. The remaining tests in V2G and the HEG heating rate experiments are to be completed during 1994. The DRA Farnborough tests are contingent on NASA Langley supplied models; and a specific schedule for model delivery has not been established.

Progress has been made at the two universities contributing to the experimental program. Cal-Berkeley has two graduate students committed to this research: one focusing on force measurements and the other on flowfield density measurements. Initial results from this activity are anticipated in the first quarter of 1994. Oxford has recently enhanced their magnetic suspension and force measuring system and has completed preliminary tests on aerobrake models. These test results are to be submitted for inclusion in the Rarefied Gas Dynamics Symposium in 1994 together with DSMC predictions. Both demonstrate anomalous behavior of the drag coefficient which is not exhibited by aerobrake models without afterbodies as shown in Figure 18 where

C_D varies monotonically with Kn_0 . Future testing on aerobrake geometries is planned.

10.2 Computations

Published results of multiple calculations are anticipated in 1994 for several of the experimental and flight test cases. As more specific information becomes available concerning test conditions and measurements, additional computational contributions are expected.

11 OTHER EXISTING DATA BASES

Existing data bases for the two test cases under consideration are quite sparse from both the experimental and computational perspectives. However, recent interest in the blunt-body/wake closure test case has generated several numerical studies that have begun to isolate critical features of wake structure for the current test configuration (Çelenligil 1993; Dogra et al. 1994; Gallis and Harvey 1994) as well as specific planetary probes and aerobrakes (Brewer 1993). Two examples of relevant experimental data for the blunt body case is given in Muthoo and Brundin (1982) and Heyman et al. (1992). Muthoo and Brundin (1982) presented experimental data for the flow structure along the wake centerline produced by a sphere at $M_\infty = 5.6$ and $Kn_\infty = 0.005$. The experiments were run in the University of Oxford low-density wind tunnel. Heyman et al. (1992) report on the forebody and afterbody heating rates obtained in a vacuum chamber facility (Mach 7 for Kn_0 of 0.057 to 0.178) for candidate Venus aerobraking spacecraft. DSMC calculations have been made for both experimental data sets and the comparisons of the DSMC results with the measured flow structure (Brewer 1993) and the afterbody heating (Heyman et al. 1982) have been shown to be favorable.

Jets in crossflow are basic flowfields which are relevant to a wide variety of applications as is discussed in Cantwell et al. (1993). Yet, only a small subset of this activity has been devoted to RCS jets for space vehicle control. The present model problem of the corner-flow/jet-interaction test case addresses the practical issues of space vehicle control jet configurations. Plumes may have a significant effect not only on the surface containing the jet nozzle, but also on other external surfaces surrounding the plume region. Therefore, results from simpler configurations such as flat plates and delta wings with jet controls do not correspond to practical RCS configurations. Allègre and Raffin (1993) review the results for both the simpler (delta wing) and the current corner-flow configuration with transverse control jets. The data that have been obtained and those that will be obtained during 1994-95 are unique and should be very valuable in the bench-marking of computational tools that are appropriate for such flows. Results of this type will be available in the Phase II report of AGARD Working Group 18.

12 RECOMMENDATIONS

A critical priority is to insure that multiple experiments are realized for both test cases: the corner-flow/jet interaction case and the blunt-body/wake-closure case. With a data base consisting of multiple sources, a more critical assessment can be made regarding the data consistency, reliability, and usefulness.

As specific test conditions are defined for the various experiments, it is important that this information be made widely available so as to encourage computational contributions. Researchers are encouraged to present and publish their findings quickly in a forum at their discretion. This approach should facilitate an open and cooperative resolution of issues associated with both test cases, and encourage infusion of lessons learned from the initial studies into the proposed research that will take place during 1995-96.

Additional computational participation is desirable for both test cases, particularly the corner-flow/jet interaction case which presents an interesting challenge to properly account for the coupling between continuum and rarefied flow regimes. For the blunt-body flight cases (Earth and Mars entry), a diversity of chemical and thermochemical modeling approaches is solicited. In order to better appreciate the importance of the chemistry on the results as well as possible differences in the computational results, it is strongly encouraged that a given code be exercised with and without reacting chemistry.

REFERENCES

- Allègre, J. and Raffin, M. 1991 Experimental Study on Control Jet Interaction. *SESSIA Report 608/91.1043/CNRS Aerothermique RC-91-11*.
- Allègre, J. and Raffin, M. 1992 Experimental Study on Control-Jet/Corner-Flow Interaction. ESA contract, *CNRS Report RC92-7*.
- Allègre, J. and Raffin, M. 1993 Jets Transversaux En Interaction Avec Des Ecoulements Hypersoniques Rarefies. in *AGARD CP 534*, Paper 19.
- Bird, G.A. 1976 *Molecular Gas Dynamics*, Clarendon Press, Oxford.
- Brewer, E.B. 1993 Hypersonic Rarefied Wake Characterization. *NASA TP-3327*.
- Cantwell, B., Çiray, C. and Jimenez, J. (Editors) 1993 Computational and Experimental Assessment of Jets in Cross Flow. *AGARD CP 534*.
- Çelenligil, M.C. 1993 *Personal communication* Middle East Technical University, Ankara 06531, Turkey.
- Cline, M.C. 1981 VNAP2: A Computer Program for Computation of Two-Dimensional, Time-Dependent, Compressible, Turbulent Flow. Los Alamos Scientific Laboratory *Report LA-8872*.
- Dogra, V.K., Moss, J.N., and Price, J.M. 1993 Near Wake Structure for a Generic ASTV Configuration. *AIAA Paper 93-0271*.
- Dogra, V.K., Moss, J.N., Wilmoth, R.G., Taylor, J.C., and Hassan, H.A. 1994 Effects of Chemistry on Blunt Body Wake Structure. *AIAA Paper 94-0352*.

- Dupuis, D. and Chauvot, J.F. 1993 Validation du Code JMC3D Sur un cas Experimental d'interaction Entre un Jet et un Ecoulement Hypersonique. Aerospatiale/Hermes contract, Report HERMES HNT 1253 ASPM.
- Gallis, M. and Harvey, J. 1994 Simulation of Chemically Reacting Flowfields Around a Generic ASTV Configuration Including the Wake. *AIAA Paper 94-0353*.
- Gnoffo, P.A. 1990 An Upwind Biased, Point Implicit Relaxation Algorithm for Viscous, Compressible Perfect-Gas Flows. *NASA TP-2953*.
- Heyman, R.J., Schmitt, D.S., Alexander, S.G., and Bienkowski, G.K. 1982 Base Heating on a VOIR Aerobraking Configuration in Rarefied Flow. *AIAA Paper 82-0877*.
- Legge, H. 1993 Heat Transfer and Forces on a Blunted 70 deg Half Angle Cone Measured in Hypersonic Free Jet Flow. *DLR Göttingen report IB 222-93 A 33*.
- Moss, J.N., Mitcheltree, R.A., Wilmoth, R.G., and Dogra, V.K. 1993a Hypersonic Blunt Body Wake Computations using DSMC and Navier-Stokes Solvers. *AIAA Paper 93-2807*.
- Moss, J.N., Dogra, V.K., and Wilmoth, R.G. 1993b DSMC Simulations of Mach 20 Nitrogen Flows About a 70° Blunted Cone and its Wake. *NASA TM 107762*.
- Muthoo, S.K. and Brundin, C.L. 1982 Near Wake Flow Field Measurements Behind Spheres in Low Reynolds Number Hypersonic Flow. *Ninth Int. Sym. on Rarefied Gas Dynamics, 1:B, 10-1*.
- Olynick, D.R. and Hassan, H.A. 1993 New Two-Temperature Dissociation Model for Reacting Flows. *J. Thermophysics and Heat Transfer, Vol. 7, 687*.
- Potter, J.L. and Blanchard, R.C. 1990 Thermomolecular Effect on Pressure Measurements with Orifices in Transitional Flow. *Proc. 17th Intn'l Symp. on Rarefied Gas Dynamics*.
- Tartabini, P.V., Wilmoth, R.G., and Rault, D.F.G. 1993 Systems Approach to a DSMC Calculation of a Control Jet Interaction Experiment. *AIAA Paper 93-2798*.
- Tartabini, P.V., Wilmoth, R.G., and Rault, D.F.G. 1994 Systems Approach to a DSMC Calculation of a Control Jet Interaction Experiment. To be published in the *Journal of Spacecraft and Rockets*.
- Tauber, M., Henline, W., Chargin, M., Papadopoulos, P., Chen, Y., Yang, L., and Hamm, K. 1992 MESUR Probe Aerobrake Preliminary Design Study. *AIAA Paper 92-2952*.
- Wilmoth, R.G., Mitcheltree, R.A., Moss, J.N., and Dogra, V.K. 1993 Zonally-Decoupled DSMC Solutions of Hypersonic Blunt Body Wake Flows. *AIAA Paper 93-2808*.

Table 1. Low-Density Wind Tunnel Flow Conditions

	T_0 [K]	P_0 [bar]	M_∞	Re_∞ [cm ⁻¹]	$\rho_\infty \times 10^5$ [kg/m ³]	V_∞ [m/s]	T_∞ [K]	λ_∞ [mm]	nozzle	Gas
(a) SR3 Wind Tunnel, CNRS Meudon										
1	1100	3.5	20.2	285	1.73	1502	13.3	1.05	conical	N ₂
2	1100	10.0	20.0	838	5.19	1502	13.6	0.35	conical	N ₂
3	1300	120.0	20.5	7277	46.65	1633	15.3	0.04	conical	N ₂
(b) V2G Wind Tunnel, DLR Göttingen										
1	575	2	15.6	715	6.65	1082	11.6	0.33	conical	N ₂
2	675	5	16.5	1210	10.80	1174	12.2	0.21	conical	N ₂
3	775	10	16.9	1910	16.90	1257	13.3	0.13	conical	N ₂
(c) V3G Wind Tunnel, DLR Göttingen										
1	295	0.163	9.0	859	14.22	759	17.2	0.16	free jet	N ₂
2	295	0.0549	9.0	286	4.74	759	17.2	0.48	free jet	N ₂
3	295	0.0163	9.0	86	1.42	759	17.2	1.60	free jet	N ₂
4	295	0.0054	9.0	29	0.47	759	17.2	4.80	free jet	N ₂
(d) LDT, RAE Farnborough										
1	2105	3.1	8.6	108	5.1	2004	134	1.12	contoured	N ₂
2	1660	1.8	9.8	534	19.4	1793	82	0.23	contoured	N ₂
3	1450	2.0	9.8	691	24.3	1676	71	0.17	contoured	N ₂
4	1170	2.1	9.8	950	31.6	1502	58	0.12	contoured	N ₂
(e) RGWT, University of California, Berkeley (UCB)										
1	300	11.1	22.0	1469	14.40	760	3.1	0.45	free jet	N ₂
2	1000	20.3	24.5	399	4.19	1450	8.6	1.60	free jet	N ₂
3	2000	28.4	27.0	214	2.33	2000	14.3	3.00	free jet	N ₂
(f) LDWT, University of Oxford										
1	290	0.067	6	1090	41.7	763	35	0.08	contoured	N ₂
2	523	0.067	6	450	23.1	1025	63	0.19	contoured	N ₂
3	290	0.020	6	325	12.4	763	35	0.27	contoured	N ₂
4	523	0.020	6	134	6.9	1025	63	0.64	contoured	N ₂
5	290	0.009	7.5	84	2.2	734	24	1.25	free jet	N ₂

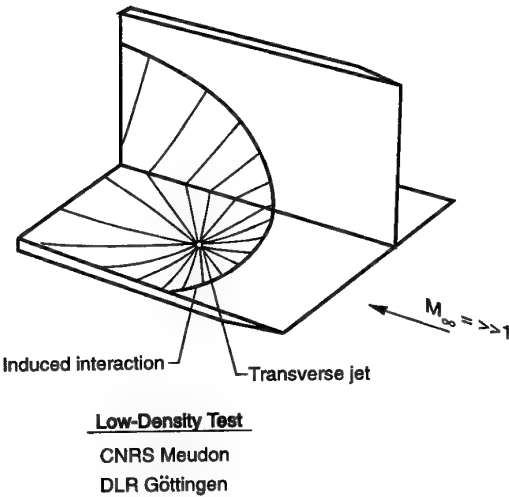


Figure 1. Schematic of corner-flow/jet interaction test model.

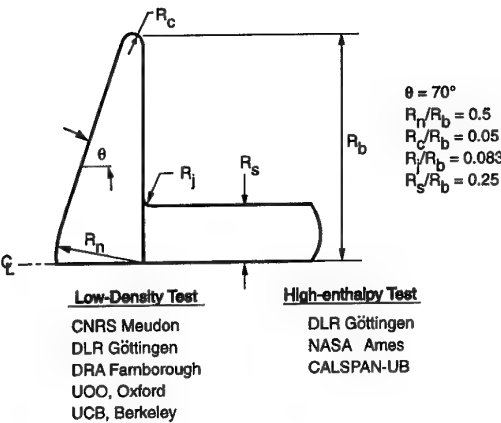


Figure 2. Blunt-body/wake-closure test model.

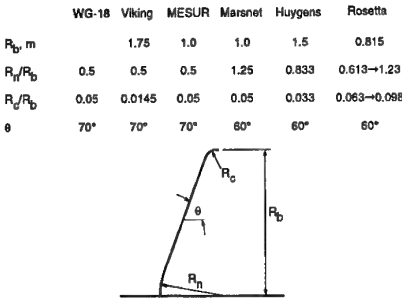


Figure 3. Planetary vehicle configurations and WG18 test model (MESUR configuration).

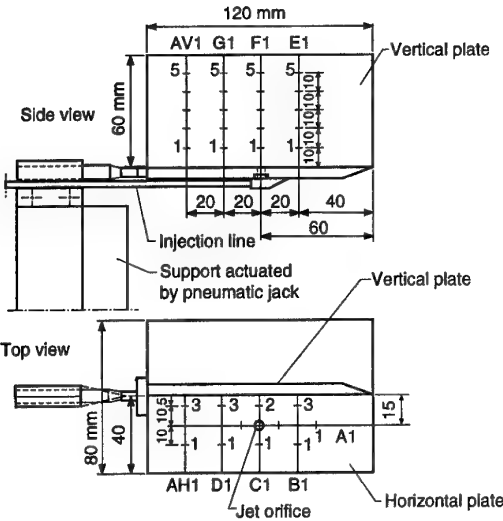


Figure 4a. CNRS Meudon corner-flow/jet-interaction test model with pressure orifice locations.

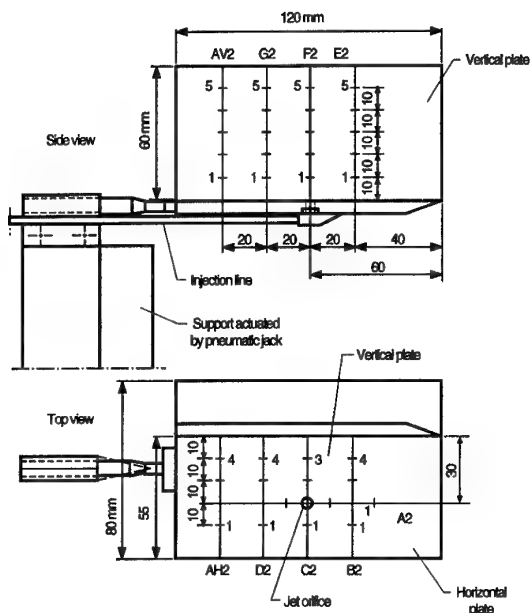


Figure 4b. Configuration 2 (vertical plate 30 mm from jet).

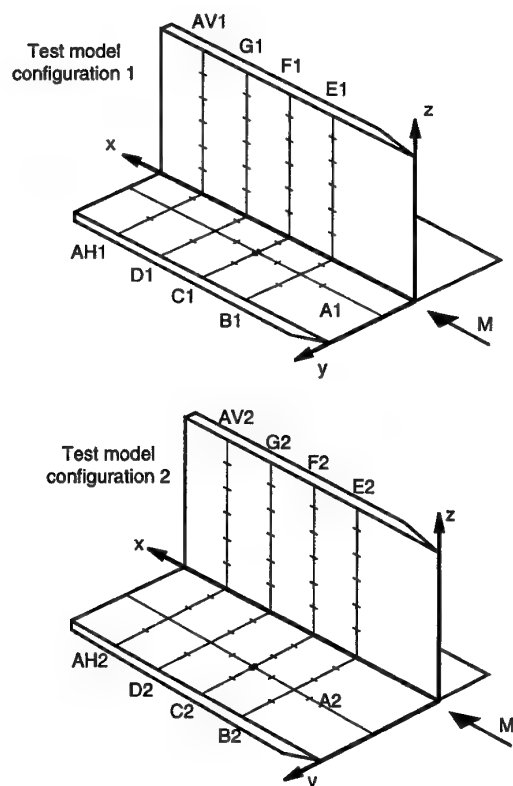


Figure 5. Reference coordinates for CNRS test model configuration.

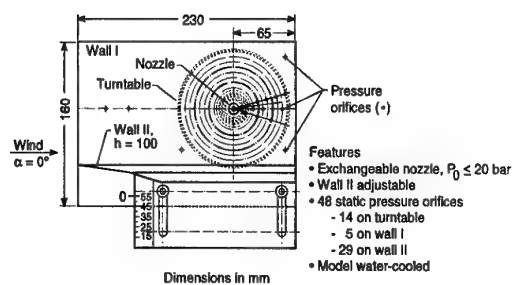


Figure 6. DLR Göttingen corner-flow/jet interaction test model with pressure orifices.

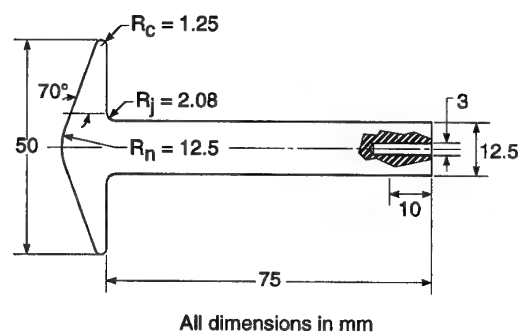


Figure 7. Force and moments models for CNRS tests.

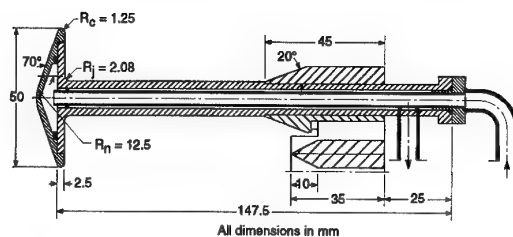


Figure 8. Water-cooled model for conducting near-wake density mappings (CNRS).

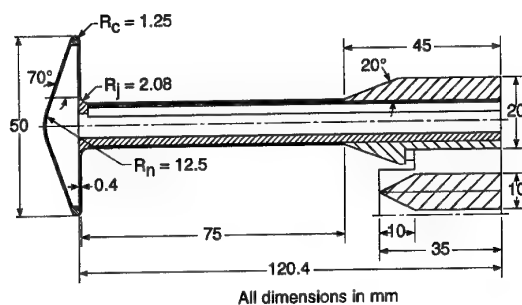


Figure 9. Model for heat-transfer-rate measurements (CNRS).

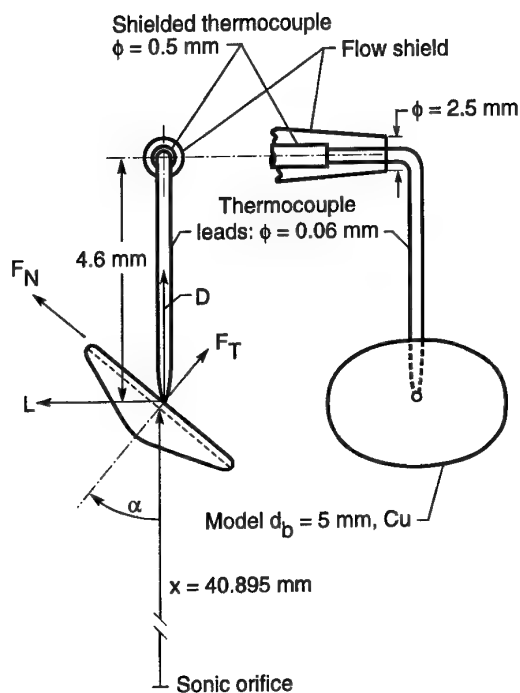


Figure 10. Suspension of cone model and coordinate system for global heat-transfer rate and force measurements in V3G (DLR Göttingen).

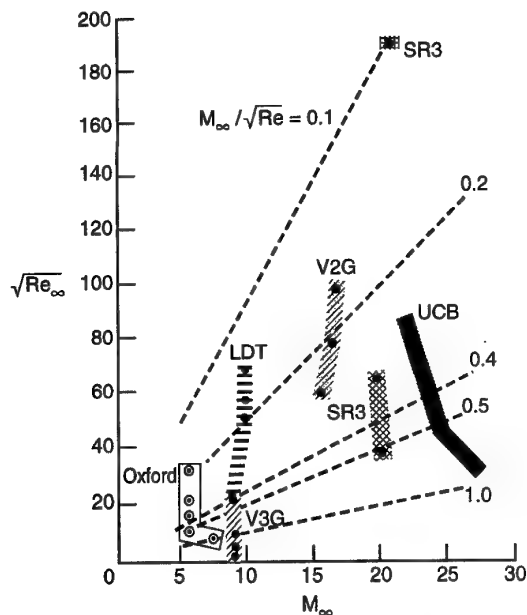


Figure 11. Low density wind tunnel conditions in terms of the rarefaction parameter $M_\infty/\sqrt{Re_\infty}$.

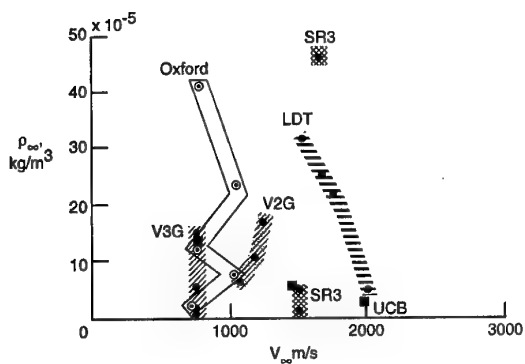


Figure 12. Low-density wind-tunnel conditions in terms of density and speed.

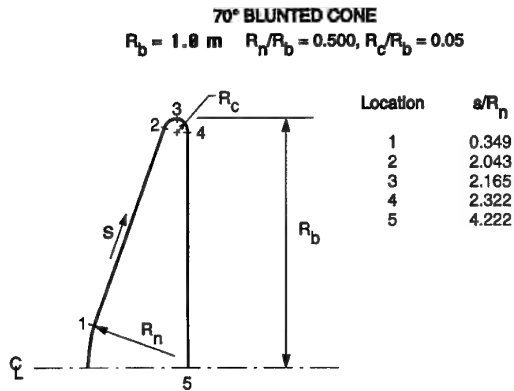


Figure 13. Flight test case configuration for Earth and Mars entry conditions.

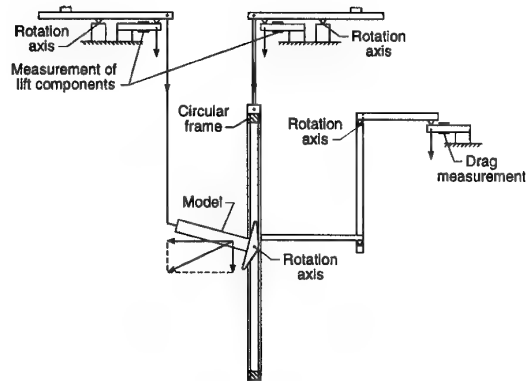


Figure 15. Three-component external balance (CNRS Meudon).

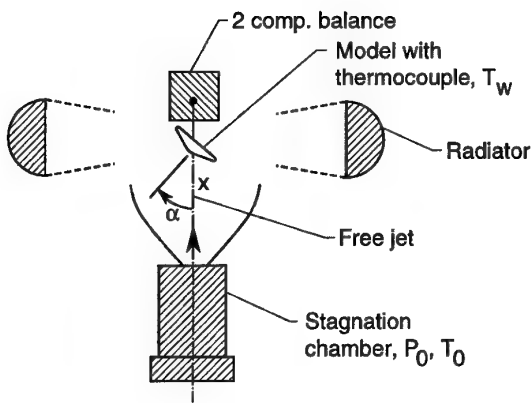


Figure 14. Scheme of experimental set-up for V3G Göttingen blunted-cone tests.

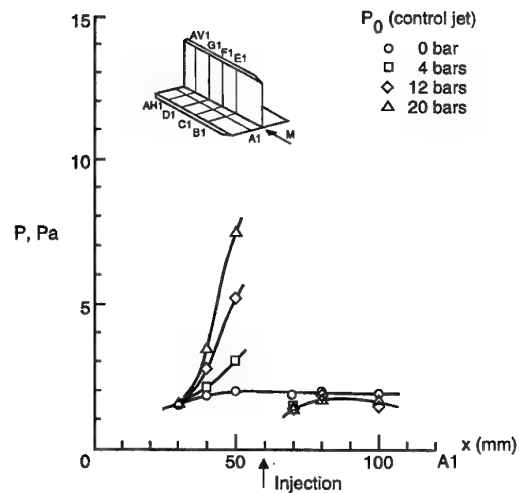


Figure 16a. Wall pressure distributions for Mach 20.2 external flow [Table 1, part (a), condition 1] and vertical plate located 15 mm from jet. (Horizontal plate)

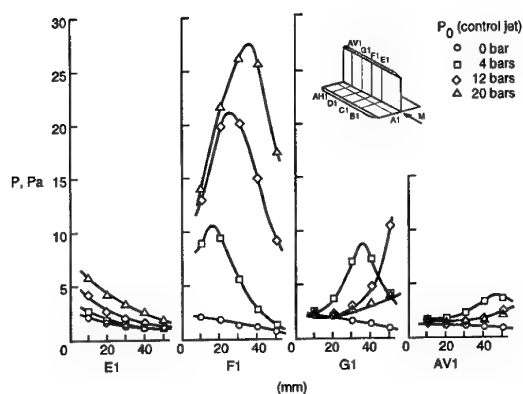


Figure 16b. Vertical plate.

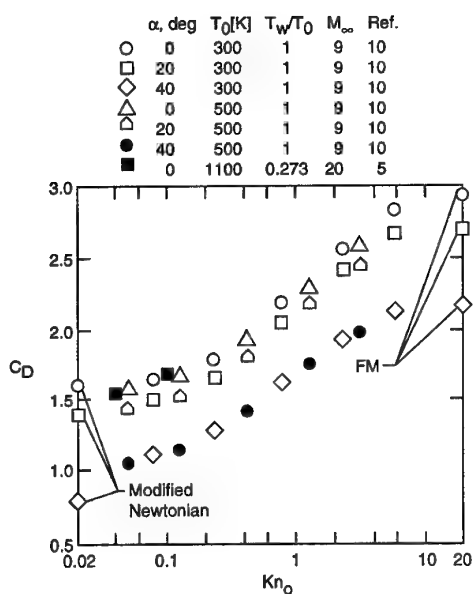
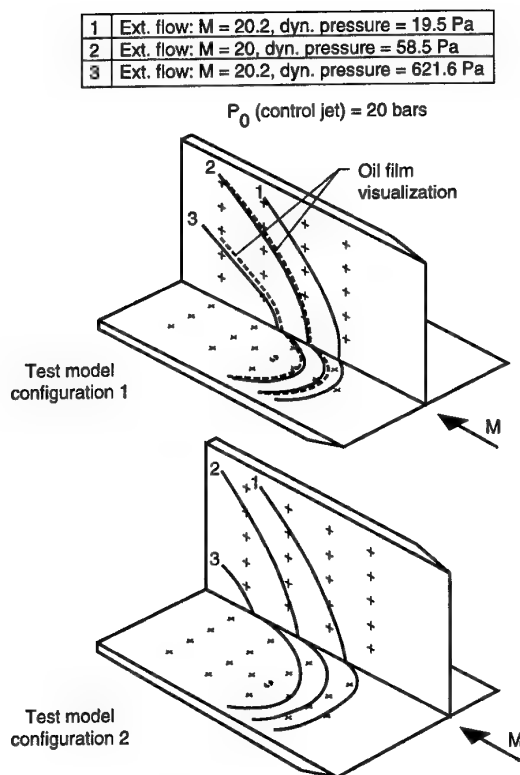
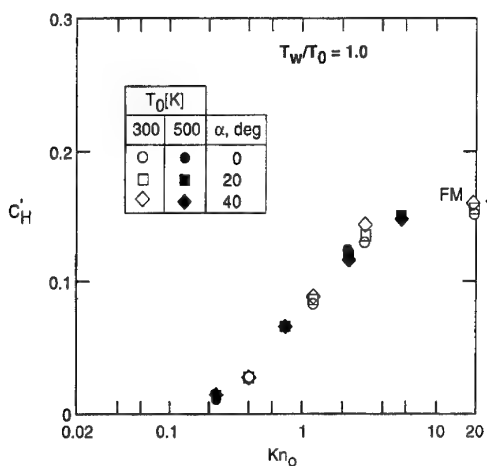
Figure 18. Drag coefficient as a function of Kn_0 and comparison of DSMC and experimental results for different flow conditions. (a) $T_w/T_0 = 1.0$.

Figure 17. Upstream limits of flow interaction as a function of the external flow rarefaction (CNRS Meudon).

Figure 19a. Heat transfer coefficients C_H' (based on $A' = A \cos \alpha$) as a function of Kn_0 (DLR Göttingen).

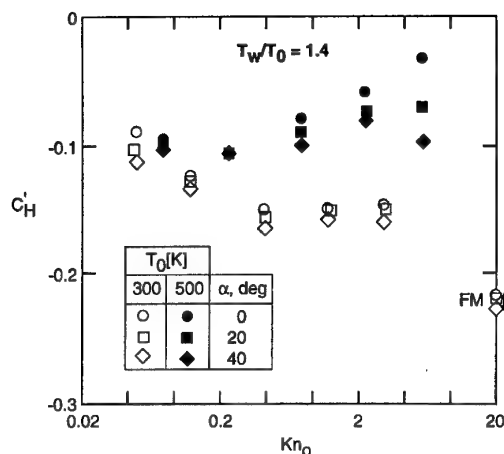
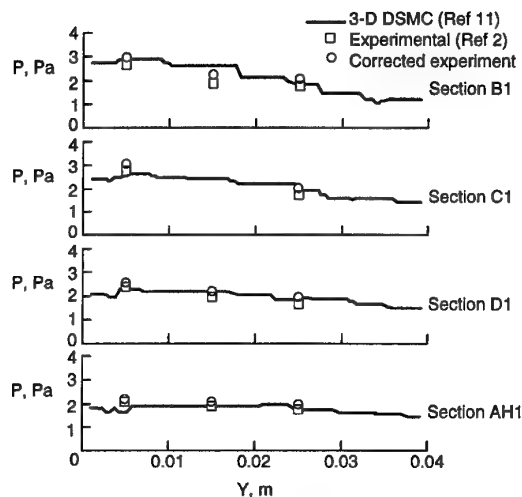
Figure 19b. $T_w/T_0 = 1.4$.

Figure 20a. Comparison of computed surface pressures with corrected and uncorrected measured wall pressures. (Horizontal Plate)

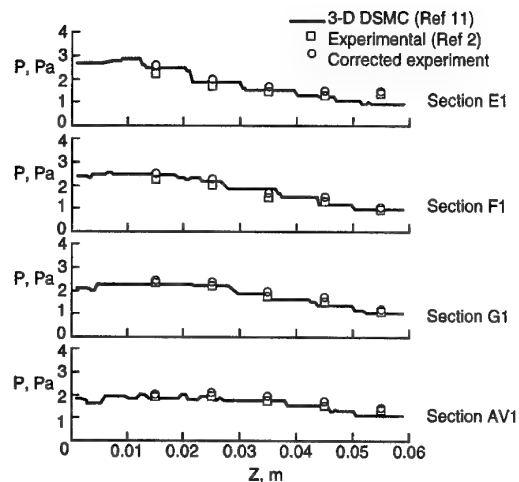


Figure 20b. Vertical Plate.

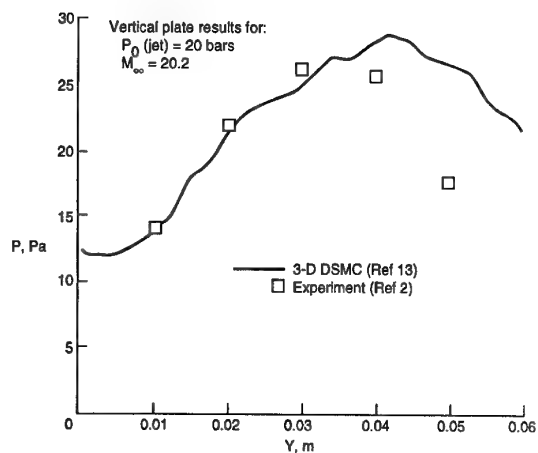


Figure 21. Comparison of computational and experimental results for corner-flow/jet interaction test case at section F1.

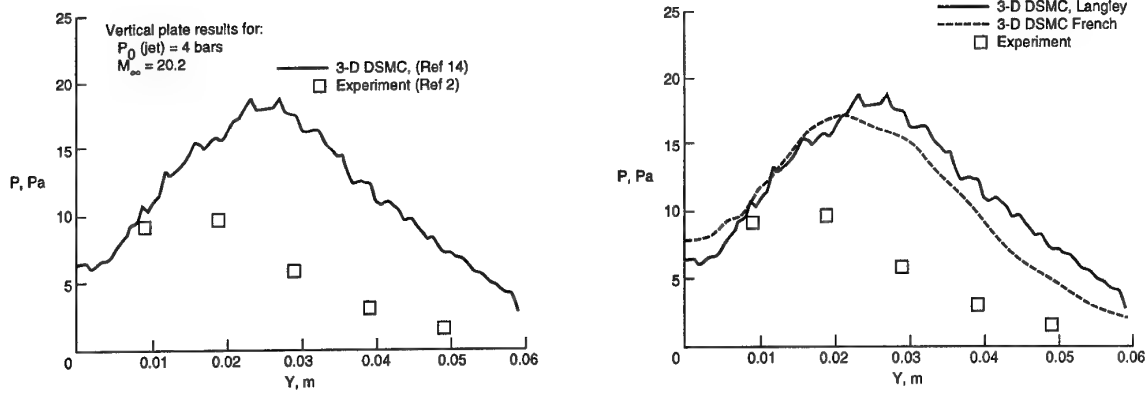


Figure 22. Comparison of computational and experimental results for corner-flow/jet interaction test case at section F1.

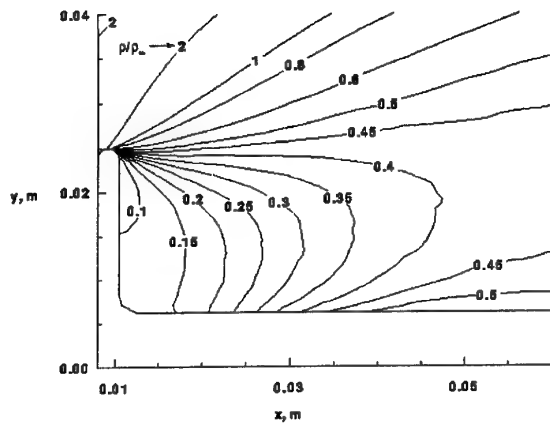


Figure 23. DSMC results for near-wake density contours [CNRS test condition 2, Table 1, part (a)].

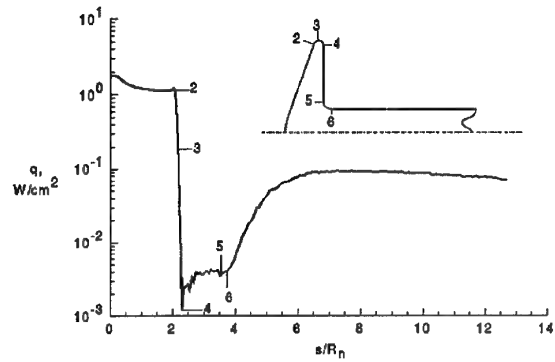


Figure 24. DSMC results for surface heating rates [CNRS test condition 2, Table 1, part (a)].

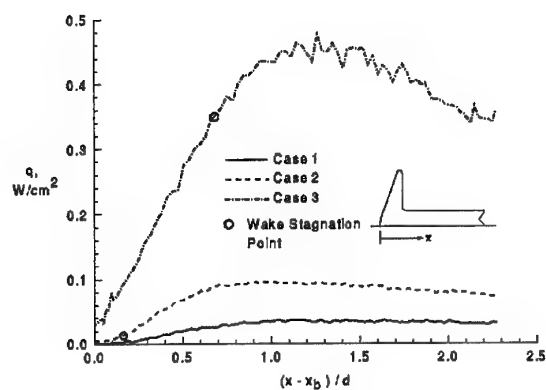


Figure 25. Calculated (DSMC) effect of rarefaction on sting heating [CNRS test cases, Table 1, part (a)].

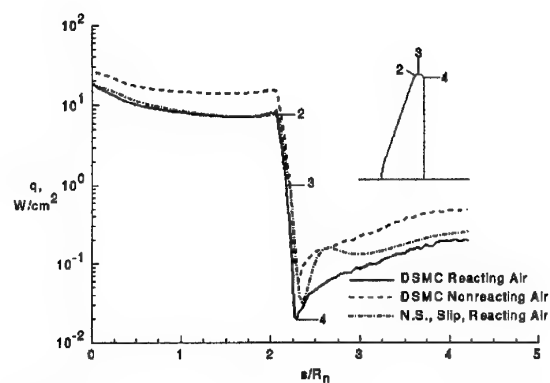


Figure 26. Computed surface heating rate distribution for flight test case in air (Alt = 85 km, $V_\infty = 7.0$ km/s).

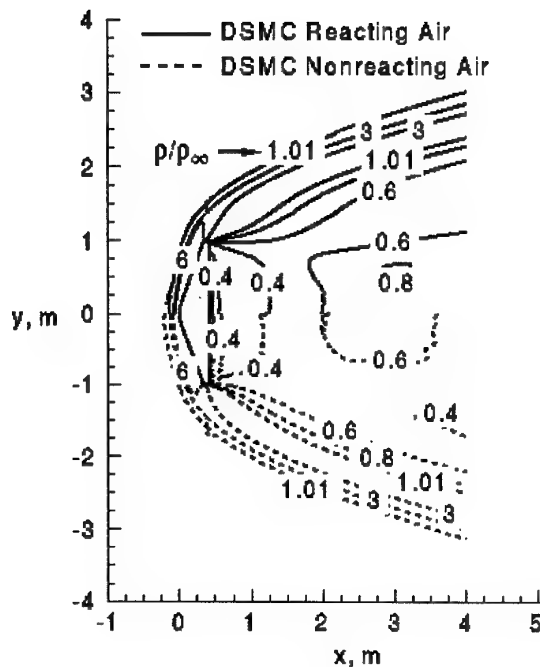


Figure 27. Computed density field for flight test case in air (Alt = 85 km, $V_\infty = 7.0$ km/s).

CHAPTER V

REAL-GAS EFFECTS

George S. Deiwert

MS 230-2/RT
NASA-Ames Research Center
Moffett Field, California, 94035-1000
USA

and

Mauricio Pandolfi

Politecnico di Torino
C. so Duca degli Abruzzi 24
10129 Torino
ITALIA

CONTENTS

1	INTRODUCTION	111
2	SCOPE OF PRESENT ACTIVITY	112
2.1	Aerodynamic Parameters	112
2.2	Forebody Heating/Heat Transfer	113
2.3	Lee and Base Flows	113
3	GROUND TEST FACILITY REQUIREMENTS	114
3.1	Aerodynamic Parameters	115
3.2	Forebody Heating/Heat Transfer	116
3.3	Lee and Base Flows	116
4	TEST CASES FOR CFD VALIDATION	117
4.1	Existing Data Bases	
	- Hemisphere/Cylinder/Blunt Cone/RAMC	117
4.2	Current Focused Test Activity	117
5	GROUND FACILITY LIMITATIONS	120
5.1	Aerodynamic Parameters	120
5.2	Forebody Heating/Heat Transfer	121
5.3	Lee and Base Flows	122
6	CONCLUSIONS	122
	REFERENCES	122
	FIGURES	124

1 INTRODUCTION

The flow behind the shock wave formed around objects which fly at hypervelocity behaves differently from that of a perfect gas. Molecules become vibrationally excited, dissociated, and ionized. The hot gas may emit or absorb radiation. When the atoms produced by dissociation reach the wall surface, chemical reactions, including recombination, may occur. The thermochemical phenomena of vibration, dissociation, ionization, surface chemical reaction, and radiation are referred to commonly as high-temperature real-gas phenomena. These phenomena cause changes in the dynamic behavior of the flow and the surface pressure and heat transfer distribution around the object.

The character of a real gas is described by the internal degrees of freedom and state of constituent molecules. The internal energy states (rotation, vibration and electronic) of the molecules are excited and, in the limit, the molecular bonds are exceeded and the gas dissociates into atomic and, possibly, ionic constituents. The process of energy transfer causing excitation, dissociation and recombination is a rate process controlled by particle collisions. Binary collisions are sufficient to cause internal excitation, dissociation and ionization while tertiary collisions are required to recombine the particles into molecular constituents. If the rates of energy transfer are fast with respect to the local aerodynamic time scale, the gas is in, or nearly in, *equilibrium*. If the energy-transfer rates are very slow, the gas can be described as *frozen*. In all other instances, wherein any of the energy exchange rates are comparable to the local aerodynamic time scale, the gas will be thermally or chemically reacting and thus, *nonequilibrium*.

Each of the definitive states of a real gas, i.e. equilibrium, frozen, or reacting, can be applied to a gas undergoing compression and heating, such as the gas flowing through a strong shock ahead of a bluff body, or to an expanding and cooling gas, such as a gas flowing away from a stagnation region of a bluff body or into a base region. In the first case the gas will be thermally excited and dissociate and ionize; in the second, the atomic constituents will recombine and internal energy states will relax to lower energy levels.

A real gas implies the existence of any, or all, of the above states. This includes the possibility that a real gas can look identical to a perfect gas or a chemically-frozen gas. In a real-gas flow the model scale is a primary parameter. The possibility exists to generate a spectrum of "real-gas" test conditions at a single geometrically-similar test point. These flows can vary from frozen to equilibrium flow.

In the limit of chemically-frozen flow there is little value to "real gas" experimentation in the nose region; if the flow is frozen at the stagnation point it will remain frozen as it expands about the blunt nose and over the afterbody where it may equilibrate. Nose-region information for such a flow will be identical to perfect-gas wind-tunnel results and can be predicted reliably within the limits of our knowledge of thermodynamic and transport properties. Afterbody data, however, may be of somewhat greater interest, particularly data describing flow over secondary surfaces which may induce further chemical activity.

Similarly, for chemical-equilibrium flow, "real-gas" experiments are not required. In this case, the extrapolation from a perfect gas to a real gas is straightforward, involving appropriate thermodynamic and transport properties for the reacting gas species.

Between these two limits, in the region of reacting-gas flows, is the greatest uncertainty and the greatest need for test data. Facilities required for CFD validation of high-enthalpy flows, and for developing and verifying phenomenological models, are devices capable of generating a reacting-gas flow over configurations of interest and must have sufficient diagnostics to describe the character and behavior of the flow.

Ground facilities which, although they have serious limitations in simulating full-scale flight conditions, are capable of examining selected aspects which are expected to be vital to success in the full-scale flights. Theoretical analyses of the real-gas phenomena, based on quantum and statistical mechanics, require experimental verification in order to assure that the analyses correctly account for all vital phenomena. The ground-test facilities offer the advantage of observations, such as optical flow visualization, which are impractical to perform in actual flight conditions. For these reasons, impulse tunnels, which include shock tubes, shock-tube wind tunnels (shock tunnels), and hot-shot wind tunnels (hot-shot tunnels), ballistic ranges, and arc-jet wind tunnels, have been built and operated since the 1960s. The experiments made therein have been effective in verifying to a first-order the results of some of the theoretical works. But

neither analysis nor test has approached the level of maturity achieved by those for the lower-flight-speed ranges.

In Chapter I, the aerothermodynamic problems are classified into seven types. Several of these problem types are the subject of the preceding chapters, some are discussed in detail in this chapter, and some are outside the scope of the present study. Facilities suitable for tests, difficulties with the facilities, and the calibration procedures necessary for the facilities are discussed herein and in Chapters VI and VIII.

2 SCOPE OF PRESENT ACTIVITY

In this chapter the issues of real gas effects on Aerodynamic Coefficients, Forebody Heating/Heat Transfer, and Lee and Base Flows are discussed. Viscous Interactions were discussed in Chapter II, Transition to Turbulence in Chapter III, and Low Density in Chapter IV. Radiation and Ablation are not treated.

2.1 Aerodynamic Coefficients

The Shuttle Orbiter flight test program has required the aerodynamicist to take a new approach in determining flight characteristics. The initial series of flights of the Shuttle Orbiter were heavily instrumented for the purpose of obtaining accurate aerodynamic data. The flight data derived from the entry Mach range provided for comparisons between flight and wind-tunnel data in the areas of both aerodynamic performance and longitudinal trim. Romere and Whitnah (1983) examined these data and showed that, in the continuum flight regime (altitudes below about 85 km), lift and drag were smaller during the Shuttle Orbiter flights than predictions based on ground test in perfect-gas wind tunnels. The center of pressure (*CP*) is displaced forward by as much as 0.7% of the overall fuselage length compared with predictions based on perfect-gas observations. This result, which is attributed to real-gas effects, is quite large considering the fact that the full deflection of the control surfaces were expected to produce a *CP* shift of, at most, about 1% of the overall length. A plot showing the comparison of *CP* location determined from flight data with preflight predictions is shown in Figure 1. Griffith and Maus (1983) show that the observed discrepancy is due, at least in part, to high-temperature real-gas effects.

Rakich et al. (1983) explain this phenomenon by performing a computational study of real-gas flows over simple wedges and cones and the flow over the Orbiter forebody. The nonequilibrium flow behavior over a pointed cone at zero incidence is described in a qualitative manner as shown in Figure 2 which illustrates the variation in bow-shock shape and a typical species (atomic oxygen) distribution over the conical forebody. Even though the body is conical, the flow has a scale that depends on the time constant for pertinent species reactions. Near the apex of the cone there is a region where time is insufficient for reactions to occur. Here the flow is conical and the species concentrations are nearly frozen at their freestream values. As the fluid moves downstream of the apex the species begin to thermalize and the flow is out of equilibrium. Far downstream, all of the reactions have equilibrated, and even those reactions induced locally by the

bow shock equilibrate in a short distance relative to the larger shock standoff distance. A quantitative description is shown in Figure 3 where the computed variation of bow-shock angle is shown for a 30° half-angle wedge at conditions corresponding to an altitude of 65.5 km and a flight speed of 6.7 km/s. These conditions are typical of the high laminar heating portion of the Shuttle Orbiter entry trajectory. And finally, in Figure 4 is shown the computed shock shapes for the Shuttle Orbiter forebody for both a perfect gas and reacting gas. These computations correspond to a flight speed of 6.7 km/s, and altitude of 65.5 km, and an angle of incidence of 30° .

Park and Yoon (1991) performed a computational study of real-gas effects on airfoil aerodynamic characteristics. The results of this study showed that the aerodynamic lift and drag coefficients are consistently reduced by thermochemical real-gas phenomena, and that, for air, the behavior can be represented by a value of γ less than the perfect-gas value of 1.4. The computed center of pressures were observed to shift forward due to the thermochemical phenomena, but the extent of the shift is also sensitive to geometry and angle of attack, and cannot be represented by a fixed value for γ . The calculated results are illustrated in Figure 5 for an airfoil of chord length 10 m, at an altitude of 74 km, a speed of 7 km/s, and an angle of incidence of 40° . These results are in qualitative agreement with the data obtained during the entry flights of the Shuttle Orbiter. Included are results for a reacting gas and results for perfect gas at constant γ values of 1.4 and 1.2. It can be seen that the constant γ of 1.2 solution agrees well with real-gas predictions for lift and drag but fails to adequately represent the CP shift between a real-gas solution and $\gamma = 1.4$ solution.

2.2 Forebody Heating/Heat Transfer

Real-gas thermochemical nonequilibrium processes are also important in the determination of aerodynamic heating; both convective (including wall catalytic effects) and radiative heating. To illustrate this we consider the hypervelocity flow over a bluff body typical of an atmospheric entry vehicle or an aerospace transfer vehicle (ASTV.)

The qualitative aspects of a hypersonic flowfield over a bluff body are discussed in two parts, forebody and afterbody, with attention to which particular physical effects must be included in an analysis. This will indicate what type of numerical modeling will be adequate in each region of the flow.

A bluff forebody flowfield, illustrated schematically in Figure 6, is dominated by the presence of the strong bow shock wave and the consequent heating, and chemical reaction of the gas. At high-altitude hypersonic flight conditions, the thermal excitation and chemical reaction of the gas occur slowly enough that a significant portion of the flowfield is in a state of thermochemical nonequilibrium. A second important effect is the presence of the thick boundary layer along the forebody surface. In this region there are large thermal and chemical-species gradients due to the interaction of the gas with the wall. Also at high altitudes the shock wave and the boundary

layer may become so thick that they merge; in this case the entire shock layer is dominated by viscous effects.

A gas is in thermal nonequilibrium if, for a given density and internal energy, it is in a thermodynamic state where the internal-energy modes cannot be characterized by a unique temperature, and is in chemical nonequilibrium if its chemical state does not satisfy chemical-equilibrium conditions. As was asserted above, a portion of the forebody flowfield is in thermochemical nonequilibrium. This can be seen by considering the trajectory of a control volume of air that enters the shock layer. The translational modes of this volume of gas are heated strongly as it passes through the bow shock wave. The translational modes transfer their energy to the other internal energy modes of the molecules through intermolecular collisions. Moreover, chemical reactions, such as dissociation and ionization, occur for the gas species. These processes require a series of intermolecular collisions for equilibrium to be reached. Thus, as the volume element of gas is convected through the shock layer, these energy exchanges and chemical reactions occur at a finite rate until, at some point on the streamline, equilibrium is achieved. Therefore, there will be significant thermochemical nonequilibrium near the bow shock wave and equilibrium will be approached a large distance along the fluid-element's pathline. The rate at which equilibration is realized is dependent on the freestream density and speed, or altitude and Mach number. A parameter that quantifies the degree of chemical nonequilibrium for a particular condition is the Damköhler number, the ratio of the fluid time scale to the chemical time scale; a similar parameter may be derived for the relaxation of energy modes.

The second important effect in the forebody region is the interaction of the wall with the thermally excited and reacted gas in the boundary layer. At the high altitudes the Reynolds number is relatively small (typically on the order of 10^4 based on freestream conditions and nose radius). Thus, the boundary layer will be thick and viscous effects will dominate much of the flowfield. Also, as the boundary layer is influenced by the cool wall, chemical reactions can be slowed or halted in the vicinity of the wall. The wall can also interact chemically with the flowfield due to catalytic effects that promote the recombination of reacted species at the wall. Thus the inclusion of viscous effects for hypersonic bluff forebody flowfield analyses is mandatory. At high altitudes, the usual assumption of perfect thermal accommodation and no-slip at the wall breaks down. Therefore, for some conditions, temperature and velocity slip effects must also be included.

2.3 Lee and Base Flow

The flow about an afterbody, illustrated in Figure 7, is dominated by two phenomena; the presence of the rapid expansion as the highly compressed gas flows around the shoulder of the vehicle and the related initiation of separation of the gas near the vehicle corner. These two effects require specific modeling approaches and capabilities.

The expansion, which is dominated by inviscid effects, has the effect of rapidly lowering the translational temperature,

density and pressure of the gas. However, the chemical state of the gas and the temperatures that characterize the energy in the internal modes will tend to remain constant, or frozen. This results in a flow where the vibrational and electronic temperatures of the gas are far higher than the translational temperature and where the gas is more dissociated and excited than predicted by equilibrium conditions. As the gas flows downstream, recombination occurs slowly and the vibrational temperature rises still higher; a result of a portion of the chemical energy of recombination being put into the higher vibrational modes of the gas. This can cause the gas to radiate significantly in the afterbody region. Another important effect present in the inviscid, expanded region is the presence of species gradients across the wake. This is caused by some portion of the gas having passed through a relatively weak oblique shock wave where reactions are weak, and another part of the gas having passed through the strong forebody shock where reactions are strong. Thus the gas near the center of the wake tends to be more dissociated than that in its extremities and consequently γ , the ratio of specific heats, varies across the wake.

A second inviscid effect associated with the wake structure is the presence of a wake shock. As the flow expands around the shoulder of the vehicle, some of it is directed toward the centerline of the body. However, this supersonic flow must change direction and a reflecting shock and an oblique shock wave is formed. The gas becomes compressed in this region, yet the vibrational and electronic temperatures remain high due to freezing, and the gas may radiate significantly.

The location of the separation on the back face of the bluff body is affected by the following: the state of the boundary layer on the shoulder, the Reynolds number, whether the flow is turbulent or laminar, the ratio of specific heats, and the body geometry. For many cases of interest, particularly at high altitude, the flow can remain attached over a significant portion of the vehicle's afterbody. The location of separation influences the dimension of the recirculation zone and the strength of the shear layer that forms between the recirculating gas and the external, rapidly expanding, supersonic flow. The recirculation zone entrains gas that was in the forebody boundary layer which was cooled during expansion into the base region, but remains highly dissociated. This recirculation zone will be unsteady, the magnitude of which depends on how the shear layer behaves and the feedback between the body motion and the state of the gas in the separated region.

The modeling of the free shear layer must account for large gradients of velocity, temperature, density and species concentration across it, and for the possibility that the flow may be turbulent and unsteady. The numerical treatment of the problem is particularly difficult because of these effects and due to the uncertain location of this structure.

The afterbody flowfield is characterized by the presence of thermochemical nonequilibrium, large gradients in thermodynamic quantities and chemical state, and a large separated region. The combination of these factors stretches computational fluid dynamics beyond its current capabilities.

3 GROUND-TEST FACILITY REQUIREMENTS

Ground-test facilities are discussed in Chapter VI regarding calibration requirements and in Chapter VIII regarding future needs. In this section, the ground-test facilities required to provide meaningful data for the real-gas issues previously identified are discussed with particular emphasis on the particular merits of different types of facilities and their capability to best simulate the various aerothermodynamic problems.

In principle, there are two ways to create relative motion between the test article and the air; accelerate the air as in a shock or wind tunnel or accelerate the model as in a ballistic range. Both techniques are being employed at present and both are needed to give insight into real-gas phenomena. The two concepts can be combined to create even higher relative speeds whereby a large shock tunnel can be utilized to provide counterflow to an aeroballistic range.

Ballistic ranges represent a unique capability for real-gas testing of configurations. They present the only experimental technique by which real-gas, viscous-interaction effects can be observed. Shock tunnels, because of the nature of their expansion process, do not generate sufficiently high test Mach numbers where viscous-interaction phenomena would be important.

To date, most data presented from ballistic-range facilities have been integrated aerodynamic data on simple geometric configurations. Early efforts by Welch et al. (1979) demonstrated a significant real-gas effect on the center-of-pressure and moment data. More recent data by Strawa et al. (1988a,b, 1989) continue these studies. Aerodynamic-coefficient data are determined through the motions of the model down the length of the tube. Drag and static moment can be determined in about half a period of motion, lift coefficient requires 1.5 to 2 cycles, and damping coefficients require even more. Recent advances (Yates 1991) in automated data taking and data-reduction techniques have resulted in significant improvements in the accuracy of aerodynamics coefficients and in the efficiency through which they are determined. Validation requires not only such overall aerodynamic data but also distributions of local flowfield quantities within the shock and boundary layer of the tested configuration.

Instream flowfield data can be determined from in-flight shadowgraphs and laser holographic interferometry (Strawa and Cavolowsky 1990; Tam et al. 1991). These data provide quantitative information on shock shape and position, turbulence onset, and instream density variations and provide complementary data to the integrated aerodynamic coefficients to provide data for CFD validation purposes. An obvious advantage of ballistic-range testing is that the freestream is accurately characterized and can precisely simulate the flight environment.

Shock tunnels, including expansion tube/tunnels, currently offer the only means of producing both the total enthalpy and pressure levels representative of flight beyond Mach 10.

Shock tubes and shock tunnels do not precisely simulate flight environment. Moreover, their freestream must be characterized. In supersonic test facilities, this has been accomplished through the use of isentropic flow expansion models. However, real-gas accelerations are *not* isentropic. Realistic CFD models of the expansion process must be used in conjunction with critical (but not exhaustive) instrumentation to fully define the freestream. The fluid-dynamic and thermodynamic state of chemically reacting air (including the species N , O , N_2 , O_2 , and NO) should be characterized accounting for viscous effects in the nozzle. Complete calibration of a real-gas nozzle expansion process can only be achieved through this collaboration between insightful, limited measurements and increasingly accurate CFD models of the expansion process. Complex real-gas flows require the use of full test-section calibrations with the key measurements being the freestream density and static temperature. CFD validation must include facility simulation; we must not pretend to simulate flight with flow accelerated ground tests.

3.1 Aerodynamic Parameters

3.1.1 Impulse Tunnels

There are two approaches to experimentally determining the aerodynamic parameters such as lift and drag coefficients and pitching, yawing, and rolling moment coefficients. In the first, the pressure distribution over a test model can be measured. The aerodynamic parameters are obtained by integrating the measured pressures over the surface area. If only the raw experimental data are used in the integration, the procedure is liable to lead to a fairly large error. However, a fairly accurate result could be obtained, at least for simple shapes, if computational tools are used appropriately. In such an approach, the aerodynamic parameters are calculated from the (CFD) solution of the flowfield studied, and the experimental data, such as pressure or density, are used to provide anchor points for the calculated values i.e. one calibrates the tunnel freestream using CFD with the measured data as input. In this approach, the imperfection of the test facility, such as spatial nonuniformity of the test flow or presence of dissociated species, can be accounted for.

In the second approach, lift, drag, and moments of a model can be measured as integrated quantities. Shock tunnels, hot-shot tunnels, and expansion tubes are usually inappropriate for measuring forces and moments. Shock tunnels and expansion tubes cannot produce test flows of sufficiently long duration to enable accurate force measurements for complex models. Hot-shot tunnels produce test times sufficiently long for force measurements, but the flow produced is generally unsteady. Even so, progress in measurement techniques is being made that appears now to permit such direct measurements. The hot-shot tunnel, F4, provides such direct measurement capability. Also, the development of such techniques are currently being explored in the United States and in Australia in facilities like the Calspan 96-inch shock tunnel, the Ames 16-inch shock tunnel, and the University of Queensland T4

tunnel. At the present time, however, there is not a standard procedure for direct measurement of these forces in an impulse facility.

In order to determine the real-gas effects in an experiment, it is imperative that the facility first create a flow of an enthalpy sufficiently high to produce the real-gas effects. Preferably, the results obtained in such a facility should be compared with those obtained in a perfect-gas facility in order to isolate the real-gas effects. Secondly, the test stream should be in a chemical state close to equilibrium. As is well known, the flow in the expanding nozzle of a high-enthalpy, high-Mach-number shock tunnel or arc-jet wind tunnel undergoes freezing of chemical reactions. Therefore, the appropriateness of a facility for the aerodynamic testing depends on the extent and influence of the chemical freezing in the nozzle on the measured quantities.

Theoretical calculations can be performed to estimate, for a given set of thermodynamic conditions in the reservoir and the given nozzle geometry, the thermodynamic state of the test gas flow and the density ratio across a shock wave in this flow. This density ratio can then be compared with that expected in flight in order to assess how closely the facility simulates the flight condition. Two extreme cases can be used to illustrate this: the normal shock which occurs over the blunt nose and an oblique shock wave of modestly small angle that will occur over the wings or other components. An oblique shock angle of 30° or smaller may be used. If the flow produced in a laboratory reproduces density ratios in flight for these two extreme cases, then one can assume that the pressure field is simulated reasonably well in the experiment.

Freezing of chemical reactions in the nozzle produces generally smaller density ratios than in flight, which leads to thicker shock layers than in flight, as long as the flow behind the shock wave is in equilibrium. In most experimental conditions, the flow behind the shock is probably not in equilibrium. The presence of atomic species, and possible elevated vibrational temperature, in the shock-tunnel flow induces faster equilibration (due to a decrease in induction time required for excitation and dissociation) of chemical reactions than when the freestream is in equilibrium. This leads to a thinner shock layer than when the freestream is in equilibrium. Thus, the nonequilibrium effect mitigates the discrepancy in density ratios seen between the laboratory and the flight cases.

Freezing occurs mostly at Mach numbers greater than 3. As the reservoir pressure is decreased, freezing occurs at smaller Mach numbers. To minimize the extent of dissociation in the test section, one might consider adopting the non-reflecting shock tunnel scheme in which the initial levels of dissociation in the driven-tube reservoir are considerably lower than those for a reflected-shock tunnel where the gas has stagnated. However, since the Mach number of the flow behind the primary shock is always less than 3, the flow at the entrance of the expansion region in a non-reflecting shock tunnel has a greater degree of dissociation than the flow in a regular shock tunnel. Thus, the flow produced in the nozzle of a non-reflecting shock tunnel undergoes a same freezing process as

in a shock tunnel. The resulting degree of dissociation in the test section of a non-reflecting shock tunnel is nearly identical to that produced in a regular shock tunnel, and, therefore, the scheme has no advantage over the regular shock tunnel in this regard.

A similar argument is applicable to the expansion tube. Since the flow at the beginning of the expansion is at a Mach number below 3, the freezing occurs in an expansion tube in the same fashion as that in the regular or non-reflecting shock tunnel. This would lead to the same degree of dissociation in the test section of an expansion tube as in the shock tunnels, if it were not for the fact that the expansion tube has a long acceleration section. Because of the large length of the expansion section, the facility provides a large flow residence time for chemical reactions to proceed, and therefore the extent of freestream dissociation in the test section is usually less than in either shock tunnels. Thus, an expansion tube can produce density ratios across shock waves closer to the flight values than the shock tunnels. In addition, the expansion tube attains an enthalpy higher than the shock tunnels, because the acceleration process in the acceleration section increases enthalpy.

3.1.2 Ballistic Range

The most appropriate method of measuring forces and moments is by a flight experiment conducted in a ballistic range. In such a test, the model flies freely through a quiescent atmosphere, and the aerodynamic parameters are deduced by analyzing the time history of the flight path and the attitude of the model (Strawa and Cavolowsky 1990). Models of relatively simple geometry can be tested in a ballistic range for this purpose (Chapman 1992).

In aeroballistic range studies of the aerodynamic properties of hypervelocity vehicles, it is a common practice to duplicate the flight speed and Reynolds number of full-scale vehicle. This is done by setting speed and the range pressure to match the Reynolds number $Re = \rho V L / \mu$ in the test as close as feasible to those of full-scale flight. This matching of both speed and Reynolds number results in matching the density-length product, ρL , because viscosity is inherently closely matched. Since the flow residence time in the flowfield around a model varies directly with scale and the time required for a chemical change resulting from binary collisions varies inversely with density, the characteristic Damköhler number is automatically preserved in such a domain. Depending on test goals, the test pressure and speed may be adjusted slightly to offset the moderate effects of density on the extent of equilibrium dissociation and ionization or for the small effect of freestream temperature on viscosity.

3.2 Forebody Heating/Heat Transfer

3.2.1 Impulse Tunnels

With a certain degree of compromise, heat-transfer measurements over complex geometries in the real-gas enthalpy regime can also be made in an impulse tunnel. A

model made of the materials of known surface catalytic characteristics can be tested in such a facility much easier than in a ballistic range. Since the test flow produced by an impulse tunnel contains certain amounts of dissociated species, the aerothermal simulation in the facilities is not as good as that in a ballistic range. However, as long as the relative concentrations of the dissociated species are small, such tests provide meaningful results that can be compared against CFD calculations.

3.2.2 Ballistic Range

The thermochemical state of the freestream is known most accurately in a ballistic range. Therefore, it becomes attractive to conduct tests in a ballistic range. Models can be made with materials of known surface catalytic properties, though they may not be the same as in the flight vehicle, and be instrumented with heat-transfer gauges. The heat-transfer rates measured in flight can either be telemetered or, if the model can be recovered, be recorded on an on-board recorder. Since the time history of heating of the model in a ballistic range test is so different from that in full-scale flight, the thermo-mechanical behavior of the material cannot be correctly replicated. However, the heat-transfer-rate distribution measured over the surface of known catalytic efficiency should be useful. At the present time the ballistic range/instrumentation capability to perform such testing is extremely limited.

3.3 Lee and Base Flows

The flows in the leeward side of a slender body at an angle of attack or base region of a blunt body are affected mostly by Mach number, Reynolds number, enthalpy, turbulence, and temporal instability of the flow. The influence of the Mach number and Reynolds number are easily understandable. Enthalpy of the flow affects the effective γ , which in turn affects the turning angles in the expansion area. Turbulence affects the momentum and energy transfer in the shear layer, which in turn influences the pressure in the region. These flows are known to be intrinsically unsteady (Behren and Ko 1971). Simulation of unsteadiness requires a quietness of the freestream flow over a substantial length of time. For meaningful experimentation of these phenomena, therefore, free-flight type ballistic ranges are the most desirable. For bluff body base/wake flows, large-scale shock tunnels can be used for real-gas flow simulations. Difficulties here include instream instrumentation for the low-density wake region and quantification of the unsteady nature of the flow. Such a test campaign is described in section 4.2.2.

In the lee or base region of a vehicle, the dominant chemical reactions are recombinations. The time required for such processes is inversely proportional to the square of density. If ρL is properly simulated in a test, $\rho^2 L$ becomes larger than in flight, resulting in a lee-side/base flow closer to equilibrium than in flight. This will probably produce a substantial error in the flow properties in the region. This point will be elaborated on later.

4 TEST CASES FOR CFD VALIDATION

The development of validated analysis tools for hypersonic flows involves a process in which real-gas CFD development and application and experimental testing are performed hand-in-hand, synergistically, until the validation is complete. Hypersonic flows inherently involve real-gas phenomena. The validation of CFD tools requires considerations associated with perfect-gas CFD validation *plus* consideration of additional complexities associated with real-gas phenomena. These complexities include thermal and chemical time scales, multiple gas species, internal-energy flow variables and properties, and coupled fluid/chemical processes.

It is equally important to identify the important issues to be studied and to identify the best procedure to use to perform such studies. This is, in part, the purpose of this discussion, and has been treated in some detail by Sharma and Park (1990a,b) and Neumann (1990).

That it is not possible to fully simulate real-gas hypersonic flight conditions in ground-test facilities is axiomatic. Ground-test experiments must be carefully selected to validate basic principles and concepts in CFD codes. It is necessary to use CFD in the design of experiments, in the definition of the test environment, in the development, application and interpretation of diagnostics, and in the analysis of the test results as a whole. The resulting test data will then form a basis for validating the process and the CFD tools. The CFD codes can be used to extrapolate to flight conditions. And, finally, flight experiments are required to confirm the process as a whole.

4.1 Existing Data Base - Hemisphere/Cylinder/Blunt-Cone/RAMC

As previously mentioned, to acquire data necessary to validate and/or calibrate real-gas code capability to predict aerodynamic performance, the aeroballistic range is appropriate. Ballistic-range data will include visual flowfield data indicating shock shape and location relative to the body (i.e. by way of shadowgraphs) and density distribution (i.e. by holographic interferograms) as well as quantitative information in the form of aerodynamic coefficients including lift, drag and pitching moment. The use of a combination of CFD with experiment has proven most effective in the interpretation of free-flight data. For example, in a recent study on trim angle for the NASA Aeroassist Flight Experiment (AFE) vehicle (Yates and Venkatapathy 1991), there was insufficient free-flight data for determining higher-order terms for series expansion representation of aerodynamic coefficients. In order to extract information from the experimental data, the curvature of the function describing the moment coefficient was required. This curvature was developed using CFD. For the analysis of data from the aeroballistic range the higher-order terms in the aerodynamic coefficient expansion were determined from CFD simulations; only the lower-order terms were found using a six-degree-of-freedom, weighted, least-squares procedure. The resulting experimental aerodynamic coefficients and trim angles agree

with those computed by CFD. The effective specific heat ratio was determined by matching the bow-shock shape and standoff distance with CFD perfect gas, constant effective γ , flowfield simulations at the test conditions. Results of these comparisons are shown in Figure 8. in which the CFD simulation bow shock is identified by a coalescence of isobars.

Moment coefficient ballistic range (HFFAF) data for an AFE model are compared with data from two NASA Langley hypersonic cold-flow facilities, the 31-inch Mach 10 tunnel and the CF_4 tunnel, in Figure 9. Results of two test entries each are shown for the Langley tunnels. Each of the three facilities can be represented by an effective γ : 1.2 for HFFAF, 1.34 for the Mach 10 tunnel, and 1.11 for the CF_4 tunnel. The measured trim angles are 14.7°, 17°, and 12°, respectively.

By minimizing the uncertainty in trim angle, design tolerances can be tightened and vehicle configurations can be optimized for specific mission requirements. By using a combination of CFD analysis and ground-based experiments, the real-gas effects can be simulated, analysis tools validated, and flight conditions can be estimated with some confidence. In many cases the aeroballistic range can be used to simulate actual flight conditions and reasonable estimates of aerodynamic trim angle and pitching moment for flight can be determined directly. The agreement shown herein between experimental and computed results for the blunt AFE configuration at the ground-test conditions indicate that, at these test conditions, the moment coefficients and trim angles can be computed using efficient ideal-gas solvers with an appropriate choice for γ ; the appropriate value of this parameter can be determined by shock-shape comparison. This is not necessarily the case, however, for slender or high-lift vehicles. In cases where actual flight conditions cannot be replicated in ground-test facilities, real-gas solvers must be used to determine if constant effective γ approximations are appropriate. As mentioned previously, the variations in γ at flight conditions can have a sizable influence on aerodynamic moment coefficient and trim angle.

Existing test data for validation of instream flow quantities include (1) flow past a cylinder where shock shape, shock standoff distance, and density fringe patterns are measured in a shock tunnel (Hornung 1972), (2) ballistic range flowfield shadowgraphs of a blunted slender cone with shock generators (Strawa et al. 1988b, 1989), and (3) the RAMC-II flight data of electron distributions over a blunted slender cone (Grantham 1970; Jones and Cross 1972). Comparison of these data to real gas CFD simulations have been made by Candler (1988) and others.

4.2 Current Focused Test Activity

4.2.1 Basic Phenomenon -

Compressive and Expanding Flows

To study the nonequilibrium processes in a compressive flow typical of the stagnation region of a bluff forebody, the detail

of a gas relaxing after being heated by an incident shock wave is studied. By acquiring a normal shock in a spectrally clean facility, the thermochemical state of the gas can be quantified as a function of time and position. By these means, such processes as vibration-dissociation coupling, vibration-translation exchange, vibration-rotation coupling, etc., are studied (Park 1988a; Sharma et al. 1988; Park 1989).

The dominant real-gas phenomenon is the relaxation process occurring in the flow around hypersonic vehicles. Considerable effort has been expended in recent years to model and numerically compute this behavior (Chandler and Park 1988; Chandler and MacCormack 1988; Gokcen and MacCormack 1989; Chandler 1989). The accuracy of such calculations needs further improvement and there are still many physical parameters that are unknown for high-temperature real gases. Three types of experimental data are needed in this model development process: 1) data which will enhance our phenomenological understanding of the relaxation process, 2) data on rates for the relevant reactions, and 3) data on bulk properties, such as spectral radiation emitted by the gas, for a given set of aerodynamic conditions. Such data have been acquired by simulating the required aerothermochemical conditions in an electric-arc-driven shock tube (Sharma and Park 1988; 1989). This NASA Ames facility (EAST) is powered by a 0.6 MJ, 40 kV capacitor bank and is capable of producing shock velocities in the range of 2 - 50 km/s. The radiation diagnostic system available at the facility, consists of 1) a linear intensified 700 element diode array and a 2-D intensified CCD array with 576 x 384 active elements, both gateable within a time range of 30 ns - 2.5 ms and both with a 200 - 800 nm spectral response. A photomultiplier tube (PMT) is used to record the total radiation from the test gas as well as from the driver gas as they pass through the test section. The signal from the PMT is used to estimate the test time and to trigger the diode array system at a given moment during the test history. A Nd:YAG laser based, double exposure, single plate interferometer is also available at the facility. A schematic of the experimental test setup is shown in Figure 10.

A one-dimensional real-gas code for thermochemical nonequilibrium (Park 1988b) is used to predict the thermochemical state of the shock-heated gas behind the incident shock. This code uses a multiple temperature description to model the nonequilibrium behavior of the internal state of the gas and to describe the rate processes. From the predicted thermochemical state of the gas synthetic emission spectra can be generated. Several modeling steps are involved in this process. First are the chemical rate expressions themselves in which there is always some uncertainty in the Arrhenius rate constants, second is the multiple temperature model used to describe both the internal energy states of the gas and the reaction rates, and third is the quasi-steady state model and peripheral approximations used to generate the synthetic spectra. By maintaining a coordinated effort between the modeling activity and the experimental effort it is possible both to improve and refine the phenomenological models as well as validate them. These

models will then, in turn, be used in multidimensional flow codes to predict and analyze real-gas behavior in more complex flow environments.

To date, two sets of experiments have been conducted: 1) measurements at a shock velocity of 6.2 km/s in 1 Torr nitrogen (Sharma 1990) and 2) measurements at a shock velocity of 10.2 km/s in 0.1 Torr air (Sharma et al. 1991). In both sets, using the linear diode array, the equilibrium and nonequilibrium spectra covering the 305-550 nm range were recorded.

Measurements in Nitrogen (6.2 km/s, 1.0 Torr): For the nitrogen case, the equilibrium temperature of the test gas based on $N_2(2^+)$ band system was found to be 6500 K. The rotational temperature at the point of peak radiation in the nonequilibrium region, based on the intensities at 314.37 nm and 315.91 nm, was found to be about 8800 K. The vibrational temperature, based on the first vibrational level and the ground state of the $N_2(2^+)$ band system was found to be about 6900 K. The vibrational temperatures of higher vibrational levels were lower than this value.

The equilibrium temperature of the test gas based on the $N_2^+(1^-)$ band system was found to be 7200 K. The rotational temperature at the point of peak radiation in the nonequilibrium region was deduced to be about 8800 K, which is consistent with the value found by using the $N_2(2^+)$ band system. Comparisons of rotational temperature with prediction and with earlier data from Allen et al. (1961) are shown in Figure 11. The vibrational temperature as measured based on the $v(1,2)/v(1,0)$ levels of the $N_2^+(1^-)$ band system was found to be about 9500 K, with the value decreasing for higher vibrational levels. The temperature based on the $v(7,8)$ vibrational level was about 8500 K. Comparisons of vibrational temperature with prediction and with earlier data are shown in Figure 12.

Measurements in Air (10.2 km/s, 0.1 Torr): For shock heated air, the equilibrium temperature was estimated to be 9620 K. The equilibrium emission spectra observed is shown in Figure 13. By using two different sets of points on the rotational envelope of the $N_2(2^+)$ band system, the rotational temperature, corresponding to the point of peak radiation, was estimated to be about 4400 K and 3990 K respectively, making a mean rotational temperature of 4195 K. Such a low value of rotational temperature was a surprise. The overshoot observed in the nitrogen tests at 6.2 km/s was absent here. The rotational temperature seems to rise very slowly to reach the equilibrium value. The emission spectra observed at the point of peak radiation is shown in Figure 14.

The vibrational temperature at the point of peak radiation was deduced using the (2,1) and (3,2) bands of $N_2^+(1^-)$ system at 356.41 nm and 354.82 nm, respectively and was found to be about 9465 K. There were no other vibrational temperature data available for these conditions. The measured vibrational temperatures based on $N_2^+(1^-)$ as well as based on $N_2(2^+)$ band systems are in line with the theoretical values as predicted by Park's model (Gokcen and MacCormack 1989). Sharma and Park (1987) shows further details and analysis of the experimental data and comparisons with theory.

Expanding flows: To study the nonequilibrium processes in an expanding flow as typified by the flow over the shoulder of a bluff body and into the base, or near-wake region, a test gas is shock heated in the Ames EAST facility to high temperature and pressure and allowed to expand rapidly in a two-dimensional nozzle. By using optical diagnostics such as laser holographic interferometry and Raman scattering (Sharma et al. 1992), the thermochemical state of the gas during the expansion process is quantified. Nonequilibrium vibrational populations are measured for levels up to $v = 13$, in an expanding flow, using spontaneous Raman scattering technique. A nozzle insert has been installed in the driven section operating in a reflected shock mode. The density flow field was mapped by laser-based holography. The results are shown in Figure 15, where good agreement can be observed between computer simulated and experimental fringe interferograms.

4.2.2 Building Block Experiments -

Bluff and Slender Blunt Cones

In addition to characterizing the thermochemical process in an expanding flow, a blunt-body base-flow test configuration is being developed as part of the Working Group 18 activity. The basic configuration, shown in Figure 16, is a 200 mm diameter, 70° spherically-blunted cone representative of a planetary-entry capsule aeroshell. Models are being fabricated by the NASA-Langley Research Center as follows: (1) two non-instrumented brass free-flying model to be used for flow-visualization studies without the presence of a sting support, and (2) an instrumented sting-mounted chromel model for which both the model and the sting support are instrumented with pressure and heat-flux gauges (flow visualization can be realized for comparison with the free-flight model,) and (3) an non-instrumented sting-mounted stainless steel model with a slot in the sting for optical access in the near-base region. The non-instrumented stainless steel model will be instrumented with a modest number of surface instruments at Calspan and at DLR. As part of the AGARD FDP WG-18 activity the free-flight and sting-mounted chromel configurations will be tested in the NASA Ames 16-inch combustion-driven shock tunnel, only sting-mounted models will be tested in the DLR free-piston shock tunnel, HEG, and only stainless steel sting-mounted models will be tested in the Calspan LENS. Each facility will be operated at the same enthalpy and the same Mach and Reynolds numbers ($H_0 = 10$ MJ/kg, $M = 7$, and $p_0 = 500$ bar). In addition, tests in the Ames facility will be performed at total enthalpies of 5 and 14 MJ/kg at total pressures of 100 bar, in the DLR HEG facility at enthalpies of 20 MJ/kg and total pressures of 500 and 1000 bar, and in the LENS at enthalpy 5 MJ/kg and pressures of 500 and 2000 bar.

The lower enthalpy levels produce only modest levels of dissociated oxygen and no dissociated nitrogen. At 10 MJ/kg there will be substantial oxygen dissociation and negligible nitrogen dissociation. At 20 MJ/kg there will be substantial dissociation of both oxygen and nitrogen. Nitrous oxide (NO) will be produced under all test conditions. The test matrix is

shown schematically in Figure 17. Instream laser-induced fluorescence (LIF) data will be acquired at DLR to determine NO temperature and concentration distribution over the shoulder expansion region. Sodium line reversal imaging and high-speed schlieren photography will be performed at Ames to identify the wake structure with and without sting support. The stingless model will be suspended in the facility test cabin by nylon threads prior to facility operation. The threads will vaporize upon facility start-up leaving a "free-flying" model. The model inertia will maintain the model in an essentially motionless position during the test period.

The first test entry is planned for the LENS facility in late 1993 or early 1994, followed by an entry in HEG in spring or summer 1994, and be the Ames entry in September 1994. Computations are being performed at NASA Ames, and, in part, at NASA Langley.

The purpose of the experiments are to quantify the shear-layer-separation point, turning angle and wake closure in the presence of flows exhibiting real-gas and/or low-density behavior. The unsteady character of the near wake will also be characterized, if possible using high-speed schlieren and surface heat-flux data. Body surface instruments will provide data for CFD simulation and calibration/validation. Both sting-mounted and free-flight models will be necessary to assess and quantify the influence of the sting on the instrumented model.

A second configuration, a slender blunted cone corresponding to the European Electre flight vehicle will also be tested with emphasis on forebody flow. The first test entry has been completed in the Caltech T5 facility. Subsequent test entries are planned for the HEG facility and the F4 facility. Depending on facility availability, the model will also be tested in the Calspan LENS and the Ames 16-inch tunnels.

4.2.3 Configuration Studies - Hermes, Hallis, Orbiter

Selection of the Configurations Real-gas phenomena can be studied in high-enthalpy facilities. However, because of simulation limitations it is important to study configurations from which good quality flight data exist. Through a computational rebuilding of these configurations in both wind-tunnel and flight conditions the extrapolation to flight methodology can be demonstrated.

The selection of a configuration is based on multiple criteria that are not always easy to quantify. However, the main drivers chosen for the WG-18 activity are the following: First, trivial, but important, is that the configuration must have flown. This limits the number of cases to candidates such as capsules (e.g. Mercury, Gemini, Apollo, etc.), experimental vehicles (e.g. FIRE, RAM, ELECTRE, BOR, etc.), and Space Transportation Systems (e.g. Space Shuttle Orbiter, Buran.)

A second driver for the selection is the quality of the data that can be obtained. The goal of the study is to have data that can challenge CFD. If the error bars for flight data are too large, there is a risk that any calculation, even of poor quality, will fall within the error band. This criterion eliminates configurations such as capsules or ELECTRE that were flown

in the same period. (These configurations are considered, however, in the previous section as building-block experiments.)

The next step is to identify available flight data that represent a set complete enough to be useful as validation test cases. For example, the BOR and Buran data were rejected here as incomplete. Other experimental vehicles were rejected at the time of selection due to difficulties with data classification.

Contrary to the rejected configurations, the flight results from the Orbiter were considered as good quality, extensive, and sufficiently available to gather a comprehensive set of data suitable for CFD validation including real-gas effects. Thus, the Orbiter configuration has been selected by WG-18 as suitable for configuration study. In addition to the Orbiter, the Halis model has been selected. It represents a simplified shape of the Orbiter where the windward side has been kept and the leeward side simplified in order to reduce the gridding constraints and limit the problems with CFD codes for expanding flows.

Achievements and Working Plan In this section only the experimental campaign will be highlighted. Chapter VI will provide more details on the flight-point definition. In order to achieve the foreseen tests, two models were selected. The first one is dedicated to force and moment evaluation and the second is instrumented with pressure and heat-flux gauges.

A review was thus performed to check whether any existing model of the Orbiter was available and compatible with the specification of the models for the European F4 wind tunnel. Such a model has been identified within the number of existing models that had been made for the design of the Orbiter. Shown in Figure 18 is a view of the model with the different possible deflection flaps. This model will be provided to Europe and prepared (sting adaptations) for testing in F4 and possible S4 in order to have a cold tunnel reference for comparison with the initial Orbiter tests at AEDC or from the Aerodynamic Data Book.

Another European test facility that can achieve high enthalpy is the HEG. Due to short test times, HEG is limited to pressure and thermal measurements. No existing model could be found to meet the requirements for testing in this facility. A new model is required to be designed and fabricated. For simplicity the Halis model was chosen. The study of real-gas effects on thermal behavior includes wall catalytic phenomena. In order to avoid problems with repeatability, the study of catalytic effects of one or two different coating in the same shot was chosen. The coating technology requires leaving the model in an oven for a long period of time. Consequently, it is necessary for the surface instrumentation gauges to withstand this long high-temperature environment. This is possible for the heat-flux gauges but not for the surface-pressure gauges. Consequently, it was decided to separate the left and right sides of the Halis model to avoid these problems and to treat each side separately. Shown in Figures 19a and 19b are sketches with preliminary specifications that were forwarded to the US for the complete definition and machining of the model.

The model will be instrumented in Europe once it has been fabricated and delivered by the US. The instrumentation selected is compatible with both F4 and HEG requirements. In addition, it is possible to perform tests in S4 using the same instrumentation as in F4.

At the present time, tests of the Halis model are planned in HEG. The study will include a single angle of attack with two flap-deflection configurations. Two Aerodynamic conditions will be considered for each configuration. Possible complimentary tests are foreseen in S4 in order to get a cold-flow reference condition in European facilities, and in F4 to get alternate high-enthalpy results. These tests have not yet been confirmed.

At the present time the expected schedule for the different tests is as follows:

Force and moment tests in F4 (Orbiter model) will begin in 1995. Pressure and thermal measurements in HEG (Halis model) are to be determined.

5 GROUND-FACILITY LIMITATIONS

In the following, the uncertainties and difficulties in conducting the proposed tests in each of the facilities identified above are cited. They are also summarily listed in the third column of Table 1 in the Introduction.

5.1 Aerodynamic Parameters

5.1.1 Impulse Tunnels

Plotted in Figure 20 is the density ratio across both a normal and oblique shock as a function of reservoir pressure in a shock tunnel operating at an enthalpy of 15 MJ/kg. The density ratios obtained in this pre-dissociated, thermally excited test gas is compared with density ratios realized at undisturbed flight conditions corresponding to the same total enthalpy and pressure. As shown in Figure 20, the degree of similitude of aerodynamic phenomena in an impulse tunnel generally improves with an increase in the reservoir pressure. For this reason, it is customary to attempt to operate an impulse tunnel at very high stagnation pressures. The combination of high pressure and high enthalpy causes the wall material to ablate in the reflected-shock region and at the nozzle throat. The ablation occurs because of both convective and radiative heat transfer. The convective heat transfer is relatively well understood. The nature of the radiative heat transfer is not well understood. Spectra taken from the flow behind the primary shock in a shock tube made of stainless steel indicated that the test gas contains a small amount of table salt (*NaCl*) and other metallic or alkali-metallic impurities even before the shock arrives at the endwall (Sharma and Park 1990a,b).

The presence of the salt is attributed to the salt contained in the atmosphere (Schneider and Park 1975). The origin of the rest of the impurities is not well understood. According to the explanation given by Schneider and Park (1975), they are produced at the inner wall of the driven tube. The wall tends

to adsorb water and oil. The water-oil mixture is irradiated by sunlight or room light. This converts the mixture into an organic acid. This acid dissolves the outermost layers of the wall material and forms a metallic salt. Such salts have a finite vapor pressure, and therefore, while the facility is evacuated, continually adsorb and fill the tube. Based on this theory, impurities have successfully been eliminated by using aluminum as the surface (Sharma and Park 1990a,b). The surface layers of aluminum are made of aluminum oxide, i.e. sapphire, which does not dissolve easily in an acid. For a regular shock tube, the radiative heat generated by the impurity radiation is negligibly small, and so there is no possibility of melting or ablation of aluminum in this case.

In contrast, in the reflected-shock region of a shock tunnel, the impurity radiation is not negligible. Because of the high temperature and pressure in the reflected-shock region, generally the inner wall of the tunnel is subject to a substantial radiative heat flux. Relatively small concentrations of impurity species result in a many fold increase in radiation in this region. The sum of this radiative heat flux and the convective heat flux can be so large that the wall material may begin to melt, boil, and spall. Spallation occurs when the less-volatile alloy grains within the wall material are ejected into the flow by the vapor pressure produced by the vaporization of the more-volatile alloy grains of the material and the intergranular stress. The particulates so ejected into the core of the flow vaporize and radiate. Thus, a snow-balling phenomenon is established that accelerates spallation and radiative heating of the wall.

The throat of a shock tunnel is subject to a convective heat-transfer rate sufficiently large to also cause ablation and spallation. The metallic vapor produced in the reflected-shock and throat regions condense during the expansion process in the nozzle. Thus, the flow in the test section may contain a mixture of the metallic vapor and the metallic condensate. These impurities increase the heat capacities of the test gas and decrease γ . The particulates can affect the pressure and convective heat-transfer rate distribution severely (Holden 1986). Since such erosion of the endwall and the nozzle throat regions is caused by high heat transfer, aluminum is not appropriate here. Molybdenum or molybdenum-based alloy may be used to a temperature perhaps of about 4500 K. Tungsten or thoriated tungsten may be used to an even higher temperature. However, no material has yet been found that can withstand the temperature in excess of 7000 K, under the pressure, and the shear stress prevailing within this environment.

There is yet no data on the extent of flow contamination by the ablation and possible spallation of the material at the entrance lip of the nozzle for the non-reflecting shock tunnel. The non-reflecting shock tunnel is free from the radiative heating from the reflected-shock region. The entrance lip must be fairly sharp in order to prevent formation of a bow shock wave. The problem of convective heat transfer is very severe for the lip. Another well known difficulty of this device is that the duration of the useful test flow is much shorter than that of the hot-shot or regular shock tunnel.

In an expansion tube, the contamination problem may be negligibly small, because there is no reflected-shock region, nozzle throat, or entrance lip. In exchange, this device poses two other problems. First, as is for the non-reflecting shock tunnel, its test times are very short. Second, the condition of the flow is uncertain. Even a very thin secondary diaphragm causes significant deceleration of the initial flow (Miller 1977). Also, the length of the expansion is usually so long that the turbulent boundary layer grown on the wall tends to reach the core of the flow. This causes deceleration and cooling of the core flow, making uncertain the state of the core flow (Miller 1977).

5.1.2 Ballistic Range

In a free-flight range test, the aerodynamic forces and moments acting on a model are deduced from the deviations of the flight trajectory of the model from those of the un-accelerated rectilinear flight. The flight trajectory deviates from the rectilinear motion because of the lateral swerving caused by the lift of the model and because of launch disturbances, namely, gun-muzzle blasts and irregular separation of the sabot. For this reason, the field of view of the optical observation stations must be quite large, particularly for long flights of lifting models. This requirement conflicts with the need for high spatial resolution in studying flowfields and verifying the undamaged condition of the model. Thus, the desired forces and moments must be determined from the relatively small detected deviations from the rectilinear motion. In order for such a procedure to be accurate, the positions and attitudes of the model must be known very accurately as a function of time. Small optical observation stations can easily be built by placing all active instrumentation outside the range. Large fields of view are difficult to achieve, however, without installing most of the electro-optical apparatus inside the range, in which case some of the components must be placed in pressure-sealed compartments to prevent electrical arcing, implosion, or explosion.

The chemical processes in the windward-side or forebody region of the flow around a launched model are well simulated in a ballistic range test when the Reynolds number is matched. However, the chemical processes in the leeside or base region are not simulated if the full-scale flow is nearly frozen but the model flow is nearly in equilibrium. This will probably produce only a small error in the measured aerodynamic parameters, because the pressures in the leeside or the base are usually very small compared with the pressures in the windward-side or forebody regions.

5.2 Forebody Heating/Heat Transfer

5.2.1 Impulse Tunnels

The distribution of relative rates of heat transfer to complicated configurations can easily be determined in shock tunnels and hot-shot tunnels. Both shock and hot-shot tunnels have been used successfully in perfect-gas flow regimes. However, in the real-gas enthalpy regime, important

deficiencies arise from the contamination of the freestream, uncertainty about the chemical state of the freestream, and the level of turbulence in the freestream. For this reason, the absolute levels of real-gas effects determined in a test in an impulse facility is questionable. Based on the experiences of the 1960s, one expects the problem of contamination to be particularly severe for the hot-shot tunnels. For those, the test flow may contain a sizable amount of solid and liquid particulates of the wall material, as well as their vapors.

5.2.2 Ballistic Range

The ballistic range offers a well-defined test environment. However, there are many practical difficulties in the ballistic-range testing of the heat-transfer rates over complex geometry. Fabricating a model with a complex geometry, coating the critical parts of the model surface with materials of desired catalytic efficiency, providing the heat-transfer gauges at those critical parts, providing telemetry for the output from the gauges, and launching the model so constructed without destroying any part of it or affecting the calibration characteristics of the gauges, would be very difficult. Such instrumentation is probably possible only if the model diameter is very large, that is, substantially larger than 100 mm. The launcher must be very long, so that the acceleration of the model can be kept small. Since the model so constructed would be so expensive, it is desirable that the model be recovered after flight. For this technique to be realized, a new ballistic range much larger than the largest existing must first be constructed. Even if such a facility is constructed, many years of development would be necessary to perfect the technique.

5.3 Leeward-Side/Base-Region Flow

As mentioned earlier, the problem of leeward-side or base-region flow can be studied best in a ballistic range. The difficulty in doing so is that the density in the leeward side or base region of a model is usually so low that the optical techniques such as shadowgraph, schlieren, or interferometry do not produce a picture with a sensitivity sufficiently high for meaningful analysis. The full-scale flight value of $\rho^2 L$ must be reproduced in order to correctly simulate chemical state of the leeward/base flows. The required free stream density is lower than that required for simulating ρL . This difficulty may be overcome in principle by adopting an optical resonance technique (Blendstrup et al. 1978; Trollinger et al. 1992). In this technique, the wavelength of the light source is selected to match that of a strongly absorbing line in a species in the flow. If the test gas does not contain a species that absorbs strongly, it can be seeded with a trace gas. Absorptive and refractive properties of the test gas are then greatly enhanced, resulting in high resolution. Seeding with such a species is perhaps not so difficult if a counterflow device is used. Such a technique has never been used before, and must be developed in the future.

If an onboard measurement of pressure or heat-transfer rate is made, then the accuracy of the measurement and the means of telemetering the data become the main difficulty. The

measurements may be "sluggish" on oscillating bodies so that only averages might be possible for such bodies. Because of the relatively low pressure and low heat-transfer rate in these regions, the sensitivity of the gauges must be made quite high to be used here. Such highly sensitive gauges will be affected by the launch acceleration. As far as the present authors are aware, no such pressure measurement has yet been made successfully.

6 CONCLUDING REMARKS

In summary it has been pointed out that real-gas effects are important in hypersonic flows both in terms of their influence on aerodynamic performance and their effect on aerothermodynamic heating. Further, it was pointed out that high-enthalpy, ground-based test facilities cannot fully simulate flight conditions and that they exhibit unique real-gas behavior themselves. Hence, the process for developing validated analysis tools is one where real-gas CFD is involved in all aspects of a real-gas ground-test program. CFD is used to design and define the experiment, to define the ground-facility test conditions, and to simulate the ground-test experiment itself. The ground-test data, in turn, are used to validate, or calibrate, the CFD simulations. Only in this manner can sufficient confidence be gained and real-gas analysis tools be validated.

REFERENCES

- Allen, R. A., Camm, J. C. and Keck, J. C. 1961 Radiation from Hot Nitrogen. *AVCO-Everett Res. Lab. Rept. 102*.
- Behren, S. W. and Ko, D. R. S. 1971 Experimental Stability Studies in Wakes of Two-Dimensional Slender Bodies in Hypersonic Speeds. *AIAA J.*, Vol. 9, 851.
- Blendstrup, G., Bershader, D., and Langhoff, P. W. 1978 Resonance Refractivity Studies of Sodium Vapor for Enhanced Flow Visualization. *AIAA J.*, Vol. 16, 1106.
- Candler, G. V. 1989 On the Computation of Shock Shapes in Nonequilibrium Hypersonic Flows. *AIAA Paper 89-0312*.
- Candler, G. V. and MacCormack, R. W. 1988 The Computation of Hypersonic Ionized Flows in Chemical and Thermal Nonequilibrium. *AIAA Paper 88-0511*.
- Candler, G. V. and Park, C. 1988 The Computation of Radiation from Nonequilibrium Hypersonic Flows. *AIAA Paper 88-2678*.
- Chapman, G. T. 1992 The Ballistic Range - Its Role and Future in Aerothermodynamic Testing. *AIAA Paper 92-3996*.
- Gokcen, T. and MacCormack 1989 Nonequilibrium Effects for Hypersonic Transitional Flows Using Continuum Approach. *AIAA Paper 89-0461*.
- Grantham, W. L. 1970 Flight Results of 25,000 Foot per Second Reentry Experiment Using Microwave Reflectometers to Measure Plasma Electron Density and Standoff Distance. *NASA TN D-6062*.
- Griffith, B. J. and Maus, J. R. 1983 Explanation of the Hypersonic Longitudinal Stability Problem - Lessons Learned. in *Shuttle Performance Lessons Learned*, NASA CP 2283.

- Holden, M. S. 1986 Studies of Potential Fluid-Mechanical Mechanisms for Enhanced Stagnation-Region Heating. *Thermophysical Aspects of Re-Entry Flows*: Prog. Astro. Aero., Vol. 102, ed: J. N. Moss, C. D. Scott, AIAA, New York, 281.
- Hornung, H. G. 1972 Nonequilibrium Dissociating Nitrogen Flow Over Spheres and Circular Cylinders. *J. Fluid Mech.*, vol. 53, 149.
- Jones, W. L. Jr. and Cross, A. E. 1972 Electrostatic Probe Measurements of Plasma Parameters for Two Reentry Flight Experiments at 25,000 Feet per Second. *NASA TN D-6617*.
- Miller, C. 1977 Operational Experience in the Langley Expansion Tube With Various Test Gases. *NASA TM 78637*.
- Neumann, R.D. 1990 Requirements in the 1990's for High Enthalpy, Ground Test facilities for CFD Validation. *AIAA Paper 90-1401*.
- Park, C. 1988a Two-Temperature Interpretation of Dissociation Rate Data for N_2 and O_2 . *AIAA Paper 88-0458*.
- Park, C. 1988b Assessment of Two-Temperature Kinetic Model for Dissociating and Weakly Ionizing Nitrogen. *J. Thermophysics and Heat Transfer*, Vol. 2, 8.
- Park, C. 1989 A Review of Reaction Rates in High Temperature Air. *AIAA Paper 89-1740*.
- Park, C., and Yoon, S. 1991 A Fully-Coupled Implicit Method for Thermo-Chemical Nonequilibrium Air at Sub-Orbital Flight Speeds. *J. Spacecraft and Rockets*, Vol. 28, 31.
- Rakich, J. V., Bailey, H. E., and Park, C. 1983 Computation of Nonequilibrium, Supersonic Three-Dimensional Inviscid Flow Over Blunt-Nosed Bodies. *AIAA J.*, Vol. 21, 834.
- Romere, P. O. and Whitnah, A. M. 1983 Space Shuttle Entry Longitudinal Aerodynamic Comparisons of Flights 1-4 with Preflight Predictions. in *Shuttle Performance Lessons Learned*, NASA CP 2283.
- Schneider, K. P., and Park, C. 1975 Shock Tube Study of Ionization Rates of NaCl - Contaminated Argon. *Phys. Fluids*, Vol. 18, 969.
- Sharma, S. 1990 Nonequilibrium and Equilibrium Shock Front Radiation Measurements. *AIAA Paper 90-0139*.
- Sharma, S. and Park, C. 1987 A Survey of Simulation and Diagnostic Techniques for Hypersonic Nonequilibrium Flows. *AIAA Paper 87-0406*.
- Sharma, S. and Park, C. 1988 Operating Characteristics of a 60 cm and a 10 cm Electric Arc-Driven Shock Tube. *AIAA Paper 88-0142*.
- Sharma, S., Huo, W., and Park, C. 1988 The Rate Parameters for Coupled Vibration-Dissociation in a Generalized SSH Approximation. *AIAA Paper 88-2714*.
- Sharma, S. P., and Park, C. 1990a Survey of Simulation and Diagnostic Techniques for Hypersonic Nonequilibrium Flows. *J. Thermophysics and Heat Transfer*, vol. 4, 129.
- Sharma, S. P., and Park, C. 1990b Operating Characteristics of a 60- and 10-cm Electric Arc-Driven Shock Tube - Part 2: The Driven Section. *J. Thermophysics and Heat Transfer*, Vol. 4, 266.
- Sharma, S., Gillespie, W. D. and Meyer, S. A. 1991 Shock Front Radiation Measurements in Air. *AIAA Paper 91-0573*.
- Sharma, S., Ruffin, S., Meyer, S. A., Gillespie, W. D. and Yates, L. A. 1992 Density Measurements in an Expanding Flow Using Holographic Interferometry. *AIAA Paper 92-0809*.
- Strawa, A.W., Chapman, G.T., Canning, T.C., and Arnold, J.O. 1988a The Ballistic Range and Aerothermodynamic Testing. *AIAA Paper 88-2015*.
- Strawa, A.W. and Prabhu, D. K. 1988b A Comparison of Experimental and Computational Results for 5 and 10 Degree Cones at High Mach Numbers. *AIAA Paper 88-2705*.
- Strawa, A. W., Molvik, G., Yates, L., and Cornelison, C. 1989 Experimental and Computational Results for 5 Degree Blunt Cones with Shock Generators at High Velocity. *AIAA Paper 89-3377*.
- Strawa, A. W., and Cavolowsky, J. A. 1990 Development of Non-Intrusive Instrumentation for NASA-Ames' Ballistic Range and Shock Tunnel. *AIAA Paper 90-0628*.
- Tam, T. C., Brock, N. J., Cavolowsky, J. A., and Yates, L. A. 1991 Holographic Interferometry at the NASA-Ames Hypervelocity Free-Flight Aerodynamic Facility. *AIAA Paper 91-0568*.
- Trollinger, J., Hess, C., Yip, B., and Hanson, R. 1992 Hydroxyl Density Measurements in a Flame with Resonance Holographic Interferometry. *AIAA Paper 92-0582*.
- Welch, C. J., Lawrence, W. R. and Watt, R. M. 1979 Real-Gas Effects on the Aerodynamics of Blunt Cones as Measured in a Hypervelocity Range. *AEDC TR 79-33*.
- Yates, L. A. and Venkatapathy, E. 1991 Trim Angle Measurements in Free-Flight Facilities. *AIAA Paper 91-1632*.

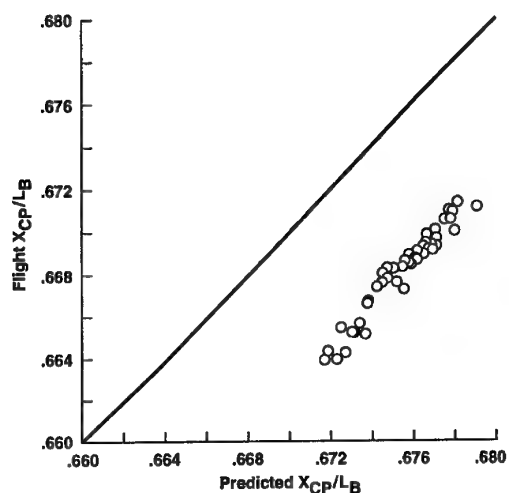


Figure 1. Hypersonic longitudinal aerodynamic center of pressure correlation of flight with predicted data for pullup/pushover maneuvers: STS-2, $M = 21$.

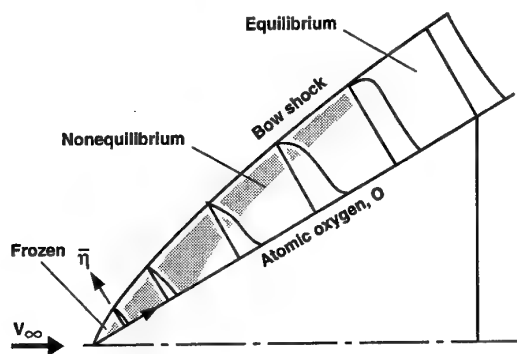


Figure 2. Schematic profiles of atomic oxygen between body and shock of a pointed cone.

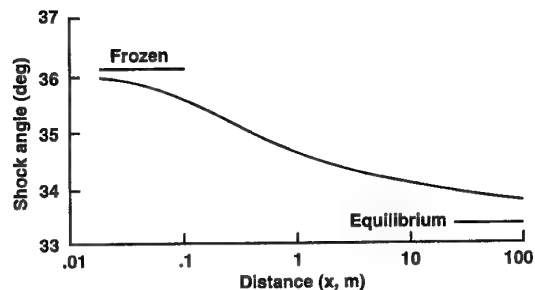


Figure 3. Shock angle for nonequilibrium flow over a 30° wedge.

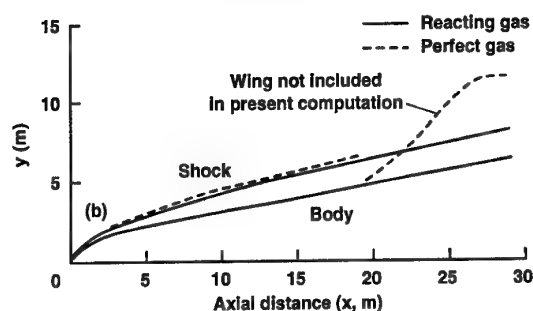
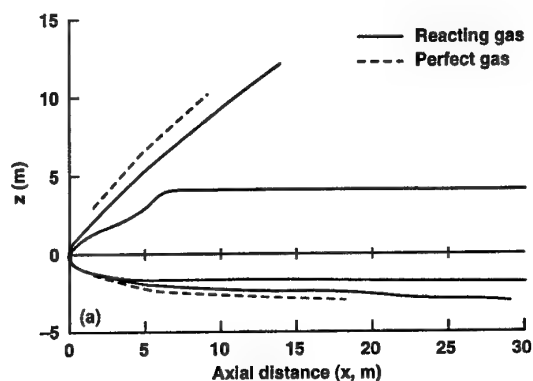


Figure 4. Shock shape for Shuttle 147 body, $\alpha = 30^\circ$, $V = 6.7$ km/s, altitude = 65.5 km: a) side view; b) plan view.

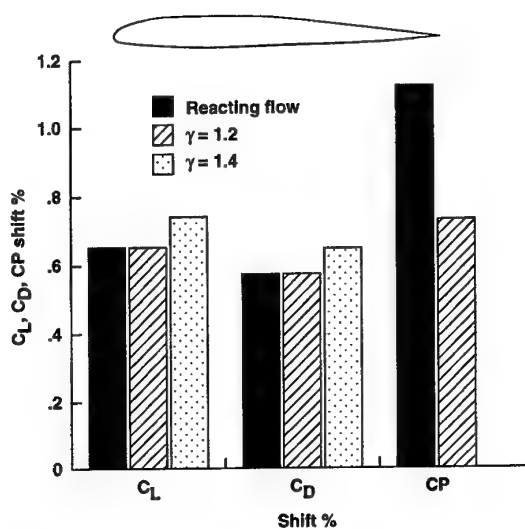


Figure 5. Lift and drag coefficients and CP shift for airfoil: chord = 10 m, alt. = 74 km, $V = 7$ km/s, $\alpha = 40^\circ$.

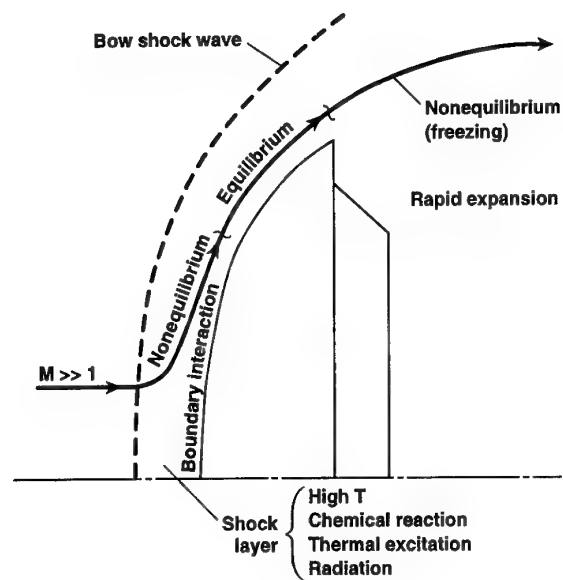


Figure 6. Schematic of hypervelocity bluff forebody flowfield.

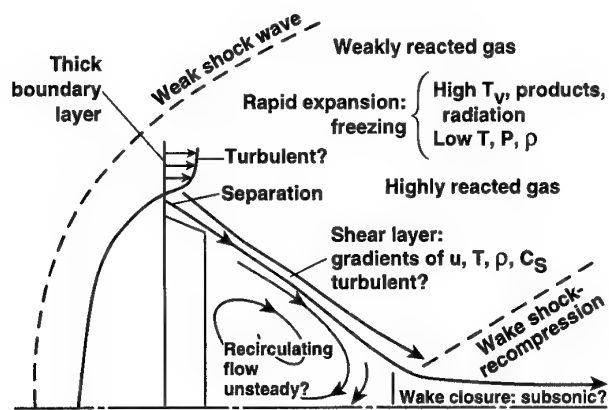


Figure 7. Schematic of hypervelocity bluffbody near-wake flowfield.

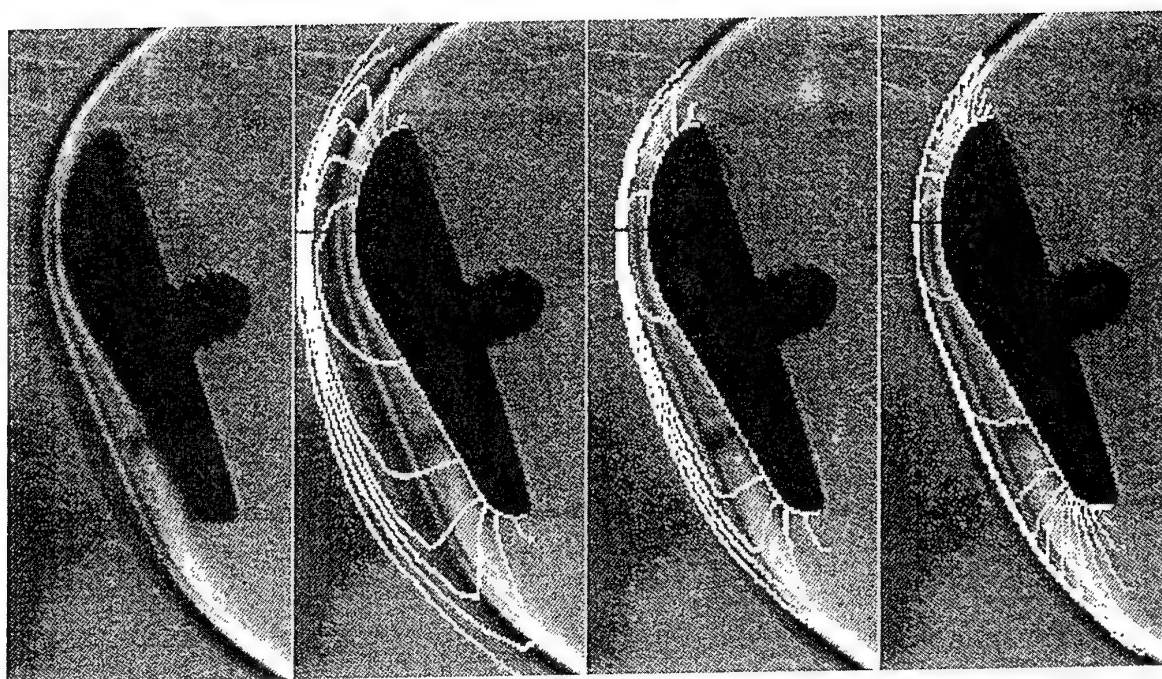


Figure 8. Experimental and computed AFE bow shock.

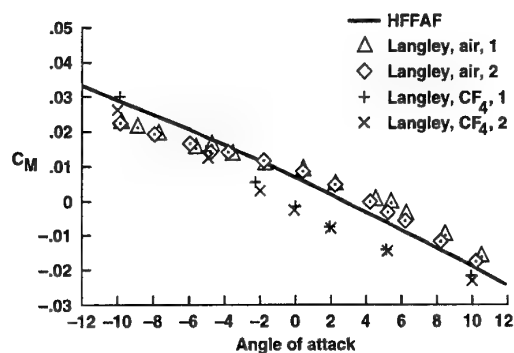


Figure 9. AFE moment coefficient comparison.

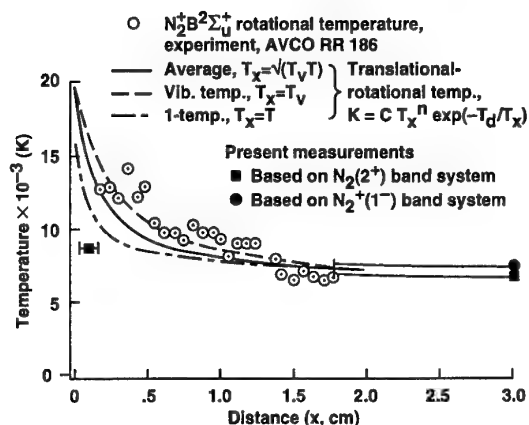


Figure 11. Rotational temperature behind normal shock in nitrogen: $U_s = 6.2$ km/s, $p_1 = 1.0$ torr.

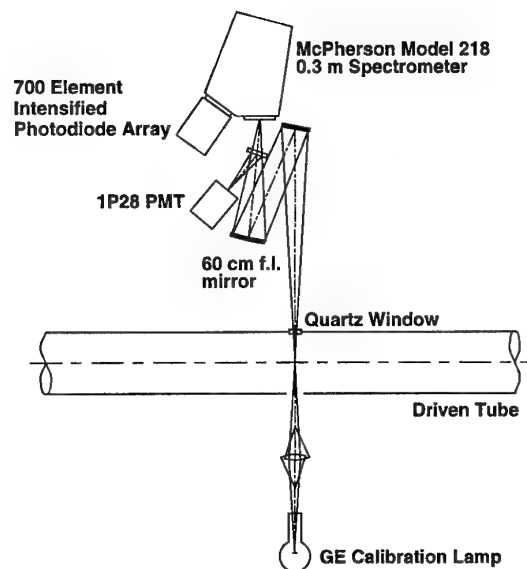


Figure 10. Schematic of shock tube emission spectra collection optics for diode array system.

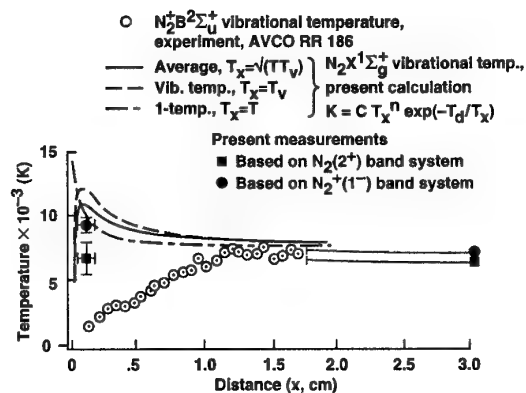


Figure 12. Vibrational temperature behind normal shock in nitrogen: $U_s = 6.2$ km/s, $p_1 = 1.0$ torr.

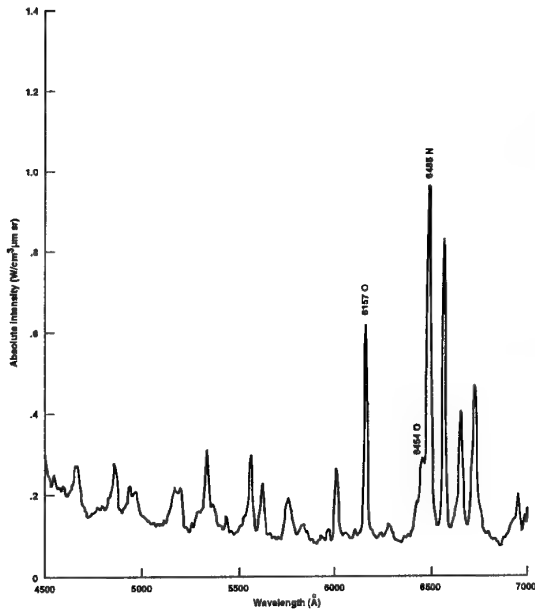


Figure 13. Equilibrium emission spectra behind normal shock in air: $U_s = 10.2$ km/s, $p_1 = 0.1$ torr, gate = 1.0 ms, slit = $60 \mu\text{m}$.

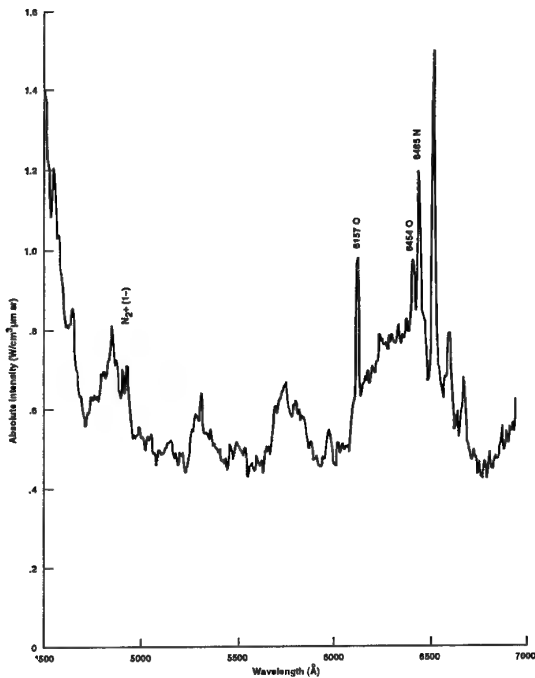


Figure 14. Nonequilibrium emission spectra behind normal shock in air: $U_s = 10.2$ km/s, $p_1 = 0.1$ torr, gate = 200 ns, slit = $60 \mu\text{m}$.

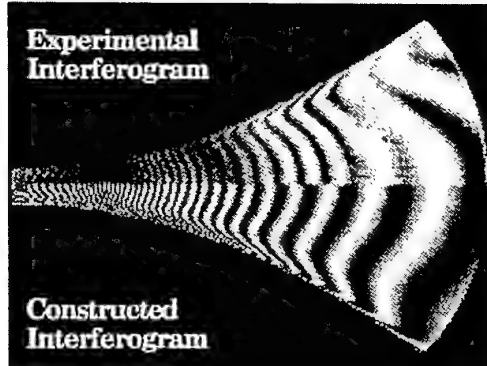


Figure 15. CFD generated synthetic interferogram compared with experimental observation: $P_0 = 105.5$ bar $T_0 = 7200$ K.

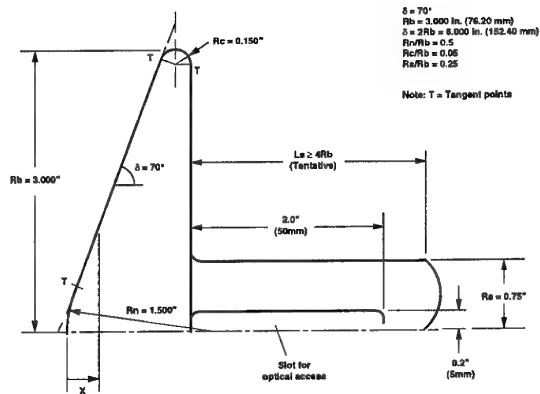


Figure 16. Blunt Cone Model for Forebody and Base Flow Tests.

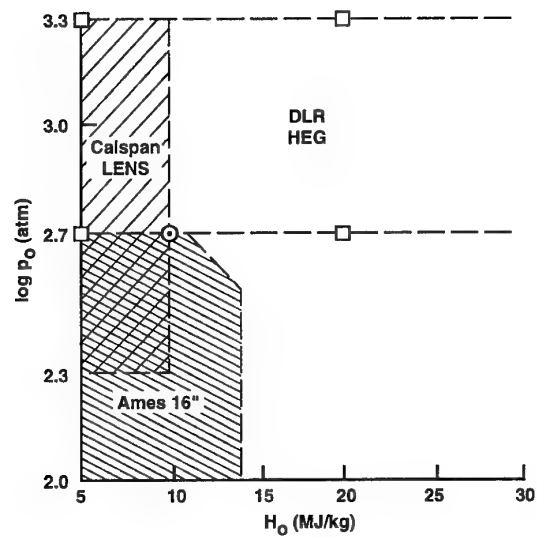


Figure 17. Test Matrix for Blunt Cone Test Campaign.

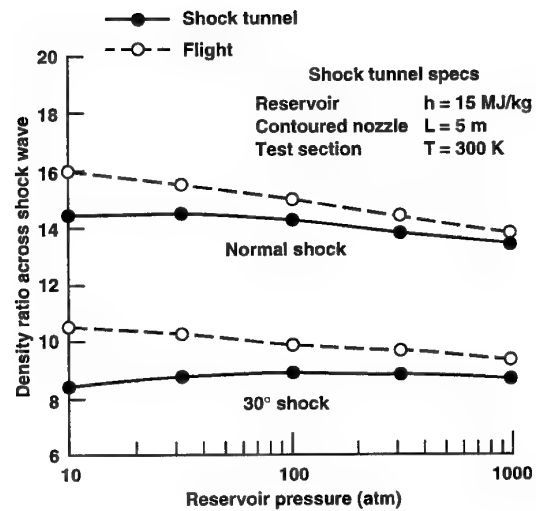


Figure 18. Oribiter Model for Testing in European F4 Wind Tunnel.

CHAPTER VI

CALIBRATION PROCEDURES FOR HIGH-ENTHALPY FACILITIES

George Eitelberg

DLR-German Aerospace Research Establishment
Bunsenstraße 10
37073 Göttingen
GERMANY

CONTENTS

1 INTRODUCTION	131
2 PHENOMENA SIMULATED IN HIGH-ENTHALPY FACILITIES	131
3 FACILITIES	132
3.1 Facilities Heating Test Gas with Electrical Power	133
3.2 Shock Tunnels and Expansion Tubes	133
4 CALIBRATION REQUIREMENTS	134
4.1 Driver Section	135
4.2 Driven-Tube/Nozzle-Reservoir	136
4.3 Test Section	139
4.4 Modeling	142
5 CONCLUSIONS AND RECOMMENDATIONS	142
REFERENCES	143
FIGURES AND TABLE	145

1. INTRODUCTION.

In various space-flight applications, be it winged or ballistic entry into planetary atmospheres, be it powered ascent to orbital flight or exploratory missions passing through planetary atmospheres, the aerodynamic design of a vehicle's performance should account for real-gas effects. In particular the desire to build vehicles capable of flying to the low-earth orbit in single stage using air breathing engines and utilizing aerodynamic lift, challenges our understanding of real-gas effects occurring both in aerodynamics and combustion. Another aspect of the same problem is the consideration of gas composition and temperature when designing the thermal protection system (TPS) of a vehicle. Further interest in real-gas effects is stimulated by the wish to understand the flight phenomena occurring prior to a meteorite striking the earth. To study the relevant real-gas effects caused by the high energy of the flight, high-enthalpy facilities are used for ground testing these phenomena

These ground-test facilities all have a limited capability to examine some aspects of free flight. The facilities, in order to be useful, have to be characterized as thoroughly as possible. Although many new measurement techniques have become available in recent years, the complete characterization of every parameter is still not possible. Therefore, the gaps in the measured data have to be filled by numerical tools, for which as much data as possible have to be made available. This generally concerns the whole facility and not just the freestream at the exit of the hypersonic nozzle.

The dominant real-gas effects in high-enthalpy flows are those caused by high-energy molecular collisions. High-pressure and compressibility effects that lead to the change in the polytropic index of a gas, occur in the simulation facilities, but they will not be considered when the simulation of flow phenomena or free flight is discussed.

It is sufficient to model the air as a thermally and calorically perfect gas in most aerodynamic applications. When this model is applied to hypervelocity flows, gas temperatures can be significantly overpredicted and densities in shock layers underpredicted. A perfect gas going through a strong shock at a near (earth) orbital velocity of $u = 7$ km/s would reach a temperature of

$$T = \frac{h}{c_p} = \frac{u^2}{2c_p} = 25 \times 10^3 \text{ K}$$

Here h is the specific enthalpy, c_p is the specific heat and u is the velocity of the flow relative to the solid body. Fortunately, real-gas effects reduce that temperature to the order of 10^4 K (Hornung 1991).

2. PHENOMENA SIMULATED IN HIGH-ENTHALPY FACILITIES

The main real-gas effects to be considered in high-enthalpy flows are: 1) vibrational excitation; 2) dissociation and recombination and; 3) electronic excitation.

It is customary to define a total temperature of approximately 3000 K as the beginning of high-enthalpy flows of air, i.e. a temperature above which oxygen molecule dissociation in equilibrium becomes significant under atmospheric pressures. This corresponds to a free flight velocity of $u = 2.8$ km/s or a specific stagnation enthalpy of $h_s = 4$ MJ/kg. When the diatomic constituents of air, O_2 and N_2 are considered, it is helpful to list their dissociation energies h_{O_2} and h_{N_2} which are given as: $h_{O_2} = 17$ MJ/kg, $h_{N_2} = 34$ MJ/kg.

In order to be able to concentrate on the simulation of the real-gas effects, we first have to discuss their phenomenological importance and the cases where these effects manifest themselves.

The phenomena of dissociation and vibrational excitation occur as a result of two-body collisions. The production of vibrationally excited molecules and the production of atoms from diatomic molecules are therefore proportional to the number density of the original species. The recombination reaction, however, requires the presence of a third collision partner, and is therefore proportional to the square of the density of the original species. When we further assume that the vibrational excitation is in equilibrium with the rotational and translational excitation, then, for the approximation of an ideal dissociating gas, the thermal and caloric equations of state (Hornung 1991; Vincenti and Kruger 1965) are given as:

$$p = \frac{k}{2m}(1+\alpha)\rho T \quad (1)$$

$$h = \frac{k}{2m}[(4+\alpha)T + \alpha\Theta_d] \quad (2)$$

Equations (1) and (2) have to be complemented by the equation describing the rate of change of the degree of dissociation α :

$$\frac{d\alpha}{dt} = C\rho T^\eta \left[(1-\alpha)e^{-\Theta_d/T} - \frac{\rho}{\rho_d}\alpha^2 \right] \quad (3)$$

where: ρ is the density; α is the degree of dissociation; Θ_d is the characteristic dissociation temperature ($\Theta_d = 1.13 \times 10^5$ K for N_2); ρ_d is the characteristic dissociation density ($\rho_d = 1.3 \times 10^5$ kg/m³ for N_2); T is the temperature; m is the molecular mass; k is Boltzmann's constant; $\eta = -2.5$; $C = 2.7 \times 10^{21}$ m³K^{2.5}/kg s.

In Equation (3) the first term describes the dissociation phenomenon and the second term describes the recombination phenomenon. In real-gas flows, where both the forward and backward reactions are in equilibrium, the degree of dissociation is described by a simple algebraic equation when the expression in the square brackets is set to equal zero. The assumption made about the vibrational equilibrium is good for stagnating dissociative flows, since the dissociation behind a shock

preferably removes molecules from high vibrational levels (e.g. Park 1990). The electronic excitation becomes significant at $h_s > 35$ MJ/kg and will not be considered in the context of aerodynamic testing here. This phenomenon, however cannot be neglected when gas kinetics for fundamental studies are considered.

From Equation (3) it is clear that the rate of dissociation is proportional to the density of the gas and the rate of recombination is proportional to the square of the density of the gas. It is possible to form a characteristic length describing the distance required by the gas to reach the equilibrium between the forward and backward reactions. In fact it is possible to form two characteristic lengths: X_d for the dissociation reaction and X_r for the recombination reaction; the latter being orders of magnitude larger than the former.

It is now possible to classify the flow fields of real gases, using the foregoing discussion:

Equilibrium flow: the characteristic relaxation length is small compared with the geometric scales in the flow field.

Frozen flow: the relaxation length is large compared with the geometry scales.

Nonequilibrium flow: the case between the above two limits.

This classification is illustrated for the earth reentry corridor of a winged vehicle and some wind tunnels in Figure 1, where the specific enthalpy of flight/simulation is normalized with the dissociation energy of nitrogen molecules and the dissociation length is normalized with the vehicle/model size L (Eitelberg et al. 1992).

The equilibrium/nonequilibrium effects can only be simulated in a wind tunnel, where the specific enthalpy of the gas is sufficiently high to excite the dissociation reaction. For aerodynamic simulation, it is obviously not sufficient to simulate the high Mach number alone and it is not sufficient to simulate the high enthalpy alone. When the enthalpy is high, but the relaxation length is long, the real-gas effects cannot be resolved.

In the following, the facilities which can simulate the real-gas effects for aerodynamic/aerothermodynamic testing are discussed. This precedes the detailed discussion of their calibration requirements.

3. FACILITIES

For the study of real-gas effects, clean conditions for high enthalpies are required. High-enthalpy flows are achieved by heating the test gas prior to expanding it through the wind-tunnel nozzle. It is possible to heat the gases by adiabatic compression, electrical plasma arcs or by shock waves. The latter two methods are predominantly used for generating high-enthalpy flow. Further, a combination of adiabatic compression with compression shocks is used in the hypersonic gun tunnels, but these do not achieve a reservoir enthalpy that is sufficiently high to generate significant real-gas

effects. For high-enthalpy flight phenomena testing ballistic ranges are also utilized. This can be done for bodies which do not produce significant lift during their flight in the range.

A substantial discussion of the utilization of different kinds of facilities and a critique of their capabilities has been provided in Chapter V of this report by Deiwert and Pandolfi. The conclusion drawn there for ballistic ranges is that since the test-gas characteristics in the range are extremely well known, these do not require a calibration procedure. Many aspects of the instrumentation required for calibration remain valid for testing in ballistic ranges - especially when stationary instrumentation is used for quantitative flow visualization. Additional aspects will have to be considered when the instrumentation has to be accelerated with the model in order to record model data. Then, either telemetry or recoverable transient recorders have to be used.

3.1 Facilities Heating Test Gas with Electrical Power

For the study of the thermal protection systems of space vehicles, where the correct simulation of the reaction lengths is not of relevance, high-enthalpy flows are produced by using electrically created plasma arcs. The arc-heated wind tunnels are continuous wind tunnels where stagnation enthalpies of up to $h_s = 40$ MJ/kg have been reported. With the application of special technologies, the specific stagnation enthalpy can be reached in excess of $h_s > 100$ MJ/kg (e.g. Auweter-Kurtz 1992), albeit at low densities so that the reaction length cannot be correctly simulated. The arc-heated continuous wind tunnels, however, produce the appropriate partial pressures of the gas component. Consequently, they are predominantly used for blunt-body aerothermal materials testing for shuttle and planetary-entry-vehicle heat-shield development (Laster et al. 1990).

A special version of an arc-heated facility is a *hot-shot* tunnel. A hot-shot tunnel is an impulsive wind tunnel where the test gas, contained in a finite volume, is heated by passing an extremely strong current through it until the desired reservoir condition is reached. When the gas, which is initially heated in a non-uniform manner, has reached the design conditions (pressure and temperature), a plug is removed from the nozzle throat and the flow starts.

In a hot-shot tunnel, the reservoir conditions change in a monotonic way after the removal of the plug from the nozzle throat. This is similar to operating a shock tunnel in an under-tailored manner. When a hot-shot tunnel is operated under perfect-gas conditions, this continuous drop in the pressure and reservoir temperature is of no significant consequence, as long as the pressure ratios and Mach numbers remain constant. However, when high-enthalpy effects are to be studied, this decrease of enthalpy during a test run has to be carefully accounted for together with the change of the Reynolds number.

The only major hot-shot tunnel currently operational is the F4 at ONERA, France (Chanetz et al. 1992). The F4 is capable of operating in both perfect-gas and real-gas regimes. The calibrated region is indicated in Figure 1. At the lower conditions, the test gas behaves like a perfect gas. At the upper conditions the oxygen dissociation reaction is significant at least in the nozzle reservoir, where the gas can be safely assumed to be in equilibrium.

At the condition $h_s = 11.2$ MJ/kg, the nozzle reservoir temperature is in equilibrium at $T_0 = 6200$ K and $P_0 = 20$ MPa and the binary scaling parameter, which is a measure of the relative dissociation reaction length, is given as $\rho L = 3 \times 10^{-4}$ kg/m². This value, although far from the reentry corridor, may still yield significant real-gas behavior for code-validation experiments.

3.2 Shock Tunnels and Expansion Tubes

The study of real-gas effects alone is frequently performed in shock tubes when only the reactions are of interest. These tools are particularly suited for the provision of controlled conditions at high enthalpies. Behind the incident shock, the tests can be performed with a moving gas and behind the reflected shock, the stagnation conditions can be utilized. Very-high-enthalpy conditions have been achieved, for example, in the Electric Arc driven Shock Tube (EAST) of NASA-Ames Research Center (Park 1991), albeit at the geometrical restrictions imposed by the size of the shock tubes. It is a logical step to use the same tools for generating high-enthalpy flows for aerodynamic testing.

A shock tube consists of a high-pressure driver and a driven section. To make it into a shock tunnel, a nozzle is added to the downstream end of the driven tube as shown in Figure 2. In this configuration, the volume of the tube between the downstream end of the driven tube and the reflected shock is used as the reservoir for the blowdown wind tunnel. Since the shock heating process is very fast, and the volume of available test gas is small, the test times are very short. Thus, the shock tunnels are not usually called blow-down tunnels but *impulse* facilities instead. When the shock is not being reflected at the end of the driven tube but further accelerated into the next section, the resulting facility is called an *expansion tube*. The expansion tubes can produce extremely high enthalpies at moderate relaxation lengths (Erdos et al. 1990). The enthalpy levels are achieved at the cost of test time when compared with the reflected-shock tunnels.

Since the specific enthalpy, h_s , achievable in a reflected mode is proportional to the square of the incident shock velocity V_s , $h_s \approx V_s^2$, Mach numbers of the incident shock, M_i , required for producing high-enthalpy flows have to be $M_i > 6$. $M = 6.16$ is the theoretical limit obtainable in simple air-to-air shock tubes, when the driver and driven gas are of identical temperatures.

In order to achieve the required high incident Mach numbers in the range $6 < M_i < 20$ for high-enthalpy testing, a number of techniques can be used. The equation for the incident shock (Becker 1965) is given by:

$$\frac{p_4}{p_1} = \frac{2\gamma_1 M_i^2 - \gamma_1 + 1}{\gamma_1 + 1} \left[1 - \frac{\gamma_4 - 1}{\gamma_1 + 1} \frac{a_1}{a_4} \left(M_i - \frac{1}{M_i} \right) \right]^{\frac{2\gamma_4}{\gamma_4 - 1}} \quad (4)$$

where p_4 is the driver pressure at burst, p_1 is the driven tube charge pressure, γ_4 is the ratio of specific heats of the driver gas, γ_1 is the ratio of specific heats of driven gas, a_4 is the speed of sound of driver gas, a_1 is the speed of sound of driven gas. Equation (4) indicates that M_i can be increased not only by increasing the pressure ratio from the driver to the driven tube but also the ratio of the sound speeds.

The increase in the ratio of sound speed from driver to driven gas is achieved by lowering the molecular weight and increasing the temperature of the driver gas. The commonly used driver gases in high-enthalpy, impulse-tunnel applications are hydrogen and helium which exhibit the highest sound speed at given temperatures. In order to further increase the sound speed, the driver gas can be heated by either external heaters, combustion, or compression.

In heated-driver tunnels like the CALSPAN tunnels (Witliff 1987) or the TH2 tunnel in Aachen (Grönig 1991), the temperature (and the sound speed) of the helium driver gas is increased by heating the driver tube by resistance heaters from outside. Reservoir enthalpies up to 8 MJ/kg are achievable with the heated-driver technique.

Another way to obtain high incident Mach numbers is to heat the driver gas by a combustion process. In the combustion-driven shock tunnel, the driver gas, He , is enriched by a combustible mixture of oxygen O_2 and hydrogen H_2 . The mixture is ignited by an electrical spark and the combustion heats the driver gas. The reservoir temperatures achieved with this type of driver technique are reported up to 8000 K, corresponding to reservoir enthalpies of up to 15 MJ/kg. The speed of sound achieved in the combustion heated drivers is limited by the formation of water vapor as the combustion product (Lukasiewicz 1973). Notable examples of combustion-driven shot tunnels are at NASA Ames Research Center (Deiwert 1992) and Boeing. A new version of a combustion driven tunnel is the detonation tunnel as proposed by Grönig (1990).

The highest driver temperatures achievable under current technology for high-enthalpy, high-density testing (binary scaling parameter simulation) are obtained by using a (near) adiabatic and isentropic compression of the helium driver gas by a heavy free-flying piston accelerated into the driver tube by compressed air (Stalker 1972). The driver-gas temperatures obtained in helium or

helium/argon mixtures are of the order of 4000 K. Here reservoir conditions at h_s in excess of 30 MJ/kg have been reported. In the new tunnels, T5 (Horning 1992) and HEG (Eitelberg et al. 1992), the standard operating conditions do not exceed $h_s = 25$ MJ/kg, because of the requirement to operate at tailored conditions. The shock tunnel T5 has been operated to study the real-gas effects in external flow as well as in supersonic air-breathing combustion. Out of consideration of the requirements of combustion experiments, the T5 nozzle expansion is such that the Mach numbers are at the lower end of the hypersonic approximation ($M = 5$) and the freestream densities very high. While this provides for a high value of the binary scaling parameter ρL , in some applications it may produce relaxation lengths which cannot be resolved with the help of existing instrumentation.

Even higher driver temperatures are achievable in the EAST facility at NASA Ames Research Center. Here driver temperatures up to 8000 K are reported. Very-high-enthalpy conditions can be achieved with this facility for studies of gas kinetics. Despite the extremely high enthalpies achieved, this facility is not used for direct aerothermodynamic simulation of flight paths due to the low operating densities and small sizes of the tube.

The HEG and the shock tunnel TCM2 at the Université de Provence, Marseille were designed for external aerodynamics, with the ultimate goal of testing in the framework of the European HERMES space-plane program in mind. Therefore the HEG was designed to produce Mach numbers in the range of $7 < M < 10$, depending on the reservoir enthalpy. For this purpose the nozzle area ratio is $A/A^* = 1600$. At perfect-gas conditions, this area ratio would produce Mach numbers around 20.

The high-enthalpy flows, coupled with the capability to produce high density (and high values of the binary scaling parameter ρL) for any significant times (approximately 2 to 3 ms in the HEG nozzle reservoir) also set the operational limits for the high-enthalpy shock tunnels. The calibration procedures for the latest tunnels HEG, T5 and the G-Range at the AEDC have all been held up by the need to replace the ablating steel tube walls with some other material which better withstands the thermal loading.

While the high-enthalpy facilities have been in use for several decades already, their use is still not without its uncertainties. Most tunnels have been through some calibration, but the determination of the freestream conditions still relies to a large extent on numerical calculations based on some reasonable assumptions. The empiricism covers the reservoir conditions and the nozzle performance and design (Hannemann 1990).

4. CALIBRATION REQUIREMENTS

Calibration of high-enthalpy facilities is to be performed by measuring parameters at various positions within the

facility and then making comparisons with currently available modeling. Of principal importance is the characterization of the flow at the exit of the facility nozzle (freestream conditions). In this region, flowfield data are required when making comparisons with computer modeling of ascent or reentry conditions as experienced by the various orbital vehicles, for example, HERMES, NASP or blunt bodies. It is also important to establish the uniformity of the flow for each of the operating conditions.

At the present stage of facility development, the aerothermodynamic state of the gas at the nozzle exit is not fully measurable. Therefore, the test conditions are determined by combining available experimental data with CFD simulation of the facility behavior. Therefore, in addition to calibration measurements in the nozzle, the flow upstream ought to be measured since it influences the determination and computer modeling of the freestream conditions, many parameters of which are determined as a result of calculations based on the data measured upstream of the nozzle. These calculations use various assumptions about the steady, but not necessarily isentropic, expansion of the high-enthalpy gas through the nozzle. A major task is to confirm the validity of these assumptions for many essentially time-dependent, flow-establishment processes. When shock-heated gas is used as the high-enthalpy gas, then both the shock driver as well as driven part of the shock-tube conditions should be monitored in order to obtain better understanding of the nozzle reservoir conditions. Measurements in the driven section provide input data on the entry conditions of the nozzle while measurements in the driver section will assist in understanding the tailoring conditions and time variations of the state of the test gas.

In the following sections, an attempt is made to provide a systematic approach to the information monitoring in a shock-tube-driven, high-enthalpy wind tunnel. The same approach used for the reflected shock tunnel is, with minor variations, also valid for expansion tubes. Hot-Shot facilities, e.g. the ONERA F4, require a modification of the approach inasmuch as they heat the test gas with the help of an electric arc. The principle of obtaining as much information as possible upstream of the nozzle remains valid.

4.1 Driver Section

The conditions in the driver tube of a shock tunnel are to be monitored before, during, and after the breaking of the diaphragm separating the driver tube from the driven tube. The pressure history, and if possible, the temperature history helps to determine whether or not the expansion fan, which travels into the driver gas after the diaphragm burst, can influence the nozzle reservoir conditions during the useful testing time (Figure 2).

The temporal information is particularly important when a short driver or free piston driver is used. This sort of

information also helps to remove ambiguities about the resultant shock speed and pressure histories in the driven tube. If the driver conditions vary during the time equivalent of the drainage time of the test gas, the enthalpy distribution in the reservoir may become non-homogeneous.

For the free-piston driven shock tunnels (Stalker tubes) the so called "tuned-piston-operation" is recommended for suppression of the expansion waves which would result from a rapid deceleration of the piston after the burst of the main diaphragm. The concept of tuned piston operation implies a piston that is moving downstream with such a velocity that it matches the flow of helium into the driven tube during a certain required period of time. There is equivalent idea possible for heated-driver or combustion-driven shock tunnels. In the latter cases, a long driver tube is required in which the upstream propagation and reflection of the rarefaction wave should be monitored.

It is possible in the free-piston tunnels to monitor the piston velocity continually by radar (e.g. T5, M. Jenkins 1993) or monitor its trajectory at discrete locations and match it to a model (e.g. HEG, Eitelberg et al. 1992). In the HEG, sensors located at 5 positions along the compression tube, monitor the passage time of the piston from which the piston trajectory is determined as a function of position and time. Comparisons of the measured piston trajectory with theoretical predictions can be made. The prediction method is described by McIntyre and Atcitty (1989) and based on work by Hornung (1987). The piston velocity, however, is not a sensitive measure of the tuning of the operation. A more sensitive measure is the pressure recording after the diaphragm burst.

It is common to obtain non-uniform shock velocities in the driven section of a shock tunnel. Some of this is attributable to the boundary-layer development in the driven section. Another contributor may be an expansion catching up with the incident shock. Monitoring the driver gas pressure in the driver section helps determine the onset of the expansion. In combustion-driven tunnels. The monitoring of the driver pressure has to be used in order to determine the uniformity of the combustion process. It is possible for the combustion to continue after the rupture of the diaphragm separating the driver section from the driven section.

In the free-piston driven tunnels, the focusing of the compression waves (Dumitrescu et al. 1993) in the helium driver gas can lead to an oscillatory component of the incident shock velocity in the driven section (Eitelberg 1993). Although the simple models of the tunnel performance do not show this shock speed oscillation affecting the reservoir enthalpy (Ueda 1993), these pressure oscillations can still affect the flow quality in the test section. A comparison of an experimental pressure trace at the main diaphragm station with a simple numerical prediction is given in Figure 3,

where the average pressure matches the prediction. The latter, however, does not show the pressure modulation observable in the experiment. When more elaborate numerical schemes are used, these pressure oscillations can also be shown to be modeled.

Related to the concept of the tuned piston operation in the Stalker-tubes is the concept of "holding time". The holding time is that time during which the piston velocity after the diaphragm burst matches the flow rate of the driver gas into the driven tube. This is the time during which the pressure at the end of the driver tube stays at or above the burst pressure. A similar measure can be defined for those other tunnels which rely on the spontaneous bursting of diaphragms like the NASA-Ames 16-inch Shock Tunnel.

In order to judge the driver/driven tube performance, the diaphragm burst time also has to be determined. This is a requirement when the driver pressure is being monitored. This information can help remove ambiguities about the shock attenuation process. It is obvious that the shocks are attenuated as they propagate down the driven tube, but by how much is still somewhat unknown for the facilities where the driver pressure is transient. The diaphragm burst time can be determined by a detector placed at the upstream end of the driven tube. Some care is required when evaluating the times with high accuracy. The diaphragms in high-enthalpy facilities do not burst open instantaneously. A simple calculation performed for the HEG accounting only for the inertia of the diaphragm petals shows that at the 50 MPa condition, the diaphragm requires approximately 0.4 ms to fully open. During this time the shock front has characteristically propagated 2 meters downstream.

Another concept employed in order to obtain uniform driver conditions during the shock propagation times is that of a detonation driver as proposed by Grönig (1990). Such a facility differs from the conventional combustion driven tunnel in that the ignition is started at only one location next to the diaphragm. As long as the combustion propagates upstream in the driver tube in the form of a detonation wave, the conditions driving the shock wave stay constant, assuming that the detonating mixture is homogeneous. In such a shock tunnel, the conditions between the detonation wave and the driver tube can be monitored by monitoring the pressure p_3 .

4.2 Driven-Tube/Nozzle-Reservoir

After rupture of the diaphragm separating the driven tube from the driver tube, a shock wave is generated which propagates along the shock tube, heating and compressing the test gas, normally air. For shock tunnels, the shock reflects after reaching the end of the tube and propagates back upstream. In expansion tubes, the incident shock passes through a secondary diaphragm without significant reflection and is further accelerated in a low-pressure section of the tube, called the acceleration

tube. The particular requirements for expansion tubes will be further discussed within the text of this section.

The behavior of the secondary diaphragm in the expansion tubes is a major field of study and a challenge for the development of this facility type. The opening time of the diaphragm can occupy a significant portion of the available test time and also cause the incident shock to reflect at it, thereby destroying some of the advantages of the expansion tube concept.

In a reflected mode shock tube, behind the reflected shock, the gas is stationary and at a high temperature and pressure. This region serves as the reservoir for the nozzle. As much information as possible about the nozzle reservoir condition should be obtained in order to provide reliable data for the calculation of those flow parameters that cannot (yet) be measured in the test section or are required for validation of the nozzle calculation codes. For expansion tubes the working assumption is that there is no reflection of a shock or no stagnating region to be considered at the secondary diaphragm.

Following is a list of parameters, which can be measured in most tunnels where the test gas is shock heated:

4.2.1 Initial shock-tube pressure: p_1

The initial shock-tube pressure together with the measured driver pressure and temperature is used to obtain a prediction for the incident shock velocity. The prediction for perfect gas is obtained from the Equation 4. In the case of significant dissociation behind the incident shock, some of the energy available to accelerate the gas is redirected into the dissociation process and the resultant shock velocity is slightly lower.

4.2.2 Shock velocity

The shock velocity can be determined either by using ionization gauges situated at various points along the shock tube to record the passing of the initial shock, or by pressure sensors. The pressure sensors, although more costly and not quite as robust as the ionization gauges can provide the pressure behind the incident shock on its passage in addition to the shock speed. The pressure behind the incident shock should reflect the influence of the non-uniform driver conditions.

The shock passage gauges, together with a (pressure) measurement at the end of the shock tube, provide average shock velocities:

$$V_s = \frac{\Delta l}{\Delta t} \quad (5)$$

where Δl is the distance between the sensors and Δt is the time between signals at these sensors. The last measurement at the end of the driven tube is generally that of pressure, since that is a necessary measurement

for describing the nozzle behavior. The actual shock velocity may vary over the length of the shock tube. This variation will result in variation of the reservoir condition. In order to substantiate the claim that these variations are not significant, or in order to be able to account for the variations, they ought to be quantified. Since the stagnation enthalpy, h_s , is approximately proportional to the square of the incident shock velocity, then in the absence of other processes, the inhomogeneity in the enthalpy distribution can become noticeable.

In general practice for the calculation of the stagnation enthalpy h_s , the downstream part of the shock velocity is used, as it is the downstream part of the driven gas, which after the nozzle starting process, is used as the test gas. The upstream portion of the driven gas is most likely to remain in the shock tube boundary layer and get mixed with the driver gas.

The predicted shock speed can be compared with the actually measured shock speed in order to obtain a measure of the losses in the shock propagation process. The shock attenuation appears to display two components: the shock speed attenuation and the pressure losses behind the (reflected) shock. It is possible, in a free-piston-driven shock tunnel, to obtain no apparent shock-speed attenuation Figure 4a Shot#53, but still obtain a lower reservoir pressure than calculated from the shock speed and initial charge pressure of the driven tube as shown in Figure 4b. The Page-Stalker correlation (Page and Stalker 1983), that attempts to correlate the experimental data on the pressure losses, does not seem to incorporate all the mechanisms governing these pressure losses, as the newer piston-driven facilities experience smaller losses than predicted. The viscous losses affecting the shock velocities as formulated by Mirels (1964) seem to provide very accurate predictions for the velocity decrease (Figure 4b).

4.2.3 Nozzle reservoir pressure ($p_5 = p_0$)

The nozzle reservoir pressure is usually obtained by locating one or more pressure sensors at the end of the shock tube. These pressure gauges at the end of the shock tube are then used to record the time history of the reservoir pressure. The positioning of the pressure transducers in the end wall has some advantages over positioning them in the side wall, as the end wall is not quite as exposed to the interaction of the reflected shock with the boundary layer created behind the incident shock. The reservoir pressure, as measured, does not generally agree with the pressure calculated for the high-enthalpy facilities, as discussed previously. The procedure for calculating the nozzle reservoir conditions from the measured parameters then involves a step that requires further confirmation by independent means. The step generally taken is based on the assumption that whatever the pressure loss mechanism is, it is an isentropic mechanism that can be accounted for by

assuming an isentropic expansion from the calculated pressure to the measured pressure in the nozzle reservoir. This method has been particularly popular, when the reflected shock tunnels are operated in an under tailored mode, Morgan et al. (1989). This procedure shows shortcomings, when tailored operating conditions are reached in the facility.

Generally piezo-electric sensors are used in the reservoir of a short run time high-enthalpy wind tunnel, as these sensors are both robust and possess a short response time. The measurement of these pressures at the reservoir of a high-enthalpy nozzle is not trivial. The pressure sensors should not be directly exposed to the high-enthalpy high pressure gas, as the membrane whose deflection enables the pressure to be measured can be severely damaged by the exposure to the temperature. Furthermore, since the heat is applied from one side only, the pressure measurement can be strongly affected by the thermal tensions created in the pressure sensitive membrane. It is standard practice to shield the sensors from direct exposure by mounting them in recesses and protecting them by screens or shields. The recesses can cause shock focusing and the screens and shields can impair the temporal response of the sensors. An example of the effects of the mounting location of the pressure sensor is given in Gourlay et al. (1989)

4.2.4 Nozzle reservoir temperature

It is desirable to obtain a measurement of the temperature in order to fully determine the thermodynamic condition of the gas in the nozzle reservoir. However, there is no reported case of this being done for high-enthalpy ground testing aerospace facilities. In a number of shock tunnels a discrepancy between pressures calculated from the shock propagation velocities and pressures measured experimentally exist. A temperature measurement would assist in explaining this discrepancy. The temperatures, which range from 4000 to 12000 K could be probed with optical methods. One possibility would be to replace a pressure sensor with a fiber optic sensor and analyze the emission spectrum of the reflected region.

4.2.5 Expansion tubes

Since there is no stagnant reservoir in an expansion tube, it is even more important to obtain not only a shock velocity, but also a pressure behind the incident shock for completeness of the information. When assuming that the expansion tube is operating in a perfect gas regime, measuring the thermodynamic parameters should be adequate. When, however, the expansion tubes are operated in the high-enthalpy regime where the chemical composition of the test gas can change, then, dependent of the time of the measurement, the gas kinetics can be frozen at various degrees of non-equilibrium or it can be in equilibrium. This is explained with the help of the Figure 5, where the basic operation of an expansion tube is presented (Erdos 1993). Different

gas particles, although all expanding to the same final state 5, have had different times for this expansion. For expansion tubes the same approach of careful calibration as used in the test sections of other real-gas facilities is required. This in particular when chemical kinetics plays a significant role.

The determination of the nozzle reservoir condition is generally performed with the help of calculations using the measured information as input. In most shock tunnels used for aerospace testing it is sufficient to consider the real-gas effects in this part of the facility to be in chemical and thermal equilibrium due to the high densities of the test gas used in the shock tubes.

In the HEG, like in many shock tunnels, the calculations for the shock tube are performed using the equilibrium shock tunnel program (ESTC) developed by McIntosh (1968). Input parameters are the initial shock tube pressure and the shock wave velocity. Predicted are the conditions behind the reflected shock. To account for non-tailored conditions (an expansion or compression of the reservoir gas), an isentropic expansion or compression is used to arrive at the measured reservoir pressure (see Morgan et al. 1989). In an analog way, the pressure rise during the heating process is measured in the reservoir of the hot shot tunnels. Assuming conservation of mass and adiabatic conditions, the enthalpy can be calculated. For calculation of test conditions, the assumption that the conditions are homogeneous in the reservoir has to be made, although at this stage this assumption is hard to verify experimentally.

The tailoring, desirable for many tests, is usually obtained as a result of trial and error. The simple predictions based on ideal shock tube theory usually over predict the required shock speeds and reflected pressure conditions. In the experimental approach, a tailored condition is reached, when the nozzle reservoir pressure stays constant over a time that is at least half the drainage time of the test gas. The requirement for only half of the drainage time is an empirical result of allowing for test-gas contamination by the driver gas after this time. The drainage time τ can be calculated by:

$$\tau = \frac{\mathcal{M}}{\rho_5 a_5 \left[\frac{2}{(\gamma+1)^{**}} - \frac{\gamma-1}{2(\gamma+1)} \right]} \quad (6)$$

where \mathcal{M} is the total mass of test gas filled into the tube, ρ_5 is the density of the test gas behind the reflected shock and a_5 is the speed of sound in the test gas behind the reflected shock, γ is the ratio of specific heats.

The desirability for tailoring, apart from being useful when aerodynamic derivatives are determined, could be of particular significance, when high-enthalpy real-gas effects are to be studied. In many perfect gas applications, when the nozzle pressures fall

proportionally with the reservoir pressure, the Ma number stays constant and only the Reynolds number changes with insignificant consequences for the tests. In high-enthalpy facilities the change in pressure and temperature also changes the enthalpy during the test run.

The testing with the new free piston driven shock tunnels (T5, HEG, TCM2, AEDC ST) so far has shown that the prediction methods used for the design of these can be made to work reliably. The main deviation from prediction of the nozzle reservoir conditions for the HEG came from the requirement to operate in the tailored interface mode, i.e. provide an approximately constant pressure in the nozzle reservoir. This condition has been reached by experimentation and shown to work up to reservoir pressures of 150 MPa at the specific enthalpy of $h_s = 25$ MJ/kg, and an empirical correlation for the tailoring of the HEG conditions has been established. This empirical correlation accounts for the loss mechanisms in the driven section of the shock tube and the transition from the driver to the driven section. Due to the high mechanical load on the facility at the higher pressure levels, as the standard operating conditions the diaphragm burst pressures $p_r = 50, 100$ MPa at enthalpies $10 \text{ MJ/kg} < h_s < 25 \text{ MJ/kg}$ are used, although driver pressures in excess of 200 MPa have been reached.

Computer codes, validated with the data from the existing facilities (Maus et al. 1992), used in the design of a brand new facility at AEDC, Tullahoma, are capable of excellent prediction of the HEG operating conditions, (McIntyre et al. 1993).

4.2.6 Reservoir Enthalpy: h_s

The reservoir enthalpy is usually calculated by using as input parameters the incident shock speed and the fill pressure of the test gas. In its simplest approximation the specific reservoir enthalpy h_s is proportional to the square of the incident shock velocity:

$$h_s \approx V_s^2 \quad (7)$$

although h_s will vary when an expansion or a compression is taking place behind the reflected shock as a result of operating in non-tailored mode. In the above simplification it is assumed that all the shocks are strong and the operation of the shock tunnel does not significantly deviate from the tailored operation. In this case the energy conservation equation across the shock, neglecting small terms (of order ϵ^2 , where ϵ is the density ratio across the shock), can be shown to yield the above result.

Computer codes, validated with the data from the existing facilities (Amuse et al. 1992), used in the design of a brand new facility at AEDC, Tullahoma, are capable of excellent prediction of the HEG operating conditions, (McIntyre et al. 1993). The newer, more sophisticated codes, show also some fine detail in the behavior of the

free piston driven compression cycle, which can safely be ignored in the design of experiments but may help in understanding the limitations of the shock tunnels. A pressure wave traveling in the driver gas, caused by the fast piston stroke, has been shown to exist by the numerical codes (e.g. Burtschell et al. 1991) and has been confirmed by experiments in the TCM2 driver (Labracherie et al. 1993). In the HEG this has been shown to influence the shock speed in the driven tube: (Figure 4).

Although the codes agree reasonably well with the existing experimental data, care should be exercised in extending the above results to enthalpies much higher than 20 MJ/kg. At densities required for binary scaling testing in the freestream of a nozzle, the reservoir densities are so high that any increase in the shock speed will result in an increase of the thermal losses to the reservoir walls and therefore Equation 7 will lose its validity. In the extreme cases this could possibly lead to droplets of the reservoir wall materials in the reservoir gas, which will absorb further energy, as suggested by Deiwert in Chapter V.

4.3 Test Section

Both contoured and conical nozzles are used in impulse facilities. The conical nozzles have the advantage of being easy to manufacture and simple to calculate. The main task in the calibration process is to determine the gradients caused by the conical nozzle contour and the state of the gas after an isentropic expansion. In general, one nozzle is used to produce a variety of test conditions, where the parameters changed are the reservoir enthalpy and the reservoir pressure. These parameters, at a given nozzle expansion ratio, provide a range of Reynolds and Mach numbers of the freestream. It is generally accepted that the conical nozzles are more forgiving for off-design conditions and the difficulties present in the tunnels using contoured nozzles are negligible.

The contoured nozzles are used in order to produce parallel, gradient-free flow in the test core. The contouring is performed for one specific condition, and since the tunnels usually operate over a range of conditions, the calibration has to show that the nozzle operates reasonably at off-design conditions as well. Particular care has to be taken to operate the nozzle at conditions where the center-line disturbances do not occur.

Since the contoured nozzles are designed for only one condition, they may produce non-uniform flows at other conditions. The non-uniformities may or may not be significant. The contoured nozzles are generally longer than the conical nozzles for the same expansion ratio, and therefore produce significant flow starting times in the nozzles. This is true for both the inviscid phenomena like the propagation of primary and secondary shocks down the nozzle (Lee and Nishida 1992; Smith 1966) as

well as for the viscous phenomena like boundary-layer growth on the nozzle walls.

The above holds also for continuous high-enthalpy facilities. As soon as real-gas effects start occurring, the fixed contour nozzle starts producing variable Mach numbers as a function of the reservoir enthalpy and the reservoir pressure. The quality of the flow may vary from condition to condition, and therefore have to be calibrated. The possible reduction of flow quality is made up for by the production of significant real-gas effects.

Measurements to be performed in the calibration of high-enthalpy wind tunnels include the same measurements as in any other wind tunnel. In addition to the standard pressure calibration, it is useful to obtain information about the enthalpy of the freestream and about the chemical composition of the above. For the chemical composition determination, some spectroscopic measurements have to be performed.

Furthermore, since the high-enthalpy tunnel reservoir conditions are practically impossible to contain for any significant duration due to the high pressure and thermal loads on the walls of the reservoir, it is advisable to monitor the contamination levels of the freestream. The contamination can occur in both gaseous and particulate form; the presence of both should be acknowledged.

For high-enthalpy facility calibration, it is helpful to determine those parameters which are unique to high-enthalpy conditions. The main effect is that of chemical reaction in the flow. The simplest chemical effects include the presence of atomic species in air, O and N in addition to the molecular ones O_2 and N_2 . As a consequence of that the flow field is affected, and the shock standoff distances in front of blunt bodies will vary significantly from the perfect gas cases for the same Mach numbers.

Furthermore, the question whether the test section flow is in equilibrium, partially frozen or frozen has to be addressed. An analysis performed by Beck and Hannemann (1993) for a moderate high-enthalpy condition of $h_s = 24$ MJ/kg and reservoir pressure 50 MPa, for a nozzle expected to produce Mach numbers $M = 10$ at this condition, shows that while the density and freestream velocity are only insignificantly affected by nonequilibrium, the freestream temperature and the static pressure may vary by a factor of 2 between equilibrium and frozen states. In this analysis the question of freezing of the vibrational modes of the molecular species in the freestream was not addressed.

4.3.1 Pitot pressure: p_t

Standard pitot rake measurements will provide information about the size of the core flow and the radial and axial gradients existing in the flow. Since the high-enthalpy aerodynamic facilities operate as impulse facilities with a certain degree of scatter in their operating conditions, it is useful, and should be used as a

standard, to use a permanently installed pitot probe in the test section to provide information about shot to shot repeatability. This together with a hemispheric probe for stagnation point heat transfer. The pitot pressure, when the density of the test gas is known, can also be used for evaluation of the flow velocity. For hypersonic flow the pitot pressure can be expressed by the simple expression:

$$p_t = \rho u^2 \left(1 - 0.5 \frac{\rho}{\rho_s} \right) \quad (8)$$

where ρ is the freestream density, ρ_s is the density of the gas behind the shock and u is the velocity. This expression accounts for the stand-off of the shock in front of the probe and for the reaching of equilibrium at the stagnation point. In this approximation, valid gas at hypersonic Mach numbers, it is assumed that the gas reaches its stagnation pressure as a result of an isentropic deceleration from the shock to the probe. For a diatomic gas this yields a handy expression of $p_t = 0.92 \rho u^2$, the same approximation can also be used for existing high-enthalpy facilities, since the dissociation length is much longer than the shock stand-off distance in front of a small probe. This expression yields the Newtonian approximation $p_t = \rho u^2$, when the density jump across the shock approaches infinity.

For fast response time both piezoelectric as well as piezoresistive gauges can be used. The sensors themselves have to be protected from direct exposure to the high-enthalpy gas. For this protection a loss of response time is endured as a penalty. The installation of pressure sensors has to be carefully considered, in order to obtain sufficient response time and no falsification of the results through heat loads on the sensors.

Pitot pressure profiles should be obtained at different axial locations downstream of the nozzle exit plane and at the exit plane also. The information about the boundary-layer growth in a long nozzle is important for evaluating the available test time, therefore temporal resolution of the pitot pressure is desirable. The change in the contour of the nozzle, caused by the boundary-layer development, may affect the core-flow development, as axisymmetric contoured nozzles can be sensitive to small variations in the contour. The information about the boundary-layer thickness is also important for further nozzle designs, as most of the existing nozzles were designed with the help of inviscid codes and boundary-layer corrections. The current calibrations can provide an experimental data base for high-enthalpy nozzle calculations.

4.3.2 Static pressure: p

The static pressure of the gas is difficult to measure in impulse facilities. A flat plate produces a viscous interaction shock. Curved surfaces can cancel the pressure rise caused by the shock through an expansion, but these

methods are not yet calibrated for high Mach number flows with real-gas effects. For a relative calibration and comparison, it might still be advisable to obtain any measure of p , even if it is affected by some other phenomenon. The use of Pinckney (1975) probes can be justified, if their response times can be made sufficiently short and if the calibration procedure, which currently has to be done with the help of CFD, is trustworthy. The sensors are not as strongly affected by the high temperature, so can be brought closer to the flow with less penalties in response time than in the case of the stagnation pressure measurements.

In the high-enthalpy facilities, which are all impulse facilities, the measurement of flow angularity poses a problem. Since the signals obtained are generally noisy, it is very difficult to obtain a quantitative measure of the angularity from pressure signals alone. Visualization of flow around a blunt body may prove helpful in this task.

4.3.3 Stagnation point heat transfer: q_{sph}

The stagnation point heat transfer on a sphere or an hemisphere can be measured at one location only or on a rake, as desired. This measurement can provide useful shot to shot and facility to facility comparison. Furthermore, together with the two measurements of the static and stagnation pressures it can be used to calculate other time dependent freestream parameters. For the above calculations the formulation as proposed by Fay and Riddell (1958) is generally used:

$$q_{sph} = 0.94 (\rho_w \mu_w)^{0.1} (\rho_s \mu_s)^{0.4} \left[1 + \left(Le^{0.52} - 1 \right) \frac{h_D}{h_s} \right] (h_s - h_w) \left(\frac{dV}{dy} \right)^{0.5} \quad (9)$$

with ρ is the density, μ is the viscosity, h is the enthalpy, and Le is the Lewis Number. The subscripts s and w denote stagnation- and wall-temperature values for the physical parameters, respectively. The factor dV/dy is the velocity gradient at the stagnation point of the sphere. In this expression the velocity gradient and the stagnation point viscosity, which both have to be provided by some analytical approximation, result in significant uncertainty in the backward calculation of stagnation enthalpy. The determination of the dissociated enthalpy h_D is not quite as significant, although it contains large uncertainties, since it contributes only a small proportion of the overall term.

Modifications to the Fay and Riddell formulations have been proposed several fold, the one described by Olivier (1993) produces good results for the heated driver tunnel TH2 at Aachen, Germany. The systematic approach used there, however, cannot be extended to facilities where the freestream is not in equilibrium. The backward calculation from the shocked state to the freestream conditions, when the level of deviation from the freestream is not known, cannot yield unique results. An independent

measurement of the freestream thermodynamic state is required when the reservoir measurements cannot be trusted to provide sufficient information, as in the cases where the enthalpy generation in the nozzle reservoir is non-homogeneous (e.g. hot shots and other plasma generated flows).

Miller and Wilder (1972) provide an extensive discussion of the various methods of predicting and evaluating the stagnation point heat transfer rates. The significant dependence of the heat transfer rate calculation or the evaluation of total enthalpy on the transport properties of the high-enthalpy gas is also discussed by Miller and Wilder. For the high-enthalpy conditions generally coaxial thermocouples are used, since their temporal response can be made almost arbitrarily fast. The development of fast calorimetric gauges for impulse facilities and high-enthalpy conditions is still in progress, Grauer-Carstensen (1991). The multitude of heat transfer gauges available for cold hypersonic facilities has not found general acceptance for the hot facilities. The relatively low density arc-jets do not impose quite the same requirements on the heat transfer instrumentation.

In many high-enthalpy facilities the measurement of the stagnation point heat transfer poses severe difficulties due to the contamination of the flow with particulate matter. In the hot shots, it has been found that it is possible to obtain a correlation between the stagnation point and shoulder heat transfer rates on an hemispherical body. In the high-enthalpy, contaminated, conditions then

4.3.4 Flow visualization.

Interferometry, shadowgraphy or schlieren visualization can be used to provide measurements of the shock stand-off distance on a blunt body such as an oblique cylinder or a sphere. The shock stand-off distance is indicative of the density jump across the shock at high Mach numbers and therefore the degree of dissociation of the flow. A comparison of the measured shock stand-off distance with various theoretical predictions can also give an indication about the characteristic thickness of the nonequilibrium layer behind a shock.

A relatively easy method of observing the level of dissociation reaction, as it affects the flow field is the recording of flow luminosity pictures. These can be recorded as time averages or with gated cameras. The luminosity recordings can only serve as illustrations, since they are utilizing the contaminant for producing the light.

4.3.5 Time-resolved interferometry.

Time-resolved interferometry can be used to provide a time resolved (but spatially integrated) measurement of the density in the freestream. Knowledge of the optical integration path will then enable, with some

assumptions about the chemical composition of the freestream, the calculation of the freestream density for both validation of the nozzle calculation and for quantitative evaluation of the full-field interferograms. The time-resolved interferometry also enables confirmation of the starting times as obtained in pressure measurements. Furthermore, the determination of the density allows for a relatively straightforward determination of the freestream velocity via the pitot pressure. The differential (or shearing) interferometer offers a robust method for time resolved spatially integrated monitoring of the temporal development of the impulse facility flow, Smeets (1991).

4.3.6 Laser-induced fluorescence, CARS, other spectroscopy methods.

These methods are to be used in order to determine the partial densities of some of the species created in the high-enthalpy facilities. Of particular interest are currently NO , N and O concentrations. The quantity of atomic oxygen present is particularly important for hypersonic combustion experiment analysis. The spectroscopic methods should also provide a measurement of temperatures and possibly freestream velocities. The usefulness of the spectroscopic methods in laboratory frame is beyond doubt. Their applicability to large aerothermal test facilities for quantitative measurements is still in a developmental stage. Particular difficulties are those of contamination in the flow, both by particular and by gaseous species.

All these methods require careful calibration and parallel measurements in a calibrated cell. A further complication is the fact that the high-enthalpy gasdynamic facilities produce flow times shorter than required for repetitive measurements, so averaging of spectral information, when pulsed laser light sources are used, is not possible. This reduces the signal to noise ratio in the above applications significantly over the laboratory bench-top experiments. An assessment

A relatively straightforward way to obtain information about the presence or otherwise of species in the flow is to use emission spectroscopy. Although it is very difficult to quantify the output of emission spectra, it can be used to determine the presence of, say, iron or sodium atoms or other contaminants or the presence of N atoms. It is also possible to simulate the emission spectra of some strongly emitting species (e.g. iron) and compare the simulation with the experimental data in order to obtain temperature information from the flow. The inverse of the above, absorption spectroscopy can yield very quantifiable results about species in the flow in a selective manner. Here the evolution of diode lasers can lead to the development of small robust diagnostic equipment. The GaAlAs diode laser based method have been used in a shock tube to measure O -atom temperatures in high-enthalpy conditions. The O -atom is a suitable species in the high-enthalpy tests, as the

capability to dissociate oxygen defines the wind tunnel as a high-enthalpy tunnel.

In order to determine the level of particulate contamination, a simple extinction measurement could be used, if the size distribution of the solid particles were known. The latter may be obtainable in cold, continuously running hypersonic facilities (Williams 1992), but there is currently no reliable way to obtain this information from hot impulse facilities. The straightforward extinction measurement can provide simple run to run monitoring, and offers also easy facility to facility comparison. It does not, however, provide information about the spatial distribution of the contaminants. When the extinction measurements are performed, care should be taken to isolate the luminosity from the recorded signal, as it tends to compensate for the extinction. It is possible to either perform two parallel measurements where only one of the two sensors is exposed to the light source from outside the test section (generally a collimated laser beam). The extinction can then be obtained by subtracting the emission signal from the signal which has been exposed to both the emission and the external source. Alternatively, the emission can be eliminated to a large extent by spatial and color filtering.

Even when the particulate contamination can be reduced to a level, where it does not significantly affect the aerodynamic testing, the contamination of the test gas by driver gas can present a significant problem. Here Stalker and Crane (1977) have reported mass spectroscopy tests in a high-enthalpy reflected shock tunnel. According to their results, only half of the calculated drainage time is available for testing prior to the arrival of the driver gas contamination.

4.4 Modeling.

Since the calibration information obtained from the tunnels is usually not complete, the above parameters have to be compared with some numerical calculation which has to reproduce the measured quantities well enough to provide confidence in the prediction of non-measured parameters like e.g. the velocity of the freestream.

The determination of a Mach number in the freestream is usually performed by calculations including the finite rate chemistry. In facilities where perfect gas flow is simulated, measuring pressures can yield the Mach number. In high-enthalpy facilities, the pressure ratios are a function of both Mach number and the level of chemical reactions. The knowledge of the freestream species concentration is therefore a prerequisite for calculating the Mach number even if the flow velocity can be determined independently.

Most codes currently in use do not include the van der Waals forces in their calculations. Holden (1993) has improved the nozzle flow calculations by including these

forces in the high pressure calculations. Also Cannap and Candler (1992) have incorporated this in their modeling with significant success.

As the determination of the flow parameters relies on the numerical calculations, and even the most sophisticated of these use empirical correlations in their modeling, it cannot be stressed enough to use particular care when choosing simulation parameters and designing experiments.

Most codes currently used utilize some empirical correlations: e.g. for determining the boundary layer state and therefore the displacement thickness.

A further step in the increase in the confidence level of both experiments and CFD is provided by testing standard models. Here simple geometries are to be used in order to provide easy experimental access and not to overextend the existing code capabilities. Standard model testing can provide information on the degree of thermochemical nonequilibrium in the freestream, it can provide a measure for the total enthalpy in the flow and it can provide valuable information for facility cross-check, if the same model is tested in various wind tunnels.

5. CONCLUSIONS AND RECOMMENDATIONS

Since both the high-enthalpy experimental facilities as well as the instrumentation usable in these facilities are still at a stage where rapid development and an increase of the understanding is taking place, it is advisable to obtain and compare as much of facility operational data as possible. An attempt has been made to provide indications of which parameters ought to be obtained and by which means these parameters are obtainable. No attempt has been made to produce a treatise on measurement techniques because of the above mentioned rapid development. Moreover, this would either repeat existing information or the result in a superficial attempt to describe complicated techniques within the framework of a chapter of a report.

It is worth repeating that the most important parameters to obtain in the calibration of a tunnel are those of the freestream. As the freestream is generally a result of a anisentropic expansion of the high-enthalpy test gas through a nozzle, the study of the nozzle flow alone can serve as a case of code validation. Therefore obtaining parameters upstream of the nozzle also becomes important. This is true more so here than in wind tunnels without real-gas effects.

Table 1 summarizes the requirements for the calibration of a high-enthalpy wind tunnel. The minimum need is to obtain the information listed in part III of this table. This Table has been distributed among the operators of the high-enthalpy facilities. As the review and response collection is still going on, the summary of the current calibration status of the existing facilities will have to be produced in the next phase of the current activity.

REFERENCES

- Auweter-Kurtz, M., Habinger, H., Laure, S., Messerschmid, E., Röck, W., Tubanos, N. 1991 The IRS Plasma Wind Tunnels for the Investigation of Thermal Protection Materials for Reentry Vehicles. *Proc. 1st European Symposium: Aerothermodynamics for Space Vehicles*, ESTEC, Noordwijk, The Netherlands.
- Beck, W.H., Eitelberg, G., McIntyre, T.J., Baird, J.P., Lacey, J., Simon, M. 1991 The High-enthalpy Shock Tunnel in Göttingen (HEG). *Proc. 18th ISSW*, Sendai, Japan.
- Beck, W.H., Hanneman, K. 1992 High-enthalpy Wind Tunnel Instrumentation. *CNES-Report*, Activity ES 7.
- Beck, W.H., Müller, M., Wollenhaupt, M. 1993 Application of Spectroscopic Diagnostic Techniques to Studies on HEG: Preparatory LIF Work and Emission Spectroscopy Results. *Proc. 15th ICIASF*, Saint-Louis, France.
- Becker, E. 1965 *Gasdynamik*. Teubner, Stuttgart.
- Chanetz, B., Coët, M.C., Nieout, D., Pot, T., Brossand, P., François, G., Masson, A. 1992 Nouveaux Mayens d'Essais Hypersoniques Developpes a L'ONERA. *AGARD Conf. Proc. 514, Theoretical and experimental Methods in Hypersonic Flows*.
- Deiwert, S.G. 1992 Issues and Approachs to Develop Validated Analysis Tools for Hypersonic Flows: One Perspective, *AGARD Conf. Proc. 514, Theoretical and Experimental Methods in Hypersonic Flows*.
- Eitelberg, G., McIntyre, T.J., Beck, W.H., Lacey, J. 1992 The High Entahlp Shock Tunnel in Göttingen. *AIAA Paper 92-3942*.
- Eitelberg, G., 1993 *Private Communication*.
- Erdes, J., Tamagnuo, J., Bakos, R. 1989 Hypervelocity Real-gas Capabilites of GASL's HYPULSE Facility, in: Rogers R.C. (ed) Workshop on the Application of Pulse Facilites to Hypervelocity combustion simulation, *NASP Workshop Publication 1008, NASA-LRC*.
- Grauer-Carstensen, H. 1991 Messung von Druck und Wärmeübergang im HEG Teil 1: *Messung des Wärmeflusses DLR IB 222- 91 A 26*.
- Grönig, H. 1991 Shock tube application: High-enthalpy European wind tunnels. *Proc. 18th ISSW*, Sendai, Japan.
- Hannemann, K. 1989 On the flow conditions occurring in the shock tube of the High-enthalpy Wind Tunnel Göttingen (HEG). *DLR IB 221-89 A 19*.
- Hannemann, K. 1990 Design of a axisymmetric contoured mozzle for the HEG. *DLR-FB 90-04*.
- Hannemann, K., Brenner, G., Brück, S. 1993 Numerical simulation of reacting flows related to the HEG. *Proc. 19th ISSW*, Marseille.
- Hornung, H.G. 1972 Nonequilibrium dissociating introgen flow over shperes and circular cylinders. *J. Fluid Mech. 53, 149*.
- Hornung, H.G. 1991 *Class notes: Ae 234, Lecture Notes*. Course given at CALCIT, Calif. Inst. of Technology, Pasadena.
- Hornung, H.G. 1992 Performance Data of the New Free-Piston Shock Tunnel at GALTIT. *AIAA Paper 92-3943*.
- Jenkins, M. 1993 *Private Communication*.
- Labracheric, L., Dumitrescu, M.P., Burschell, Y., Honas, L. 1993 On the Compression Process in a Free Piston Shock Tunnel. *Shock Waves 3.1*.
- Laster, M.L., Arnold, J.O., Nichols, F., Horn, D. 1990 Electric arc heaters, Report written for AGARD *High-enthalpy facility study group*.
- Lee, M.G. and Nishida, M. 1992 Numerical simulation of starting process in a hypersonic nozzle, in *Memoirs of the faculty of engineering. Kyushu University, Vol 52, No. 3*.
- Lukasiewicz, J. 1973 Experimental Methods of Hyper-sonics. *Gas Dynamics Series, Vol. 3*. Dekker, NY.
- Maus, J.R., Laster, M.L., Hornung, H.G. 1992 The G-Rauge Impulse Facility: a High-Performance Free Piston Shock Tunnel, *AIAA Paper 92-3946*.
- McIntosh, M.K. 1968 Computer program for the numerical calculation of frozen and equilibrium conditions in shock tunnels. Australian National University.
- McIntyre, T.J. and Atcitty, C. 1990 Pistons and Compression Tubes - Piston motion in the high-enthalpy shock tunnel (HEG). *DLR IB 222 - 90 A 20*.
- McIntyre, T.J., Maus J.R., Laster M.L., Eitelberg G. 1993 Comparison of the flow in the High-enthalpy Shock Tunnel in Göttingen with numerical simulations. *Proc. 19th ISSW*, Marseille, France.
- Mirels, H. 1964 Shock tube test time limitation due to turbulent wall boundary layer. *AIAA J. Vol. 2, No 1*.
- Morgan, R.G., Paull, A., Stalker, R.J., Jacobs, P., Morris, N., Stringer, I. and Brescianini, C. 1989 Shock tunnel studies of scramjet phenomena. *NASA-CR-181721*.
- Page, M.W., Stalker, R.J., 1983 Pressure losses in free piston driven shock tubes. *Proc. 14th Int. Symp. on Shock Tubes and Shock Waves*, Sydney.
- Palma, P.C., Houwing, A.F.P., Sandeman, R.J. 1993 Absolute intensity measurements of imper emissions in a shock tunnel and their consequences for laser-induced fluorescence experiments. *Shock Waves, 3.1*
- Park, C. 1990 *Nonequilibrium Hypersonic Aerothermodynamics*, Wiley, NY.
- Park, C. 1990 Overview of Ames experimental aerothermodynamics. *Proc. 18th ISSW*, Sendai, Japan, Springer

- Shahpar, S., Kennaugh, A., Hall, I.M., Poll, A. 1992 Comparison of Computation and Experiment for a High-enthalpy, Heated-Driver, Shock-Tube Environment. *AGARD Conf. Proc. 514. Theoretical and Experimental Methods in Hypersonic Flows.*
- Smeets, G 1992 Interferometry in rarefied gas flows, in New trends in instrumentation for hypersonic research, A. Boutier. ed. Kluwer.
- Smith, C.E. 1966 The starting process in a hypersonic nozzle. *J. Fluid Mech., Vol 24.*
- Stalker, R.J. 1972 Development of a hypervelocity wind tunnel. *J. Roy. Aeronaut. Soc.* 76.376-384.
- Vincenti, W.G. and Kruger, C.H. Jr. 1965 *Introduction to Physical Gas Dynamics*, Wiley, NY.
- Witliff, C.E. 1987 A Survey of Existing Hypersonic Ground Test Facilities - North America. *AGARD Conf. Proc. 428, Aerodynamics of Hypersonic Lifting Vehicles.*

Reentry trajectory

Non-dimensional

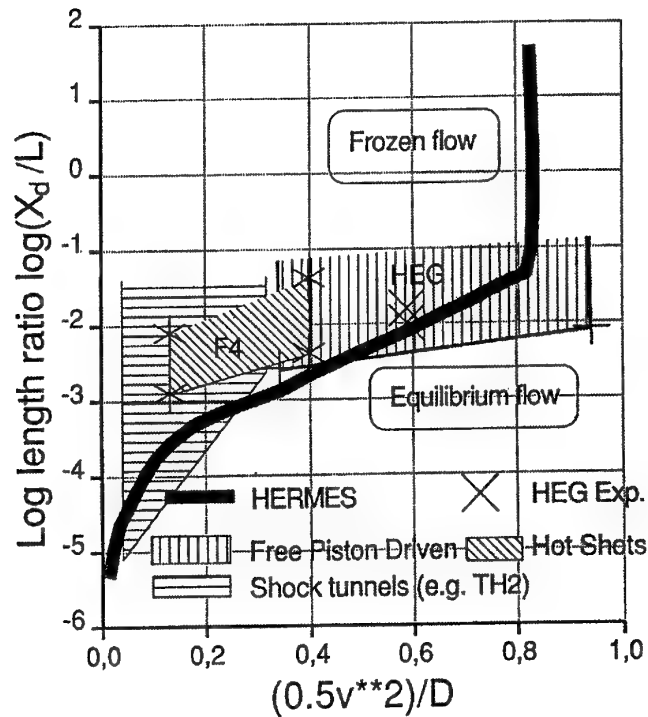


Figure 1. Dissociation length as a function of specific enthalpy. L is model length and D is dissociation energy.

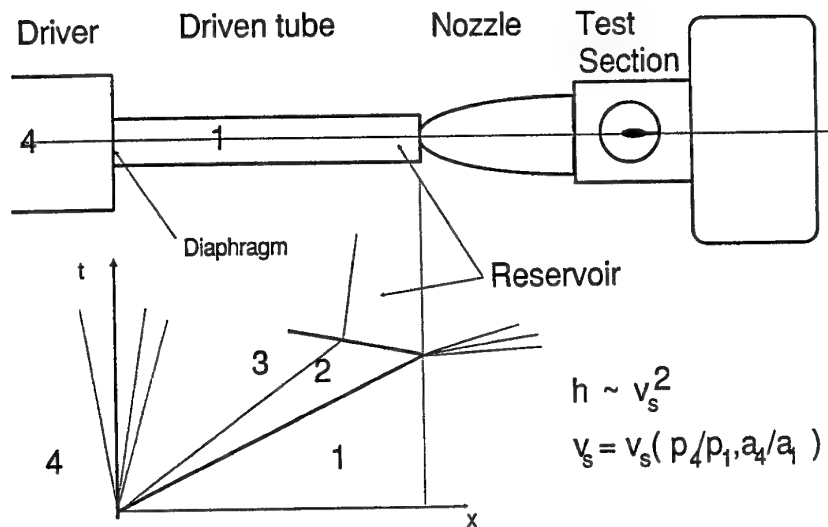


Figure 2. Schematic of Schock Tunnel.

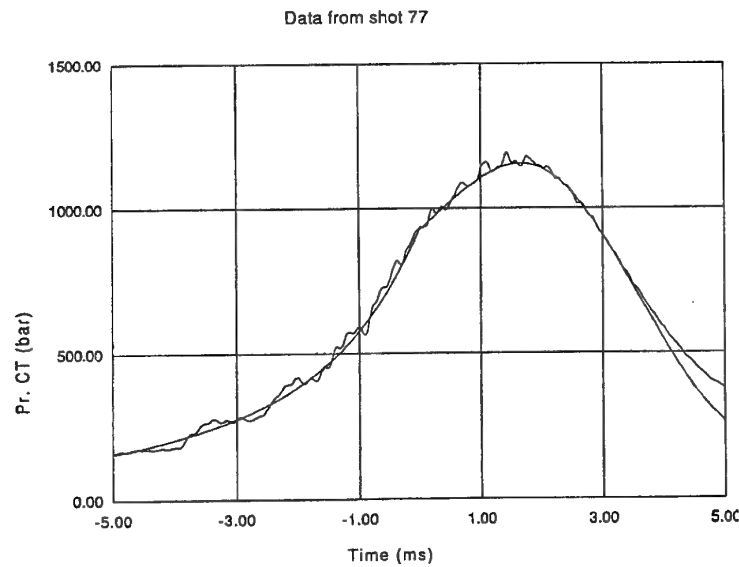


Figure 3. Comparison of Experimental Pressure Trace with Computations. Eitelberg (1993).

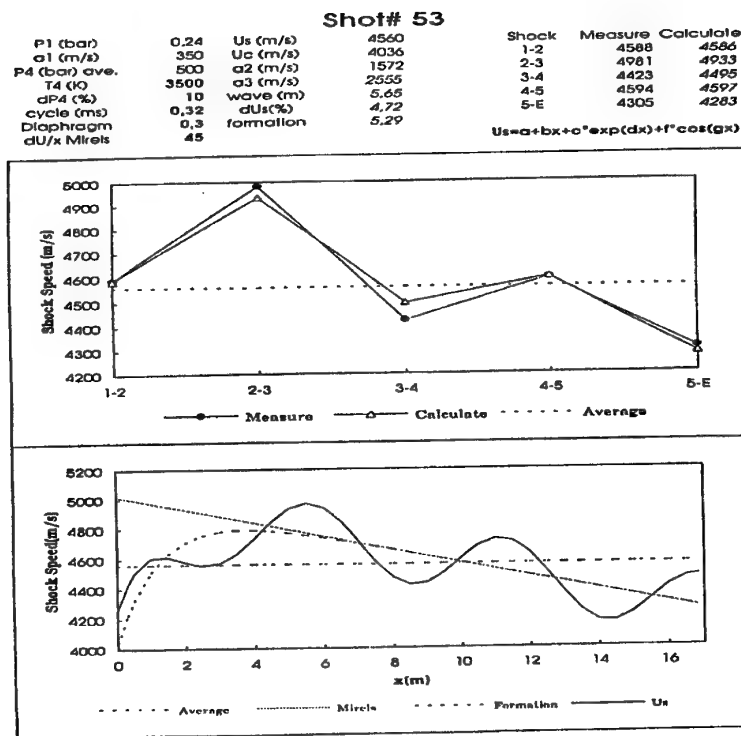


Figure 4. Shock attenuation: (a) is upper figure; (b) is lower figure.

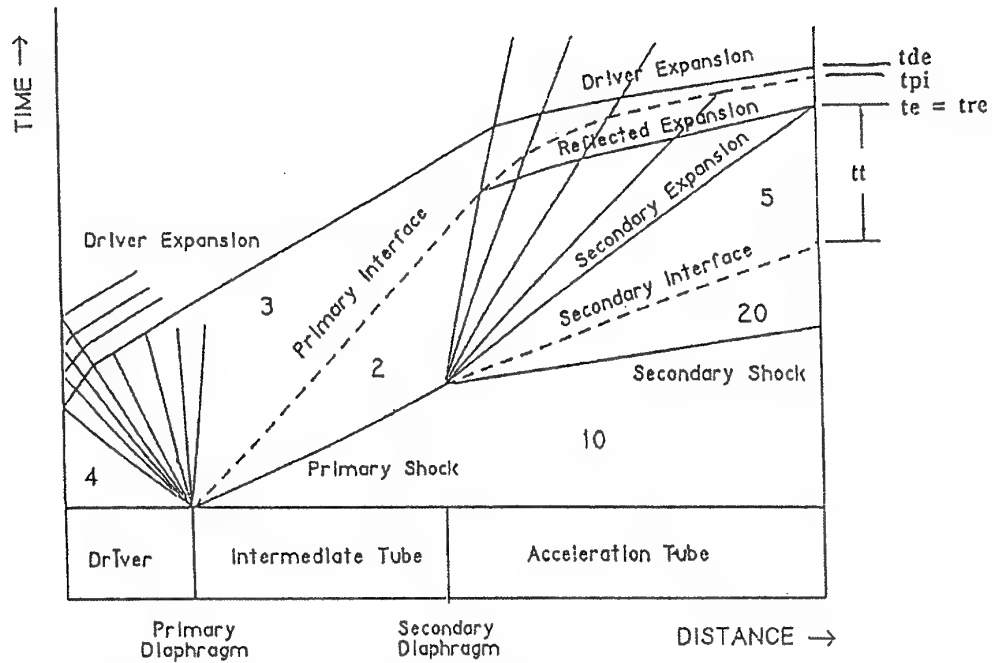


Figure 5. Expansion Tube Operation $x-t$ Diagram.

Facility calibration questionnaire

I Facility type (tick one)

1. Shock tunnel
2. Expansion tube
3. Hot shot tunnel
4. Other:

II The nozzle reservoir conditions

	p_r	p_r/p_d	$\frac{p_{r,max}-p_{r,min}}{p_r}$	tailored/non
Cond 1				
Cond 2				
Cond 3				
Cond 4				

p_r = reservoir pressure during the test time

p_d = pressure of the driver gas at diaphragm burst

	v_s	$\frac{v_{s,max}-v_{s,min}}{v_s}$	meas	T_r calc	h_r
Cond 1					
Cond 2					
Cond 3					
Cond 4					

v_s = incident shock speed in the driven tube

T_r = nozzle reservoir temperature

h_r = nozzle reservoir specific enthalpy

calculated from:

and assuming equilibrium/
non-equilibrium

HEG

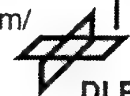


Table 1. Facility Questionnaire 1 of 3.

III Nozzle exit plane

	p	p/p	q	p	T	
					meas	calc
Cond 1						
Cond 2						
Cond 3						
Cond 4						

p = Pitot pressure

q = hemisphere stagnation point heat transference

p = static pressure

T = static temperature

Driver gas arrival time as determined by:

	spectral analysis	Calc.	heat flux	shock shape	other
Cond 1					
Cond 2					
Cond 3					
Cond 4					

Spectral analysis:

Other:

HEG



DIRA

Table 2. Facility Questionnaire 2 of 3.

IV Comments



HEG

DLR

CHAPTER VII

EXTRAPOLATION TO FLIGHT

J. Muylaert

European Space Research and Development Center

ESA-ESTEC

P.O. Box 299, 2200 AG, Noordwijk

NETHERLANDS

CONTENTS

1 INTRODUCTION	151
2 FLIGHT EXTRAPOLATION APPROACH	152
2.1 General Philosophy	152
2.2 Wind Tunnel and Flight Rebuilding Using CFD	152
2.3 Real-Gas Validation Methodology	152
3 SIMULATION AND SCALING	153
4 ANALYSIS OF EXTRAPOLATION TO FLIGHT ISSUES	154
4.1 Flap Efficiency and Heating	154
4.2 Wall Catalycity	156
5 RECOMMENDATION FOR PHASE 2 ACTIVITIES	157
REFERENCES	157

1 INTRODUCTION

The purpose of this chapter is to review the problems associated with the issue of extrapolation from wind tunnel to flight. It is clear that the ultimate goal is to understand and to be able to quantify, in flight conditions, the aerothermodynamic phenomena such as

- Transition to turbulence,
- Reaction and Control System (RCS) interaction with oncoming flow,
- Plume impingement,
- Low-density effects,
- Real-gas effects, and
- Gas-surface interactions

on a given configuration and more specifically on its trim, flap efficiency, and heating rate.

The numerical tools which predict these phenomena require validation as to their physical modeling as well as

to space and time convergence. Due to the fact that it is not possible to simulate in ground-based facilities all dimensionless parameters at the same time, it is important to set up a strategy using existing facilities for partial validation so that one can extrapolate to flight with the highest confidence possible. We will concentrate in this chapter on the problems associated with real-gas effects which embrace the chemical kinetics, transport, and thermodynamic coefficients, as well as the gas-surface interactions.

Due to the limitations of ground-based facilities in duplicating flight conditions, it can happen that some of the critical parameters in flight regime are not found to be critical in wind-tunnel conditions. For a winged re-entry vehicle, the influence of real-gas effects on flap efficiency and subsequently the influence of transition, at lower altitudes, on the separated shear layer upstream of deflected flaps, are examples of aerothermodynamic phenomena which are critical in flight and which are not possible to be entirely studied in ground-based facilities.

In this chapter a flight-extrapolation approach will be outlined first and combined with a real-gas validation methodology. The derivation of *binary scaling*, which is a scaling parameter used to compare the extend of dissociation reactions, is added so as to understand its origin and therefore its limitations.

Later some computational examples will be shown in order to stress the differences between wind tunnels and flight. Simple axisymmetric shapes have been designed to highlight the difference in heating and pressure recovery downstream of a separated shear layer in wind tunnel and in flight.

Here examples will be shown on a hyperboloid flare for the study of the flap efficiency and heating. It will be shown how flap efficiency and heating differ in wind tunnel and in flight.

Moreover, the issue of wall catalycity will be addressed. Computational results will be shown on a blunt cone with partial catalytic wall. The coating used for the blunt-cone computations is silica as was used on the Orbiter Shuttle tiles. Finally, recommendations are made for activities to be accomplished during Phase 2 of the working group.

2 FLIGHT EXTRAPOLATION APPROACH

2.1 General Philosophy

The issue of the extrapolation to flight must be seen in the light of a general aerodynamic and aerothermodynamic strategy of progressive building up of confidence in the design of a space vehicle (Perrier 1994). This general strategy consists of a development phase and a qualification phase. We shall not elaborate on the qualification phase but we shall outline possible approaches which will allow the designer to verify his ability to rebuild critical points in wind tunnel and in flight. Some elements in critical points follow the well-known physical laws so that scaling effects are well identified but others are not at all evident and require detailed analysis using advanced numerical tools. For a feasibility demonstration of a space plane, not only are the mean probable aerothermodynamic values important, but the minimum and maximum values associated with realistic uncertainties are more critical. Such uncertainties are low or at least well known in the flight envelope of conventional supersonic aircraft and are associated with a high level of technology. The uncertainties in hypersonics are large and not well known. Margins needed to cover uncertainties are decreasing with the increase of knowledge and the quality of quantification of the phenomena. Quantification of the phenomena is to be done with good experimental tools including instrumentation, good modeling of the physics and good numerical analysis for the computation of the solution of the equations around vehicles in wind tunnel and in flight. The conventional approach for the evaluation of the margins used in the past i.e., adding all errors as evaluated from experiments and computations leads to excessive requirements for the margins and can not be adopted anymore today.

The approach to be taken is a hand-in-hand computational/experimental progressive improvement of the physical modelization through a better understanding and use of existing facilities. The points in the wind-tunnel performance envelope to be selected for testing are not just those which are the closest to the flight trajectory but those which give the smallest uncertainty band. Usually this is the nozzle design point.

Designing the wind-tunnel models using CFD, such that in wind-tunnel conditions one approaches the flight phenomenon of interest, is part of this modern approach. Because of the impossibility of duplicating flight conditions in ground-based facilities, a computational modeling approach is required. Indeed, Mach numbers in shock tunnels or hot-shot tunnels are far from those in flight. Due to nozzle-expansion processes, the distribution of the energy is different compared to flight. This problem of redistribution of energy is avoided when testing free-flight models in ballistic ranges when the Reynolds number is matched.

However chemical processes at the base or lee side are not simulated because recombination reactions are dominant in those regions. The time required for the recombination reactions to occur are inversely proportional to the square of the density whereas for the dissociation reactions, it is inversely proportional to the density. This

means that if a test is set to scale with the forebody dissociation reactions (ρL), it results in simulating a lee-side flow or a base flow which is closer to equilibrium than in flight. All this means that corrections are always required for flight extrapolation.

2.2 Wind Tunnel and Flight Rebuilding Using CFD

Figure 1 shows a possible approach to validate an extrapolation to flight methodology. The right branch shows the classical testing in cold wind tunnels where Mach and Reynolds number simulation is possible and where, using generic forms, code validation for perfect-gas phenomena is feasible. Examples are the hyperboloid flare for the study of the boundary-layer separation and reattachment and associated shock/boundary-layer interaction (Durand 1992), the capsule-like blunt cone in rarefied flow for the study of the wake (Dogra et al. 1994), the delta wing for the study of vortex flow fields and the Electre blunt cone for the detailed study of nozzle flow quality and which as such serves as a standard model (Sagnier 1992). On the left branch of the figure are the similar generic models for the study of real-gas effects. CFD validation includes here facility simulation because of the necessity to take into account the nozzle freestream species concentrations and vibrational temperatures. The study of extrapolation to flight includes testing of flown configurations in the so-called cold as well as high-enthalpy facilities (Muylaert et al. 1993). High-quality, real-gas flight data are few and only a few examples are available i.e., Shuttle Orbiter (Weilmuenster et al. 1993), Bourane (Neiland 1991) and OREX (Inouye 1994). Computations in wind-tunnel conditions as well as in flight conditions are to be performed. The computational rebuilding will provide a better understanding of the facility performance and employed measurement techniques as well as a better understanding of the conditions to be used for design; in particular for the high-enthalpy facilities. Obviously this implies the availability of 3-D nonequilibrium Navier-Stokes codes or Euler coupled with boundary-layer codes. Because of the large computing power required to perform 3-D nonequilibrium computations, combined with the fact that most of the existing 3-D codes still require detailed validation, a framework for real gas high-enthalpy validation is needed.

2.3 Real-Gas Validation Methodology

A proposed real-gas validation methodology is shown in Figure 2. The thermodynamic coefficients, transport properties, radiation properties and chemical kinetics need to be reassessed using modern shock tubes combined with the latest nonintrusive measurement techniques. Because most of the existing data on relaxation rates and thermodynamic properties come from shock-tube experiments performed more than 25 years ago, where the relaxation processes behind a moving normal shock was measured; it is believed that new shock-tube experiments combined with the latest nonintrusive measurement techniques are required to reassess

the vibration-dissociation couplings and the vibrational-translational and rotational exchange rates and thermodynamic properties.

In addition to the relaxation behind a sudden compression caused by the moving shock in a tube, the relaxation during expansion processes from high-pressure, high-temperature equilibrium reservoir conditions in a nozzle to frozen exit conditions should be analyzed.

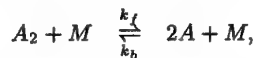
There is an urgent need to standardize the chemical and vibrational reaction rates for air and other gases such as CO_2 for specific classes of high-enthalpy flows e.g., flows encountered in shock tubes or hot shots which do not necessarily require modeling of ions. Standardization of reaction rates will also take away source of discrepancies when performing code-to-code comparisons.

In addition, there is an urgent need to improve our understanding of the reaction mechanisms associated with ablation and pyrolysis; and in particular with catalytic reactions on different surfaces or coatings. These fundamental experiments could be performed in arc jets or in more clean environments such as solar furnaces or induction-heated facilities or plasmotrons. We shall call the validation of the physical modeling the level 1 validation. Once the level 1 validation has been performed the level 2 validation can be embarked on in shock tubes or hot shots where the numerical algorithms, requirements in terms of space and time convergence will be assessed by comparison with experiments performed on simple geometries. At level 2, any difference between experiment and computation should not be attributed to incorrect modeling of the physics but to discretization or convergence errors as long as the validation at level 1 was performed under conditions similar to those locally obtained in the shock layer and at the wall respectively in the shock tube and e.g., the plasmatron. In other words, real-gas validation can only be performed when different experimental facilities, each with their own characteristics covering only a part of the global fluid dynamic problem, are tuned so that together they contribute to the global validation process. It is realized that at present this frame work is not in place but it is believed that it is possible to improve herewith our knowledge of nonequilibrium real-gas flows.

3 SIMULATION AND SCALING

The objective of this section is to derive the binary scaling so as to understand its limitations for use as a method to extrapolate to flight. The Lighthill-Freeman ideal dissociating gas is used for this derivation. It assumes a diatomic inviscid gas where the vibration of the molecules are in equilibrium with the translational temperature.

The dissociation of the molecule A_2 is a result from a collisional process with a second body M which can be either another molecule or a dissociated atom A :

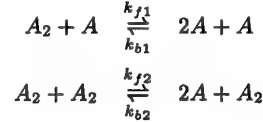


where k_f and k_b are the forward and backward reaction rate. The net rate of change of the molar concentration

of A is given by

$$\begin{aligned} \frac{d[A]}{dt} &= 2[M] \{k_f[A_2] - k_b[A]^2\} \\ &= 2k_f[M] \left\{ [A_2] - \frac{[A]^2}{K_e} \right\}, \end{aligned} \quad (1)$$

where $K_e = k_f/k_b$ is the equilibrium constant. If the species A_2 or A constitutes the catalytic body M , one must take into account two reactions:



which gives

$$\frac{d[A]}{dt} = 2 \{k_{f1}[A] + k_{f2}[A_2]\} \left\{ [A_2] - \frac{[A]^2}{K_e} \right\}. \quad (2)$$

We consider now the dimensionless quantity, α , as the mass fraction of the dissociated A atoms,

$$[A] = \frac{\rho\alpha}{\hat{M}_A} \quad \text{and} \quad [A_2] = \frac{\rho(1-\alpha)}{\hat{M}_{A_2}} = \frac{\rho(1-\alpha)}{2\hat{M}_A},$$

where \hat{M}_A is the molar mass of the species A .

From Equation (2), $d[A]/dt$ corresponds to the rate of change of concentration $[A]$ resulting from chemical reactions. Hence by substituting α into (2), we must regard ρ as a constant:

$$\begin{aligned} \frac{d\alpha}{dt} &= \left\{ k_{f1}\alpha + k_{f2} \frac{1-\alpha}{2} \right\} \frac{\rho}{\hat{M}_A} \\ &\quad \times \left\{ (1-\alpha) - \frac{2\rho}{\hat{M}_A K_e} \alpha^2 \right\}. \end{aligned} \quad (3)$$

According to the law of mass action for the ideal dissociating gas (see Vincenti and Kruger 1967), at equilibrium

$$\frac{\alpha^2}{1-\alpha} = \frac{\rho d(T)}{\rho} e^{-\theta_d/T}$$

with θ_d and $\rho d(T)$ defined as the characteristic temperature and density for the dissociation. However,

$$\frac{\alpha^2}{1-\alpha} = \frac{\hat{M}_A [A]^2}{2\rho [A_2]} = \frac{\hat{M}_A}{2\rho} K_e = \frac{\rho d(T)}{\rho} e^{-\theta_d/T},$$

hence Equation (3) may be rewritten as

$$\begin{aligned} \frac{d\alpha}{dt} &= \left\{ k_{f1}\alpha + k_{f2} \frac{1-\alpha}{2} \right\} \frac{\rho}{\hat{M}_A} \\ &\quad \times \left\{ (1-\alpha) - \frac{\rho}{\rho d(T)} e^{\theta_d/T} \alpha^2 \right\} \\ &= \left\{ k_{f1}\alpha + k_{f2} \frac{1-\alpha}{2} \right\} \frac{\rho e^{\theta_d/T}}{\hat{M}_A} \\ &\quad \times \left\{ (1-\alpha) e^{-\theta_d/T} - \frac{\rho}{\rho d(T)} \alpha^2 \right\} \end{aligned} \quad (4)$$

Freeman assumes further that the first parenthetical factor is for all practical purposes independent of α and can be written in the form: $\{k_{f1}\alpha + k_{f2} \frac{1-\alpha}{2}\} = C T^\eta e^{-\theta_d/T}$

where C and η are constants. With these changes we obtain

$$\frac{d\alpha}{dt} = \frac{C}{\hat{M}_A} T^\eta \rho \left\{ (1 - \alpha) e^{-\theta d/T} - \frac{\rho}{\rho d(T)} \alpha^2 \right\}. \quad (5)$$

Considering dimensionless quantities

$$T' = \frac{\hat{R}T}{V_\infty^2}, \quad \theta' d = \frac{\hat{R}\theta d}{V_\infty^2}, \quad \rho' = \frac{\rho}{\rho_\infty}, \quad t' = \frac{t V_\infty}{L'}$$

we obtain

$$\begin{aligned} \frac{V_\infty}{L'} \frac{d\alpha}{dt'} &= \left\{ \frac{C}{\hat{M}_A} \frac{V_\infty^{2\eta}}{\hat{R}^\eta} \rho_\infty \right\} \rho' T'^\eta \\ &\times \left\{ (1 - \alpha) e^{-\theta' d/T'} - \frac{\rho' \rho_\infty}{\rho d(T)} \alpha^2 \right\} \\ \frac{d\alpha}{dt'} &= \left\{ \frac{C}{\hat{M}_A} \frac{V_\infty^{2\eta}}{\hat{R}^\eta} \right\} \frac{\rho_\infty L'}{V_\infty} \rho' T'^\eta \\ &\times \left\{ (1 - \alpha) e^{-\theta' d/T'} - \frac{\rho' \rho_\infty}{\rho d(T)} \alpha^2 \right\} \quad (6) \end{aligned}$$

Hence, for the general situation of nonequilibrium inviscid flow, the similitude imposes that $\rho_\infty L$, V_∞ and ρ_∞ must be fixed.

If we are now interested to specific situations, like just behind strong shocks where dissociation dominates over recombination, it means that

$$k_b[A]^2 \ll k_f[A_2]$$

or

$$\frac{\rho}{\rho d(T)} \alpha^2 \ll (1 - \alpha) e^{-\theta d/T}.$$

In such cases, Equation (6) becomes

$$\frac{d\alpha}{dt'} = \left\{ \frac{C}{\hat{M}_A} \frac{V_\infty^{2\eta}}{\hat{R}^\eta} \right\} \frac{\rho_\infty L'}{V_\infty} \rho' T'^\eta (1 - \alpha) e^{-\theta' d/T'} \quad (7)$$

Hence, the function $\rho d(T)$ does not appear in the dimensionless equation and similitude does not require ρ_∞ to be fixed: we can have different similar inviscid flow if we keep the same V_∞ and $\rho_\infty L$. This similitude is referred to as the binary scaling, since it comes from the fact that dissociation involves binary molecular collisions, giving a linear dependency on ρ , whereas recombination involves tertiary collisions leading to a quadratic dependency of ρ .

It is of interest to note that if the gas is assumed to be in local chemical equilibrium, the expression of $d[A]/dt$ given by Equation (2) is no longer valid because

$$[A_2] - \frac{[A]^2}{K_e} \rightarrow 0, \quad \text{thus} \quad \frac{[A]^2}{[A_2]} \rightarrow K_e$$

and

$$k_{f1}[A] + k_{f2}[A_2] \rightarrow \infty$$

In that case, if we refer to the following equation:

$$\frac{d\alpha}{dt} = \frac{C}{\hat{M}_A} T^\eta \rho \left\{ (1 - \alpha) e^{-\theta d/T} - \frac{\rho}{\rho d(T)} \alpha^2 \right\} \quad (8)$$

the dissociation rate term $(1 - \alpha) e^{-\theta d/T}$ should be equal to the recombination rate term $\frac{\rho}{\rho d(T)} \alpha^2$ and so, the binary scaling similitude rule is no more valid (Taquin 1993).

It is concluded that the classical similitude rules Mach, Re , and binary scaling have a limited range and their use must be carefully considered.

4 ANALYSIS OF EXTRAPOLATION TO FLIGHT ISSUES

We will discuss the problem of flap efficiency and heating on a generic axisymmetric form followed by a discussion of the problem of wall catalycity on a blunt cone. The generic axisymmetric form is similar to a hyperboloid flare whereas the blunt cone is the Electre standard model (Muylaert et al. 1992). The discussion will be centered on computations performed in a high-enthalpy wind tunnel and in flight. The high-enthalpy wind tunnel selected is the HEG situated at DLR Göttingen. The purpose of presenting this analysis is to elaborate on the importance of developing suitable nonequilibrium codes for the understanding and interpretation of the wind-tunnel measurements and for the study of the extrapolation to flight. Because of the fact that at present we are building up the required expertise as to how these facilities should be used and what their flow quality really is, simple configurations are being tested which can be computed with present-day tools. The so-called "rebuilding" of these generic shapes in wind-tunnel conditions is part of the validation process to understand the physical phenomenon involved i.e., chemical/vibrational modeling and gas surface interactions and to learn what the required level is in terms of time and space convergence. For this reason, simple computable axisymmetric configurations have been selected so that the cpu-time effort is still acceptable.

4.1 Flap Efficiency and Heating

The hyperboloid flare is an axisymmetric configuration which contour corresponds to the Hermes windward-centerline. This concept of an "equivalent axisymmetric body" was first proposed by Adams et al. (1977) who showed that an appropriate axisymmetric body at zero degree angle of attack could model the windward-centerline flowfield over the shuttle at a given angle of attack. The results of their investigation demonstrated good agreement between experimental heat transfer data on the windward side of the shuttle at 30° angle of attack and computed heating rates on a 31° half-angle hyperboloid. This concept was further extended to include an axisymmetric flare to study the physical phenomenon associated with flap efficiency and heating (Durand 1992). For the present Hyperboloid Flare the forward part is not a hyperboloid but the Hermes windward centerline at 30° angle of attack, nevertheless the terminology "Hyperboloid Flare" was kept.

A series of numerical computations were carried out by Schwane and Muylaert (1992) to design the scale of this hyperboloid flare as well as the details of the flare deflection angle and flare length. On one side the separated

region must be large enough to be able to obtain the required measurement resolution and on the other side care must be taken to avoid wind-tunnel blockage.

We will discuss a computational analysis performed on this model in high-enthalpy conditions corresponding to the HEG reservoir conditions of 500 bar and 9500 K. The nozzle exit conditions are computed with a 1-D chemical and vibrational multi-temperature nonequilibrium Euler code called LORE1D (Walpot 1991). The Edenfield boundary-layer correction is included in this code. Figure 3 shows the centerline evolution of static and vibrational temperatures and the growth of the boundary layer. Note the rapid freezing of the vibrational temperatures and the velocity which quickly reaches constant values. All the important chemical kinetic effects occur at and just downstream of the throat.

This 1-D code provides the required input parameters to start subsequently a 2-D axisymmetric nonequilibrium Navier-Stokes code called TINA (Netterfield 1992). The exit conditions for the HEG as computed with LORE1D are shown in Table 1. The first column shows the exit conditions when chemical and vibrational nonequilibrium is assumed, the second column shows the nozzle exit conditions when the vibrational excitation is assumed to be in equilibrium and the others columns will be discussed below. When comparing the two columns we can see that the translational temperature is increased with 262 K for the vibrational equilibrium case because of the release of the vibrational energy which is locked into the vibrational modes. This increase in temperature, causes the Mach number to drop similar to the "melting effect" as discussed by Boudreau and Adams (1988).

Figure 4 shows the results for both inlet conditions on the hyperboloid flare computed with TINA. It has to be noted that both computations were carried out with chemical and vibrational nonequilibrium TINA. It can be seen that the nonequilibrium vibrational contribution in the nozzle has no measurable effect on the C_p and St distribution.

The way to study the extrapolation to flight is to perform computations in wind tunnel and in flight conditions following some scaling law and to verify that in doing so one remains in the same domain where the physical modelization is applicable. The scaling law used is the above discussed binary scaling which simulates the dissociation reactions combined with the speed to simulate the kinetic energy. The binary scaling parameter is the product of the density times the length. Table 1, last column, shows the flight conditions when scale factor of 120 is used. The latter corresponds to the Hermes full scale body length. Note that in Table 1 columns 1 and 4 have the same speed and the same ρL , but not the same Reynolds number.

Figures 5 and 6 show respectively the C_p and the St distribution as computed by TINA for the nonequilibrium HEG wind tunnel condition, for the nonequilibrium flight and the equilibrium flight condition. Some important conclusions can be drawn: an increase in pressure recovery on the flare for flight of approximately 15% relative to the wind tunnel case is noted and another increase for flight in equilibrium of approximately 25% relative to the flight nonequilibrium case can be seen. Similarly, for

Figure 6, one can see that an increase in Stanton number on the flare for flight of 30% relative to the wind tunnel and another increase of approximately 50% for equilibrium flight relative to nonequilibrium flight is obtained. Clearly the assumption of chemical and vibrational equilibrium leads to a significant overestimation of the peak pressure and peak heat flux on the flare. Going from wind tunnel to flight, a reduction is seen in separation length combined with a forward shift of the pressure peak giving rise to an increase in flap efficiency.

What is still not clear is whether this is a pure real-gas nonequilibrium effect or whether there is also a Re or perhaps a Mach effect. Indeed Table 1 shows that going from wind tunnel (column 1) to flight (column 4), we have an increase in Re primarily due to the much lower static temperature in flight as compared to the wind tunnel notwithstanding the fact that ρL and the speed is the same. To answer this question perfect-gas computations were performed in wind-tunnel and flight conditions with input conditions as shown in column 3 and 4 of Table 1. Figure 7 shows a comparison between the nonequilibrium wind-tunnel computation and three sets of perfect-gas computations with different γ : 1.2, 1.4 and 1.6. The perfect-gas computations were started with the exit conditions as Table 1 column 1 but with $\gamma = 1.4$ in order to compare perfect gas with nonequilibrium real gas. Note that there is a slight difference in Mach due to the small increase in γ for the nonequilibrium nozzle case ($\gamma = 1.44$). Figure 7 shows a remarkable influence of γ . This is also shown in Figure 8 by the iso- C_p plots to highlight the change in structure of the shock wave boundary layer interaction. Decreasing γ , with constant Re and only a slight increase in Mach (less than 10% relative to $\gamma = 1.4$), produces a reduction in size of the separation combined with an increase and forward shift of the pressure peak. Therefore, decreasing γ also produces an increase in flap efficiency as obtained above when discussing the extrapolation from wind tunnel to flight. Comparing the $\gamma = 1.4$ perfect-gas results with the nonequilibrium wind-tunnel results one finds that the separation length is not much altered but that the pressure distribution on the flare follows first the $\gamma = 1.4$ results and more downstream drops to the $\gamma = 1.6$ results and then back to the $\gamma = 1.4$. What is happening?

To try to understand these complex nonequilibrium interactions Figure 9 is plotted. It shows the O_2 and N_2 mass fractions plotted perpendicular to the wall along the hyperboloid flare in wind tunnel and in flight corresponding to Table 1 column 1 and 4; but let's focus here to the wind tunnel N_2 mass fractions. If one follows a line perpendicular to say the $x = 0.05$ m position, then the N_2 mass fraction starts with the nozzle free stream value of 0.754 in accordance with Table 1 column 1; following this line perpendicular to the wall one crosses the bow shock which dissociates the N_2 molecules up to a value in mass fraction of 0.715, further in the shock layer and in the boundary layer due to the cold wall and full catalytic wall boundary conditions the N_2 molecules are forced to recombine to reach there equilibrium conditions at the wall i.e., a mass fraction of 0.77. Comparing Figure 7 with Figure 9 in the region of the shock interaction one can see that at $x = 0.09$ m the N_2 mass fraction is re-

	chem/thermal non-equil.	chemical non-equil.	perfect gas	flight extrapolation
Re_L	38000		38000	121000
Ma	9.75	8.34	10.56	23.32
$Ma/\sqrt{Re_L}$	0.05		0.054	0.067
U [m/s]	5953	5996	5953	5953
T_∞ [K]	789.29	1051	789.29	162
Tv_∞ [K]	3930	1051		
ρ [kg/m ³]	2.017e-3	2.122e-3	2.017e-3	$\rho/120$
L [m]	0.1114	0.1114	0.1114	$L \times 120$
C_{N_2}	0.75446	0.7548		0.77
C_N	0.00006	0		0
C_{O_2}	0.03649	0.0346		0.23
C_O	0.18197	0.1843		0
C_{NO}	0.02709	0.0263		0
T_w [K]	300	300	300	300

Table 1: HEG exit conditions: $P_0 = 500$ bar, $T_0 = 9500$ K.

duced again because of the existence of the separation and reattachment shock; at $x = 0.1$ m the expansion waves coming from the interaction point with the bow shock balance or freeze the composition at that level until at $x = 0.115$ where the stronger flare shock produces the N_2 molecules to dissociate until up to a level of 0.670. The C_p distribution for the nonequilibrium wind tunnel in Figure 7 follows quite closely the perfect gas $\gamma = 1.4$ distribution until $x = 0.1$ m downstream of which it follows the $\gamma = 1.6$ curve up to the $x = 0.115$ point to follow again the $\gamma = 1.4$ curve.

Let us check now what happens in flight. Figure 10 compares a perfect-gas wind tunnel with perfect-gas flight, both with $\gamma = 1.4$ according to Table 1. Only a slight reduction of the separation is seen combined with an increase of the pressure peak and a shift upstream. This increase of pressure peak seems Mach number driven as with a constant γ and same shock inclination angle, the pressure ratio across an oblique shock is only a function of the local normal shock Mach number. In flight this local normal shock Mach number is approximately 3.8 and in the wind tunnel this is 3.2 as taken from the present computations.

Figure 11 compares perfect gas flight with non-equilibrium flight C_p distribution. A reduction of the separation bubble is seen combined with a shift forward in pressure peak. Here the change from perfect gas to nonequilibrium in C_p is not so dramatic as in wind tunnel (Figure 7). A similar behavior was obtained by Brenner et al. (1993) but for a higher Mach and altitude.

It can be concluded that the influence of the enthalpy is to reduce the separation length (separation point moves aft) resulting in a steeper pressure rise on the flap due to a stronger oblique shock interaction.

4.2 Wall Catalycity

Here some sensitivity computations are shown on the Electre in the HEG wind tunnel in order to study finite-

rate catalysis and the influence of the wall temperature on some of the important recombination mechanisms. Two reaction mechanisms are possible. The first one is the recombination between an atom from the gas and an adsorbed one: the free gas atom strikes the adsorbed atom, called an adatom, and reacts with it. The result is a recombined molecule. This is called the Eley-Rideal (E-R) mechanism. After the recombination, the molecule is still adsorbed. The second mechanism is the recombination between two adatoms: This is called the Langmuir-Hinshelwood (L-H) mechanism.

A finite-rate catalytic model CORICO was proposed by Nasuti et al. (1993) for a silica coating and incorporated in the TINA code. Silica was used as a TPS coating on the shuttle. The reservoir conditions for the HEG are the same as for the hyperboloid flare study in previous chapter.

Figure 12 shows the Electre wall heat flux distribution with a wall temperature of 343 K. A comparison is shown between full catalytic and CORICO which at that low wall temperature is very close to a noncatalytic wall. A 60% increase in heat flux is noted for the full catalytic wall relative to the noncatalytic wall. The figure shows also the translational, vibrational and diffusive contributions to the total heat flux. It is clear that the full catalytic condition is a diffusive dominated process. For the vibrational contribution we see that the full catalytic wall condition is lower than CORICO. This is because the large amount of molecules that leave the wall in local thermal equilibrium cool the gas close to the wall and therefore reduce the vibrational temperature. This is referred to as "quenching".

Figure 13 shows again the heat flux distribution and its contributions on Electre but now with wall temperatures which vary from 500 K to 1500 K as computed with CORICO. The translational heat flux decreases when the wall temperature increases as well as the vibrational contribution where, in addition, the "quenching" action of the molecules become more intense. The total

heat flux increases when increasing the wall temperature due to the diffusive contribution which increases rapidly from 500 K to 900 K and less rapidly from 900 K to 1500 K. The reason for this rapid rise is explained in Figure 15 and in Figure 14 which shows the contribution of the above explained E-R and L-H mechanisms to respectively the O and N particle flux. The E-R is the dominating mechanism for the O particle flux over the entire temperature range whereas around 1000 K the L-H mechanism takes over from the E-R for the N particle flux.

The above Electre computations show that for this coating the noncatalytic assumption was good enough if the wall remains cold, but that it is necessary to use a finite-rate catalytic model if the wall is hotter than say 700 K in wind-tunnel conditions. In addition, and perhaps more important, the computations have shown that when increasing the wall temperature to flight values as 1500 K, the recombination mechanism change! So care should be taken in the analysis of high-enthalpy wind-tunnel wall heat fluxes on so called noncatalytic materials and when extrapolating to flight.

5 RECOMMENDATION FOR PHASE 2 ACTIVITIES

For Phase 2 of the working group it is recommended to embark on the study of extrapolation to flight using the available data on the Shuttle Orbiter. Already very important work was done as part of the Langley OEX workshop; examples are the recent publications of Gnoffo et al. (1993) on the Shuttle Orbiter re-entry heating; by Weilmuenster et al. (1993) on the aerodynamic characteristics with emphasis on pitch trim and body flap; by Kleb and Weilmunster (1992) on the Shuttle Orbiter lee side flow phenomena; and by Wang and Caram (1994) on the comparison of the wing leading-edge heating rates and comparison with experimental and flight data.

Within the framework of the working group the definition of the Shuttle Orbiter shape was provided for use for all members of the working group. The Halis model, which is a generic form for the study of the flap efficiency and heating and which is derived from the Shuttle Orbiter by duplicating the windward side combined with a simplification of the lee side will be tested in the shock tube HEG, the hot shot F4 and in the S4 Modane facility so as to have a perfect gas reference. In the HEG environment different coatings will be put on this model to study influence of catalycity. The objective is to compute in wind-tunnel and in flight conditions and to address issues like flap efficiency and heating.

The application of the proposed methodology to the Halis configuration allows to close the loop with the flight results and finally to assess its global validity as well as the quality of each of its contributing elements, wind tunnel and computation. More contributions are encouraged on the computational side to allow cross-checks and widen the base of the method.

REFERENCES

- Adams, J. C., Martindale, W. R., Mayne, A. W., and Marchand, E. O. 1977. Real gas scale effects on shuttle orbiter laminar boundary layer parameters. *J. Spacecraft* 14(5).
- Boudreau, A. H. and Adams, J. C. 1988. Characterization of hypersonic wind tunnel fields. In *AIAA 15th Aerodynamic Testing Conference*, San Diego. AIAA paper 88-2006.
- Brenner, G., Kordulla, W., and Bruck, S. 1993. Further simulations of flows past hyperboloid-flare configurations. Technical Report DLR-H-NT-O-2058, DLR-Braunschweig.
- Dogra, V. K., Moss, J. N., Wilmoth, R. G., Taylor, J. C., and Hassan, H. A. 1994. Effects of chemistry on blunt body wake structure. In *AIAA 32th Aerospace Sciences Meeting and Exhibit*. AIAA paper 94-0352.
- Durand, G. 1992. Hyperboloid flare combination: a hypersonic testcase for the qualification of compressible navier-stokes codes including high temperature effects. Technical Report DLA/ED/3A no 032.09.92, CNES.
- Gnoffo, P., Weilmuenster, K. J., and Alter, S. 1993. A multiblock analysis for shuttle orbiter reentry heating from mach 24 to mach 12. In *AIAA 28th Thermophysics Conference*, Orlando, FL.
- Inouye, Y. 1994. Orex flight—quick report and lessons learned. In *Proceeding of the Second European Symposium on Aerothermodynamics for Space Vehicles*, Noordwijk, The Netherlands. ESA SP-367.
- Kleb, W. L. and Weilmunster, K. J. 1992. Characteristics of the shuttle orbiter leeside flow during a reentry condition. In *AIAA 27th Thermophysics Conference*, Nashville, TN. AIAA 92-2951.
- Muylaert, J., Walpot, L., and Durand, G. 1993. Computational analysis on generic forms in european hypersonic facilities: standard model electre and hyperboloid flare. In *19th international shock wave symposium*, Marseile.
- Muylaert, J., Walpot, L., and Haeuser, J. 1992. Standard model testing in the european high enthalpy facility F4 and extrapolation to flight. In *AIAA 17th Aerospace Ground testing Conference*, Nashville, TN. AIAA 92-3905.
- Nasuti, F., Barbato, M., and Bruno, C. 1993. Material dependent catalytic recombination modeling for hypersonic flows. In *AIAA 28th thermophysics Conference*, Orlando, FL. AIAA papere 93-2840.
- Neiland, V. Y. 1991. Aerothermodynamic configuration of first-generation aerospace planes (buran-type) and first flight results. In *Proceeding of the First European Symposium on Aerothermodynamics for Space Vehicles*, Noordwijk, The Netherlands. ESA SP-318.
- Netterfield, M. P. 1992. Validation of an navier-stokes code for thermo chemical nonequilibrium flows. In *AIAA 27th Thermophysics conference*. AIAA paper 92-2878.

- Perrier, P. 1994. Major lessons learned in hypersonic design of hermes. In *Proceeding of the Second European Symposium on Aerothermodynamics for Space Vehicles*, Noordwijk, The Netherlands. ESA SP-367.
- Sagnier, P. 1992. Usefulness of electre flight experiment within the hermes program. Technical Report RT 38/6121 SY (H-NT-0-2047-ONER), ONERA.
- Schwane, R. and Muylaert, J. 1992. Design of the validation experiment: Hyperboloid-flare. Technical Report Document: YPA/1256/RS, ESA-ESTEC.
- Taquin, G. 1993. Private communications. *Aerospatial*.
- Vincenti, W. G. and Kruger, Jr., C. H. 1967. *Introduction to Physical Gas Dynamics*. Malabar, Florida: Robert E. Krieger Publishing Company.
- Walpot, L. M. G. 1991. Quasi one dimensional inviscid nozzle flow in vibrational and chemical non-equilibrium, diploma thesis. Technical Report ESTEC EWP-1664, T.U. Delft, Dept. of Aerospace Eng.
- Wang, K. C. and Caram, J. M. 1994. Comparison of space shuttle orbiter wing leading edge heating rate calculations with experimental and flight data. In *AIAA 32th Aerospace Sciences Meeting and Exhibit*. AIAA paper 94-0453.
- Weilmuenster, K. J., Gnoffo, A., and Greere, A. 1993. Navier-stokes simulations of the shuttle orbiter aerodynamic characteristics with emphasis on pitch trim and body flap. In *AIAA 28th Thermophysics Conference*, Orlando, FL.

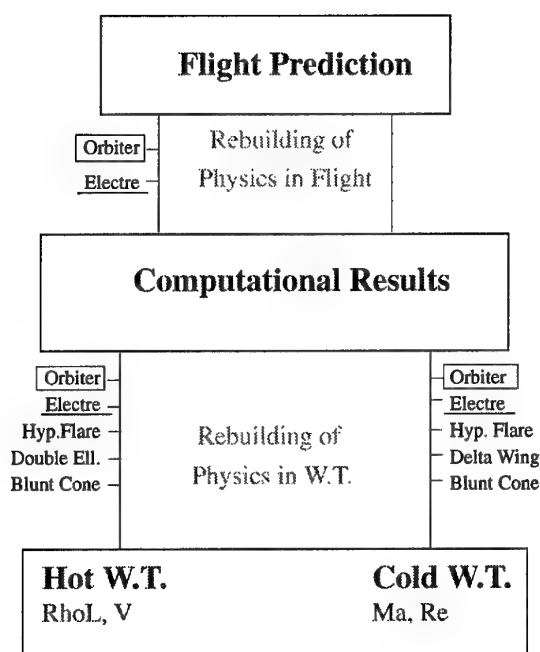


Figure 1: Extrapolation to flight approach.

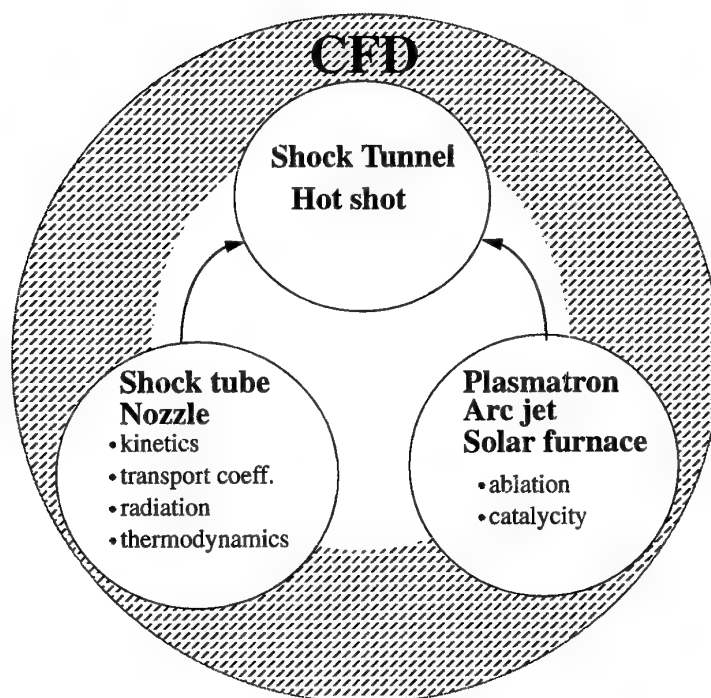


Figure 2: Real gas validation methodology.

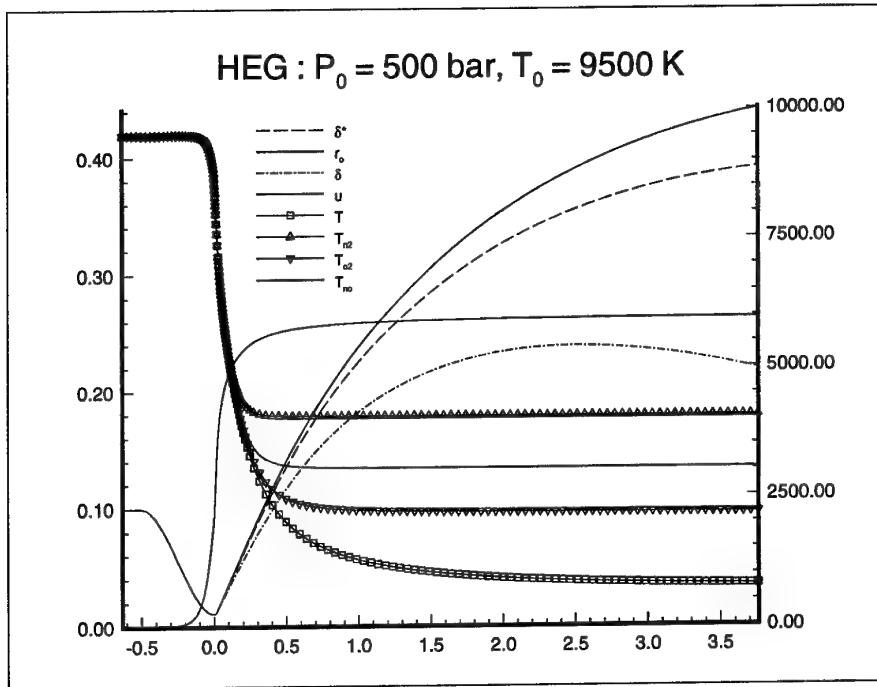


Figure 3: HEG wall boundary-layer and center-line temperatures as computed with LORE1D.

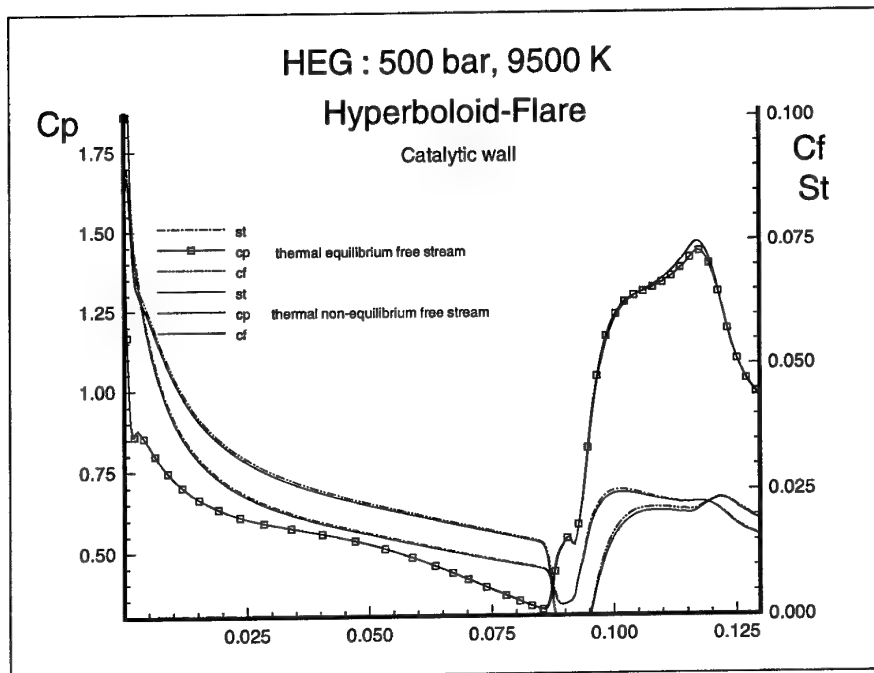
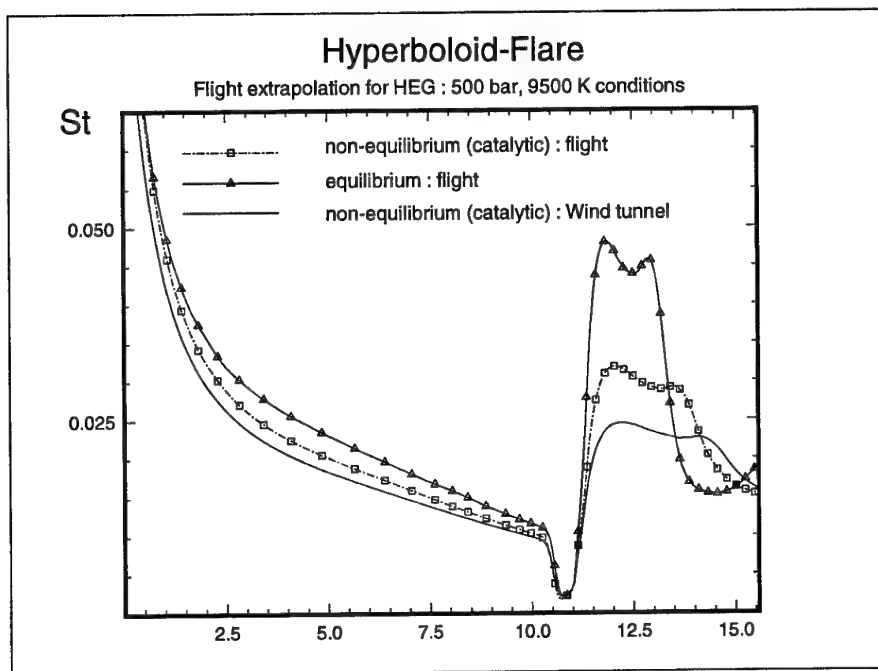
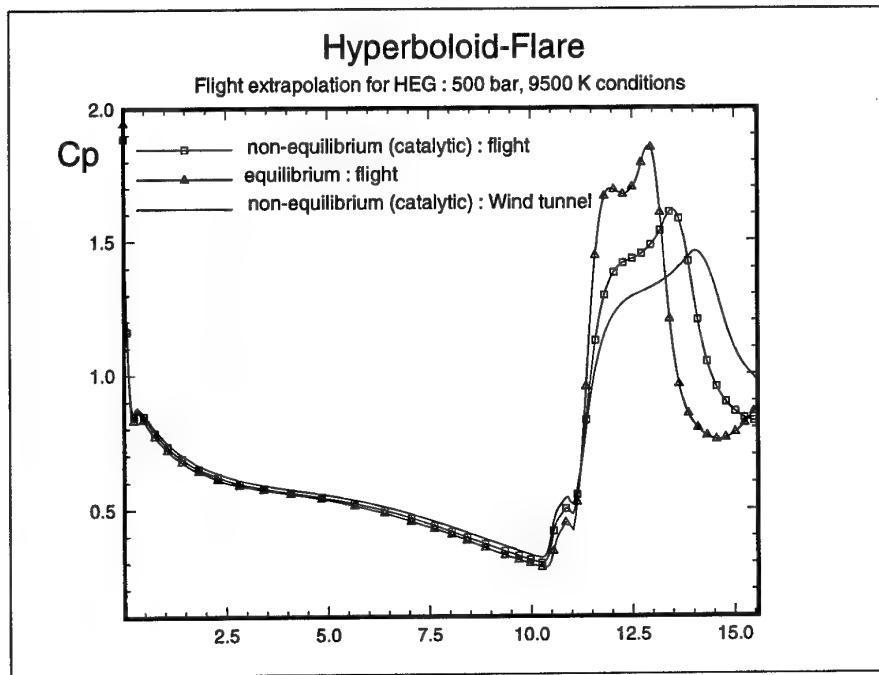


Figure 4: Influence of nozzle vibrational nonequilibrium on the hyperboloid flare C_p distribution.



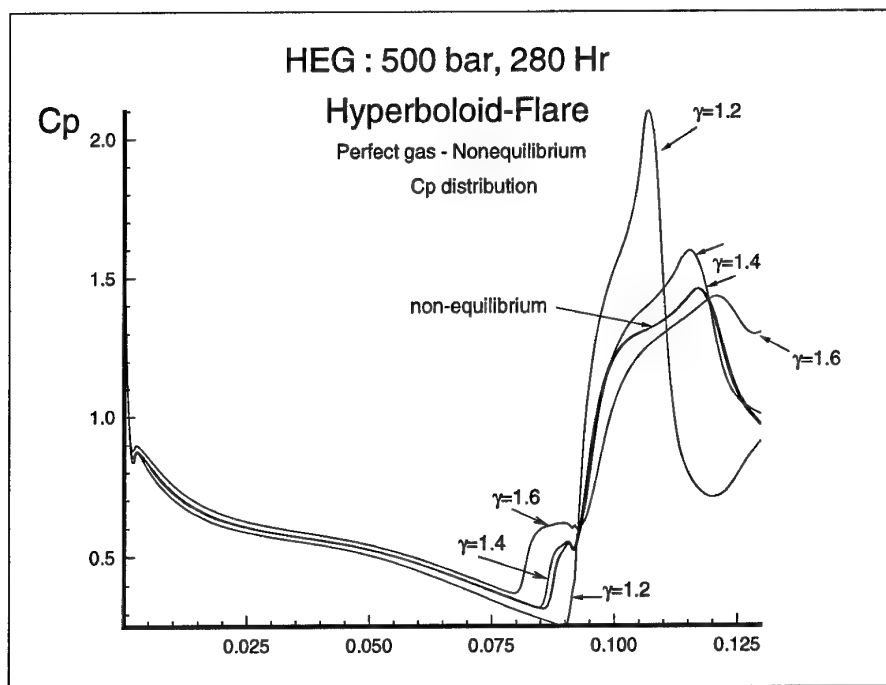


Figure 7: Influence of γ on hyperboloid flare C_p distribution.

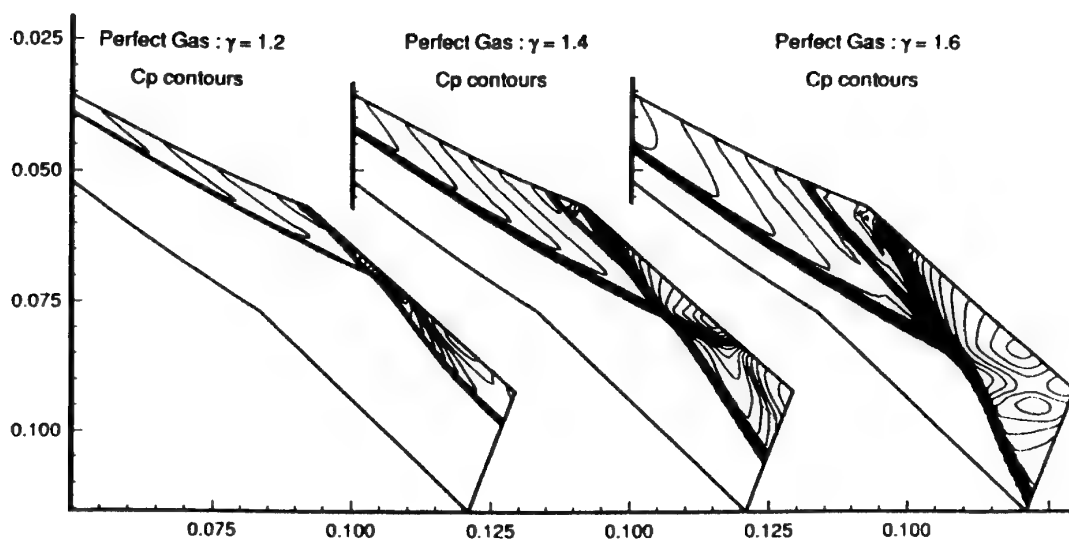


Figure 8: Influence of γ on shock-wave/boundary-layer interaction.

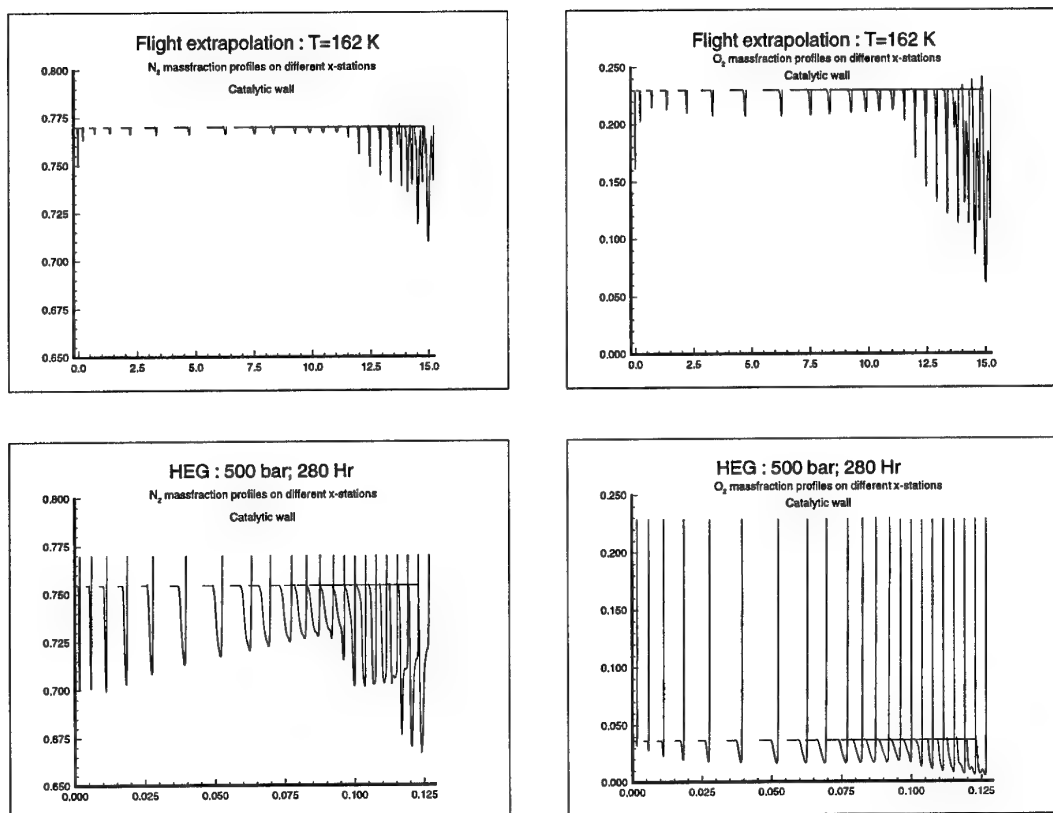


Figure 9: Comparison between wind-tunnel and flight O_2 and N_2 mass-fraction profiles perpendicular to the wall.

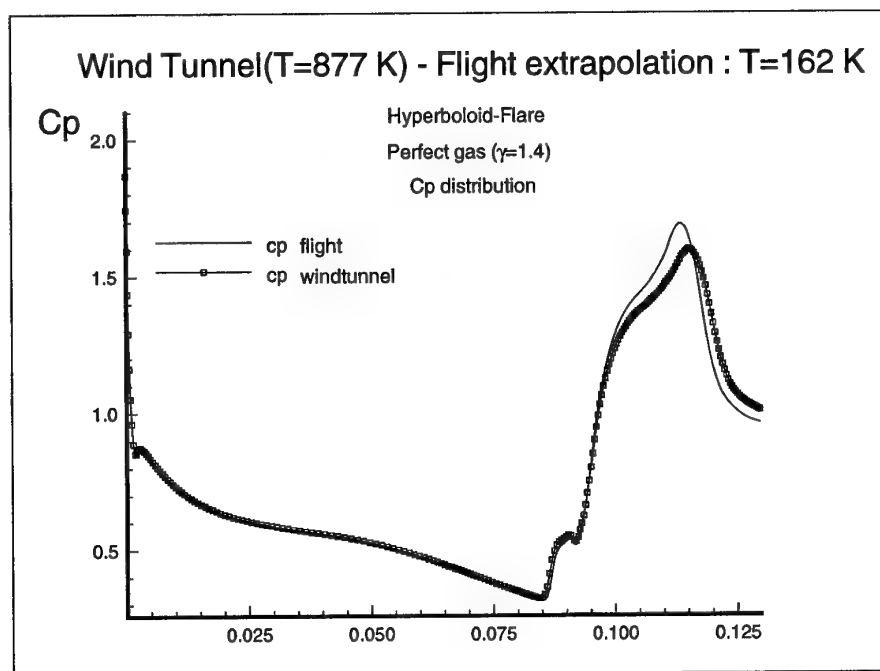


Figure 10: Comparison between equivalent wind tunnel HEG $\gamma = 1.4$ and perfect gas flight.

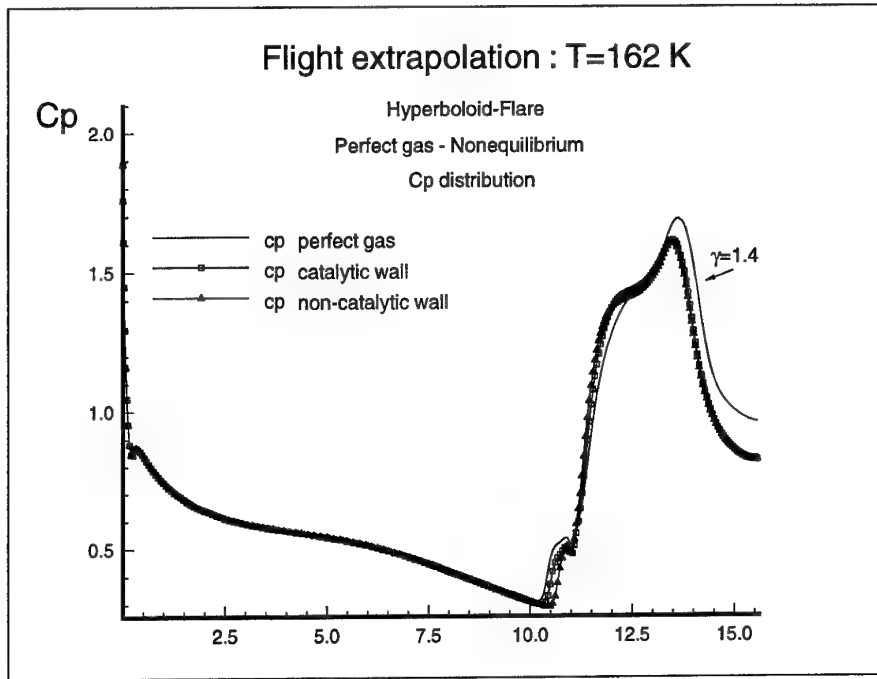


Figure 11: Comparison between flight perfect gas and flight nonequilibrium.

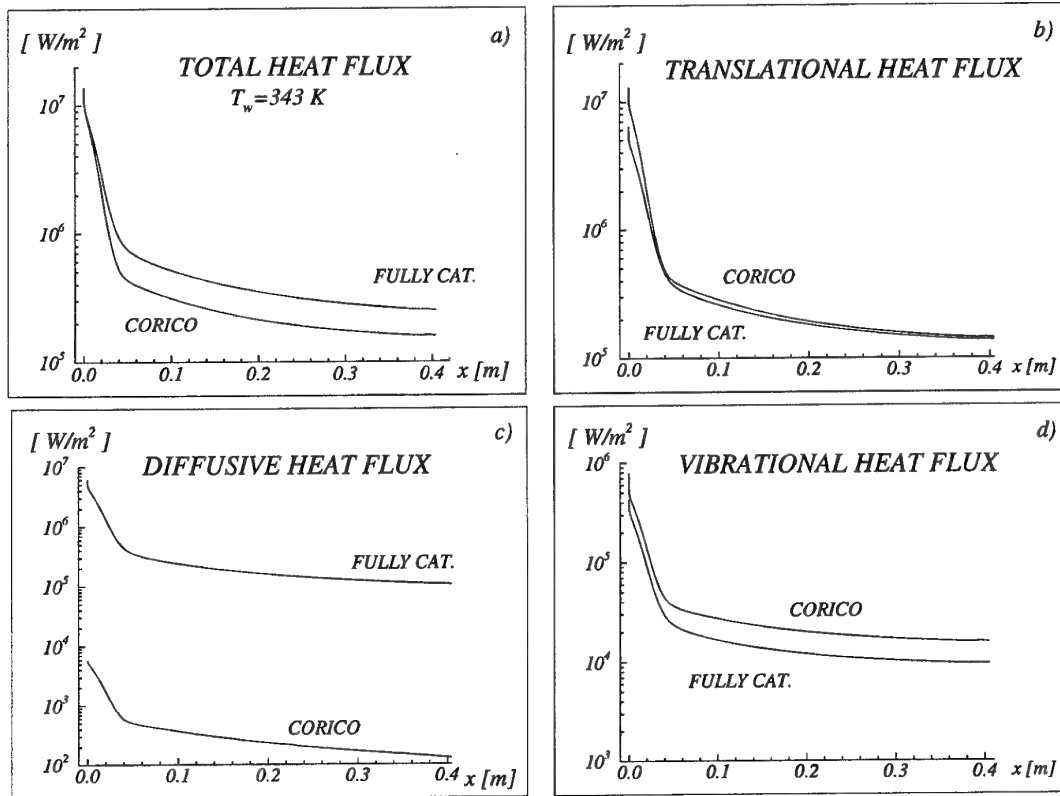


Figure 12: Total heat flux and its contributions along Electre model in HEG with $T_w = 343$ K.

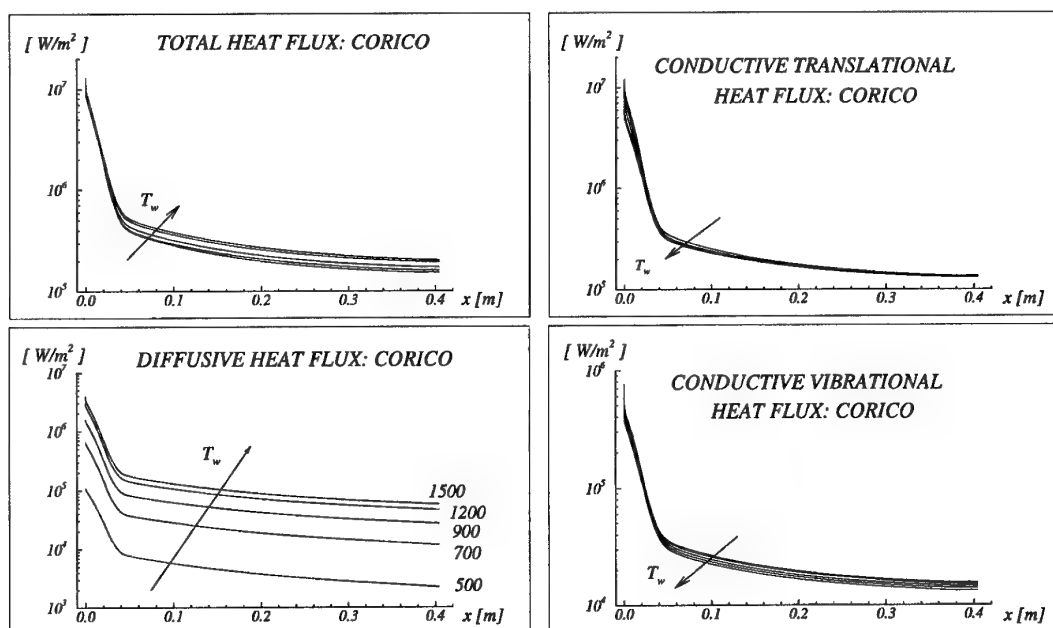


Figure 13: Total heat flux and its contributions along Electre model in HEG: influence of silica coated wall temperature.

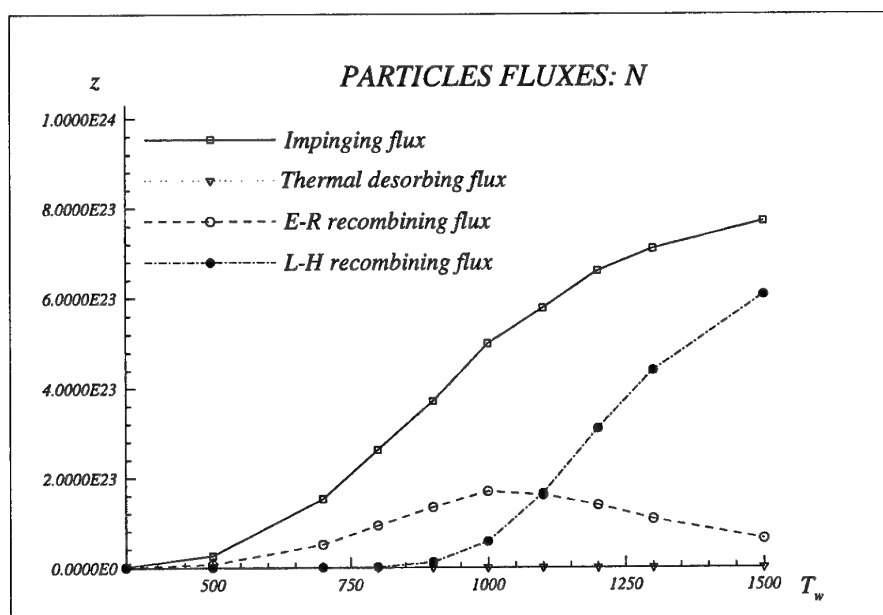


Figure 14: Nitrogen particles flux contributions as a function of the wall temperature.

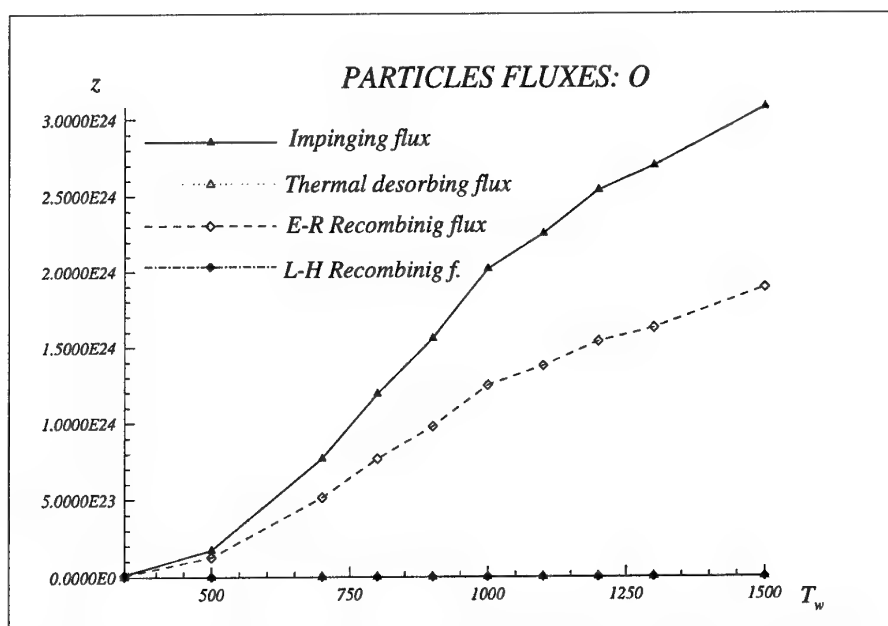


Figure 15: Oxygen particles flux contributions as a function of the wall temperature.

CHAPTER VIII

TEST FACILITIES

James Arnold

Thermosciences Division
MS 229-3/RT
NASA Ames Research Center
Moffett Field, California 94035-1000
USA

and

John F. Wendt

Von Kármán Institute
Chaussée de Waterloo 72
B-1640 Rhode Saint Genèse
BELGIUM

CONTENTS

1	INTRODUCTION	167
2	MISSION NEEDS	167
3	MODERN APPROACH TO AEROTHERMODYNAMICS	169
4	EXISTING FACILITIES	170
4.1	U.S. Facilities	171
4.2	European Facilities	174
4.3	Russian Facilities	176
5	ASSESSMENT OF FACILITIES	177
6	ASSESSMENT OF INSTRUMENTATION	178
7	FUTURE FACILITY NEEDS	180
7.1	Results of U.S. Studies	180
7.2	Results of European Studies	181
8	RECOMMENDATIONS ON POSSIBLE AREAS OF COOPERATION AND POTENTIAL BENEFITS	181
9	SUMMARY	182
	ACKNOWLEDGMENTS	182
	REFERENCES	182
	APPENDIX	184
	FIGURES	186

1 INTRODUCTION

This chapter provides an overview of the current ground-based aerothermodynamic testing capabilities in Western

Europe, Russia and the United States. The focus is on facilities capable of producing real-gas effects (dissociation, ionization, and thermochemical nonequilibrium) pertinent to the study of atmospheric flight in the Mach number range of $5 < M < 50$. Perceived mission needs of interest to the Americans and Western Europeans are described where such real-gas flows are important.

The role of Computational Fluid Dynamics (CFD) in modern ground testing is discussed and the capabilities of selected Western and Russian real-gas facilities are described. An update on the current instrumentation in aerothermodynamic testing is also outlined.

Finally, future needs for Aerothermodynamic testing, including instrumentation, are discussed and recommendations for implementation are reported.

2 MISSION NEEDS

Figure 1 (adopted from Howe 1990) is an altitude-velocity map of past missions and representative missions of future interest to the aerothermodynamics community in the United States and Western Europe. For reference, the reentry corridor of the Space Shuttle Orbiter is depicted by the line labeled Space Transportation System (STS). The black dot on the curve represents the peak heating point for the STS trajectory as do those for other trajectories to be discussed below. The higher-density ascent flight envelope for the National Aerospace Plane (NASP) type scramjet-propelled vehicle is shown by the shaded bar. Both trajectories asymptote at speeds of about 6.7 km/s to meet their mission objectives of access to Low Earth Orbit (LEO).

The Apollo lunar-return trajectory is also shown for reference on Figure 1 with its entry speed of 11 km/s. This trajectory

involved landing and is called a "direct" entry as contrasted to aerobraking type maneuvers to be discussed below. Future missions of interest to the American community (in addition to access to LEO by NASP-type airbreathing vehicles and future rocket-powered ascent vehicles) include new return missions into the Earth's atmosphere from the Moon and Mars where aerobraking maneuvers will be used to decelerate vehicles by dipping into the atmosphere and exiting the atmosphere into a prescribed, lower energy orbit. The flight envelope for the aerobrake maneuver for return from bodies other than the moon are not shown. They are similar to the lunar-return case except with higher entry speeds. Also plotted on Figure 1 is the aerobraking trajectory that was planned for the canceled American Aeroassist Flight Experiment which was to have been launched from the Shuttle Orbiter. Future piloted Mars missions must account for abort scenarios with entry speeds of up to 15 km/s as depicted by the Mars abort trajectory with a direct entry to the Earth's surface.

Recently, the Magellan spacecraft used aerobraking (Haas and Schmitt 1993) to circularize its orbit about Venus by making many high-altitude "dips" in the atmosphere. While this mission did not exhibit aerobraking where significant aeroheating occurred, it does illustrate the viability of such maneuvers.

Additional missions of interest to the Americans include planetary entry into the atmosphere of Mars by the MESUR/Pathfinder probe vehicle which is a precursor to the landing of a network of surface stations in a proposed new program called MESUR/Network. The Americans also are considering new Venus entry probes similar in nature to those of the past Pioneer-Venus mission.

Huygens-Cassini, a joint European-American program, will send a sampling probe into the atmosphere of Titan, one of Saturn's moons. This will entail an entry speed of about 6 km/s.

European manned mission needs are first focused on the independent access capability to space. The initial mission of the European vehicles is to perform the servicing of manned or man-tended space stations, either in the frame of an international cooperation, or possibly later in full autonomy. The planned duration of the stay in orbit varies from a week to several months, depending on the operational scenario. The vehicles considered have to take into account particular geographic and geopolitical constraints, namely a launch capability from Kourou (French Guyana) and a return capability on European countries. These constraints include a preference for medium-or high-inclination orbits, but imply the need for a maneuverable vehicle with significant crossrange in case this vehicle is to be operated regularly. The European vehicles, as they are envisaged today, should rely on medium-level technology and yield performance capacities which are unique and complementary to those of the USA and Russia. The aerodynamic shapes under study provide a good lift-to-drag ratio (0.6 to 1) and a positive aerodynamic control

in hypersonics, but do not allow a conventional landing as an airplane. Other landing modes are under study, ranging from conventional parachutes to guided paragliders.

The fulfillment of these ambitions implies a large effort in Europe in the field of aerothermodynamics where both computational and experimental design tools are developed. The creation of this new center of competence in Europe is of a nature, through the dialogue between scientists, to speed up scientific progress within NATO in hypersonic aerodynamics.

In the longer term, Europe also considers participating in manned space exploration, most probably in the frame of an extended cooperation. However, the present tight-budget restrictions do not allow to start conceptual studies for the time being. Finally, Europe is putting together a technology program to prepare the development of future reusable launchers. For the time being, both single-stage-to-orbit and two-stage-to-orbit concepts are considered and both airbreathing and advanced rocket options are studied. A technology effort is made in aerothermodynamics, propulsion, and other relevant technologies.

In addition to the European programs described above, some national programs are also underway.

The German government funds research on airbreathing vehicles under the National Hypersonic Program; the goal is a two-stage-to-orbit, fully-reusable vehicle characterized by a significantly lower cost-per-kilogram in orbit. It has been given the name Sanger. The first stage is envisaged as a hypersonic airbreathing aircraft powered by turbo-ramjets which would cruise at Mach 4 to 5 and then accelerate to Mach 6 or 7 when the upper stage, HORUS, would be propelled by a rocket engine into orbit. Return would be much like Hermes. Sanger's first stage will exhibit many of the necessary characteristics of a hypersonic commercial aircraft.

The French PREPHA (Programme de Recherche en Propulsion Hypersonique AvancHe) activity has defined two main goals. One is to validate the principle of supersonic combustion in the range Mach 6 to 8; the second has the objective of demonstrating the feasibility of an engine that will operate over a wide range of Mach numbers from subsonic to hypersonic. An important element of the program is collaboration with various Russian laboratories.

Figure 1 indicates regions of important real-gas flow phenomenon which must be adequately accounted for at increasing speeds. Boundaries are shown in the figure where dissociation of O_2 and N_2 occur and where ionization effects become important. These boundaries are for normal shock/stagnation regions of the flow. At altitudes below about 45 km, flow simulations can be made assuming equilibrium thermochemistry on moderately-sized blunt bodies within the Navier-Stokes approximations. On small bodies or sharp leading edges, these approximations may not be valid. At altitudes above about 45 km, finite-rate chemistry must be taken into account. In many instances single-temperature CFD models break down requiring more complicated treatments

such as the two-temperature, non-thermochemical models (Park 1990). At higher altitudes, the Navier-Stokes approximations break down requiring treatments for rarefied flows (Lumpkin and Chapman 1991).

3 MODERN APPROACH TO AEROTHERMODYNAMICS

The traditional aerodynamic design tools for aeronautics and space projects, i.e. wind tunnels, semi-empirical codes, and flight testing, have been supplemented by CFD due to rapid advances in computer power and algorithm developments.

As with all design tools, the CFD codes must be validated; i.e., they must be checked against a range of experiments and experimental conditions spanning the range of involved flow physics and chemistry before they can be considered as serious design tools.

There currently is a dearth of archival quality, benchmark experimental data suitable for CFD code validation and calibration. What defines a benchmark experiment is still open to question and debate. One version of the structure that sorts and classifies the types of testing is shown in Table 1. Included is a statement on the necessary acceptance criteria for the data, the facilities that cover the range of testing required, desirable acceptance criteria and data completeness and accuracy requirements.

TABLE 1

CALIBRATION OF HYPERSONIC CFD CODES

CLASS	PURPOSE	EXAMPLES
1. Phenominological data	Understand flow physics	Studies of large-scale structures
2. Unit problem data	Assess a model incorporate in a CFD code	Simple shear-layer data
3. Component data	Assess code's ability to analyze comp of overall flow field	Rotor blade in wind tunnel
4. Performance data data/complete flowfield	Assess if code predicts eng. parameters	Nozzle thrust
5. Full or sub-scale	Assess code ability to analyze specific flow parameters	Blunt body heat

Necessary Acceptance Criteria:

1. Baseline applicability ($M > 3$)
2. Simplicity
3. Specific applicability
4. Well-defined experimental boundary conditions
5. Well-defined experimental error bounds
6. Consistency criterion

7. Adequate documentation of data
8. Adequate spatial resolution of data

Facilities Required:

- conventional hypersonic wind tunnels
- high enthalpy facilities
- rarefied facilities
- airbreathing propulsion testing
- materials testing

Table 2 shows another set of criteria for an ideal benchmark experiment for CFD validation as reported from the Antibes meeting on CFD code validation.

TABLE 2

CRITERIA FOR AN IDEAL BENCHMARK EXPERIMENT FOR CFD VALIDATION

1. Appropriate For CFD Validation:
 - a. Simple enough for economical CFD treatment.
 - b. Universal enough for applicability to numerous real world problems.
2. Model Flowfield Adequately Characterized:
 - a. Boundary conditions defined: T_w , $\sqrt{\rho ck}$, m , catalytic effects, etc.
 - b. Boundary-layer surveys made (laminar or turbulent state defined)
 - c. Force, pressure, and heat data available as appropriate.
 - d. Shock locations measured (Optically or other means)
 - e. Model attitude accurately measured ($\leq 0.1^\circ$)
 - f. Base pressure measured.
3. Model Fidelity Sufficient:
 - a. Sharpness/bluntness accurately manufactured, maintained and defined.
 - b. Surface conditions quantified.
 - c. Model shape faithful to the defined configuration.
4. External Flowfield Characterized:
 - a. Mach and Reynolds numbers, T_0 , T_∞ , T_{vib} , P_∞ , and time accurately defined.
 - b. Chemical/energy states of test gas defined (frozen, non-equilibrium, etc.)
 - c. Gradients of pressure, temperature, velocity defined in terms of the primary variables.
 - d. Contamination levels measured, potential effects noted.
 - e. Flow angularity measured in the test area.
5. Variables Identified and Controlled:
 - a. External flowfield variables varied in an orderly and rational manner.
 - b. Model variables varied in an orderly and rational manner.
6. Facility and Instrumentation Adequately Described:
 - a. Principles of operation as they affect data.
 - b. Limitations.
7. Data Uncertainties Defined For All Measurements:
 - a. Defined by standard methods and convention.
 - b. Repeatability demonstrated.

CFD clearly can be an essential design tool for hypersonic vehicles because wind tunnels do not provide full simulation at velocities above about 3 km/s (or Mach number above 5 - 10). Semi-empirical codes are inadequate and flight tests are exceedingly expensive. Moreover, CFD can directly assist in the improvement of wind-tunnel designs and in the efficient utilization of wind tunnels. Examples of methods already in use are:

1. Hypersonic nozzles are designed with CFD methods, using available models for transition and turbulence;
2. Decisions on the relative importance of a given flow parameter for vehicle design are made by performing sensitivity studies using CFD;
3. Estimations of the allowable uncertainty for a given measurement technique are made by performing sensitivity studies with CFD.

However, CFD has the potential to play an even more important role in the future. CFD codes could replace the role of empirical design codes when new facility concepts are considered. For example, CFD can be used to predict the time-dependent operation of a new facility concept by simulating the influence of diaphragms, valve ports, shock propagation and reflection, etc. on the overall flow development. In other words, the entire aerodynamic design of a proposed new facility could be carried out with CFD. Optimization of the design may also be envisaged.

This process would permit the construction of a pilot tunnel with enhanced confidence; the pilot tunnel, in turn, would serve to validate the codes whose improved versions could then be employed to design the full-scale facility.

Clearly the procedure can be continued to predict the gasdynamic state of the flow in the test section and even the flow non-uniformities. Such knowledge will improve the credibility of wind-tunnel testing and in the long run will reduce the number of wind-tunnel tests required for a given design effort.

This philosophy is already producing results. Wilson et al. (1993) have published time-dependent simulations of reflected-shock/boundary-layer interactions in a cold-flow model of the NASA Ames Electric Arc Shock Tube called the E.A.S.T. Facility. The results on the mixing of driver/driven gas are in qualitative agreement with experiments and have shed new light on the effect of this phenomenon on the prediction of reservoir conditions. At present, these computations are very CPU intensive, but if past experience is a guide, continued increases in computer power and algorithm efficiency will reduce this limitation.

It can be concluded that the pacing item in the use of CFD for facility design and flow characterization is code validation carried out through the use of building-block experiments. Only when facility designers have confidence in CFD codes will these codes be used for the design of major facilities. The

promise to aerothermodynamics held out by this modern approach is so large as to fully justify the important investments that will be necessary to bring it to fruition.

4 EXISTING FACILITIES

This chapter begins with a broad overview of the simulation capabilities of various types of wind tunnels designed to study hypersonic flows and to simulate aspects of hypersonic flight. Then a brief summary of the characteristics of the major real-gas, high-Reynolds-number, and rarefied facilities for aerodynamic research will follow. In addition to the American and European facilities, a synopsis of selected Russian hypersonic facilities is presented because they are not well-known in the West.

Above Mach numbers of 8 to 10, *duplication* of flight conditions cannot be attained in most existing ground-based facilities with models of realistic size, even for entry from LEO; the upper limit is even lower if scramjet vehicles or entry from lunar or higher energy orbits are considered. Thus, *simulation*, which is the duplication of the essential dimensionless parameters characterizing the specific flow problem of interest, is the only methodology available at present. (It must be emphasized that if non-equilibrium chemical reactions are present, full simulation cannot be achieved in the most general case. Only full-scale testing at real flight conditions will suffice) As a general rule, blunt bodies require Mach-number, binary-gas-number (ρL), and T_0/T_w simulation; slender bodies require Reynolds-number simulation as well. If surface radiation effects are important, then absolute wall temperature must be duplicated which leads to the so-called "hot-model" technique (Hirschel 1991).

Figure 2 summarizes the Reynolds-Mach capabilities of European and American facilities; an overlay of two mission trajectories is shown for comparison. A clear need for high-Reynolds-number tunnels is evident if the mission is to be a single-stage-to orbit (SSTO), air-breathing vehicle. Figure 3 shows the situation with regard to the simulation of ρL for the European facilities. The newest European and American facilities (F4, HEG, T5, etc.) were designed with this phenomenon in mind.

Figure 4 summarizes the capabilities of existing facility types in terms of stagnation temperatures they can produce as a function of run time. The figure shows that shock tubes are useful in simulating gasdynamics and kinetics where the duration of chemical processes are the same or greater than that for which the flow persists ($1 \mu s$ to $10 \mu s$). For example, nonequilibrium radiation behind normal shocks. The next realm from $10 \mu s$ to $10 ms$ can be studied by shock tubes, shock tunnels and ballistic ranges. Gasdynamics and kinetics can be studied at the lower range of the time scale. At the upper end of the time scale, the researcher can study aerodynamics and flowfield definition in the hypersonic regime where real-gas effects are important. Shock tunnels are generally driven with a free-piston driver or a shock tube. Flow quality and chemical cleanliness are of concern to these

facilities. Ballistic ranges generally launch into a quiescent gas and contamination is not a concern. However, current ballistic-range-model scales are quite small. The realm of simulation from 10 ms to 2 s of flow can be explored with hot-shot and long-shot tunnels and high-performance blowdown tunnels. Here, the flow duration is sufficiently long to observe controlled motion of the test article, enabling detailed studies of aerodynamics. Finally, conventional blowdown tunnels can provide long-duration flows of up to minutes, but these facilities cannot usually produce real-gas flows. Most arc-jet facilities can provide long-duration, real-gas flows. An arc jet is basically a wind tunnel in which energy is added to the flow with a high-power arc discharge. Arc jets generally do not have aerodynamic quality flows and are used to study heat shield materials. This chapter will not consider further conventional blowdown tunnels or arc jet facilities.

Thus, a given mission and flight vehicle will define the relative importance of the various dimensionless parameters whose values must be matched in the facility. In addition to the fluid dynamic parameters, it is clear that such elements as cleanliness (freedom from solid particles) and flow uniformity (spatial and temporal, including wind-tunnel-generated pressure fields) must be quantified. It should be noted that some types of measurements may be carried out to an acceptable degree of precision in spite of the presence of noise, dirt, fluctuations, etc.; however, other important phenomena may be totally obscured by some of these effects. (The well-known influence of nozzle -wall turbulent boundary layers on the location and character of boundary-layer transition is a classic example).

An accurate knowledge of facility characteristics is obviously essential if tests of high quality are to be undertaken. High-enthalpy facilities are, however, particularly difficult to characterize due to their short running times, the presence of particles, non-equilibrium conditions, etc. Therefore, the need for sophisticated instrumentation techniques, which is summarized in Chapter VI, is of paramount importance.

4.1 United States Facilities

4.1.1 NASA Ames 16-inch Shock Tunnel

The 16-inch Shock Tunnel is being currently used for scramjet propulsion testing in support of the NASP program and the NASA Hypersonics Research Programs. The description herein is a contraction of information contained in Cavolowsky et al. (1992).

A schematic of the 16-inch Shock Tunnel is shown in Figure 5. The driver section consists of a tube 21 m long with an inside diameter of 432 mm. The driven section is 26 m long with an inside diameter of 305 mm. The shock tunnel received its name from the 16-inch naval rifles used to construct its driver section. The shock tunnel is rated at 680 atm maximum driver pressure. The contoured Mach 7 nozzle is 5.8 m long and has an exit diameter of 990 mm. Interchangeable throat

sections are used to vary the nozzle area ratio. Recent results have been obtained for area ratios of 190, and a minimum of 95 as attainable without sacrificing test time or ideal shock tube end wall behavior. The test cabin is a 1.82 m long by 1.37 m square cross section box located immediately downstream of the nozzle exit. Flow simulations equivalent for Mach 12, 14 and 16 have been achieved in the tunnel. Uncontaminated flow times of 3-5 ms are routinely seen in the 16-inch Shock Tunnel.

It is important to note that although present efforts are directed toward propulsion testing and research studies, the 16-inch Shock Tunnel is not restricted to this use. It will be valuable to experimental and computational research involving real-gas, blunt-body aerothermodynamics. This includes flight trajectories for spacecraft that will be studied as part of the Mars mission program and NASA's efforts to return to the lunar surface. Future plans will include calibration of test conditions required for these and other flight programs.

4.1.2 Large Energy National Shock Tunnel (LENS)

The basic components of the LENS facility (Calspan 1991) are shown in Figure 6. The driver/driven configuration consists of a chambered shock tube with an area ratio (driver/driven) of 2. The 292 mm internal diameter driver is 7.6 m long and is externally heated by a resistance heater to 2270 K. The 203 mm internal diameter driven tube is 15.2 m long. A hydrogen-nitrogen or helium-air mixture is used as the driver gas. Air is generally the driven gas, although other gases may be used. The tailored-interface mode of operation is used to provide the longest possible steady-state reservoir conditions. Maximum driver pressure is 2040 atm which yields a maximum pressure behind the reflected shock of 2040 atm.

Four axisymmetric nozzles are available:

Nozzle	Type	Exit Diameter [m]	Test Section Mach Number
A	Contoured	0.61	6.5 - 8.2
D	Contoured	1.22	10 - 17
E	10.5° cone	1.22	7 - 22
F	10.5° cone	1.83	8.6 - 24

The contoured nozzles provide parallel flow with no pressure gradients in the streamwise direction for several feet. The nozzles employ replaceable throat inserts of different diameters so that, with a particular nozzle, the test Mach number can be varied. Test air passes through the test section into a receiver tank of size sufficient to maintain the desired flow for durations of 2 to 27 ms. All nozzles are calibrated using pitot pressure survey rakes over the Mach number range indicated.

The LENS Hypersonic Shock Tunnel is capable of simultaneously duplicating velocity (i.e., enthalpy) and density over a wide range of hypersonic flight conditions.

This range of conditions referenced to a typical continuous flight corridor is shown in Figure for the Calspan 48-inch shock tunnel and the LENS facility. Reservoir temperatures associated with the velocity range of interest are also shown for reference purposes.

The 3 to 18 ms test time available from tailored-interface operation permits accurate measurement of model pressures, forces, heat transfer rates, and skin friction, as well as flowfield measurements of pitot pressure and total temperature. Additional instrumentation developed includes direct gas-sampling probes and instrumentation associated with microwave transmission through the plasma sheath, electron-beam density measurements, transpiration cooling, behavior of molten metal droplets in an oxidizing hypersonic airstream, as well as refraction and/or dispersion effects of the shock wave and turbulent airstream on a collimated beam of light.

4.1.3 Boeing Hypersonic Shock Tunnel

The Boeing Hypersonic Shock Tunnel HST was built in the early 1960's and was brought on-line to support the development of the X-20 program. It was deactivated in 1981, and restored in 1987.

The major components of the HST are a 4 m long, 76 mm diameter combustion heated driver, a 7.6 m long, 76 mm diameter driven tube, contoured nozzles (305 mm and 762 mm exit diameter), a test section/dump tank and a high-speed data recording system. Ignition of the driver gases (hydrogen and oxygen in helium) is initiated by 21 spark plugs placed in a spiral pattern along the length of the driver.

The HST uses a double diaphragm arrangement and operates as a reflected-wave shock tunnel. The Mach 5 to 8 range is covered with the 305 mm diameter nozzle while the 762 mm diameter nozzle is used for the Mach 8 to 20 range. Test times range from 2.5 to 5 ms, depending upon the total temperature being run. Reservoir conditions to 8000 K and 400 atm are available for high-enthalpy simulations.

The primary measurements made in the tunnel are surface pressure and aerodynamic heating rates using either platinum thin-film gauges or coaxial thermocouples.

Freestream velocity has been measured using an exploding wire and a photo diode array. Instrumentation also includes, high-speed cameras, shadowgraph and Planar Laser-Induced Fluorescence (PLIF).

4.1.4 Grumman Research Detonation Shock Tunnel

The Grumman Research detonation shock tunnel has been used for over 25 years to simulate high-temperature gas flows for programs including the Shuttle Orbiter and the National Aerospace Plane.

The tunnel consists of a 19.8 m long, 127 mm ID sectional tube assembly exiting through a nozzle into a 1.83 m diameter by 3.7 m long vacuum chamber. The nozzle has a rectangular

cross section with a nearly square throat 38 mm in height, varying to a 38 x 114 mm exit plane.

The Grumman shock tunnel operates by first rupturing its primary diaphragm allowing pressurized helium from the 6.1 m long driver to propagate into the driven tube. The driven gas for combustion simulation studies consists of a detonable mixture of nitrogen, oxygen, hydrogen and argon. The driven section is isolated from the vacuum chamber by a secondary mylar diaphragm at the entry to the facility nozzle. Test times of 2-3 ms are achievable with this facility.

Total enthalpy conditions corresponding to freestream Mach numbers between 8 and 12 are produced by varying the composition of the driven gas and the pressure of the helium driver gas.

4.1.5 GALCIT T5 Shock Tunnel

The T5 facility is a free-piston, reflected-shock tunnel located at the Graduate Aeronautical Laboratory of California Institute of Technology. The tunnel became operational in December, 1990. Hornung (1992) describes the facility and its performance in detail.

The compression tube is 30 m in length and is 300 mm in diameter, while the driven tube is 12 m in length and is 90 mm in diameter. The nozzle has a throat diameter of 31 mm, an exit diameter of 310 mm and a length of 1 m. The driver gas is helium or a helium/argon mixture, and the maximum burst pressure is 1,300 atm. The facility test times range from 0.2 to 5 ms, depending upon operating conditions. The tunnel is equipped with a hydrogen injection system with speeds up to 5 km/s. Instrumentation consists of wall pressure, heat flux and optical systems: schlieren, interferometry and differential interferometry.

4.1.6 GASL HYPULSE Facility

The HYPULSE Facility is an expansion tube which was originally built at NASA-Langley in the 1960's, deactivated in 1983, and reconstructed at the General Applied Science Laboratories, Ronkonkoma, New York, in 1987, and returned to operational status in 1989.

Figure 22, to be discussed later, shows a wave diagram of the operation method of an expansion tube. About two thirds of the total enthalpy and total pressure is generated through the unsteady expansion fan, and occurs at the test section mainly in the form of velocity.

The HYPULSE Facility consists of a 2.44 m long driver section with a 165 mm ID, a 7.5 m long intermediate section with an ID of 152 mm, an acceleration section 14.6 m long with an ID of 152 mm and finally an 11 m long 1.2 m ID test section/dump tank. The driver gas is room temperature helium and the maximum pressure is 140 atm. The facility has a variable Mach number range achieved by varying initial loading conditions: The lengths of tube elements also can be varied.

The "best" operating condition for this facility is at a stagnation enthalpy of 15.2 MJ/kg, freestream velocity of 5.33 km/s static temperature of 1200-1300 K at 2.0 kPa, and a test time of about 0.3 ms. Static pressure for this condition is 1.8 kPa, providing an effective total pressure of 163 MPa and a unit Reynolds number of $6.6 \times 10^5 \text{ m}^{-1}$. The facility has also been calibrated at total enthalpies of 9.1, 10.2, 11.8 and 17.1 MJ/kg, for which the test-section velocities vary from 3.8 to 5.7 km/s.

Instrumentation at HYPULSE includes surface pressure, heat flux and optical devices: laser holographic interferometry, schlieren, shadowgraph and Raman Spectroscopy, and time-averaged Mie-scattering imagery.

4.1.7 NASA-AMES Electric Arc Shock Tube

NASA Ames's electric arc driven shock tube facility has been in existence since the 1960's. The operating characteristics of the facility are described in Sharma and Park (1990) as shown in Figure 8. The facility consists of one driver system and two parallel driven tubes. One is a 100 mm ID tube 12 m in length, and the other is a 600 mm ID tube 21 m in length. The driver can be operated in two configurations: (1) a 177 mm conical drive configuration with a 101.6 mm exit (driver volume = 0.632 ℓ), and (2) a variable length (340-1370 mm) 100 mm ID cylindrical configuration (driver volume = 2.7 to 10.7 ℓ). The length of the cylindrical drivers can be varied by using a Lexan filler plug.

Energy to the driver is supplied by a 1.24 MJ, 40 kV capacitor energy storage system. By using the two different driven tubes, varying the driver/driven gas combination, driver charge pressure and preset capacitor bank voltages; normal shock velocities in the range of 3.0 - 50.0 km/s with unshocked test gas pressures at the higher velocities in the range of several tenths to several torr have been obtained. In order to minimize the level of impurities, contact of the test gas with steel and any material containing carbon or hydrocarbons has been minimized. Past experience shows that the spectra of the test gas, which was in contact with steel wall and carbon (burned mylar diaphragm), were overwhelmed by spurious emission spectral lines of iron and CN-violet (Sharma and Park 1990). For this reason, aluminum diaphragms and an aluminum 100 mm ID driven tube are used.

4.1.8 NSWC Hypervelocity Tunnel Number 9

The Hypervelocity Wind Tunnel 9, located at the Naval Surface Warfare Center in White Oak, Maryland, is a blowdown facility which currently operates at Mach numbers of 8, 10, 14, and 16.5. Tunnel 9 provides a high Mach-number and Reynolds-number testing environment with long test times and large test section size.

A schematic of Tunnel 9 is shown in Figure 9. A vertical heater vessel is used to pressurize and heat a fixed volume of nitrogen to a predetermined operating pressure and

temperature. The test section and vacuum sphere are evacuated and separated from the heater by a pair of metal diaphragms. When the nitrogen in the heater reaches the desired temperature and pressure, the diaphragms are ruptured. The gas flows from the top of the heater, expanding through the contoured nozzle in to the test section at the desired test conditions. As the hot gas exits the top of the heater, fast acting valves are opened allowing cooler nitrogen from four pressurized driver vessels to enter the heater base and maintain a constant heater pressure. The cold gas drives the hot gas out of the heater in a "fluid piston" fashion while maintaining constant conditions in the test section during the run.

Tunnel performance characteristics are given below:

Contoured Nozzle	Supply Pressure	Supply Temp	Reynolds Number	Run Time
Mach	[MPa]	[K]	[10^6 m^{-1}]	[sec]
8	6.9 - 83	870	14.8 - 165	0.33 - 5
10	3.5 - 97	1005	2.8 - 65.6	0.23 - 8
14	0.7 - 138	1785	0.24 - 12.5	0.7 - 15
16.6	145	1855	10.5	3

Tunnel 9 capabilities are under continuous development. Planned facility upgrades for 1994 include a new Mach 7 full-flight duplication Capability which includes true temperature and pressure operation at altitudes from 15 to 40 km for run times of 3 to 6 s respectively.

4.1.9 Ballistic Ranges

With its clean test-gas environment, the ballistic range provides correct thermochemistry at true flight enthalpy. The enthalpy comes from the use of light-gas guns which can launch projectiles at speeds in the 4 to 9 km/s range. However, the model scale is currently very small and there is concern that the test capability is inadequate. A very detailed AGARD Report (AGARDograph 138) primarily discussing the NASA Ames ballistic ranges of the 1970 time frame, details the methodology of the ballistic range including the use of a shock tunnel to provide a counter flow, enabling the simulation of lunar return (11 km/s) entry of the Apollo vehicles. With the advent of CFD, the role of the ballistic range has changed to become more of a validation tool.

Below is a synopsis of ballistic ranges in the U. S. as in the 1992 time frame adopted from Chapman (1992).

NASA Ames Research Center: Ames has several two-stage light gas launchers, the largest being 37.5 mm in diameter. These launchers have never been optimized for low-acceleration launching. The aerodynamic facility utilizes the 16-inch Shock Tunnel discussed above as its counterflow source, but the facility has not been operated in this mode for over 20 years. The facility has a 25 m long test section with 16 shadowgraph stations. The test section was sized to the capability of the shock tunnel to provide a slug of moving test gas of this length. It is capable of conducting aerodynamic

testing at hypervelocities and can yield good quality flow visualization and aerodynamic coefficients for simply-shaped vehicles. The aerodynamic range is in standby while its 16-inch Shock Tunnel is operating as a stand-alone facility.

Arnold Engineering and Development Center: AEDC has several launchers. The largest is 62.5 mm in diameter, and there is one being designed and built which is 82 mm in diameter. All of these launchers have been optimized with operational experience for low acceleration launch loads. The new launcher has been optimized from the design stage. There are two long variable pressure ranges, the longest being 300 in length. This range is also designed for either free-flight launches or launching onto a rail. The rail launch system also allows for recovery of models. Besides the conventional range instrumentation, this range is currently instrumented with spectrometers for wake-flow diagnostics. There is also ongoing work to develop planar laser induced fluorescence (PLIF). This facility has the best set of diagnostics equipment of any in the United States at the present time.

University of Alabama, Huntsville: This range was previously located at the Delco facility in Santa Barbara, CA. It has a 62.5 mm diameter launcher that has been extensively optimized to minimize launch accelerations. The range is over 300 m long with variable pressure capability. This facility has the radiometric instrumentation that was at Delco. This instrumentation needs to be updated if it is to be useful for detailed flow field studies and CFD code validation.

Wright Laboratory Armament Directorate at Eglin Air Force Base: This is a sea-level atmospheric pressure range of over 200 meters in length. The launcher room is small and hence the light-gas launcher is small and not optimized for soft launches. It also has an optical system that can not reject optical radiation from the model and hence is limited to 3 to 4 km/s. However, in this speed range it has the best developed aerodynamic determination system in operation at the present time. There are plans to replace all of the conventional cameras with electronic cameras and to fully automate the aerodynamic data-reduction procedure to provide rapid determination of aerodynamic parameters.

Lawrence Livermore National Laboratory: LLNL is presently developing a 100 mm two-stage light-gas launcher, for potential application as a space launcher. This launcher has two novel features. First, the driver tube (1st stage) and the launch tube (2nd stage) are at right angles, hence the launch tube can be elevated for firing without altering the driver. This could be a useful feature for saving space in a constrained area. It also presents an opportunity for using the pump tube (first stage) as a free-piston driver for a shock tunnel without significant interference with the ballistic-range portion of the facility. The second feature is that it uses methane-oxygen combustion as the driver for the first stage piston rather than the conventionally used gun powder. This launcher with the extensive advanced instrumentation base that exists at LLNL could be the nucleus of an aerothermodynamic testing capability. What is missing is a variable pressure test range.

Whether this facility contributes to the aerothermodynamic testing capability remains to be seen.

4.1.10 UC-Berkeley Rarefied Gas Wind Tunnel

The configuration and instrumentation of the University of California at Berkeley rarefied-gas wind tunnel have changed greatly from their state in the 1960s and 1970s (see Figure 10 for schematic of present facility Gochberg 1993). Currently, the electron-beam fluorescence technique is used as the primary experimental diagnostic tool, measuring density, and rotational and vibrational temperatures in the hypersonic, low-density flows generated using free-jet expansions. A ceramic resistance heater with a maximum operating temperature of 2000 K functions as the flow reservoir, and can be operated with virtually any gas, including oxygen. The facility is capable of producing shock Mach numbers for nitrogen in excess of 20 at the highest stagnation temperature available. The shock barrel is 65 mm long with a Mach disk diameter of 55 mm for this condition.

4.1.11 Facility in Development

A new concept for a very high pressure free-piston shock tunnel being developed at AEDC has been described in Maus et al. (1992). Figure 11 depicts the evolution of this concept from the conventional free-piston, light-gas gun. In the light-gas gun, the disposable piston is driven by gunpowder, compressing hydrogen to a high pressure. The diaphragm bursts at a prescribed pressure and the projectile is accelerated through the launch tube into free-flight.

In the disposable free-piston shock tunnel, the piston propellant is moderate to high pressure air, and the compression gas is helium. The diaphragm bursts, and drives the rest of the facility as a conventional shock tunnel. Conventional free-piston shock tunnels are limited to about 2000 atm stagnation pressures to avoid damage to their reusable pistons and gas leakage. In the light-gas-gun operation, the deformable piston seals the gases by extruding the piston into a tapered section. Pressures in excess of 10^4 atm are routinely achieved in this manner. Maus et al. (1992) state that this concept for a disposable free-piston shock tunnel has the potential of attaining stagnation pressures as high as 10^4 atm with enthalpies over 20 MJ/kg. This paper discusses pilot experiments for this concept and makes comparisons against theory. Also discussed, is a preliminary layout for such a facility in the basement of the G-Range building at AEDC. In this configuration, the compression tube would be 25.9 m long with an ID of 203 mm, the shock tube would be 12.2 m long with a 76.2 mm ID, and the conical nozzle would have an exit diameter of 457 mm.

4.2 European Facilities

4.2.1 HEG Shock Tunnel (Germany)

The HEG Göttingen facility is a free-piston-driven shock tunnel (Figure 12). The tunnel is 60 m long with an internal

diameter of 200 mm and has a test section diameter of 0.88 m. The maximum reservoir pressure achievable is 2000 atm which allows a maximum binary scaling parameter, ρL , of 10^{-3} kg/m^2 (Figure 13). This parameter represents the number of molecule collisions. The total temperature can reach 13800 K. The speed reached in the test section varies from 5 to 8 km/s. The core of parallel flow has been estimated to be 0.6 m with a static temperature of 3000 K. In the conical part of the nozzle, the flow is that of a real gas, while perfect-gas conditions exist in the test section. The nozzle exit Mach number is approximately equal to 7. The testing time is currently about 1 ms. It is desired to reach 4-6 ms of run time in order to be able to measure forces and moments with the help of accelerometers inserted in the models. The instrumentation consists of pitot tubes and static pressure transducers to measure the pressure and Mach number, and laser-induced fluorescence to measure density and possibly temperature to get the flow velocity. For flow visualization, a 2-D holographic interferometer is used, from which the density can also be computed.

4.2.2 ONERA F4 (France)

The F4 depicted in Figure 14 is the ONERA's high-enthalpy hypersonic testing facility. It is an intermittent blowdown (impulse) "hot-shot" type of wind tunnel. It has three different steel and fiberglass contoured nozzles with different exit diameters, the largest measuring 0.67 m and a length of 3.9 m. The electric power needed to operate it is 150 MW. This arc-heated facility can attain a stagnation pressure of 2000 atm. The flow velocity can reach 5.5 km/s, and the binary scaling parameter ρL goes from 10^{-3} kg/m^2 at a velocity of 5.5 km/s to 10^{-2} kg/m^2 at a velocity of about 3 km/s (see Figure 13). The testing time is between 50 and 150 ms. The Mach number range of the facility is 7 to 18. The main area of interest is at a Mach number of about 16 and a unit Reynolds number of about $3 \times 10^6 \text{ m}^{-1}$. A typical model size is about 0.3 m in length. With the relatively long testing time, accurate force and moment measurements can be performed. The instrumentation includes balances, heat transfer gauges, and pressure transducers.

4.2.3 RWTH Aachen Shock Tunnel (Germany)

The RWTH Aachen facility TH2 is a high-enthalpy shock tunnel (Figures 15) driven by a resistance-heated helium driver. In the reflected mode, the shock tunnel has a driver section of 6 m, a driven section of 16 m, and conical nozzles with exit diameter of 0.57 m, 1 m and 2 m. A contoured nozzle with an exit diameter of 0.57 m is also available. The tunnel can simulate Mach (6 to 24) and Reynolds ($12 \times 10^6 \text{ m}^{-1}$) numbers, duplicate the flight velocity up to 4 km/s, and simulate real gas effects. Measurements include pressure and heat transfer. Flow visualization is achieved by schlieren and shadow optics, and interferometry. The maximum total pressure is 1500 atm, and the maximum total temperature is 5000 K; the maximum testing time is 10 ms.

4.2.4 LRBA C2 Reflected Shock Tunnel (France)

The LRBA C2 is a classic shock tunnel with stagnation conditions to 2400 K and 350 bar; test times are 10 to 20 ms. The main feature of this tunnel is the large nozzle exit diameter of 1.2 m. Mach numbers can be varied from 8 to 16 using conical nozzles; however, a contoured nozzle for Mach 16 is generally employed.

4.2.5 VKI Longshot (Belgium)

The von Karman Institute's Longshot free-piston tunnel (Figure 16) is a short duration facility. It operates with nitrogen and can reach high Reynolds numbers at hypersonic speeds. It has one contoured nozzle with a 0.43 m exit diameter and a 6° conical nozzle with a 0.60 m exit diameter. The Mach number range is 15 to 20. The maximum Reynolds number at Mach 15 is about $30 \times 10^6 \text{ m}^{-1}$. The total pressure can reach 4000 atm and the total temperature about 2500 K. The models are mounted on a high precision incidence mechanism for pitch, yaw, and roll. The test section is 4 m^3 . Instrumentation includes a 6-component force balance with accelerometers to account for impulse forces; infrared photography, thin-film and coaxial thermocouples for heat transfer measurements; piezo-electric pressure gauges; and a schlieren system for flow visualization. The testing time is about 10-15 ms.

4.2.6 CNRS SR-3 Low-Density Tunnel (France)

The SR-3 wind tunnel (Figure 17) of the National Center of Scientific Research can achieve Mach numbers from 6.7 to 30. Its flow is of low density and the maximum Reynolds number obtainable is 7×10^3 at Mach 30. The gas used in the tests is nitrogen. The nozzle exit diameter goes from 0.15 m to 0.40 m. The tunnel flow is continuous and the flow regimes can be near-free-molecular or free-molecular. The instrumentation includes electron-beam probes for low-density measurements, pressure transducers, devices for heat-flow measurements, i.e. thin-wall technique and infrared thermography, hot-wire probes and aerodynamic balances. Flow visualization is obtained by sweeping the electron beam, by glow discharge, and by infrared thermography. The research conducted includes plume interaction studies at reentry conditions, launcher stage separation, directional control of satellites, and similar studies.

4.2.7 VG Low-Reynolds-Number Tunnels (Germany)

The V1G and V2G facilities at the DLR Göttingen are resistance-heated continuous tunnels which were designed for hypersonic low-Reynolds number (low-density) flow research. V1G and V2G have nozzle exit diameters of 0.25 m and 0.4 m, respectively. Because they are low Reynolds-number facilities, the useful cores are much smaller than the geometric cores: from 0.05 m to 0.3 m depending on selected conditions. Reservoir temperatures can reach 1500 K. Force balances, electron-beams, thin-wall heat transfer techniques,

flow visualization by glow discharge are just some of the instrumentation methods which have been developed over many years.

4.2.8 Facilities in Development

ISL - RAMAC (France)

Ram-accelerator research has been underway at the Institute Saint Louis (France) since 1988. The largest facility now operational is RAMAC 90 consisting of a ram accelerator tube of 90 mm in diameter and a conventional powder gun as pre-accelerator. The length of the accelerator tube is at present 9.5 m. Extension to about 30 m length is planned within the next two years. The facility is located in a 120 m long ballistic range, already existing in ISL since 1958.

The first ram-acceleration was attained in March 1992. A recent result increased the velocity of a 1.23 kg body from 1440 m/s to 1840 m/s within a tube of 9.5 m length. The main future objective of this facility is the acceleration of important masses to velocities up to 3 km/s.

A smaller facility is RAMAC 30, which consists of a ram accelerator tube of 30 mm in diameter and a conventional powder gun as the pre-accelerator. The length of the accelerator tube is 12 m. Stepwise extension up to about 40 m is planned during the next years.

The facility was built for basic research mainly in the superdetonative flight mode. The objectives are to achieve velocities beyond 4 km/s and to identify and overcome possible limiting factors such as aerodynamic heating which may lead to ablation and unstart.

4.3 Russian Facilities

The purpose of this section is to provide information on the performance of Russian hypersonic wind tunnels so as to ascertain whether the use of the Russian facilities is indicated.

Moscow is the Russian center for theoretical, numerical, and experimental research in aerospace. TsNIIMASH, the Central Institute of Machine Building; TsAGI, the Central Aerodynamics and Gasdynamics Institute and TsIAM, the Central Institute of Aviation Motors are located in the greater Moscow metropolitan area. TsNIIMASH's principal activities involve elaboration and optimization of spacecraft development programs, theoretical and experimental research in aerogas dynamics, heat transfer, thermal protection, static and dynamic strength of boosters and spacecraft for atmospheric and space flights. TsAGI is the largest complex for aerodynamic research from subsonic to hypersonic velocities. Its activity comprises fundamental and applied research. Experiments and theory are integrated with numerical solutions using modern computers and sophisticated algorithms. Emphasis is given to the design of aerodynamic configuration and structure of control systems. TsIAM is the biggest R&D center for aircraft engines and their components under conditions close to real flight. Its research scientists perform research on control characteristics,

compressor performance and stall margin, distortions, vibrations, and propulsion unit operational stability, gas turbines, fuel spray and supersonic combustion, jet nozzle performance, and other related topics.

TsIAM is mentioned here to inform scientists and engineers who might not know that it flight tested the alleged first hydrogen scramjet at Mach 8 in November 1991 (Figures 18 and 19). The engine was recovered in almost perfect condition after the flight. It is not known if and how much thrust was produced. No information about the LII facility is given herein in as much as its flight research activity is generally performed at subsonic and supersonic speeds only.

4.3.1 TsNIIMASH

Facilities of interest in hypersonic aerogas dynamics (Anfimov 1992) are a large-scale hypersonic piston gasdynamic unit (PGU U-7, U-11), an electric-arc gas dynamic unit (U-15T1), a large shock tube (U-12), and a large ballistic range (KBT). The PGU units (Figure 20) consist of large-scale hypersonic tunnels which reproduce an environment close to real flight conditions (Anfimov 1992). The Mach number range goes from 6 to 15 and is being updated to reach 25.

The PGU U-11 can generate dense, high-temperature gas especially good for aerodynamic testing and for hypersonic-gas-flow simulation. A multistage compression method was implemented some time ago to improve the compressed-gas stagnation parameters. The PGU were used for testing flight vehicles with simulation of propulsion jets. Practically all the Russian supersonic flight vehicles models, including the "Buran" (similar to the Shuttle Orbiter), were tested in this facility. Tests for measuring the heat flow distribution on the surface of the Hermes space plane's 1/40 scale-model on its descent leg for Mach 10-15 and Reynolds numbers of 50 million were also run in the facility. Appendix A gives a summary of the studies at Mach 10. The PGU U-11 has a tube length of 45 m, a diameter of 0.46 m, and a piston weight of 1500 kg. The nozzle is contoured. The total pressure can reach 2000 atm (diaphragm burst pressure) and the total temperature can reach 3500 K. Upgrades will increase the temperature to 10,000 K. Large models can be tested, up to 1.5 m in length and 0.5 m in diameter. The testing time can go from 0.5 to 3 s which is very long for a shock tunnel. Note that maximum pressures, temperatures and testing times cannot be realized simultaneously. Experimental data are obtained in aerogas dynamics and heat transfer with engine simulation; flight vehicle dynamic characteristics using a high-speed, 4-degree-of freedom traversing mechanism; heat transfer on reentry vehicles; kinetic characteristics of oxidation of natural gas and other hydrocarbons with pressures up to 1000 atm; processes in high-degree-compression engines using different fuels. The facility is equipped with an instrumentation system that allows the measurement of Mach and Reynolds number in the flow, that determines the attitude of flight vehicles and their relative position with respect to separating stores; that collects electric, optical, and physical data; that uses thermovision research units for research on heat transfer. The flow

visualization is obtained by an infrared system and a schlieren system. Supersonic combustion processes of scramjet engines used in hypersonic transportation systems can be tested in this facility because of the long testing time.

The U-15 T1 is an electric-arc gas dynamic unit Figure 21. The working gases used are air and nitrogen. The maximum total pressure achievable is 400 atm, and the maximum total temperature 12,000 K. The power input is 50 MW. A Mach number of 8 and a Reynolds number of 10^7 m^{-1} can be obtained. Models of 1 m length and 0.5 m diameter can be tested. The testing time is 600 s. This unit is extensively used to test heat-protective material thermal resistance in high-temperature gas flows, to obtain heat transfer measurements in hypersonic flows, and to determine plasma radio-physical characteristics so as to provide radio communication with flight vehicles.

The U-12 is a large shock tube with a 0.5 m inner diameter and a total length of 200 m. The large test section has a diameter of 3.2 m and a length of 23 m. The total pressure reaches 200 atm. In the hypersonic mode, the pressure chamber terminates in an 8° conical nozzle which allows a Mach number up to 8 and a Reynolds number up to $50 \times 10^6 \text{ m}^{-1}$. The testing time is 50 ms at Mach 10. The facility is equipped with six-component strain-gauge balances to measure forces and moments; with plasma diagnostic devices and radio-physical instruments to measure flow parameters. Flow visualization is realized by using schlieren photography and interferometry.

The KBT is a large ballistic range; its total length is 525 m. The test chamber has a length of 300 m and a diameter of 3.4 m. The pressure in the range goes from a minimum of 1 Pa to 0.5 MPa (about 5 atm). There are 53 optical registration stations (2-D), and 3 interferometric tomography stations. The velocity that can be attained in the range is up to 7 km/s. The range is equipped with snow, rain, and dust simulators which allows the investigation of the erosion of hypersonic vehicles when passing through heavy-weather conditions. Flow visualization is obtained with x-ray shadowgraph, schlieren, holographic images, and model pictures in reflected light. Research is performed in aerodynamic characteristics and stability of hypersonic vehicles of various configurations; in flow-pattern characteristics and model wakes; and high-speed impact processes.

There are a number of low-density facilities that can simulate continuous and free-molecular flow at an altitude of 70-80 km, at a Mach number from 7.5 to 15.5, and at a Reynolds number from 10^2 to 10^5 .

4.3.2 TsAGI

There are many hypersonic tunnels at TsAGI. Some of them have small test sections, less than 0.30 m, but they can attain Mach numbers up to 22 using air, helium, and carbon-dioxide. One is a "hot shot" type wind tunnel, and another a shock tunnel. The BAT-3, for instance, is a low-density tunnel that can simulate the conditions at 100 km altitude at Mach 20.

The main hypersonic tunnels of interest are the IT-2 and the T-117. The IT-2 is a "hot-shot" type wind tunnel with a Mach number range from 10 to 22. The maximum total pressure is 1500 atm and the maximum total temperature 5000 K. The Reynolds number at Mach 10 is about $20 \times 10^6 \text{ m}^{-1}$. Three different nozzle exit diameters are used for different Mach numbers, i.e. 0.20 m, 0.53 m, and 0.90 m. Nitrogen, carbon dioxide, and argon are the gases used in testing. The testing time is 100 ms. Pressures, temperatures, and forces are usually measured.

The T-117 is also an arc-heated hypersonic wind tunnel and must be considered the best that the Russians have. Its Mach number range goes from 10 to 20.5. The maximum total pressure is 200 atm and the maximum total temperature 2600 K. At Mach 10 the tunnel is used in the continuous mode; at Mach 20 the testing time is 120 s. The Reynolds number is $2 \times 10^6 \text{ m}^{-1}$ at Mach 10. The test section has a diameter of 1 m which allows the testing of very large models. The instrumentation includes a pressure rack to obtain pressure distributions, heat transfer gauges, balances to measure forces and moments, optical sensors, and flow visualization. The models are injected in the test section in 0.675 s; for heat transfer tests, they can be injected in 50 ms; they can be pitched at an angle of attack from -6° to 50° and at a yaw angle from -30° to 30° . The facility has three different diffusers that can be rotated in place in a very short time to allow for flow and configuration changes. Appendix A discusses results of Hermes testing in T-117 at Mach 10.

5 ASSESSMENT OF FACILITIES

As shown in Figures 2, 3, and 4, no facility can reproduce all the conditions required for complete reentry simulation. Consequently, each class of facilities has aimed at reproducing some of the required conditions and all classes can be seen as complementary to one another. Depending on the problem to be investigated, certain characteristics of a given class may range from very undesirable to acceptable; e.g. contamination may strongly influence combustion processes but have negligible influence on force measurements.

All the facilities discussed above which are more than five years old can be said to be useful contributors to our experimental data base within their specific limitations and advantages. The newer facilities: F4, HEG, LENS, RAM, T5, etc. will require one to several years more of regular calibration, operation, and practical testing before their envelope of useful performance can be clearly determined. They all represent very valuable but complex additions to our testing capabilities and in particular to our code validation capabilities.

Some observers have given very high marks to the Russian tunnels. They have received continuous attention and improvements over many years and, on paper at least, appear very promising. Questions still remain regarding instrumentation and data acquisition systems. Recently,

Dassault Aviation has conducted some trial tests at TsAGI and TsNIIMASH. A report has been prepared by Ph. Vancamberg which is reproduced in Appendix A. It seems clear that while more studies are needed, the Russian tunnels are clearly of interest but are not unique in concept.

6 ASSESSMENT OF INSTRUMENTATION

Experimental testing in hypervelocity flows must consider four basic parameters (Seibert et al. 1992):

- (1) The total temperature or enthalpy determines the maximum velocity attainable.
- (2) The total pressure determines the test pressure and, therefore, the altitude to be simulated and it has a profound effect on the nature of the test gas.
- (3) The size of the facility determines the largest model scale that can be used.
- (4) Test duration determines the type of instrumentation that can be used, the ability to "soak" structures in the hot flow and the relationship of the chemical relaxation times.

The following fluid properties need to be measured: pressure, P , density, ρ , temperature, T , the components of velocity, u , v , w , the stream or global velocity, U , and the sound speed in the flowing medium, a . Flow profiles of chemical species, X_i , ionization, and the transport properties: viscosity, μ , thermal conductivity, k , and diffusion, D_{ij} , must be measured or determined.

In order to provide the physical interpretation of the experiment, the following topics must be characterized.

Flow Patterns: Shock Shape, shock locations, boundary-layer transition locations, reattachment, boundary-layer thickness and profiles, and vortex patterns all significantly affect the determination of flight performance and ultimately the design of the flight vehicle.

Turbulence: Fluctuations in pressure, P' , density, ρ' , temperature, T' , and velocities u' , v' , w' , as well as frequency spectra and power spectral densities must be measured or determined. Since the determination of these parameters depends heavily on statistical analyses, extreme care must be taken in their measurement, estimation or calculation.

Thermodynamic States: Spectroscopic techniques must be employed to measure the state of the gases in conditions where physical probing is not feasible or would so adversely effect the measurement that the data could not be adequately corrected. Measurements include but are not limited to rotational lines, vibrational bands, luminescence, induced fluorescence, Rayleigh scattering, excited electronic states (electronic excitation), net charge, currents, and electron beam fields.

These measurements may be made in conjunction with or separately from forces and moments and heat transfer rates. In

addition, combustion requirements and effects must be considered if propulsive studies are to be made. All this must include measuring the parameters that describe performance in flight and those that describe deviations or departure from the flight conditions.

One of the driving forces behind the research and development of diagnostic techniques for hypersonic flows is the need to validate CFD codes (Marvin 1988). This is discussed in some detail in Section 3.

AGARD-CD-514, Theoretical and Experimental Methods in Hypersonic Flows, published in April 1993, extensively categorized the state-of-the-art in hypersonic diagnostics. A hypersonics mini-symposium, held at Wright-Patterson AFB in May 93 was the forum for update discussions on some of the technologies presented and discussed one year earlier at the AGARD meeting. This report, therefore, will concentrate on updating the activities that have occurred in the U.S. since the AGARD meeting.

Diagnostic developments in hypersonic flow measurements in the United States, since that symposium have reached, essentially, an evolutionary phase in their progress. Direct measurement of skin friction and heat transfer in rough and smooth surfaces were made in the Mach 6, high-Reynolds-number facility at WPAFB Wagner (1993). The direct use of skin-friction and heat-flow sensors gave performance levels of $\pm 6.0\%$ in the conventional heat-transfer coefficient and $\pm 0.2\%$ full scale (nonlinearity and hysteresis) in shear-stress measurement.

Also at Wright Laboratory, LDV measurements were accomplished at $M = 6$ and $M = 12$ in the cold-gas facilities in the Flight Dynamics Directorate (Maurice 1993; Schmisser and Maurice 1994). 2-LDV measurements were made in a Mach 6 flow over and through a generic hypersonic inlet model where the flow had been calculated using a Navier-Stokes code. Particle response through oblique shocks was corrected for particle lag and comparisons were made with the CFD solutions showing good agreement where there was no shock-wave/boundary-layer interaction but a significant discrepancy existed internally in the nozzle where the shock-wave pattern was complex. Pressure distributions on the cowl and ramp matched the CFD solution, indicating the danger of just matching pressure distributions with the CFD solution.

Additional measurements in the 20-inch Mach 12 tunnel were made in the shear layer at the nozzle exit in the freestream and behind the shock on a cylinder model injected into the flow. CFD solutions of the nozzle flow field were made using a full N-S solution in the throat region, a PNS code in the expansion section and an Euler scheme in the free-jet portion of the test section. A notable result of the work showed that the alumina seed, regardless of size, never reached the theoretical freestream velocity even though it had three meters of nozzle length within which to equilibrate.

Other particle techniques that have emerged include an LV system proposed by Smeets which is being developed at

NSWC for their hypervelocity facilities. This technique allows the use of submicron size particles and since it incorporates a spectrometer with a one microsecond response, the measurement of highly turbulent flow is possible.

A technique proposed for propulsion testing in HYPULSE at GASL involves seeding the H_2 plenum chamber with Silane and some O_2 , which then spontaneously burns creating SiO_2 as a by-product in the submicron size range. A long-pulsed, flash-lamp, pumped-dye laser with a 50 μs pulse width, giving 150 mm of flow passing through the sheet, is used to track the flow using Mie scattering. This gives the opportunity to observe mixing and also relate concentrations to intensity to get time averaged measurements of the H_2 mass fraction. CFD calculations are also being made. Standard video cameras are being used to prove the concept before going to higher resolution optics. A practical problem is the vaporization of the SiO_2 at very high temperatures causing data drop out.

Efforts at AEDC include PLIF imaging in the Mach 8-14 impulse facility, imaging NO to determine concentration and temperature and also doing non-absorptive Rayleigh scattering to determine He arrival. Dual pulse LIF is planned for the next fiscal year. Work will also be done in Tunnel B at Mach 8 measuring jet-interaction phenomena using LIF of NO looking at parts/trillion.

Later this year a dual line LIF system using O_2 in the H2 facility measuring temperature and density and LIF velocity measurement using atomic copper also in H2 will be attempted. Plans also included the use of a pulsed e-beam in H2 to measure densities. AEDC has also looked at flow fields in shuttle engines using naturally occurring sodium in the hydrogen, where the sodium is vaporized in the hot hydrogen and imaged. One can scan the laser and then measure temperature, density, and pressure.

Boeing is continuing to pursue PLIF measurements in their shock tunnel looking at large NO concentrations (1% or more) to enhance signal levels. Quantitative measurements of temperature and density are being sought. Coaxial thermocouple heat transfer gauges are being used instead of thin-film gauges due to reliability. Iron-constantan gauges are used in steel models or plugs are used in aluminum models.

The LENS facility at CALSPAN is using advanced version of pulsed e-beam and LIF technologies to probe the flowfield for measurements of temperature and density (Calspan 1991).

NASA Ames is continuing development of optical techniques in their 16-inch Shock Tunnel including an optical-probe layout in a scramjet model looking at the Raman scatter of nitrogen (Cavolowsky et al. 1993). NASA Ames is also looking at two classes of laser systems that are being developed and applied to absorption measurements of the critical species O_2 , OH and H_2O in hypersonic reacting flow. An Argon-ion pumped tunable ring-dye UV laser system at 306 nm probing OH has been tested.

Also under development are two laser-diode systems; one for the measurement of O_2 in the near IR at about 760 nm and the other for the measurement of H_2O , also in the IR at about 1385 nm. These systems have great potential for flight-vehicle application since they are small and rugged. The systems have all been validated in shock tube experiments simulating pressures, temperatures, and velocities applicable to hypersonic simulations. OH mole and temperature was measured in an expanding nozzle flow in the 16-inch Shock Tunnel at a simulated flight Mach number of 14.

Flow-visualization techniques included double-pulsed laser holographic interferometry in the Ballistic Range Facility at a Mach number of 14.4 (Tam et al. 1991). "Synthetic" infinite fringe interferograms are also calculated to examine the intensity pattern of the experimental finite fringe interferogram. These results show flow features in the wake region not found on the experimental interferograms.

Work is ongoing for the development of Resonant Holographic Interferometry Spectroscopy Tomography (RHIST) flow diagnostics of hypersonic flows and combustion. RHIST will be used to quantitatively measure OH concentration in a combustor flows.

NASA Langley is continuing to pursue their CARS technique for the measurement of temperature and species in scramjet flow.

NASA Langley is also testing the use of modulation absorption spectroscopy for their 8-foot High Temperature Hypersonic Tunnel to perform scramjet thrust tests, measuring gaseous concentration and temperatures. Both amplitude modulation spectroscopy and wavelength modulation are being tested. Infrared absorption spectra of constituent gases by using diode lasers is measured. Test-cell results measure changes in oxygen concentration of 0.1% using the $X^3\Sigma_g^- \rightarrow b^1\Sigma_g^+$ transition. Raleigh imaging is being used at Langley looking at condensate fog in the $M = 6$ realm where velocity can be measured.

In Europe, work continues in the application of spectroscopic diagnostic techniques to studies on HEG in Göttingen (Bech et al. 1993). LIF measurements have been carried out in the vacuum wind tunnel V2G in Göttingen, the arc-heated tunnel LBK in Cologne, and on the shock tunnel TH2 in Aachen in preparation for measurements in HEG. Emission spectra over the range of 200-850 nm from the hot gases behind a model bow shock has been carried out. NO excitation spectra were measured in V2G and LBK with temperature and NO concentration being measured in the freestream in LBK.

Freestream temperature and NO concentration were also measured in TH2 using a single-shot, two-line measurement. Early emission spectra in HEG shots with nitrogen reevaluated that a major limiting species was atomic iron (FE) requiring the introduction of a copper liner in HEG to prevent the ablating wall effect.

Other work in Göttingen using LIF with an ArF excimer laser (192.8-193.8 nm) in V2G using 90% He + 10% NO and

90% N_2 + 10% NO revealed the rotational temperatures of NO and O_2 at low densities (Grundlach and Hirai 1993). Rotational-temperature measurements were made near a hot copper model of the reflected NO molecules coming back from the surface at nearly free-molecular conditions. Results show a significant deviation from total accommodation at surface temperatures $T_w > 600$ K where the results indicate that the gas surfaces can be studied by LIF spectroscopy.

A study has been conducted at the Von Kármán Institute looking at the application of Particle Image Velocimetry (PIV) in hypersonic facilities (Moraitis and Simeonides 1993). Mie scattering calculations indicate that very small particles, with a diameter of 50 nm or smaller can be detected with readily available lasers and films. Problems from flow contamination by foreign particles would have to be investigated.

ONERA has conducted tests on a heat flux measurement technique based on a luminescence coating in their R3CL Hypersonic Blowdown Wind tunnel at Mach 10 (LeSant and Edy 1993). Tests were performed at a stagnation pressure of 12.5 MPa and a stagnation temperature of 1050 K. Work was done using a model made of insulating material since the coating has insulating thermal properties. The technique must be proven on metal models to allow for standard temperature measurements.

Work at Caltech in their shock tubes/shock tunnels is being done with PLIF techniques using multiple lines in the same shot looking at more complex flows. Measurements are being made to study chemical effects on boundary-layer stability, boundary-layer transition and on nonequilibrium flows. Resonant Holography is being used to take holograms of flows that are resonating in some species like O_2 or NO and capturing shock structures.

Rayleigh imaging is being considered by several researchers but whether it works in the low densities of hypersonic facilities is questioned. One approach is to use multiple-reflecting-mirror sets where one passes the laser beam time and again through the flow and then raster down to take an image. This way one increases laser power by 10 or 20 to compensate for low signal levels. This combined with filtered Rayleigh scattering can eliminate the background scattering from windows and walls.

Another technique getting another look is sodium laser induced fluorescence previously called Resonant Doppler Velocimetry. In heated facilities, which have sodium and copper, one can look at laser induced fluorescence from these species and get good images of the flow structure. One can look at flows with sodium in the parts per billion range.

Many other diagnostic concepts and variations of existing techniques are under development or test in various centers around the world. The evolutionary process for diagnostic development continues in all speed regimes; whether it continues to expand in hypersonic facilities will be dictated by rapidly changing events.

7 FUTURE FACILITY NEEDS

7.1 Results of American Studies

Potential future missions planned by the Americans involving hypersonic flight (air-breathing access to orbit/hypersonic cruise/planetary and earth entry/aerobraking) will require ground-test capabilities for aerothermodynamics testing which cannot be met with simple modifications to existing facilities. Further, some of the required technologies and methodologies for new facilities which can meet the requirements are not in place. This shortfall has led to advocacy within the United States for substantial investments in "facilities research" which will ensure the efficient design/construction/operation of the next generation of U.S. hypersonic facilities.

The following is a synopsis from the aerothermodynamics section of the December, 1992 United States Department of Defense/NASA Hypersonics Test Investment Plan (HTIP). This plan is for U.S. Government use only, but the following synopsis has been approved for inclusion in this AGARD document by the HTIP Co-Chairs K. Richey (USAF) and Wayne McKinney (NASA). According to the HTIP report, facilities filling the anticipated needs for aerothermodynamics in the near, mid and far term are specified below:

Near Term: Research should be done to enable the implementation of a large-scale, advanced expansion-tube/shock-tunnel to be used for study in the true-enthalpy flight regime of Mach 16 - 20+. Real-gas effects could be studied in air and planetary atmospheres. The facility would employ the double-diaphragm, shock-tube approach where energy is added to the moving stream as depicted in Figure 22. Arbitrary test gases can be used and, ideally, low dissociation will be experienced in the freestream because the flow is not stagnated. In full scale, this facility would use a 610 mm diameter free-piston driver, a 1.52 m diameter test section, and would have test times of approximately 2 ms. Early research for this facility would include analysis of driver options as well as issues of losses/disturbances and unwanted dissociation effects associated with the secondary diaphragm. The research will include CFD and experimental studies in existing small expansion tubes.

Mid term: Studies are advocated to proceed pre-construction of a large facility with several second flow duration at Mach 16+ equivalent enthalpies in a 1.52 m test section. These flows would be driven by a reservoir with temperatures and pressures of 8000 K and 14000 atm, respectively. Facility research would focus early on exploring an extension of the Russian approach to increasing flow time in impulse facilities by using the type of driver depicted in Figure 23. This driver, called a Piston Gasdynamics Unit (PGU), is operational at the TSNIMASH research center (Anfimov 1992; Anfimov and Kislykh 1990) and uses special valves between a piston and the stagnation chamber to subject the test gas to multiple shock passage/heating cycles. Early research on this facility would include analysis of nozzles which minimize reservoir

dissociation products (*O* and *NO*) in the test section as well as studies of materials which can withstand formidable heat transfer to the accumulators, valves, stagnation chamber and nozzle throats.

Far term: Research includes work on a large ballistic range which would employ large (up to 300 mm diameter) models up to 15 km/s with advanced on-board and non-intrusive instrumentation. A major research issue here is a model launcher. Possible solutions are the University of Washington's "Ram accelerator" and the Russian TSNIMASH approach with an evacuated tube and timed explosives on walls to accelerate the model (Figure 24 from D. Wilson at University of Texas at Austin). Advantages of ballistic ranges for aerothermodynamics are well documented in Witcofski et al. (1991).

Finally, the general feeling in the U.S. documented in the HTIP report is that new, innovative ideas for hypersonic facilities should be nurtured. An example is the high pressure, cryogenic arc concept as described by Rizkalla et al. (1992).

The United States Air Force Scientific Advisory Board, SAB, (May 1989) document also is available only to U. S. Government Agencies. The recommendations listed therein are consistent with those discussed in the HTIP report outlined above. The SAB report recommended that research on large arc jet wind tunnels be conducted at the NASA Ames Research Center and at the Arnold Engineering and Development Center, and this is being done, albeit at low levels.

7.2 Results of European Studies

An ESA study was initiated in the early 1980's to assess the level of European competence in hypersonic facilities and computational tools required for the design of specific two-stage launchers to LEO. Recommendations were made which concentrated on bringing back into useful operation a series of tunnels that had been constructed in the 1960's. Many of the recommendations were put into effect as the Hermes program developed. However, to the author's European knowledge (J. F. W.), no more recent ESA study looking toward an entire series of missions involving hypersonic flight has been commissioned.

Except for a thermal protection testing facility called Sirocco which is under construction, no new facility is currently planned in Europe for high enthalpy aerodynamic studies. The efforts will be devoted in the short term to get fully in line the HEG and F4 wind tunnels and to develop appropriate flow diagnostic methods.

The time is not well chosen to consider the possible development in the longer term of new facilities. There is certainly no money available in the foreseeable future for new developments of large size, and there is not even enough activity to keep the present facilities busy. As far as facilities are open for industrial testing, any new duplication should

certainly be avoided within NATO in order not to decrease further the workload of each facility.

However one should keep in mind, when looking at the technical needs, that the development of such facilities take 5 years if on a national basis, and up to 15 years if in the frame of an international agreement. Therefore it is still time for AGARD to think about technical needs for future hypersonic aerodynamics facilities, as far as really new needs are identified, or new opportunities appear to fulfill unsatisfied needs. Selected authors have expressed their personal views (Muylaert et al. 1992; Wendt 1992; Kuczera and Weingartner 1993; Hirschel 1993).

The long-term objective should be seen as full flight simulation with clean equilibrium flows to Mach 16-18 and constant conditions for at least some tens of ms. It is clear that much effort must be expended in the interim on such areas as :

1. specially-designed code validation tunnels (e.g. the iodine vapor facility of Pham-Van-Diep et al. 1992);
2. the "hot-model" technique for radiation dominated flows.
3. transition triggering mechanisms, so that a rational decision concerning the need for a "quiet" hypersonic tunnel can be made;
4. instrumentation to reliably measure all appropriate temperatures and constituent concentrations with sub-ms response times in the harsh environment of real facilities;
5. techniques to add energy to a flowing gas, e.g. by lasers, to avoid the need of stagnating the flow;
6. large-scale ballistic ranges and associated instrumentation; e.g., the ram accelerator method.

8 RECOMMENDATIONS ON POSSIBLE AREAS OF COOPERATION AND POTENTIAL BENEFITS

The benefits of collaboration will be more pronounced if a specific joint project(s) can be defined; at the present time, only Huygens/Cassini is firm and collaboration on the aerothermodynamic issues is not part of the accord.

However, members of the AGARD WG 18 hope that the future will bring one or more joint projects involving Earth or planetary entry. Prior to this time, a certain number of actions will be very useful as precursors to an eventual joint project.

Based on the perspective of the space transportation and space vehicle programs considered by Europe in the near and far future, ESA should initiate a comprehensive study on Europe's needs for new facilities; the study should take into account opportunities offered by CFD to supplement experimental tools. It should also take into account the facilities existing worldwide and the effective possibility to use them for development purposes. The results of this study should be confronted within AGARD in a manner similar to the studies performed in the U.S. The role of flight testing in design tool validation should be analyzed together with the AGARD community. The result of these studies should bring

near-term, mid-term, and long-term recommendations and may bring forward a basis for a possible collaborative effort on an international scale.

Within the limited travel funds available, AGARD-FDP-sponsored Symposia, workshops, professional visits, etc., should focus on real-gas hypersonics. Stress should be put on experiences with testing techniques in the recently-developed real-gas facilities such as T5, LENS, 16-inch, Electric Arc-Driven Shock Tube, HEG, F4, etc.

Exchanges of experience with Russian hypersonic facilities to understand their potential should be undertaken in cooperation between Russian, Western European and Americans. This will serve to ensure that critical decisions at a later date concerning the possible construction of new facilities in the West versus the use of existing Russian facilities can be made with full background knowledge and confidence.

9 SUMMARY

Missions of current and future interest to the United States and Europe which involve hypersonic flight within or entry into the atmosphere of the Earth or other planets have been summarized. Aerothermodynamic issues such as heating and chemical reaction rates which arise because of the high flight velocities have been discussed.

The problems posed for the simulation of these effects in ground-based facilities can be summarized as follows. It should be clear that at present that a wide variety of facility types is required to simulate, even partially, the expected effects. As a result, Computational Fluid Dynamics is an essential tool in the regime, assuming that the codes can be fully validated by means of appropriate experiments on the ground and in flight.

A number of new facilities have been developed in recent years for the express purpose of addressing the crucial aerothermochemistry problems posed by hypervelocity flight. These facilities are still the "shake-down" phase, as are the non-intrusive instrumentation techniques which have been introduced to provide a clearer understanding of the flow conditions which characterize these tunnels.

Recommendations for the near and mid-term are:

Various agencies in the United States have conducted individual or joint studies on future facility needs; a similar study should be undertaken by the European Space Agency.

AGARD symposia, workshops, lecture series, etc. will also serve as a mechanism to bring researchers interested in hypersonic flight together for an exchange of ideas and experiences. The AGARD WG 18 will be an important part of this activity.

A continuing effort should be made to understand Russian Facilities and their methodology of testing and design. This activity should be a cooperative one between Western Europeans, Americans and the Russians.

ACKNOWLEDGMENTS

The following persons have made important contributions to this chapter: W. Calarese of WPAFB (Section 4, Russian facilities), P. Vancamberg of Dassault Aviation (Section 5), and G. Siebert of WPAFB (Section 6). Acknowledgment is also made to G.S. Deiwert of NASA Ames for many useful discussions.

REFERENCES

- AGARDograph 138 1970 Ballistic Range Technology. Ed. Thomas N. Canning, Alvin Seiff, and Carlton S. James.
- Anfimov, N. 1992 TSNIMASH Capabilities for Aerogasdynamic and Thermal Testing of Hypersonic Vehicles. *AIAA Paper 92-3962*.
- Anfimov, N. A. and Kislykh, V. V. 1990 Multi-Cascade Compression Effective Means to Obtain High Temperature Dense Gas in Piston Gas Dynamic Units (PGU). In Current Topics in Shock Waves. *Proc. 17th Intl. Symp. on Shock Waves and Shock Tubes*.
- Bech, W. H., Miller, M., and Wollenhampt, M. 1993 Application of Spectroscopy Diagnostic Techniques to studies on HEG; Preparatory LIF Work and Emission Spectroscopy Results. *ICIASF '93 Record, ISL, France*.
- Calspan-UB Research Center 1991 Large Energy National Shock Tunnel (LENS) Description and Capabilities.
- Cavolowsky, et al 1992 Flow Characterization in the NASA Ames 16 Inch Shock Tunnel. *AIAA Paper No. 92-3810*.
- Cavolowsky, J. A.; Newfield, M. E., Loomis, M. P. 1993 Laser Absorption Measurement of OH Concentration and Temperature in Pulsed Facilities. *AIAA Journal, Vol. 31, No.3*, pp. 491-498.
- Chapman, Gary T. 1992 The Ballistic Range-Its Role and Future in Aerothermodynamic Testing. *AIAA Paper No. 92-3996*.
- Gochberg, L.A. 1993 Rotational Nonequilibrium in Low Density Heated Free Jet Expansions of Nitrogen. *Ph.D. Dissertation*, University of California, Berkeley.
- Grundlach, G., Hirai, E. 1993 Rotational Temperature on NO and O2 in Hypersonic Free Test Flows Near a Hot Model Surface Measured by LIF. *ICIASF's 93 record ISL, France*.
- Haas, Brian L., and Schmitt, Durwin A. 1993 Simulated Rarefied Aerodynamics of the Magellan Spacecraft During Aerobraking. *AIAA Paper No. 93-3676*.
- Hirschel E.H., Deutsche Aerospace Munchen 1993 Hypersonic Aerodynamics. *2nd Space Course on Low Earth Orbit Transportation*. Munich Univ. of Technology.
- Hirschel, E. H. 1991 Aerothermodynamic Challenges of the Sanger Space Transportation System. *ESA Paper No. SP-318*.

- Hornung, H. 1992 Performance Data on the New GALCIT Free Piston Shock Tunnel. *AIAA Paper 92-3943*.
- Howe, John T. 1990 Hypervelocity Atmospheric Flight: Real Gas Flows. *NASA reference Publication 1249*.
- Kuczera H., Weingartner S., Deutsche Aerospace Munchen 1993 Guidelines for the Selection and the Design of Future Space Transportation Systems. *2nd Space Course on Low Earth Orbit Transportation*. Munich Univ. of Technology.
- LeSant, Y., Edy, J. L. 1993 Phosphor Thermography Technique in Hypersonic Wind Tunnels; First Results. *ICIASF '93 record, ISL, France*.
- Lumpkin, Forrest E. III and Chapman, Dean R. 1991 Accuracy of the Burnett Equations for Hypersonic Real Gas Flows. *AIAA Paper No. 91-0771*.
- Marvin, J. C. 1988 Accuracy Requirements and Benchmark Experiments for CFD Validation. *AGARD CP-437*.
- Maurice, M. S. 1993 Quantitative Laser Velocimetry Measurements in the Hypersonic Regime by the Integration of Experimental and Computational Analysis. *AIAA Paper No. 93-0089*.
- Maus, J. R., Laster, M. L., and Hornung, H. G. 1992 A High Performance Free Piston Shock Tunnel. *AIAA Paper No. 92-3946*.
- Moraitis, C. S., Simeonides, G. A. 1993 Application of Particle Image Velocimetry to Hypersonic Flows; Perspectives and Impedimenta. *ICIASF '93 Record, ISL, France*.
- Muylaert J., Voiron R., Sagnier P., Lourme D., Papirnyk O., Hannemann K., B8tefisch K., Koppenwallner G. 1991 Review of the European Hypersonic Wind Tunnel Performance and Simulation Requirements. *ESA Paper No. SP-318*.
- Park, C. 1990 Nonequilibrium Hypersonic Aerothermodynamics. *John Wiley & Sons*.
- Pham-Van-Diep, G. C. Muntz, E. P., et al. 1992 An Iodine Hypersonic Wind Tunnel for the Study of Nonequilibrium Reacting Flows. *AIAA Paper No. 92-0566*.
- Rizkalla, O.; Chinitz, W.; Witherspoon, F. D. and Briton, R. 1992 High Pressure Hypervelocity Electrothermal Wind Tunnel-Performance Study and Subscale Tests. *AIAA Paper No. 92-0329*.
- Schmisser, J. D., Maurice, M. S. 1994 An Investigation of Laser Velocimetry Particle Behavior within Flow Structures at Mach 12. *AIAA Paper No. 94-0668*.
- Seibert, G. L., Miles R., Van Kuren, J., Heath, W. 1992 Optical Measurement Techniques for Hypervelocity Flows. *AIAA Professional Studies Series Notes*.
- Sharma, S. P. and Park, Chul 1990 A Survey of Simulation and Diagnostic Techniques for Hypersonic Nonequilibrium Flows. *J. Thermophysics and Heat Trans. Vol. 4, No. 2*, pp. 129-142.
- Tam, T. C.; Brook, N. J, Cavolowsky, J.A., Yates, L. A. 1991 Holographic Interferometry at the NASA Ames Hypervelocity Free-Flight Aerodynamic Facility. *AIAA Paper No. 91-0568*.
- Wagner, M. 1993 Skin Friction and Heat Transfer Measurements in Mach 6 High Reynolds Number Flows. *ICIASF '93 Record, ISL, France*.
- Wendt J.F. 1992 A Review of European Hypersonic Facilities. *Proc. of Wind Tunnels and Wind Tunnel Test Techniques*.
- Wilson G., S.P. Sharma, W.D. Gillespie 1993 Time-Dependent Simulations of reflected-Shock/Boundary Layer Interaction. *AIAA Paper No. 93-0480*.
- Witcofski, R.; Scallion, W.; Carter, D., Jr., and Courter, R. 1991 An advanced Hypervelocity Aerophysics Facility: A Ground-Based Flight-Test Range. *AIAA Paper No 91-0296*.

APPENDIX A

DASSAULT AVIATION TESTING ON HERMES MODELS IN RUSSIAN TUNNELS TsAGI T-117 AND TsNII U 7: COMPARISONS WITH ONERA S4 Ma RESULTS

M. Philippe Vancamberg

Dept. d'Aerodynamique Theorique
Dassault Aviation
78 Quai Marcel Dassault
92214 SAINT-CLOUD
FRANCE

A1 INTRODUCTION

The frame of the European Space Programme HERMES, Dassault Aviation was responsible for the aerodynamic design of the vehicle. This responsibility led Dassault Aviation to define and follow-up aerodynamic and thermal tests to be performed in Russia due to the new political situation. The choice of the institute was performed after an analysis of the existing facilities. After selection of two of them, it was decided to set a first program to start the cooperation. The technical goals of this program were not very ambitious but it was set in order to build a first round of cooperation between Russia and Europe in the hypersonic field for reentry vehicles.

A2 DESCRIPTION OF THE SELECTED FACILITIES

Two Russian facilities have been selected to perform aerodynamic and thermal tests for hypersonic conditions. The reasons that led to this choice are that T117 has been the working horse for the Buran aerodynamic and thermal identification and in addition, it covers aerodynamic conditions that can be made in the French S4Ma wind tunnel from ONERA that is also the work horse for the Hermes identification. Concerning the thermal identification, it seemed that the TsNII-MACH U7 could offer similar techniques to the ones used in Europe, but also with different model techniques.

A2.1. TsAGI T117

T117 is an electric-arc-heated facility. Its stagnation temperature can reach 2600 K and it operates at stagnation pressures up to 160 bars. The Reynolds number $7.5 \times 10^4 \text{ m}^{-1}$ to $6 \times 10^6 \text{ m}^{-1}$. This facility is running with air and the testing time can vary from 1 to 3 minutes, depending on the exhaust system that is used. The wind tunnel is equipped with different contoured nozzles that provide "fairly uniform flow field" for Mach numbers ranging from 10 to 20 (10, 12, 14, 18 and 20.5). The exit nozzle diameter is equal to 1.0 m that gives a core of roughly 0.65 m at Mach 10. Pollution in this facility is relatively low and models sustain very little damage during the tests. This feature is interesting since most of the

hypersonic facilities have problems with pollution and sand blasting of their models.

A2.2 TsNII-MACH U7

U7 is a heavy-piston driven facility. The maximum stagnation temperature that can be reached is of the order of 3500 K. The Reynolds number can vary from $2.5 \times 10^5 \text{ m}^{-1}$ to 10^7 m^{-1} . This facility runs with nitrogen and the testing time is equal to 0.3 s which is rather long for this type of facilities. The wind tunnel is equipped with different contoured nozzles that provide Mach numbers ranging from 10 to 20. The exit diameter is slightly smaller than for T117 but the size of the core stays above 0.4 m at Mach 10 allowing to tests similar size models than in T117.

Tests in TsNII-MACH are only devoted to thermal measurements. They have a good knowledge and capability in infrared thermal studies. They use an AGEMA camera running at 25 frames per second.

A3 DEFINITION OF THE TESTS

A3.1 TsAGI T117

Tests performed by TsAGI in the T117 wind tunnel used a 1/40 Hermes "0.0" model. They were divided in two parts. The first one deals with force and moment measurements and the second with thermal identification.

The stainless steel model was provided to TsAGI by the European side. It is sting mounted. The sting holds the six component balance that will measure the aerodynamic forces and moments. Different configurations with different flap settings have been tested up to large deflection angles. Angle of attack has been varied from 16° to 50° and side slip from -8° to $+6^\circ$ allowing a complete survey of the vehicle behavior.

The flow parameters that have been selected are the following:

Mach number:	10.5
Reynolds number:	1.6×10^6
(reference length 0.3875 m)	
Stagnation pressure:	95 bars
Stagnation temperature:	1200 K

It can be noted that for this set of experiments, the conditions are quite far from the limits that are claimed (in theory) for this wind tunnel but these conditions served best the comparison with existing European facilities.

For the thermal identification, only one geometric configuration has been retained and the corresponding model has been made by TsAGI in insulating material. A deflection angle was defined for each flap in order to get heat fluxes data on deflected surfaces which is a critical problem for hypersonic vehicles. The elevons and body-flap were deflected 10° downwards and the winglet rudder 15° outwards it has been equipped with a few thermocouples (around 20).

The measurements of the heat fluxes have been performed by two different means: thermocouples and thermosensitive paints.

Two different flow conditions have been retained for the tests. The first one is similar to the one for aerodynamic identification and the second one is as follows.

Mach number:	14.0
Reynolds number:	0.29×10^6
(reference length 0.3875 m)	
Stagnation pressure:	94 bars
Stagnation temperature:	1830 K

Angles of attack varied from 30 to 50° for the Mach 10 case and 30 to 40° for the Mach 14 case. In addition, only thermocouple measurements were performed at Mach 14.

A3.2 TsNII-MACH U7

The tests performed in U7 are only related to the thermal behavior of Hermes "0.0". Two different models at two different scales (1/40 and 1/90) were made by TsNII-MACH in an insulating material. A deflection angle was defined for each flap in order to get heat flux data on deflected surfaces. The elevons and body-flap were deflected 10° downwards and the winglet rudder 15° outwards. The models were sting mounted and rotations could be achieved in order to have the best view angle for the infrared thermal mapping device.

Tests were performed at Mach 10 and 14. Reynolds number based on the model reference length ranged from 1.8×10^6 to 2.8×10^6 . Angle of attack was varied from 30° to 50° and side slip from -5° to 0° allowing a good survey of the vehicle behavior.

A4 RESULTS

TsAGI and TsNII-MACH have produced good quality reports concerning the results and also the test techniques. Only a few results that demonstrate best the Russian capabilities will be discussed in the following sections.

In general, Russian results compare well with the ones obtained in western Europe facilities. The comparison done for the pitching moment of a Hermes space plane show results from S4Ma (ONERA) at two different Reynolds numbers that are in very good agreement with the T117 (TsAGI) ones for the whole range of angle of attack. This comparison on this sensitive parameter shows that the basic tests on a space plane (i.e. cold hypersonic force and moment measurements) give satisfactory answers. More interesting than the results themselves, are the procedures and devices that are used by the Russians in order to get more convenient and reliable results. Among others one can quote the capability to make flow field calibration very often.

Comparisons have also been performed for the thermal behavior of the space plane. Different model techniques have been used for these tests (thermocouples and infra-red

recording). Taking into account the different possibilities of scatter (geometry definition, accuracy of each method,...) one can say that the agreement between the different results is quite good. In a similar way to the force and moment campaign, the thermal tests have allowed to investigate the effects of different techniques that have been used to design and qualify a space vehicle. This is the case, for example, for insulating models compared to metallic ones for thermal measurements, or for infrared thermography in impulse facilities. Another interesting feature is the short injection time of the model into the flow field that allows to minimize the transient effects on the thermal parameters due to the crossing of the edge of the stream.

A5 CONCLUSION

The first tests that have been performed in Russia (TsAGI and TsNII-MACH) have proved to be successful. The results have been obtained correlated well with the ones obtained in similar conditions in western Europe. In addition, the long habit of hypersonic studies and especially testing have lead to specific procedures and devices that improve the accuracy and the confidence in the results.

However, this first series of tests cannot be considered as the best they can achieve since, the experimental program was aiming at comparisons on basic configurations and test cases. This cooperation has allowed to have a better idea of the possible capabilities of these two Russian institutes in the hypersonic field. This is the reason why a follow-on of the activities has been set in order to deeper investigate in the possibilities they can offer. Different ways have been selected among which one can quote:

- detailed thermal measurements on complex geometries such as canopy area, gaps between flaps or Thermal Protection System.
- extended simulation ranges in terms of Mach number, Reynolds numbers in order to investigate the effect of these parameters.
- High altitude jet interaction from the Reaction Control System with the external flow field. These tests have not been performed yet but they are funded and should be finished by mid 1994.

(b)

MODEL LENGTH SET
EQUAL TO ONE-HALF
NOZZLE DIAMETER

ReL

10⁸

6

2

10⁷

6

4

2

10⁶

6

4

2

0 5 10 15 20 M

NLR SST

BAe GW

RAE LUDWIG

FFA

RAE 3'-L

DLR-G B

IC No 2

S4MA

VKI

LONGSHOT

DLR-G C

HORUS

HERMES ENTRY

FL

LRBA

TH2

HEG

ONERA Rech 2,3

SCRAMJET ASCENT

The graph, titled "Reentry trajectory Non-dimensional", plots the Log length ratio $\log(X_d/L)$ on the y-axis (ranging from -6 to 2) against the non-dimensional parameter $(0.5v^2)/D$ on the x-axis (ranging from 0.0 to 1.0). A solid black curve represents the "HERMES" trajectory. A dashed line represents the "FRODO" trajectory. A horizontal line at $\log(X_d/L) \approx -1.5$ is labeled "F4". A shaded region is labeled "P4". A region labeled "Frozen flow" is above the dashed line, and a region labeled "Equilibrium flow" is below it. A legend indicates that 'X' marks represent "HEG Exp." and the shaded regions represent "Free-Piston-Driven" (horizontal lines) and "Hot-Shots" (diagonal lines). The curve rises sharply after $(0.5v^2)/D \approx 0.8$.

Figure 3. Simulation Capabilities with Respect to Gas Dissociation.

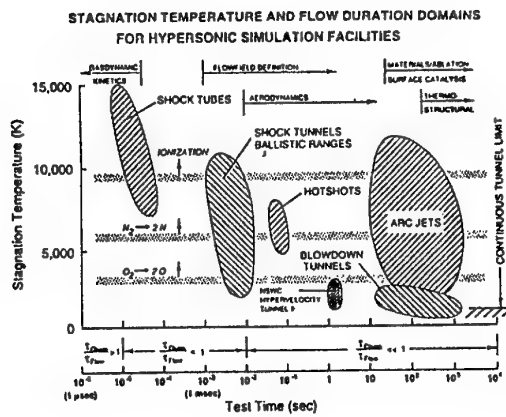


Figure 4. Stagnation Point Temperatures and Flow Duration Domains For Hypersonic Simulation Facilities.

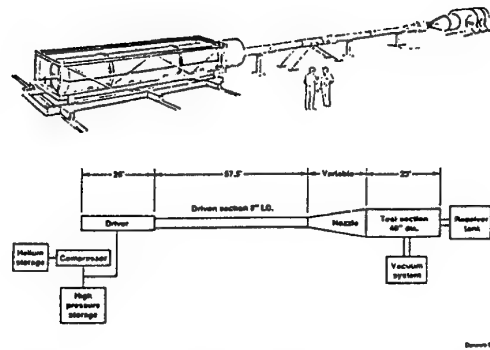


Figure 6. Basic Components of the LENS Hypersonic Shock Tunnel.

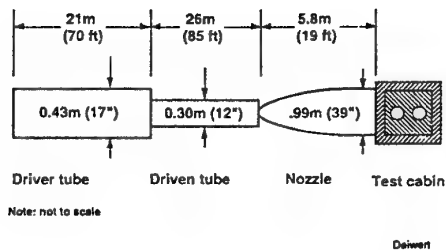


Figure 5. Schematic of NASA Ames 16-Inch Shock Tunnel.

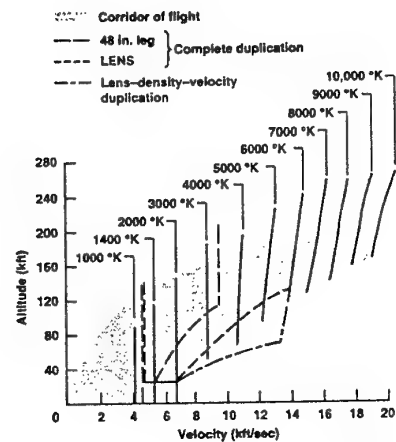


Figure 7. Performance Range of Calspan Hypersonic Shock Tunnel.

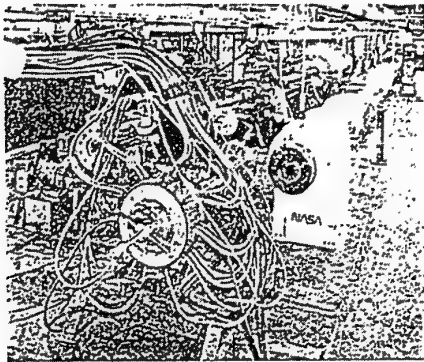


Figure 8. NASA Ames Electric Arc Shock Tube.

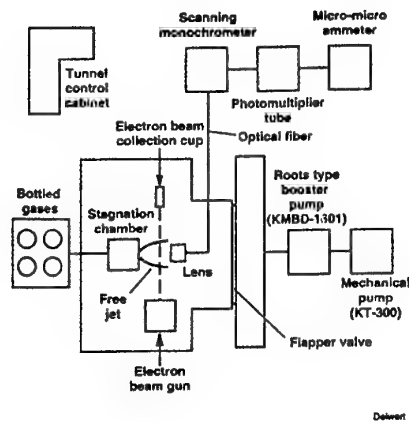


Figure 10. Schematic for University of California at Berkeley Low Density.

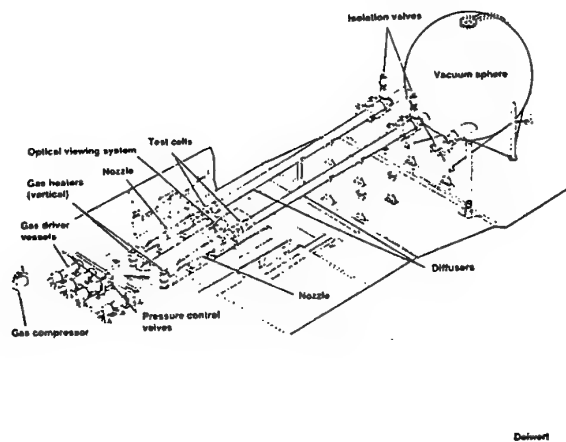


Figure 9. Naval Surface Warfare Center Hypervelocity Tunnel Number 9.

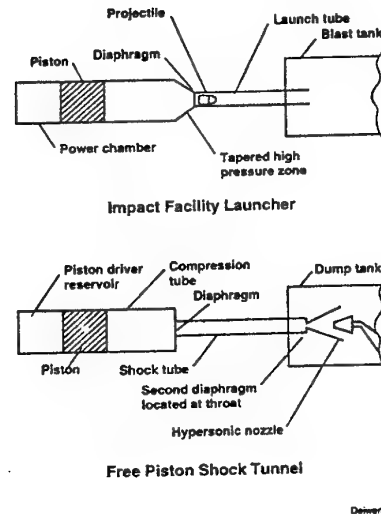


Figure 11. Comparison of Light-Gas Gun and AEDC Concept for Disposable-Piston, High Performance Shock Tunnel.

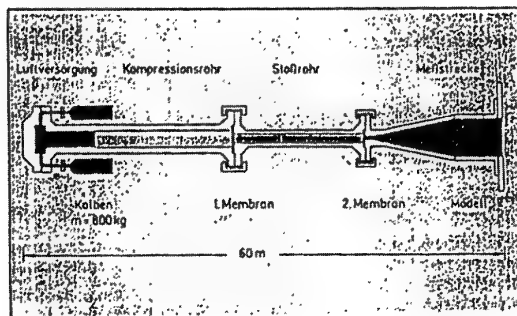


Figure 12. Sketch of the HEG DLR Free Piston Shock Tunnel in Goettingen.

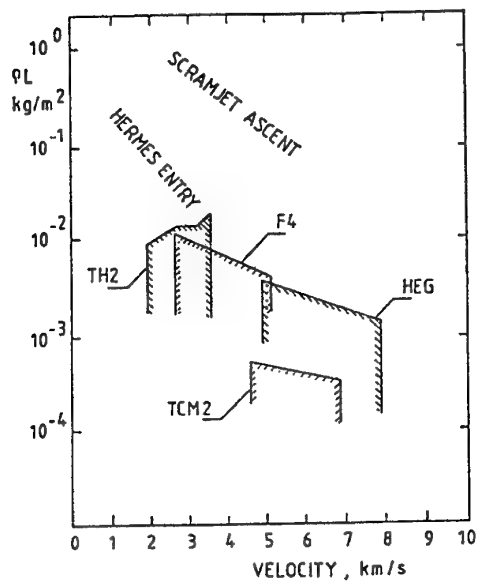


Figure 13. HEG Performance and HERMES reentry Trajectory.

ONERA Large testing facilities high enthalpy wind tunnel F4

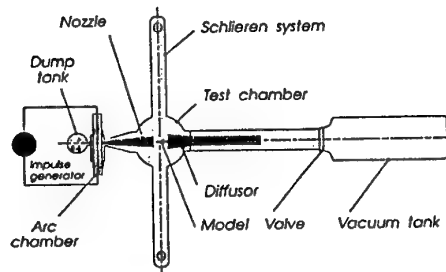


Figure 14. The ONERA High Enthalpy Wind Tunnel F4.

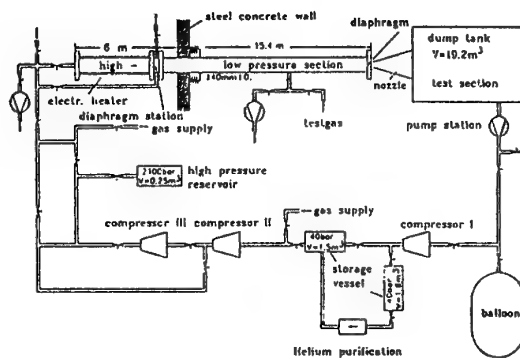
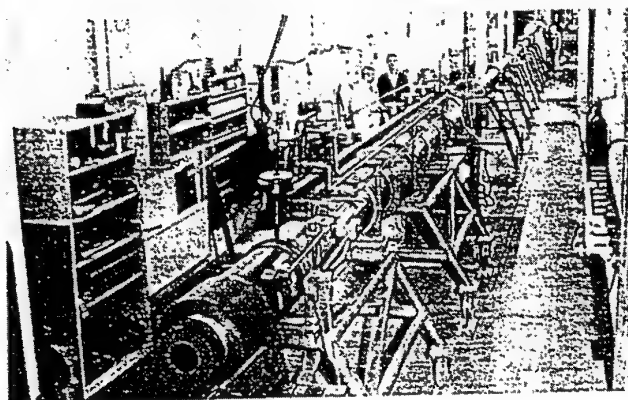
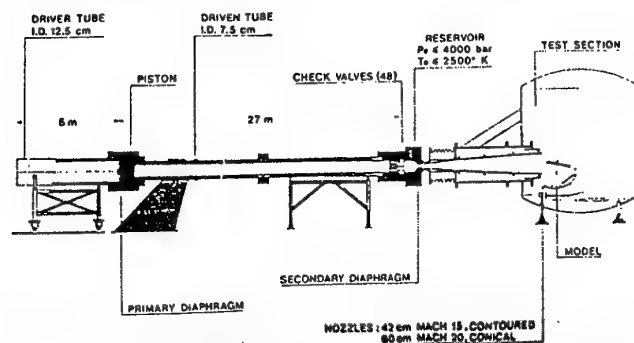


Figure 15. Basic Components of the Aachen Shock Tunnel TH2.

MACH 14 LONGSHOT FREE PISTON HYPERSONIC WIND TUNNEL



The VKI Longshot free piston tunnel is a short duration facility operating with nitrogen and designed for the attainment of very high Reynolds number hypersonic flows. It has a Mach 14 contoured nozzle of 0.43 m exit diameter and a 6° conical nozzle of 0.60 m exit diameter which can be used throughout the Mach number range from 15 to 20. Typical Reynolds numbers at Mach 15 range from 5×10^6 to $15 \times 10^6/\text{m}$. A high precision incidence mechanism for pitch, roll, and yaw is mounted in the open-jet 4 m^3 test section. Instrumentation includes a force/moment balance, accelerometers, thin-film and coaxial thermocouples for heat flux measurements, piezoresistive pressure transducers, and a schlieren system; 64 channels of transient recorders with a 50 kHz sampling rate are controlled by a PC.

Figure 16. The VKI Longshot Shock Tunnel.

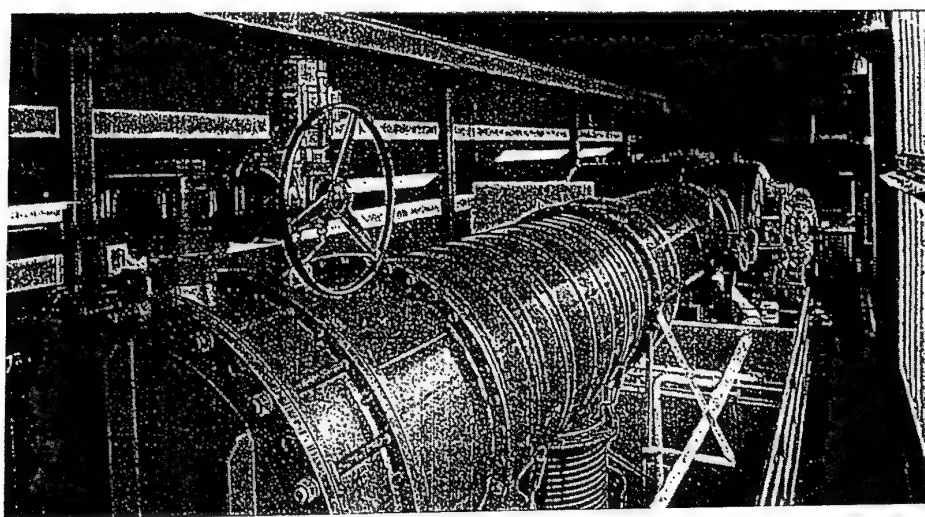


Figure 17. Photograph of the SR-3 Wind Tunnel at the CNRS (France).

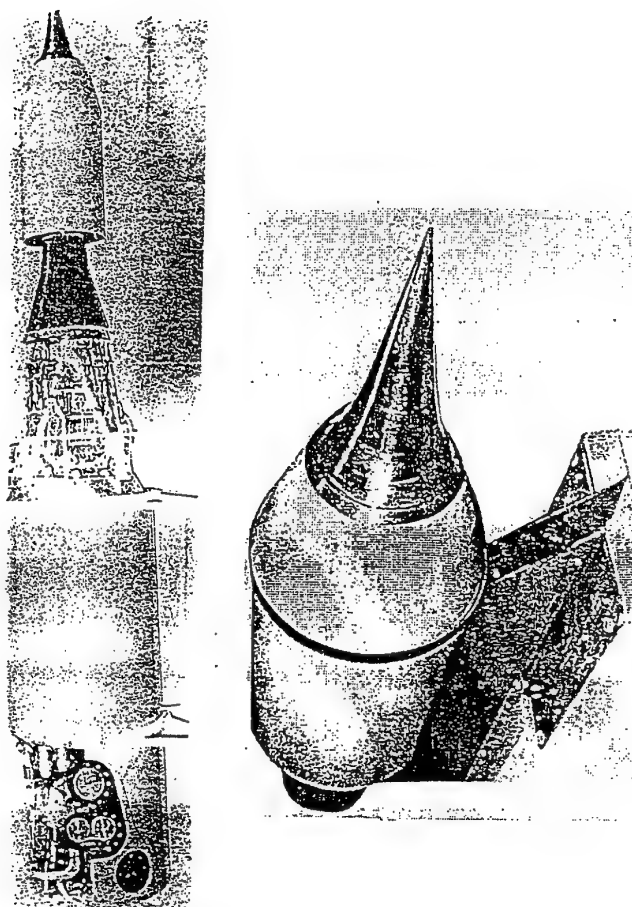
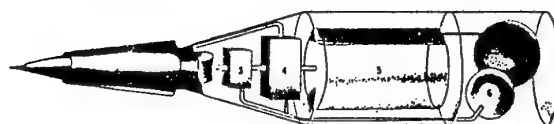


Figure 18. TsIAM Scramjet - A Flight Test Article.

HYPERSONIC FLYING LAB



- | | |
|-------------------------|-------------------------|
| 1 EXPERIMENTAL SCRAMJET | 5 LIQUID HYDROGEN TANK |
| 2 MEASUREMENT SYSTEM | 6 GAS NITROGEN CAPACITY |
| 3 CONTROL SYSTEM | 7 GAS HELIUM CAPACITY |
| 4 REGULATOR | |

LAB IS INTENDED FOR TESTING HIGH-VELOCITY HYDROGEN-BURNING ENGINES

LAUNCHING AND MAIN STAGES OF GROUND-TO-AIR MISSILE ARE USED FOR PROGRAMED FLIGHT

FLIGHT MACH NUMBER	8.0
ALTITUDE	30 KM
ONBOARD LIQUID HYDROGEN	
WEIGHT	17 kg
WEIGHT	595 kg
BASIC LENGTH	4.3 M
DIAMETER	750 MM

Figure 19. Hydrogen Scramjet First Flight was Performed in November, 1991.

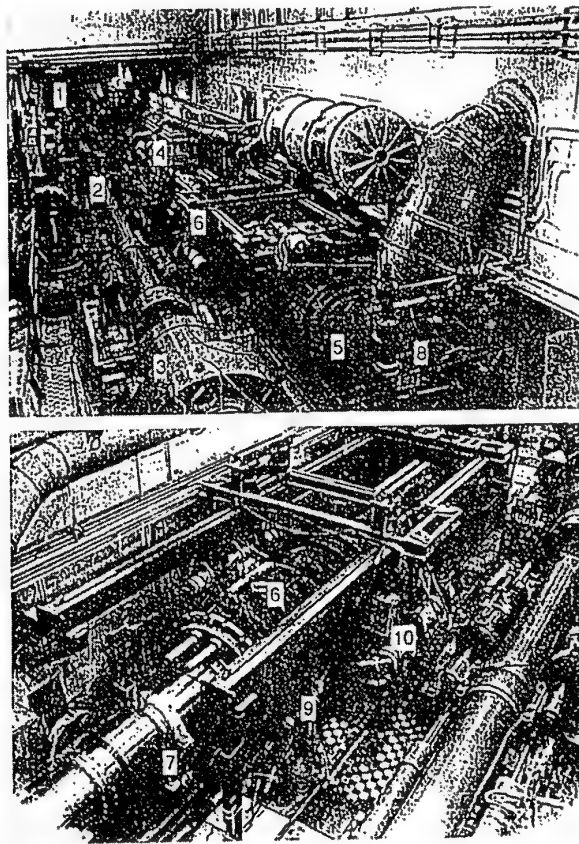
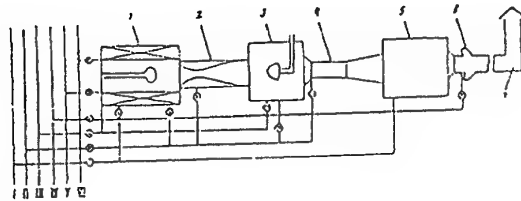


Figure 20. View of Piston Gasdynamic Units U-7 and U-11.



The unit diagram

I - water, $P_y = 5 \cdot 10^5$ Pa; II - water, $P_y = 1.6 \cdot 10^6$ Pa; III - water, $P_y = 10^7$ Pa; IV - air, $P_y = 2 \cdot 10^7$ Pa; V - nitrogen, $P_y = 3.2 \cdot 10^7$ Pa; VI - air, $P_y = 3.2 \cdot 10^7$ Pa.

I - electric-arc heater; 2 - nozzle; 3 - working section;
4 - diffuser; 5 - cooler-neutralizer; 6 - ejector;
7 - exhaust passage.

Figure 21. U-15 T1 Electric Arc Gas Dynamic Unit.

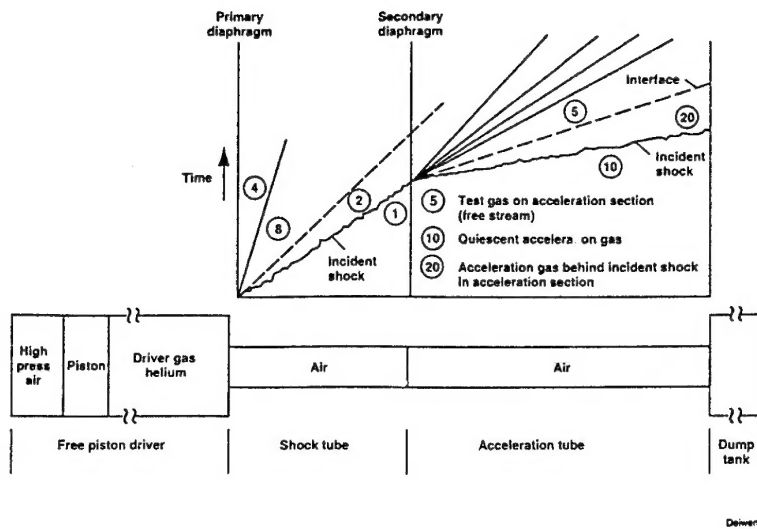


Figure 22. Operation of Shock Expansion Tunnel with Free Piston Driver.

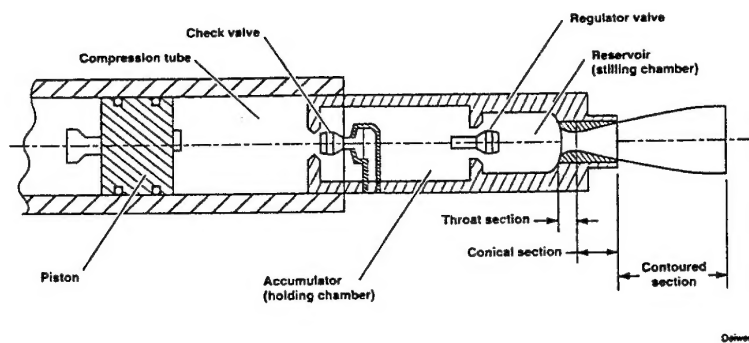


Figure 23. General Arrangement of PGU Compression Cascade.

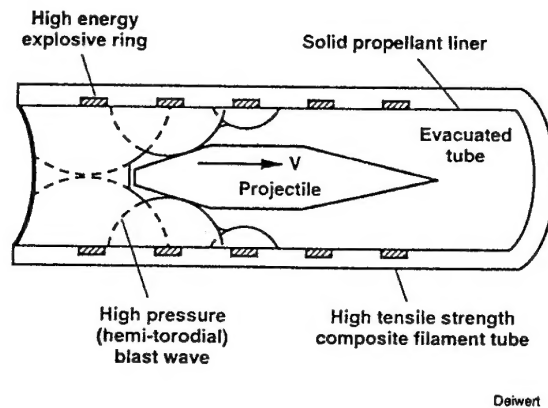


Figure 24. Oblique Detonation Wave Driver.

REPORT DOCUMENTATION PAGE

1. Recipient's Reference	2. Originator's Reference AGARD-AR-319 Vol. I	3. Further Reference ISBN 92-836-1037-7	4. Security Classification of Document UNCLASSIFIED/ UNLIMITED														
5. Originator	Advisory Group for Aerospace Research and Development North Atlantic Treaty Organization 7 rue Ancelle, 92200 Neuilly-sur-Seine, France																
6. Title	Hypersonic Experimental and Computational Capability, Improvement and Validation																
7. Presented at/sponsored by																	
8. Author(s)/Editor(s) Multiple			9. Date May 1996														
10. Author's/Editor's Address Multiple			11. Pages 203														
12. Distribution Statement	There are no restrictions on the distribution of this document. Information about the availability of this and other AGARD unclassified publications is given on the back cover.																
13. Keywords/Descriptors <table><tr><td>Experimentation</td><td>Viscous flow</td></tr><tr><td>Research projects</td><td>Computation</td></tr><tr><td>Hypersonic flow</td><td>Measurement</td></tr><tr><td>Test facilities</td><td>Rarefied gas dynamics</td></tr><tr><td>Aerothermodynamics</td><td>Boundary layer flow</td></tr><tr><td>Aerodynamics</td><td>Spacecraft</td></tr><tr><td>Fluid dynamics</td><td>Aerospace environment</td></tr></table>				Experimentation	Viscous flow	Research projects	Computation	Hypersonic flow	Measurement	Test facilities	Rarefied gas dynamics	Aerothermodynamics	Boundary layer flow	Aerodynamics	Spacecraft	Fluid dynamics	Aerospace environment
Experimentation	Viscous flow																
Research projects	Computation																
Hypersonic flow	Measurement																
Test facilities	Rarefied gas dynamics																
Aerothermodynamics	Boundary layer flow																
Aerodynamics	Spacecraft																
Fluid dynamics	Aerospace environment																
14. Abstract <p>The results of the phase I effort conducted under AGARD Working Group 18 on Hypersonic Experimental and Computational Capability, Improvement and Validation are presented in this report. A discussion of issues and problems classified into seven topic areas precedes the individual sections on Shock/Boundary-Layer Interactions, Laminar-Turbulent Transition, Rarefield Flow, Real-Gas Effects, Facility Calibration Procedures, Extrapolation to Flight and Hypersonic Test Facilities. Recommendations for future work in these areas is included at the end of each section. Conclusions for the work conducted during the phase II of this Working Group will be presented in Volume II.</p>																	

Aucun stock de publications n'a existé à AGARD. A partir de 1993, AGARD détiendra un stock limité des publications associées aux cycles de conférences et cours spéciaux ainsi que les AGARDographies et les rapports des groupes de travail, organisés et publiés à partir de 1993 inclus. Les demandes de renseignements doivent être adressées à AGARD par lettre ou par fax à l'adresse indiquée ci-dessus. *Veuillez ne pas téléphoner.* La diffusion initiale de toutes les publications de l'AGARD est effectuée auprès des pays membres de l'OTAN par l'intermédiaire des centres de distribution nationaux indiqués ci-dessous. Des exemplaires supplémentaires peuvent parfois être obtenus auprès de ces centres (à l'exception des Etats-Unis). Si vous souhaitez recevoir toutes les publications de l'AGARD, ou simplement celles qui concernent certains Panels, vous pouvez demander à être inclu sur la liste d'envoi de l'un de ces centres. Les publications de l'AGARD sont en vente auprès des agences indiquées ci-dessous, sous forme de photocopie ou de microfiche.

CENTRES DE DIFFUSION NATIONAUX**ALLEMAGNE**

Fachinformationszentrum Karlsruhe
D-76344 Eggenstein-Leopoldshafen 2

BELGIQUE

Coordonnateur AGARD-VSL
Etat-major de la Force aérienne
Quartier Reine Elisabeth
Rue d'Evere, 1140 Bruxelles

CANADA

Directeur, Services d'information scientifique
Ministère de la Défense nationale
Ottawa, Ontario K1A 0K2

DANEMARK

Danish Defence Research Establishment
Ryvangs Allé 1
P.O. Box 2715
DK-2100 Copenhagen Ø

ESPAGNE

INTA (AGARD Publications)
Carretera de Torrejón a Ajalvir, Pk.4
28850 Torrejón de Ardoz - Madrid

ETATS-UNIS

NASA Headquarters
Code JOB-1
Washington, D.C. 20546

FRANCE

O.N.E.R.A. (Direction)
29, Avenue de la Division Leclerc
92322 Châtillon Cedex

GRECE

Hellenic Air Force
Air War College
Scientific and Technical Library
Dekelia Air Force Base
Dekelia, Athens TGA 1010

ISLANDE

Director of Aviation
c/o Flugrad
Reykjavik

ITALIE

Aeronautica Militare
Ufficio del Delegato Nazionale all'AGARD
Aeroporto Pratica di Mare
00040 Pomezia (Roma)

LUXEMBOURG

Voir Belgique

NORVEGE

Norwegian Defence Research Establishment
Attn: Biblioteket
P.O. Box 25
N-2007 Kjeller

PAYS-BAS

Netherlands Delegation to AGARD
National Aerospace Laboratory NLR
P.O. Box 90502
1006 BM Amsterdam

PORTUGAL

Estado Maior da Força Aérea
SDFA - Centro de Documentação
Alfragide
2700 Amadora

ROYAUME-UNI

Defence Research Information Centre
Kentigern House
65 Brown Street
Glasgow G2 8EX

TURQUIE

Millî Savunma Başkanlığı (MSB)
ARGE Dairesi Başkanlığı (MSB)
06650 Bakanlıklar-Ankara

Le centre de distribution national des Etats-Unis ne détient PAS de stocks des publications de l'AGARD.

D'éventuelles demandes de photocopies doivent être formulées directement auprès du NASA Center for AeroSpace Information (CASI) à l'adresse ci-dessous. Toute notification de changement d'adresse doit être fait également auprès de CASI.

AGENCES DE VENTE

NASA Center for
AeroSpace Information (CASI)
800 Elkridge Landing Road
Linthicum Heights, MD 21090-2934
Etats-Unis

ESA/Information Retrieval Service
European Space Agency
10, rue Mario Nikis
75015 Paris
France

The British Library
Document Supply Division
Boston Spa, Wetherby
West Yorkshire LS23 7BQ
Royaume-Uni

Les demandes de microfiches ou de photocopies de documents AGARD (y compris les demandes faites auprès du CASI) doivent comporter la dénomination AGARD, ainsi que le numéro de série d'AGARD (par exemple AGARD-AG-315). Des informations analogues, telles que le titre et la date de publication sont souhaitables. Veuillez noter qu'il y a lieu de spécifier AGARD-R-nnn et AGARD-AR-nnn lors de la commande des rapports AGARD et des rapports consultatifs AGARD respectivement. Des références bibliographiques complètes ainsi que des résumés des publications AGARD figurent dans les journaux suivants:

Scientific and Technical Aerospace Reports (STAR)
publié par la NASA Scientific and Technical
Information Division
NASA Headquarters (JTT)
Washington D.C. 20546
Etats-Unis

Government Reports Announcements and Index (GRA&I)
publié par le National Technical Information Service
Springfield
Virginia 22161
Etats-Unis
(accessible également en mode interactif dans la base de
données bibliographiques en ligne du NTIS, et sur CD-ROM)



AGARD holds limited quantities of the publications that accompanied Lecture Series and Special Courses held in 1993 or later, and of AGARDographs and Working Group reports published from 1993 onward. For details, write or send a telefax to the address given above. *Please do not telephone.*

AGARD does not hold stocks of publications that accompanied earlier Lecture Series or Courses or of any other publications. Initial distribution of all AGARD publications is made to NATO nations through the National Distribution Centres listed below. Further copies are sometimes available from these centres (except in the United States). If you have a need to receive all AGARD publications, or just those relating to one or more specific AGARD Panels, they may be willing to include you (or your organisation) on their distribution list. AGARD publications may be purchased from the Sales Agencies listed below, in photocopy or microfiche form.

NATIONAL DISTRIBUTION CENTRES

BELGIUM

Coordonnateur AGARD — VSL
Etat-major de la Force aérienne
Quartier Reine Elisabeth
Rue d'Evere, 1140 Bruxelles

CANADA

Director Scientific Information Services
Dept of National Defence
Ottawa, Ontario K1A 0K2

DENMARK

Danish Defence Research Establishment
Ryvangs Allé 1
P.O. Box 2715
DK-2100 Copenhagen Ø

FRANCE

O.N.E.R.A. (Direction)
29 Avenue de la Division Leclerc
92322 Châtillon Cedex

GERMANY

Fachinformationszentrum Karlsruhe
D-76344 Eggenstein-Leopoldshafen 2

GREECE

Hellenic Air Force
Air War College
Scientific and Technical Library
Dekelia Air Force Base
Dekelia, Athens TGA 1010

ICELAND

Director of Aviation
c/o Flugrad
Reykjavik

ITALY

Aeronautica Militare
Ufficio del Delegato Nazionale all'AGARD
Aeroporto Pratica di Mare
00040 Pomezia (Roma)

LUXEMBOURG

See Belgium

NETHERLANDS

Netherlands Delegation to AGARD
National Aerospace Laboratory, NLR
P.O. Box 90502
1006 BM Amsterdam

NORWAY

Norwegian Defence Research Establishment
Attn: Biblioteket
P.O. Box 25
N-2007 Kjeller

PORTUGAL

Estado Maior da Força Aérea
SDFA - Centro de Documentação
Alfragide
2700 Amadora

SPAIN

INTA (AGARD Publications)
Carretera de Torrejón a Ajalvir, Pk.4
28850 Torrejón de Ardoz - Madrid

TURKEY

Millî Savunma Başkanlığı (MSB)
ARGE Dairesi Başkanlığı (MSB)
06650 Bakanlıklar-Ankara

UNITED KINGDOM

Defence Research Information Centre
Kentigern House
65 Brown Street
Glasgow G2 8EX

UNITED STATES

NASA Headquarters
Code JOB-1
Washington, D.C. 20546

The United States National Distribution Centre does NOT hold stocks of AGARD publications.

Applications for copies should be made direct to the NASA Center for AeroSpace Information (CASI) at the address below.

Change of address requests should also go to CASI.

SALES AGENCIES

NASA Center for

AeroSpace Information (CASI)
800 Elkridge Landing Road
Linthicum Heights, MD 21090-2934
United States

ESA/Information Retrieval Service
European Space Agency
10, rue Mario Nikis
75015 Paris
France

The British Library
Document Supply Centre
Boston Spa, Wetherby
West Yorkshire LS23 7BQ
United Kingdom

Requests for microfiches or photocopies of AGARD documents (including requests to CASI) should include the word 'AGARD' and the AGARD serial number (for example AGARD-AG-315). Collateral information such as title and publication date is desirable. Note that AGARD Reports and Advisory Reports should be specified as AGARD-R-nnn and AGARD-AR-nnn, respectively. Full bibliographical references and abstracts of AGARD publications are given in the following journals:

Scientific and Technical Aerospace Reports (STAR)
published by NASA Scientific and Technical
Information Division
NASA Headquarters (JTT)
Washington D.C. 20546
United States

Government Reports Announcements and Index (GRA&I)
published by the National Technical Information Service
Springfield
Virginia 22161
United States
(also available online in the NTIS Bibliographic
Database or on CD-ROM)



Printed by Canada Communication Group
45 Sacré-Cœur Blvd., Hull (Québec), Canada K1A 0S7